Development and assessment of a blind component separation method for cosmological parameter estimation

Caterina Umiltà

École Doctorale d'Astronomie et Astrophysique d'Île-de-France
UNIVERSITÉ PARIS VI - PIERRE & MARIE CURIE

DOCTORATE THESIS

Presented by

Caterina UMILTÀ

Development and assessment of a blind component separation method for cosmological parameter estimation

Thesis Advisors: Karim BENABED
Jean-François CARDOSO

prepared at Institut d'Astrophysique de Paris, CNRS (UMR 7095)
with financial support from the Institut Lagrange de Paris

Composition of the jury

Reviewers:	Carlo BACCIGALUPI	-	SISSA, Trieste, Italy
	Jacques DELABROUILLE	-	APC (Paris VII), Paris, France
Advisors:	Karim BENABED	-	IAP, Paris, France
	Jean-François CARDOSO	-	IAP, Paris, France
Examinators:	Nabila AGHANIM	-	IAS, Orsay, France
	Bertrand LAFORGE	-	LPNHE (Paris VI), Paris, France
	David MARY	-	Univ. S. Antipolis, Nice, France
Invited member:	Maude LE JEUNE	-	APC (Paris VII), Paris, France

Jusqu'ici, tout va bien.
[La Haine]

Abstract

The Planck satellite observed the whole sky at various frequencies in the microwave range. These data are of high value to cosmology, since they help understanding the primordial universe through the observation of the Cosmic Microwave Background (CMB) signal. To extract the CMB information, astrophysical foreground emissions need to be removed via component separation techniques.
In this work I use the blind component separation method SMICA to estimate the CMB angular power spectrum with the aim of using it for the estimation of cosmological parameters. In order to do so, small scales limitations as the residual contamination of unresolved point sources and the noise need to be addressed. In particular, the point sources are modelled as two independent populations with a flat angular power spectrum: by adding this information, the SMICA method is able to recover the joint emission law of point sources. Auto-spectra deriving from one sky map have a noise bias at small scales, while cross-spectra show no such bias. This is particularly true in the case of cross-spectra between data-splits, corresponding to sky maps with the same astrophysical content but different noise properties. I thus adapt SMICA to use data-split cross-spectra only.
The obtained CMB spectra from simulations and Planck 2015 data are used to estimate cosmological parameters. Results show that this estimation can be biased if the shape of the (weak) foreground residuals in the angular power spectrum is not well known. In the end, I also present results of the study of a Modified Gravity model called Induced Gravity.

Résumé en Français

Le rayonnement fossile, aussi connu sous l'acronyme anglo-saxon CMB (pour Cosmic Microwave Background), est un sujet d'étude clé pour la cosmologie. En effet, le CMB est constitué de la première lumière de l'univers, émise à peine 400 000 ans après le Big-Bang. Cette lumière, observable dans le ciel dans la bande de fréquences des micro-ondes, a gardé l'empreinte de l'état de l'univers à cette époque et c'est donc une précieuse source d'information pour la cosmologie. Ces informations peuvent nous aider à mieux quantifier certains paramètres des théories actuelles, comme la courbure spatiale de l'univers ou sa vitesse d'expansion.
La difficulté de l'étude du CMB provient du fait qu'il existe beaucoup d'autres processus astrophysiques, appelés "avant-plans", qui émettent dans la même gamme de fréquences que le rayonnement fossile. C'est le cas par exemple de la poussière galactique ou des galaxies lointaines. Comme ces sources émettent aussi dans la bande des micro-ondes, il est indispensable de savoir traiter les données de manière à séparer les differentes composantes, astrophysique ou rayonnement fossile. Vu la richesse d'information contenues dans le rayonnement fossile, plusieurs missions ont été lancées pour l'étudier, basées aussi bien sur Terre que dans l'espace. Parmi elles, la mission spatiale Planck vient de délivrer ses données et les résultats qu'elle a obtenus. Dans cette analyse, j'utilise principalement ces données.
De nombreuses méthodes de séparation de composantes ont été développées afin de réduire la contamination des avant-plans. Elles sont généralement très complexes, car elles nécessitent une connaissance fine des caractéristiques des émissions astrophysiques dans la bande de fréquences des micro-ondes. Pour cette raison, la méthode utilisée dans ce travail est une méthode aveugle, c'est-à-dire qu'elle ne fait pas d'hypothèses sur la physique des avant-plans. Cette méthode s'appelle SMICA (pour Spectral Matching Independent Component Analysis) et, pour différencier les avant-plans du CMB, utilise la différence de leur signature à travers les différentes fréquences, ainsi que leur spectre de puissance angulaire. SMICA s'appuie sur le spectre de puissance angulaire des cartes du ciel publiées par Planck pour obtenir une estimation directe du spectre de puissance angulaire du CMB, qu'elle utilise ensuite pour reconstruire une carte du rayonnement fossile nettoyée des avant-plans. C'est en effet ce spectre de puissance qui est utilisé pour les études cosmologiques.
Néanmoins, il n'a pas été possible jusqu'à présent d'utiliser les résultats de SMICA pour des études cosmologiques. La détermination des petites échelles du spectre de puissance angulaire du CMB est limitée par les avant-plans comme les galaxies lointaines, ou "sources ponctuelles", et le biais du bruit. Dans cette analyse, ces deux limitations sont abordées. En ajoutant des hypothèses sur la physique des avant-plans, il est possible de guider l'algorithme pour détecter les contaminations des source pontcuelles : nous savons que ces

sources sont réparties en deux populations indépendantes, qui dominent dans deux bandes spectrales différentes, le radio et l'infrarouge. Introduire des hypothèses sur les galaxies lointaines signifie être capable de caractériser les contaminations résiduelles dans le CMB, mais aussi diminuer le caractère aveugle de la méthode.
Quand on obtient un spectre de puissance d'une carte du ciel, ce spectre a un biais dû au bruit à petites échelles. Par contre, les spectres obtenus en croisant différentes cartes n'ont plus ce biais. Or la méthode SMICA suppose la présence de ce biais dans les données. Dans cette analyse j'ai adapté la méthode SMICA pour qu'elle n'utilise que les spectres de puissance angulaire obtenus par les différentes cartes, diminuant l'incertitude due au bruit dans l'estimation du CMB.
Cette méthode à été étudiée sur de nombreuses simulations ainsi que sur les données Planck 2015. Utilisant l'estimation du spectre de puissance angulaire de SMICA, il a été possible d'estimer les paramètres cosmologiques. Les résultats montrent que la contamination résiduelle des avant-plans présente dans le spectre, bien que fortement réduite, peut néanmoins introduire des biais dans l'estimation des paramètres, si la forme des résiduels n'est pas bien connue.
L'estimation du spectre de puissance angulaire du CMB devient critique lorsqu'on l'utilise pour étudier des modèles cosmologiques différents. Dans cette thèse, je montre les résultats obtenus en étudiant un modèle de gravité modifiée.

Contents

Introduction

The CMB is a gold mine for cosmology since it provides an image of the state of the universe more than 13 billion years ago. This signal has an almost perfect black-body spectrum of $T \sim 2.7$ K, and on the sky the CMB appears as an homogeneous and isotropic signal with small Gaussian-distributed temperature anisotropies of the order of $\delta T/T \sim 10^{-5}$. The evolution of these small fluctuations has shaped the universe as we observe it today. The CMB thus contains all the ingredients necessary for the later evolution, but their properties can be described in a much more straightforward way than the present day universe. In particular, the CMB angular power spectrum contains all the cosmological information of the CMB.
The CMB primordial signal is not directly accessible since we observe other emissions of more recent astrophysical origin on top of it. These "foregrounds" are the microwave emission of our Galaxy and that of background galaxies, and arise from a number of different physical processes. In particular, background galaxies, or "point sources", can be divided in two different populations, one that dominates in the radio band and one that dominates in the infrared band.
Characterizing and removing the contamination of the foregrounds is the aim of component separation methods. Among the different existing techniques, blind methods are particularly interesting since they only use minimal assumptions on the signals, and to achieve separation they exploit the different statistical properties of the foregrounds and the CMB. In order to well characterize the foregrounds properties, it is important to look at their emission at various frequencies.
Various observational missions have been led, both from the ground and from space, to study the CMB. Space missions have the advantage of observing the full sky and of accessing a wider frequency range than what can be done from Earth, since they do not suffer from the limitations of the atmosphere. The Planck satellite has observed the sky in 9 frequency bands with an unprecedented resolution from 30 GHz to 857 GHz. The *Planck Collaboration* has used these data to produce four foreground-cleaned CMB maps using different component separation methods. Among them, the SMICA (Spectral Matching Independent Component Analysis) technique is a blind method that works at the spectral level, by fitting a (blind) model for the CMB and foregrounds to the data angular power spectra.
The Planck CMB maps can be used for studies on lensing, non-Gaussianity and statistical isotropy of the CMB. However, these maps have a small scale residual foreground contamination which is not well characterized that prevents their use for cosmological purposes. For this reason, the *Planck Collaboration* cosmological analysis is not based on the reconstructed CMB maps but on a likelihood built on the data itself. The Planck likelihood uses the angular power spectra of a few data maps, chosen since they have a low

foreground contamination. Even though a part of this contamination can be reduced by masking, a contribution of the foregrounds is still present in the data spectra. The likelihood function accounts for this incorporating a large parametric model for the foregrounds, whose parameters are jointly fit with the cosmological ones. The small scale extragalactic contamination however is difficult to constrain and some assumptions on the cosmological model for the CMB are required when computing the likelihood covariance matrix.
This work tries to reconcile both approaches, using the CMB spectrum obtained via component separation as an input to the likelihood in order to estimate cosmological parameters. In order to do so, it is necessary to adapt existing methods to characterize the extragalactic contamination. The small scales of the angular power spectrum are particularly important for cosmology since they have more statistical weight than large scales. I use a particular configuration of the blind method SMICA to estimate the CMB power spectrum, with particular attention to two small scales limitations: the noise and the extragalactic point sources.
To target background galaxies, I use a foreground model that accounts for two independent populations of point sources. In order to target the noise bias instead, I construct the data statistics used by SMICA only using cross-angular power spectra between the maps. I then use the resulting CMB angular power spectrum for estimating cosmological parameters. Contrary to the Planck likelihood approach, no assumption on the underlying cosmological model is done.
This is particularly important when investigating alternatives to the standard cosmological model. One possible alternative comes from models that consider a theory of gravitation different from General Relativity. This class of models is referred to as Modified Gravity. In this thesis I present the results of the study of a scalar-tensor Modified Gravity model, in which a scalar field drives the accelerated expansion of the universe.
This thesis is organised as follows:

- the first Chapter introduces the relevant informations about the CMB, like its origin, the definition of the angular power spectrum and how it relates to cosmological parameters;
- the second Chapter describes the characteristics of the principal foregrounds, as well as the existing component separation methods;
- the third Chapter presents the principles on which the SMICA method is based;
- the fourth Chapter resumes the main results of this work, describing the modified SMICA configuration, its results and the obtained cosmological parameters;
- the fifth Chapter presents a modified Gravity Model, called Induced Gravity, and the constraints that can be put on its regulating parameter γ by present data.

Then, I present my conclusions and some perspectives for the future.

Chapter 1

The CMB from a cosmological perspective

Contents

The Cosmic Microwave Background is one of the most important probes of the cosmological model. In this Chapter I will first describe the basic concepts of the standard cosmological model and then how the CMB arises within this framework and what are its main characteristics. The last two Sections are dedicated to the CMB data: what are the principal telescopes and a few considerations on the treatment of data on the sphere.

1.1 The cosmological framework

Our description of the universe is based on various pieces of observational evidence. By looking at the universe on large scales, we see that it is homogeneous and isotropic.

Measuring the peculiar velocities of galaxies in the nearby universe, we see that the universe is expanding and we can compute its expansion rate H_0 (Riess et al., 2016). When looking farther, we note that this expansion is accelerating, meaning that farther objects move away from us faster than those close by (Conley et al., 2011). The light curves of galaxies compared to their visible light as well as strong lensing observations (Fort & Mellier, 1994) tell us that an invisible type of matter exists, called dark matter, that does not interact electromagnetically with radiation. The abundances of light elements in low metallicity environments constrain the density of baryonic matter (Fields et al., 2014). Finally, the Cosmic Microwave Background gives us a picture of the primordial universe (Planck Collaboration I et al., 2016).
The expansion of the universe, the abundance ratio of light elements and the presence of a relic microwave radiation are all observed predictions of the Big Bang theory formulated by Gamow in 1946 (Gamow, 1946). The equations that govern the expansion of the universe are derived from the theory of General Relativity (GR). GR describes how the geometry of the universe and its energetic content are related. Given that the universe is isotropic and homogeneous on large scales, its metric is well described by the Friedmann-Robertson-Walker (FRW) metric, whose line element in spherical coordinates (r, θ, ϕ) is:

$$ds^2 = dt^2 - a(t)^2\left[\frac{dr^2}{1 - Kr^2} + r^2(d\theta^2 + sin^2\theta d\phi^2)\right], \tag{1.1}$$

where ds is the distance in time and space between two events, $a(t)$ is the scale factor of the universe and K is the curvature parameter. The curvature parameter depends on whether the geometry of the universe is open, flat or closed, and takes the value -1, 0 and 1 respectively. Observationally, the universe seems flat (Planck Collaboration XIII et al., 2016), so we use $K = 0$ in the following. The scale factor a describes how the universe scales in time, and the convention is to consider $a_0 = 1$, where the subscript 0 commonly denotes values at present time.

1.1.1 The Friedmann equations

Solving GR equations using FRW metric and assuming that the content of the universe behaves as a perfect fluid[1], one obtains Friedmann equations:

$$\left(\frac{\dot{a}}{a}\right)^2 = \frac{8\pi G}{3}\rho, \tag{1.2a}$$

$$\frac{\ddot{a}}{a} = -\frac{4\pi G}{3}(\rho + 3P), \tag{1.2b}$$

where P and ρ are the pressure and density of the fluid, G is Newton's gravitational constant and an overdot represents derivation with respect to cosmic time. These equations describe how the scale factor a evolves. Friedmann equations have a singularity for $a = 0$. The Hubble parameter H, which denotes the derivative of the logarithm of the scale factor, is defined as:

$$H(t) \equiv \frac{d \ln a}{dt} = \frac{\dot{a}}{a}. \tag{1.3}$$

Its value at present time is the Hubble constant H_0. It is sometimes parametrized with the adimensional factor h, which is defined as $H_0 = 100\ h\ kms^{-1}Mpc^{-1}$. We express the

[1] i.e., a fluid that can be described only in terms of its density and pressure.

time evolution in terms of cosmic time t, the scale factor $a(t)$ or the redshift z, defined as:

$$1 + z \equiv \frac{a_0}{a}. \tag{1.4}$$

The density of a fluid evolves as $\rho \propto a^{-3(\omega+1)}$, where $\omega = P/\rho$ is the equation of state.
The standard fluids considered by Eqs. (1.2) are matter, radiation, neutrinos and dark energy, where matter comprises both dark matter and baryonic matter.
There are different hypotheses on the nature of dark matter, and the standard description is to consider heavy non-relativistic particles, labelled cold dark matter (CDM). Matter has negligible pressure thus $\omega = 0$ and $\rho \propto a^{-3}$, while radiation and neutrinos have $\omega = \frac{1}{3}$ and $\rho \propto a^{-4}$. Combining these relations with Friedmann equations and observational data it is possible to see that the universe in the past was much denser and the scale factor was much smaller. The dark energy component instead has radically different properties from the other observed components, and behaves as a fluid with negative pressure. This type of fluid is necessary in order to have an accelerated expansion in Eq. (1.2b), as we observe it today. A minimal model of dark energy can be expressed in terms of the cosmological constant Λ, that corresponds to a fluid of constant energy density and equation of state ω = -1.
In the early phases of evolution of the universe, its energetic content was dominated by radiation. Eventually, since radiation density dilutes faster than matter density, matter became the dominant component. The shifting point between these two epochs is called matter-radiation equality. This change in the dominant component determines a change in the expansion rate of the universe, which is slower in the matter dominated epoch. At recent time, the dark energy component has become dominant and the universe entered a phase of accelerated expansion, which lasts until today. The dominant components across various epoch are shown in Figure 1.1. The model described above is commonly referred to as ΛCDM.

1.1.2 Beyond this framework

The ΛCDM model well describes the observational evidence we have, from the CMB features to the galaxy cluster counts. There are however a few unexplained questions in this model. One of them is the nature of dark matter. Various hypotheses have been formulated, the main candidates being the Weakly Interacting Massive Particles (WIMPs) or axions (see Arcadi et al. (2017) and Marsh (2016) for a review). Since dark matter does not interact electromagnetically with radiation, direct observations are quite challenging. Annihilation or collision of these particles could potentially emit observable radiation, but up to now no detection has been confirmed (Cirelli, 2015).
Another issue is the nature of dark energy. The common interpretation of the cosmological constant is that it represents the vacuum energy. However, theoretical estimates do not agree by several orders of magnitude with the observed dark energy density (Weinberg, 1989). This is an open problem of the ΛCDM model. Alternative theories such as quintessence explain dark energy in terms of a scalar field which drives the acceleration. The behaviour of this time-evolving dark energy depends on the form of the potential of the scalar field (Tsujikawa, 2013).
Another possibility for explaining dark energy is to consider the problem from a radically

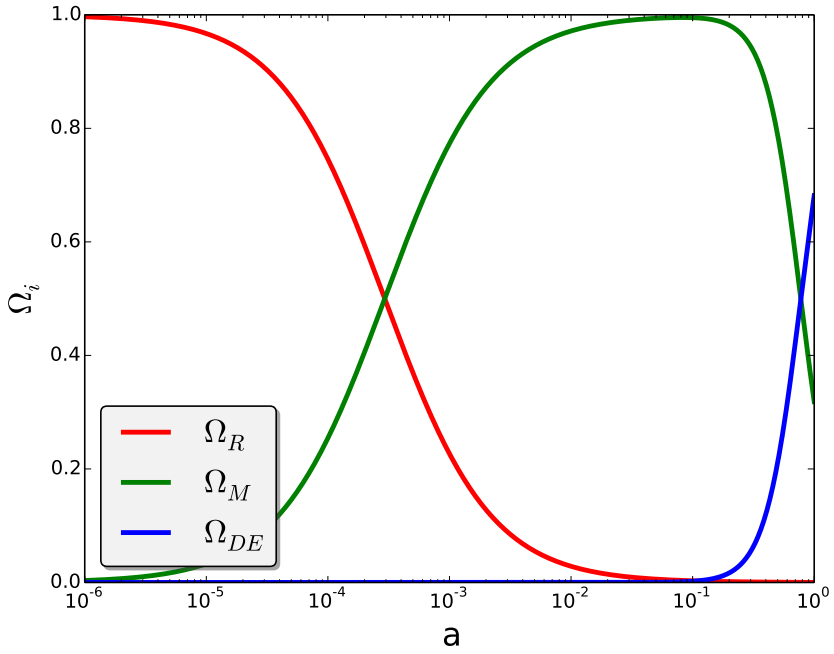

Figure 1.1 – The evolution of the radiation (R), matter (M) and dark energy (DE) density parameters defined in Eq. (1.8). Three epochs are clearly distinguishable: a radiation dominated epoch in early times, then a matter dominated epoch, while, at very recent times, the dark energy component prevails over matter.

different perspective: a different theory of gravitation. Models that do not assume GR can formulate the gravitational interaction in a way that leads naturally to an accelerated expansion. However these models must also explain all the observational evidence on solar system scales that GR as been successful in explaining, which is not a trivial task. This class of alternative models is referred to as Modified Gravity. A study of a Modified Gravity model, called Induced Gravity, is presented in Chapter 5.

1.2 The Cosmic Microwave Backround

The CMB radiation originates in the early phases of evolution of the universe. For this reason, it represents a (narrow) window on epochs that are otherwise inaccessible to observations. Its existence is a striking evidence in support of the Big Bang theory.
Today we see that the universe is expanding, so we expect, out of thermodynamics considerations, that is was hotter and denser in the past. Looking backwards in time, there is one epoch where temperature is so high that atoms are completely ionized. In this epoch, photons interact with free electrons and are in thermal equilibrium with them. This imprints on the photons a black-body spectrum; we say that the photons and baryons are coupled. Due to frequent interactions, the photons have a short mean free path and the universe is optically thick, i.e., non transparent. As time passes, the density decreases and the temperature lowers. Because of these collisions between electrons and photons, the temperature decreases as $T \propto a^{-1}$. Eventually the universe has cooled enough that ions and electrons form neutral atoms, and this lowers the scattering rate. This process is called recombination.

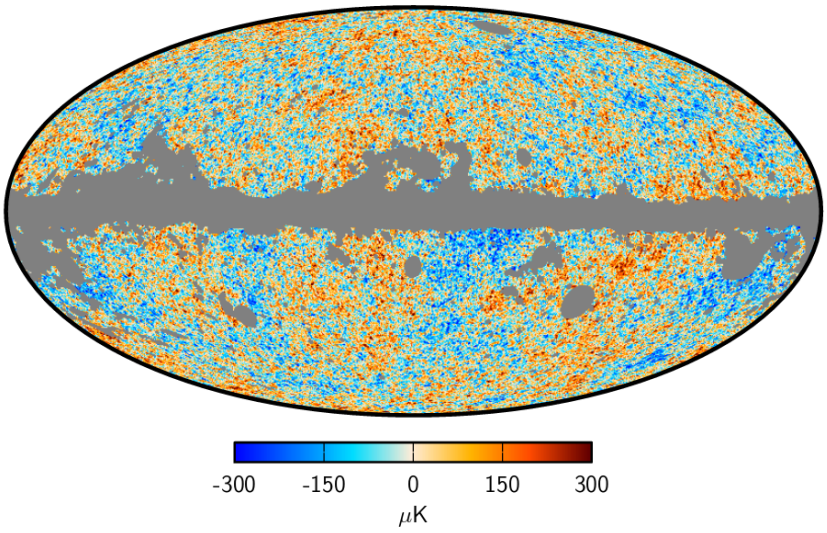

Figure 1.2 – The CMB temperature anisotropies map reconstructed with the SMICA method. Figure taken from Planck Collaboration IX et al. (2016).

At around T∼3000 K, the temperature is low enough that the universe is almost entirely neutral, the photons mean free path becomes infinite and the universe becomes transparent. Most of these photons do not have any further interaction until today and the radiation we observe is almost like a snapshot of the state of the universe at the time of recombination. The temperature of photons continues to decrease and has reached today a value of ~ 2.7K. To a present day observer, this radiation appears like coming from a spherical surface whose radius is the distance a photon has travelled since its last scattering interaction with an atom, which is at $z_{ls} \approx 1100$. This is called the last scattering surface. Of course, the distance to last scattering is slightly different for each photon, since recombination happens in a narrow window of time but it is not an instantaneous process.
Today we observe a CMB temperature that is by a large degree homogeneous and isotropic. This reflects the state of the universe at z_{ls}. There are however small anisotropies of the order of $\delta T/T \sim 10^{-5}$, which are an extremely valuable source of information for cosmology. In fact, these fluctuations in the temperature field depend on the matter perturbations at the epoch of recombination, which have since then grown to form the large scale structure we observe today.
The isotropy of the CMB radiation poses an issue, since on the sky we observe photons coming from zones that apparently are more distant than their horizon size, i.e., not in causal connection. This implies that these regions have been put in causal connection before due to the previous expansion history of the universe. The more credited explanation is the theory of inflation, originally proposed by Guth (Guth, 1981). This theory states that, for a brief period of time, the universe has a phase of highly accelerated expansion, faster than the expansion of the horizon. This happens in the very early phases of its evolution, much before recombination. Due to this very fast expansion, any inhomogeneity present before is washed out and only very small perturbations are left. These perturbations are approximately scale invariant, and since they are generated at the same epoch they begin to oscillate with the same phase on all Fourier modes. For a good review on the physics of the CMB see for example the review papers Kamionkowski & Kosowsky (1999); Hu &

Dodelson (2002); Samtleben et al. (2007) and the textbooks Dodelson (2003); Weinberg (2008).

1.2.1 The angular power spectrum

Since the CMB anisotropies are approximately Gaussian random fluctuations (Planck Collaboration et al., 2016c), they are fully characterized by their angular power spectrum. The map of the CMB temperature anisotropies is shown in Figure 1.2. We can then describe the anisotropies $\delta T(\theta, \phi)$ of the temperature field $T(\theta, \phi)$ as:

$$\delta T(\theta, \phi) \equiv T(\theta, \phi) - \langle T(\theta, \phi) \rangle = \sum_{l=1}^{\infty} \sum_{m=-\ell}^{\ell} a_{\ell m} Y_{\ell m}(\theta, \phi), \tag{1.5}$$

where the rightmost term is the expansion in spherical harmonics $Y_{\ell m}(\theta, \phi)$. The physical information is contained in the spherical harmonics coefficients $a_{\ell m}$. The $Y_{\ell m}(\theta, \phi)$ are a spatial frequency basis for representing functions defined over the sphere. More details about them are given in Section 1.4.1. The index ℓ, called multipole, is the angular frequency which is related to the angular scale; $\ell = 0$ is the monopole terms, $\ell = 1$ the dipole, and $\ell = 2$ the quadrupole. Large ℓ correspond to small angular scales, and vice-versa. Since the temperature anisotropies are Gaussian stationary and isotropic, the average of the spherical harmonics coefficients is zero $\langle a_{\ell m} \rangle = 0$. Nevertheless their variance is non null and its angular power spectrum C_ℓ, which is independent of m:

$$\langle a^*_{\ell m} a_{\ell' m'} \rangle = C_\ell \delta_{\ell \ell'} \delta_{m m'}, \tag{1.6}$$

where δ is the Kronecker delta and the average is ideally performed aver an ensemble of different realizations and the superscript * denotes complex conjugation. Since we observe only one universe, we can only average over the m modes. The empirical estimation of the angular power spectrum is:

$$\hat{C}_\ell = \frac{1}{2\ell + 1} \sum_{m=-\ell}^{\ell} |a_{\ell m}|^2 \tag{1.7}$$

where the factor $2\ell + 1$ appears since that is the number of m modes at each ℓ.
Figure 1.3 shows the CMB angular power spectrum as obtained by the *Planck Collaboration* in terms of $D_\ell = \frac{\ell(\ell+1)}{2} C_\ell$. The black dots represent the data points, while the red curve represents the theoretical spectrum obtained from the fiducial cosmological model. It is evident that the ΛCDM model fits very well Planck data.
The C_ℓ spectrum can be divided between large angular scales, which are the scales larger than the horizon size at recombination and correspond to small ℓ, and the small angular scales, which conversely correspond to large ℓ and describe the perturbations inside the horizon. While small angular scales depend on various effects due to interactions between photons and matter, large scales are not affected by causal physics and represent the state of perturbations as they where set by inflation. A good review of the physical mechanisms that determine the CMB angular power spectrum features can be found in (Hu et al., 1996).
At small angular scales we observe a number of peaks, which result from the fluctuations of the coupled fluid of baryons and photons. Before recombination, due to gravitational attraction, dark matter clusters in overdensities surrounded by underdense regions. The

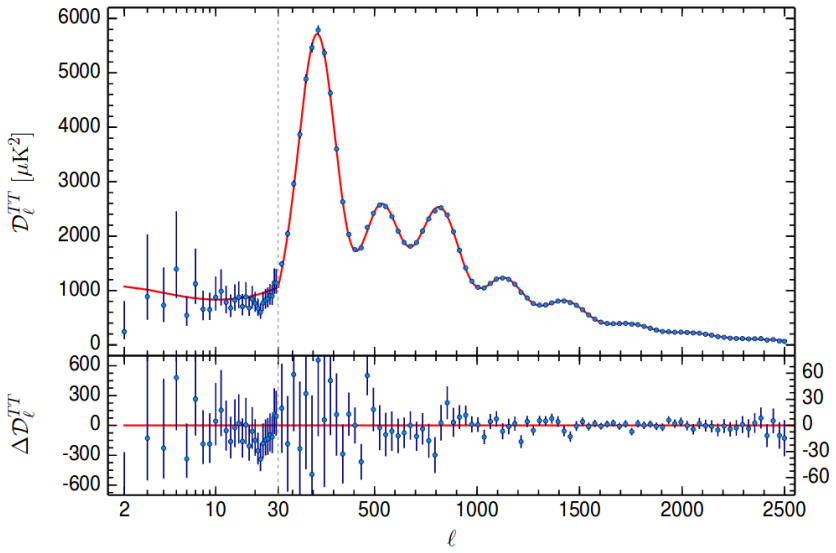

Figure 1.3 – Figure taken from Planck Collaboration I et al. (2016). *Upper panel:* The angular power spectrum of CMB temperature anisotropies as observed by Planck. At multipole $\ell \geq 30$ the data points show the maximum-likelihood frequency-averaged spectrum computed with the cross-halfmission likelihood, where foregrounds and other nuisance computed from a Monte Carlo Markov Chain (MCMC) analysis of the ΛCDM model have been subtracted. At multipoles $\ell \leq 29$ the data points are an estimate of the Commander component separation methods, described in Chapter 2. At low multipoles, error bars are larger due to cosmic variance. The red line shows the theoretical prediction of the best fit ΛCDM model, which is in very good agreement with the observational data points. *Lower panel:* Residuals of the data with respect to the theoretical model.

photon-baryon fluid, attracted by dark matter, falls in the gravitational potential wells of the overdense regions, and oscillates inside these wells subject to its own repulsive radiation pressure given by the compressed photons and the gravitational attraction. Oscillations happen on all scales inside the horizon and translate into density and velocity variations of the fluid. The presence of baryons, which are massive and thus deepen the potential wells, induces an enhancement in the fluid compression. These oscillations are called "acoustic", and produce temperature variations in the photons. The oscillations are also imprinted in the baryon density perturbations, and are called baryon acoustic oscillations (BAO).
Scales that are in the extrema of their oscillation at recombination have enhanced temperature fluctuations. In the angular power spectrum we observe a peak corresponding to these scales. The first peak corresponds to the scale which compressed inside the potential well just once. The second peak corresponds to the scale which compressed and then rarefied, the third peak to the scale which compressed two times, and so on.
At large angular scales photons are subject to matter inhomogeneities: overdense regions are hotter than underdense ones. Also, photons experience an energy shift if at recombination they have to climb out of potential wells or roll down potential hills created by dark matter perturbations. This is called the Sachs-Wolfe effect.
These anisotropies originate at the epoch of last scattering and are called *primary anisotropies*. Anisotropies that arise as the photons travel towards us are termed *secondary anisotropies* and they may provide information on the expansion history and structure

formation of the universe (Aghanim et al., 2008). They are usually smaller than primary anisotropies and can arise due to different reasons. For example, photons passing through a gravitational potential that changes in time have a net gain or loss of energy (integrated Sachs-Wolfe effect). The features of the integrated Sachs-Wolfe effect appear at low multipoles. Since this effect depends mainly on the low redshift dynamics, it could be useful to distinguish between different models of dark energy (Perrotta et al., 2000). If photons travel through a galaxy cluster, the interaction with the hot gas also changes their energy: this is instead a small scale effect (see Section 2.3.3 for more details). Additionally, due to gravitational lensing, photons are deflected from their original trajectories and this blurs the CMB map. Furthermore, after the advent of first stars and the galaxies, the universe was reionized due to the emission of highly energetic photons: this also affects the CMB photons since they can interact with the free electrons. In particular this produces an enhancement of the polarization angular power spectrum at scales corresponding to the horizon size at reionization. Another effect is the suppression of anisotropies within the horizon (Zaldarriaga et al., 1997; Seljak & Zaldarriaga, 1997).

1.2.2 Polarization

A fraction of the CMB radiation is linearly polarized. As atoms begin to recombine, the existing perturbations give origin to a quadrupole anisotropy in the distribution of photons. Because of the difference in the intensity of radiation coming from perpendicular directions, the still existing fraction of free electrons oscillates in a preferential direction. When photons scatter off these electrons they are linearly polarized.
The polarization pattern in the sky is specified by a degree of polarization and the preferred direction of the electric field. This can be described by two scalar fields which, in analogy to the decomposition of an electromagnetic radiation vector field into a curl-free electric field and a divergence-free magnetic field, are called “E mode” and “B mode” respectively. The E mode is a scalar function that describes the component of polarization with even parity, while the B mode is a pseudo scalar function that describes the odd parity component of polarization. Temperature fluctuations are also even functions, so they correlate with the E mode but not with the B mode. It is more convenient to describe polarization in terms of E and B modes than in terms of U and Q polarization Stokes (shown in Figure 1.4) since, due to their scalar nature, they do not depend on the coordinate system used to calculate them.
Scalar density perturbations produce the E mode only. The B mode comes from the tensor distortions of the space-time metric, since these have a handedness. Gravitational waves generated during the inflationary period are supposed to produce a B mode signal (Seljak & Zaldarriaga, 1997). This is however quite difficult to detect since it is a very weak signal. Also, due to lensing effects, a fraction of the E mode is transformed into the B mode, thus making the primordial B mode detection even more challenging.
Similarly to the temperature anisotropies, we can map the E mode and B mode components on the sky and then expand them in spherical harmonics. The resulting angular power spectra are usually referred to C_ℓ^{EE}, C_ℓ^{BB} and C_ℓ^{TE}, where the latter is the temperature polarization cross-correlation. The temperature spectrum is denoted as C_ℓ^{TT}. Since the temperature fluctuations are even functions, the expected C_ℓ^{TB} spectrum is null.

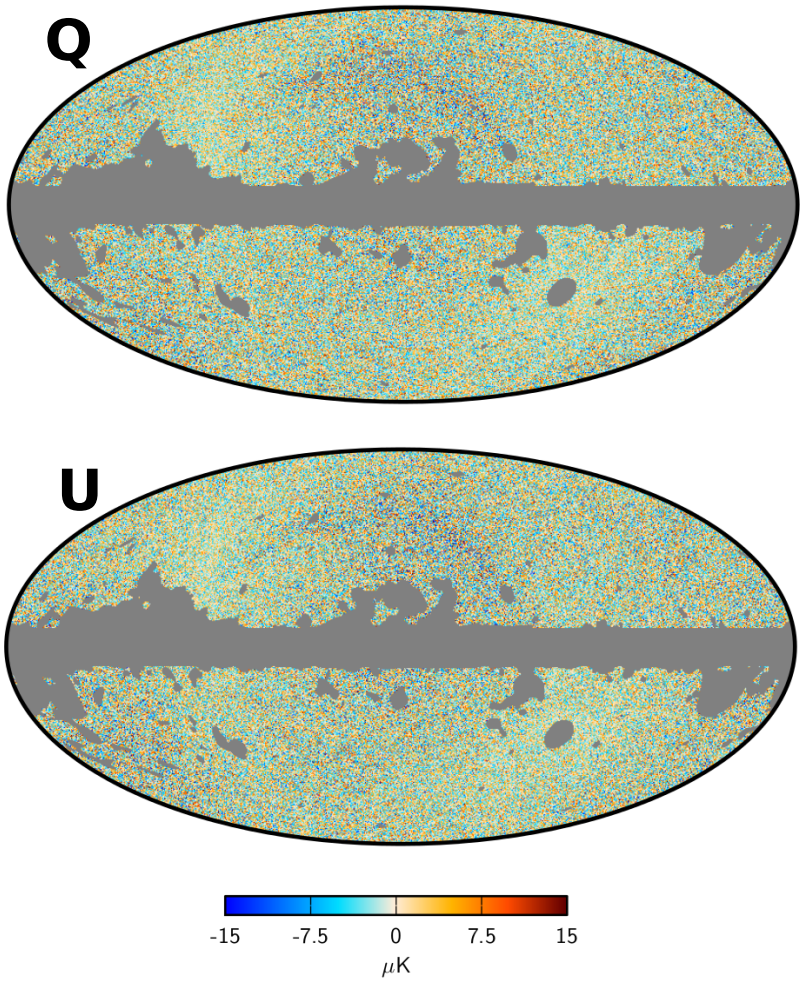

Figure 1.4 – The CMB Q and U polarization Stokes reconstructed with the SMICA method. Figure taken from Planck Collaboration IX et al. (2016).

1.2.3 The main cosmological parameters

The base ΛCDM model is well described by 6 parameters, that determine the C_ℓ shape and that provide information on different aspects of the physics of the universe. The standard parameters are ω_b, ω_c, θ_*, τ, A_s and n_s. The features of angular power spectrum, such as for example the position of the peaks and their relative height, are used to constrain these parameters. This description based on only six parameters is an approximation. However other parameters are secondary and have less influence on the shape of the CMB angular power spectrum, being thus less constrained by CMB data. Among these there are for example the primordial helium fraction y_{He} or the mass of neutrinos m_ν.
The ω_b and ω_c parameters are the baryon and cold dark matter density respectively. They are defined as $\omega_i = \Omega_i h^2$, where Ω_i is the density parameter of a given component:

$$\Omega_i \equiv \frac{\rho_i}{\rho_c} = \frac{8\pi G \rho_i}{3H^2}, \tag{1.8}$$

which denotes relative contribution of the component to the total density of the (flat) universe. The time evolution of the density parameters is shown in Figure 1.1. Here ρ_i

is the component's density, and ρ_c is the critical density, that is the total density of the universe required in order to have a flat geometry. The density parameter of the whole universe is $\Omega_{tot} = \sum_i \Omega_i = \sum_i \rho_i/\rho_c$, and for a flat universe Ω_{tot} =1. The curvature is expressed in terms of $\Omega_k = 1 - \Omega_{tot}$. Constraints are given in terms of $\Omega_i h^2$ instead of Ω_i since the characteristics of the peaks of the angular power spectrum depend on the former expression.
Typical values for the present day densities are $\Omega_{0,b} \sim 0.04$, $\Omega_{0,c} \sim 0.26$ and $\Omega_{0,DE} \sim 0.7$, where the subscripts b, c, and DE indicate baryons, cold dark matter and dark energy respectively. While the geometry of the universe cannot change, the density parameter evolves in time: in the past Ω_{DE} was much lower and the universe density was dominated by radiation first and by matter then. At present, neutrinos and radiation densities have values $\ll 1$.
The parameter θ is determined by the peaks positions and represents the angular scale of the sound horizon at decoupling:

$$\theta \equiv \frac{r_s}{d_A} \tag{1.9}$$

where r_s is the comoving[2] sound horizon at decoupling, that is the distance a density wave could have travelled in the photon-baryon plasma, and d_A is the angular diameter distance, that multiplied by an observed angle gives the size of the observed feature at the time of decoupling. Since θ is associated with the position of the acoustic peaks, and of the first peak in particular, it is very well determined by current data (Page et al., 2003).
The position of the first peak is important to determine the geometry of the universe, but cannot constrain it alone. Since this position depends on the curvature, the matter and dark energy density parameters, there is an intrinsic degeneracy among these three. In particular, by changing the value of H_0, it is possible to obtain the same θ for different combinations of these parameters (Efstathiou & Bond, 1999). The degeneracy is broken by taking into account external information, such as BAO or local measurements of H_0 (Planck Collaboration XIII et al., 2016).
The parameters A_s and n_s represent the amplitude and the tilt of the primordial spectrum of scalar perturbations. In terms of the CMB angular power spectrum, they determine its normalization and its slope. It is evident that a wider range of available multipoles can improve the determination of n_s. However, as we will see in Chapter 4, a residual astrophysical contamination is particularly harmful for the estimation of this parameter (Huffenberger et al., 2006).
The parameter τ is the optical depth to the last scattering surface. Due to the universe reionization, the CMB photons encounter free electrons and scatter again. If many CMB photons are re-scattered, i.e., if the optical depth is high, anisotropies are washed out. Thus τ translates into an attenuation of the spectrum within the horizon size at reionization: the net effect is a suppression by a factor $e^{-2\tau}$ of small scales with respect to large scales. This is approximately degenerate with the parameter A_s that sets the overall normalization of the spectrum, and their combination $A_s e^{-2\tau}$ is much better constrained then the two individual parameters (Zaldarriaga et al., 1997). The optical depth is not well constrained by temperature data alone, and a more precise determination comes from the low ℓ polarization data.

[2]The proper distance d_{pr} is the physical distance of an object from the observer. This distance changes in time due to the expansion of the universe. The comoving distance is defined as $d_c = d_{pr}/a(t)$. Both distances depend on the geometry of the universe.

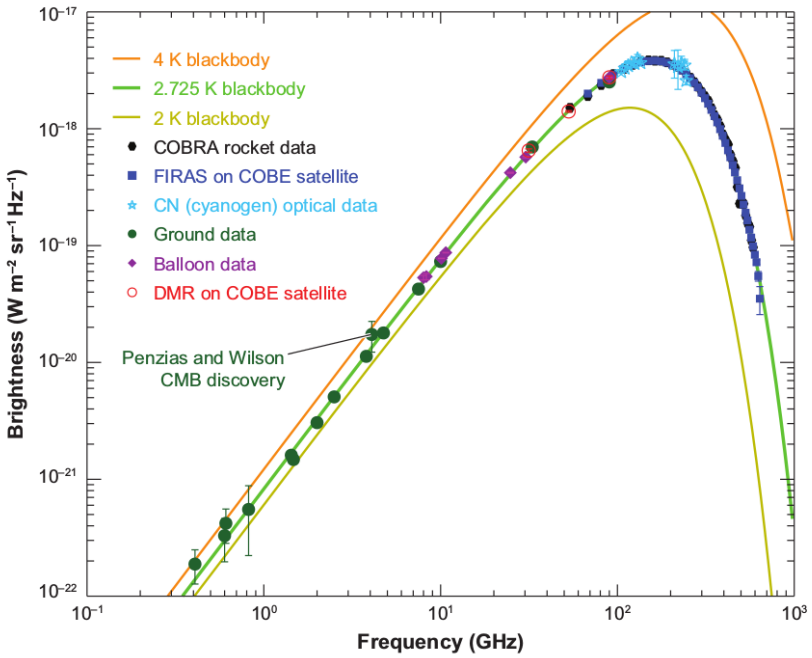

Figure 1.5 – Figure taken from Samtleben et al. (2007), which shows various measurements of the CMB flux versus frequency. The curves represent the theoretical black-body flux at different temperatures. We can see how the data points follow the curve of a black-body of $T = 2.725$ K.

Even though these degeneracies limit the precision with which we can measure cosmological parameters with the CMB, improving the sensitivity of the data and jointly exploiting temperature and polarization can greatly reduce the expected degeneracies.

1.3 CMB observations

The first observational evidence of the CMB has been found in 1964, when A. Penzias and R. Wilson discovered a uniform background isotropic over the whole sky. After that, various measurements were performed to probe the CMB black-body spectrum and to look for its anisotropies (Samtleben et al., 2007), but for as much as they tried, astronomers could only observe the monopole and the dipole due to Earth's motion. Some of these observations are plotted in Figure 1.5, and it is possible to see how the data fit particularly well the black-body curve. It was only with the satellite COBE that the first detection of the anisotropies was found. The more, COBE data sampled the peak of the black-body, as seen in Figure 1.5, determining with high precision the average temperature $T = 2.72548 \pm 0.00057\,K$ (Fixsen, 2009). After that, two other satellites were launched targeting the CMB anisotropies, which they observed with increasing resolution and frequency coverage: WMAP first and Planck then. Other missions have observed the CMB from the ground. While having less sky coverage, ground missions are cheaper and more reactive to advances in the available technology. However, they suffer from extinction of the atmosphere due to water vapour and are thus located in very dry areas.

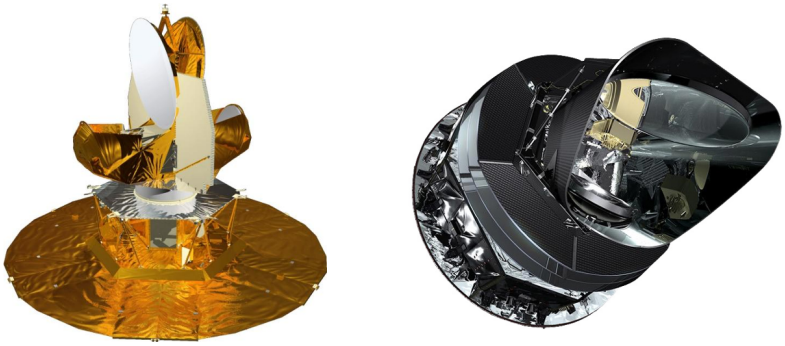

Figure 1.6 – The WMAP (left) and Planck (right) satellites.

1.3.1 WMAP

The WMAP (Wilkinson Microwave Anisotropy Project) mission was financed by the NASA. It was launched in 2001 and, although initially it was planned to operate for a little more than two years (Bennett et al., 2003), it was able to observe the sky for nine years. The WMAP satellite is shown in Figure 1.6. WMAP had 5 frequency channels which collected data both in intensity and in polarization, with bands centred at 23, 33, 41, 61 and 94 GHz named K, Ka, Q, V and W respectively. With respect to Planck, WMAP samples narrower range in frequency, but its data are complementary to Planck data since they are taken at slightly different band centres and also reach lower ν.
WMAP data has enabled us to put stringent constraints on cosmological parameters such as for example the age of the universe - 13.74 ± 0.11 Gyr at 68% CL[3] -, and its flatness - $|\Omega_k| < 0.0094$ at 95% CL (Bennett et al., 2013a; Hinshaw et al., 2013a). The WMAP results are in agreement with the standard ΛCDM model. WMAP released sky maps with resolution up to $\sim 0.2^o$ and a CMB angular power spectrum up to $\ell \sim 1200$ in intensity, with a good determination of the first three acoustic peaks.

1.3.2 Planck

The Planck mission was financed by the European Space Agency with the objective of observing the Cosmic Microwave Background. Combining a high sensitivity $\Delta T/T \sim 10^{-6}$ and a finer resolution than precedent satellites, Planck was able to observe the CMB emission to a high degree of accuracy. In particular, the accuracy of the Planck measurement of the temperature angular power spectrum is limited by cosmic variance[4] up to $\ell \sim 1600$, meaning that the comic variance is the principal source of uncertainty up to these scales (Planck Collaboration XI et al., 2016).
Planck was operative between 2009 and 2013, and it observed the microwave sky in nine frequency bands centred at 30, 44, 70, 100, 143, 217, 353, 545 and 857 GHz. The Planck satellite is shown in Figure 1.6. It measured the CMB temperature anisotropies both in intensity and in polarization, although polarization data were only taken in seven bands

[3] Confidence level

[4] Cosmic variance is the statistical uncertainty due to the small number of samples availables for large cosmological scales. More details are given in Sect. 1.4.2

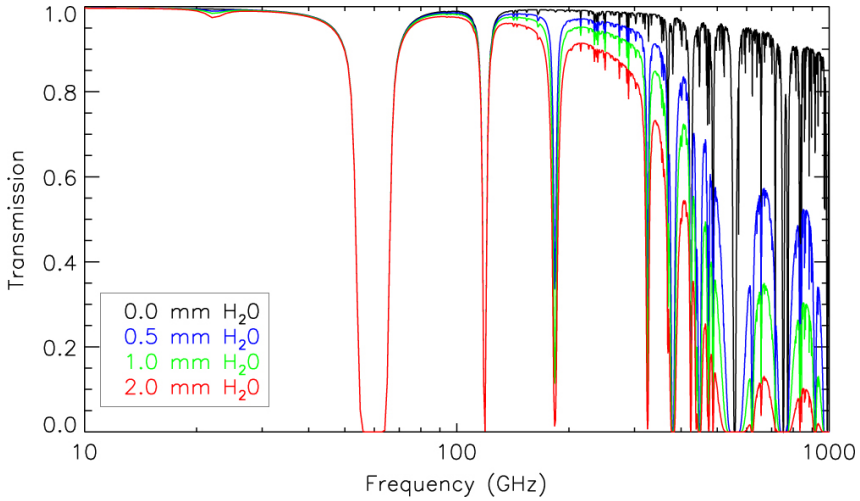

Figure 1.7 – Figure taken from (Errard et al., 2015), showing the atmospheric transmission from the Atacama plateau in Chile for different amounts of precipitable water vapour.

up to 353 GHz. It flew two instruments deploying a different type of technology, the Low Frequency Instrument (LFI) (Bersanelli, M. et al., 2010), that observed at the three frequency bands with $\nu \leq 70$ GHz, and the High Frequency Instrument (HFI) (Lamarre et al., 2010), that observed at $\nu \geq 1000$ GHz. The LFI used radiometers, as used before by COBE and WMAP. The LFI radiometers needed to be cooled only to 20 K, but the data had a lower resolution than HFI observations. The HFI used bolometers, which are instruments that absorb the incident radiation and measure the resulting increase of temperature: they operated at 0.1 K and thus needed a more aggressive cryogenic cooling. For this reason the HFI instrument only performed a little more than 2 years of observations, until the refrigerating liquid expired, while the LFI was able to stay operative for a much longer period of time.
The Planck data have been analysed by the *Planck Collaboration*, which has provided sky maps at the 9 frequencies of observation. As described in Chapter 2, the *Planck Collaboration* has provided four foreground-cleaned CMB maps at $5'$ resolution, and an intensity angular power spectrum up to $\ell \sim 2500$. Of particular interest for this work are data split maps, which are data maps constructed with only half of the time ordered information. There are many possible ways to split the data: in this work we use "halfmission" data split, which are obtained by dividing the data between the first and the second part of the mission.

1.3.3 Ground telescopes

There is a wide range of telescopes that have observed the CMB from the ground or by flying a balloon. When observing from the ground, the atmosphere is only partially transparent at microwave frequencies, and this is a strong limitation to observations. At 60 GHz and 119 GHz the atmospheric absorption is due to oxygen bands, while at frequencies between 100 GHz and 1THz the absorption is due to water vapour: even 2 mm of precipitable water vapour can result in a strong attenuation of the signal (Errard et al., 2015), as seen in Figure 1.7. For this reason, observations are carried out in dry locations such as the Atacama desert in Chile or in Antarctica. Balloons suffer less from

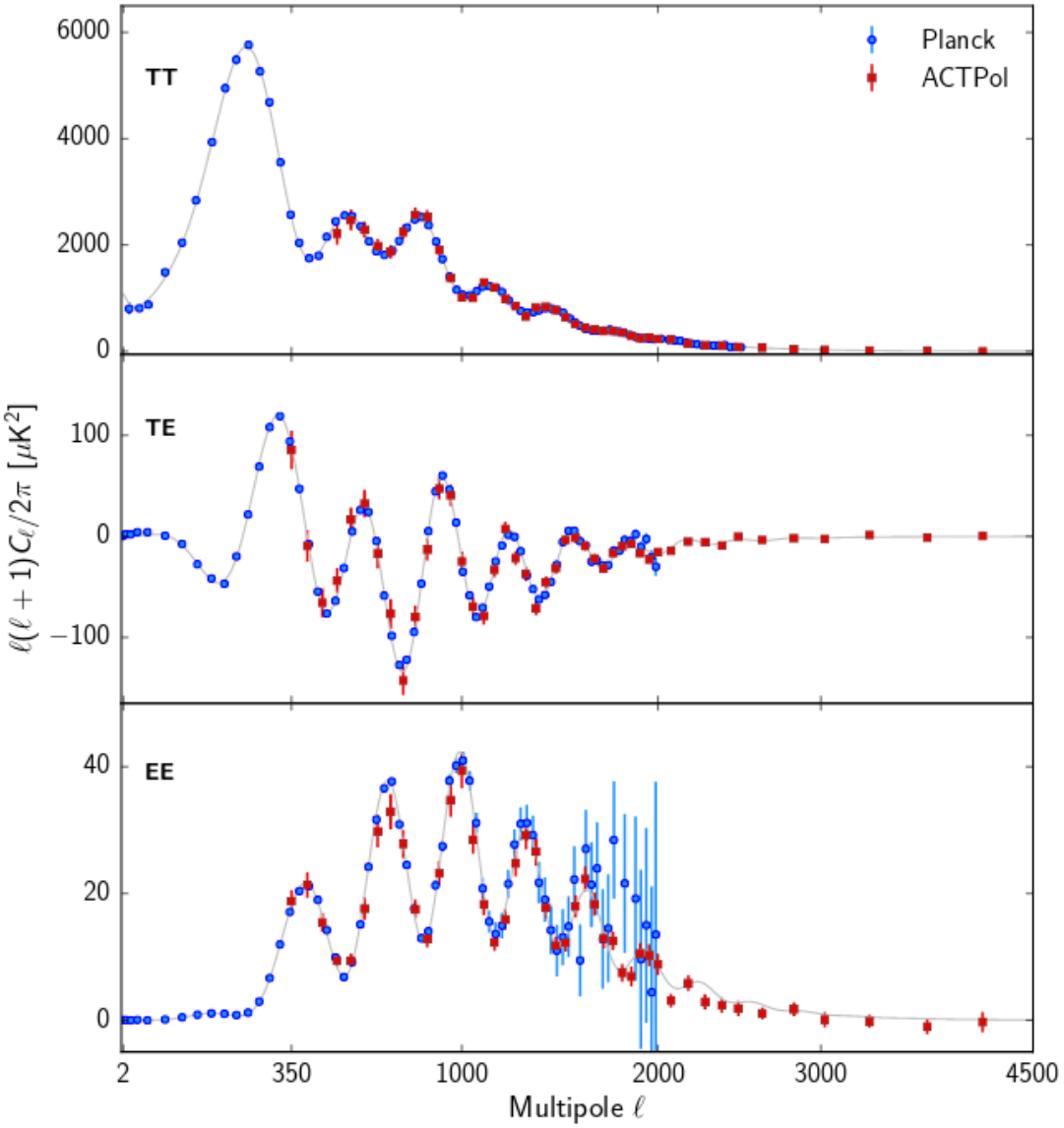

Figure 1.8 – Figure taken from (Louis et al., 2017), showing the temperature and polarization angular power spectra with data points from Planck and ACTPol.

atmospheric contamination with respect to ground telescopes, since they observe from higher spots, however the time duration of these missions is often quite limited.
With respect to satellites, ground telescopes and balloons have the advantage of being easily accessible and can be upgraded with new technology, more detectors and an extended frequency range. Among the most recent balloon missions there are EBEX (The EBEX Collaboration et al., 2017), PIPER (Lazear et al., 2014) and SPIDER (Crill et al., 2008). Among the principal ground telescopes there are:

- the Atacama Cosmology Telescope (ACT), which is located in Chile and has had three generations of detectors, from ACT to ACTPol and finally AdvACT. The latter two have detectors that are sensitive to polarization. The first generation instrument mapped the sky at 148 and 218 GHz at arcminute resolution, covering a multipole range of $500 \leq \ell \leq 10000$ (Dunkley et al., 2013). ACTPol had two

arrays of detectors observing at 148 GHz and one operating simultaneously at 97 and 148 GHz (Thornton et al., 2016), with spectra ranging between $500 \lesssim \ell \lesssim 9000$ (Louis et al., 2017). Figure 1.8 shows the ACT spectra combined with Planck data. The current ACT configuration is AdvACT, which uses the same type of receiver as ACTPol and spans five frequency bands from 25 to 280 GHz (Duff et al., 2016);

- the South Pole Telescope (SPT) is located in Antarctica and has also deployed different types of receivers (SPT, SPTpol, SPT-3G) which observe the sky at 95, 150 and 220 GHz. First installed in 2007, it has provided high-ℓ multipoles spectra that range between $2000 \lesssim \ell \lesssim 9500$ (Reichardt et al., 2012). SPTpol has also released data of the lensing BB angular power spectrum at $300 \leq \ell \leq 2300$ (Keisler et al., 2015);

- the BICEP-Keck Array telescopes (in chronological order: BICEP1, BICEP2, KeckArray and BICEP3) (BICEP2 and Keck Array Collaborations et al., 2015; Grayson et al., 2016) are installed at the South Pole and target the CMB B-modes. Each generation increases in sensitivity over the former. The Keck Array deployed an array of detectors of the same type as BICEP2. The observed frequencies are 95, 150, 220 and 270 GHz;

- POLARBEAR is a telescope in Chile built to study CMB polarization (The POLARBEAR Collaboration et al., 2017). It currently observes only at 150 GHz, but new receivers at other frequencies are under development for an extension of the project (POLARBEAR-2) (Inoue et al., 2016). The Simons Array is a project that will extend POLARBEAR-2 by mounting more receivers of the same type, and it will observe at 95, 150 and 220 GHz (Suzuki et al., 2016).

Also, the Simons Observatory has been financed and will be built in the Atacama desert. The long term plan, termed CMB S4 (Abazajian et al., 2016), is to reach a few hundred thousand detectors on the ground to collect CMB data and possibly to observe, among other scientific goals, the polarization B modes generated by primordial gravitational waves.

1.4 Working on the sphere

In this section we introduce a few concepts of data treatment that will be useful for the understanding of the following Chapters.

1.4.1 Spherical harmonics

We have seen in Section 1.2.1 that it is possible to expand a function on the sphere in terms of a basis of spatial frequencies called spherical harmonics. In spherical coordinates, the spherical harmonics functions are:

$$Y_{\ell m}(\theta, \phi) = \sqrt{\frac{2\ell + 1}{4\pi} \frac{(\ell - m)!}{(\ell + m)!}} P_\ell^m(\cos\theta) e^{im\phi}, \tag{1.10}$$

where P_ℓ^m are the Legendre polynomials.
Spherical harmonics functions are orthonormal:

$$\int_0^{2\pi} d\phi \int_{-1}^{1} d(cos\theta)\ Y^*_{\ell' m'}(\theta,\phi) Y_{\ell m}(\theta,\phi) = \delta_{\ell\ell'}\delta_{mm'} \tag{1.11}$$

where the superscript * denotes complex conjugation.
The spherical harmonics are not the only possible choice to work on the sphere. For example needlets are spherical wavelets introduced by Narcowich et al. (2006). They form a tight frame, that is they provide a basis-like representation but are redundant. Needlets have some interesting properties, since they enjoy localization both in real space and in harmonic frequency. For a practical implementation of needlets see Guilloux et al. (2007).

1.4.2 Cosmic variance

There is a statistical limit in the precision with which we can determine the angular power spectrum. This derives from the fact that we observe only one realization of our universe, while the theory can only predict the properties of the ensemble. From Eq. (1.7), we see that we estimate the angular power spectrum by averaging the variance of the $a_{\ell m}$ over the 2ℓ+1 modes at each ℓ. At a given multipole, the spherical harmonic coefficients $a_{\ell m}$ are drawn from the same distribution: this means that at small scales we have a good determination of their variance, i.e., the C_ℓ spectrum, since the number of samples is large. On the other hand, at large scales we have a very poor estimate of the angular power spectrum. This translates into a variance in the empirical estimate $\hat{C}_\ell$ of Eq. 1.7 which is called cosmic variance.
The variance of the empirical angular power spectrum can be written as:

$$\begin{aligned}
Var(\hat{C}_\ell) =& \langle \hat{C}_\ell^2 \rangle - \langle \hat{C}_\ell \rangle^2 \\
=& \langle \hat{C}_\ell^2 \rangle - C_\ell^2 \\
=& \frac{1}{2\ell+1} \sum_m \sum_{m'} \langle a_{\ell m} a^*_{\ell m} a_{\ell m'} a^*_{\ell m'} \rangle - C_\ell^2 \\
=& \frac{1}{2\ell+1} \sum_m \sum_{m'} \Big[\langle a_{\ell m} a^*_{\ell m} \rangle \langle a_{\ell m'} a^*_{\ell m'} \rangle + \langle a_{\ell m} a^*_{\ell m'} \rangle \langle a_{\ell m'} a^*_{\ell m} \rangle + \langle a_{\ell m} a_{\ell m'} \rangle \langle a^*_{\ell m} a^*_{\ell m'} \rangle \Big] - C_\ell^2,
\end{aligned} \tag{1.12}$$

where the last expression is derived making use of Wick's theorem [5].
Since temperature anisotropies are real, we use real value spherical harmonics and the expression $a^*_{\ell m} = a_{\ell -m}$ holds. By using the fact that $\langle a_{\ell m} a^*_{\ell' m'} \rangle = \langle a_{\ell m} a_{\ell' -m'} \rangle = \delta_{\ell\ell'}\delta_{mm'} C_\ell$

[5] Wick's theorem states that, given n Gaussian random fields, the expectation of their product is given by partitioning the Gaussian fields in all possible distinct pairs, taking the expectation of each pair, and then summing over all the possible products of such partitioning. Considering four variables a, b, c, d, this theorem states that $\langle abcd \rangle = \langle ab \rangle \langle cd \rangle + \langle ac \rangle \langle bd \rangle + \langle ad \rangle \langle bc \rangle$.

we can derive:

$$\begin{aligned} Var(\hat{C}_\ell) =& \frac{1}{2\ell+1}\sum_m\sum_{m'}\Big[\langle a_{\ell m}a^*_{\ell m}\rangle\langle a_{\ell m'}a^*_{\ell m'}\rangle + \langle a_{\ell m}a^*_{\ell m'}\rangle\langle a_{\ell m'}a^*_{\ell m}\rangle + \langle a_{\ell m}a_{\ell m'}\rangle\langle a^*_{\ell m}a^*_{\ell m'}\rangle\Big] - C_\ell^2 \\ =& \frac{1}{2\ell+1}\sum_m\sum_{m'}\Big[\langle a_{\ell m}a_{\ell -m}\rangle\langle a_{\ell m'}a_{\ell -m'}\rangle + \langle a_{\ell m}a_{\ell -m'}\rangle\langle a_{\ell m'}a_{\ell -m}\rangle + \langle a_{\ell m}a_{\ell m'}\rangle\langle a_{\ell -m}a_{\ell -m'}\rangle\Big] - C_\ell^2 \\ =& \frac{\Big[(2\ell+1)^2 + (2\ell+1) + (2\ell+1)\Big]}{(2\ell+1)^2}C_\ell^2 - C_\ell^2 \\ =& \frac{2}{2l+1}C_\ell, \end{aligned} \tag{1.13}$$

where many terms cancel out in the sum due to the fact that $m \neq m'$.
The cosmic variance uncertainty adds to the other uncertainties such as noise or systematics. When the sky maps are masked, only a fraction of the data are used in the analysis, and the effective number of available modes is reduced. This effect, sometimes referred to as sample variance, translates into an uncertainty (Scott et al., 1994):

$$Var(\hat{C}_\ell) = \frac{2}{(2l+1)f_{sky}}C_\ell. \tag{1.14}$$

where f_{sky} is the retained sky fraction.

1.4.3 The effect of masks

Masking the sky means imposing a weighting to the pixels that sets a fraction of them to zero. This procedure is sometimes necessary since some areas on the sky are strongly contaminated by astrophysical emissions and cannot be analysed. Nevertheless, the sky cut affects the map angular power spectrum, since it breaks the orthogonality of the spherical harmonics and it induces a coupling between modes. If the mask has sharp boundaries, the range of the coupled modes is large. In order to mitigate this problem, it is necessary to apodize the mask, that is to use a soft transition at the edges of the mask. Also, the mask reduces the C_ℓ power by $\sim \frac{1}{f_{sky}}$.
When a sky cut is applied to a map of temperature fluctuations δT, the spherical harmonics expansion can be approximated as:

$$\tilde{a}_{\ell m} = \int d\mathbf{n}\delta T(\mathbf{n})W(\mathbf{n})Y_{\ell m}(\mathbf{n})^* \tag{1.15}$$

where $\tilde{a}_{\ell m}$ represents the spherical harmonics of the masked sky, $W(n)$ is the mask weighting, $\mathbf{n}$ is the direction on the sky and the integral is performed over the sphere. The retained sky fraction is $f_{sky} = \frac{1}{4\pi}\int d\mathbf{n}W(\mathbf{n})^2$. The resulting angular power spectrum, called pseudo-power spectrum $\tilde{C}_\ell$ is:

$$\tilde{C}_\ell = \frac{1}{2\ell+1}\sum_{m=-\ell}^{\ell}|\tilde{a}_{\ell m}|^2. \tag{1.16}$$

The pseudo-power spectrum relates to the ensemble average power spectrum as:

$$\langle\tilde{C}_\ell\rangle = \sum_\ell M_{\ell\ell'}\langle C_\ell\rangle \tag{1.17}$$

where $M_{\ell\ell'}$ describes the mode-mode coupling deriving from the mask. It depends only on the geometry of the sky cut and can be expressed in terms of the angular power spectrum of the mask. By computing $M_{\ell\ell'}$, it is possible to correct the power spectrum for the effect of the sky cut. This is referred to as the Monte Carlo Apodized Spherical Transform Estimator (MASTER) correction and has been developed by Hivon et al. (2002).
Another important effect to consider is the map beam. When observing a point-like object, a telescope returns a finite size image: the shape of this image defines the telescope point spread function, or beam. This characteristics limits the resolution of the telescope, since any two sources which are closer than the beam width are not distinguishable. The observed image can be represented as a convolution of the beam and the true image. Thus a correct characterization of the beam is important for data analysis.
Dealing with the beam in the harmonic domain is much easier, since the convolution turns into a simple product. If we approximate the beam to be spherically symmetric, we can model is at as function b_ℓ of the multipole. At first order, we can describe the beam as a Gaussian, and the resolution is given by its full width half-maximum (FWHM). Given its shape, it is evident that the effect of the beam is to attenuate the signal at small scales. The observed signal $y_{\ell m}$ in one frequency channel can be written as:

$$y_{\ell m} = s_{\ell m} * b_\ell + n_{\ell m} \tag{1.18}$$

where $s_{\ell m}$ are the spherical harmonics of the astrophysical signals and $n_{\ell m}$ is the noise. By knowing the beam properties, it is possible to change the resolution of the image. However this comes at the cost of boosting the noise. In fact the noise appears in the detector and in the subsequent processing, and is not affected by the beam. When the image is debeamed, i.e., it is divided by the beam function, the noise is increased, especially at small scales. This must be kept in mind when working with observations at different resolutions.

Chapter 2

Dealing with foregrounds

Contents

Many different astrophysical components can be observed in the microwave domain. One of them is the CMB, which originates in the first phases of evolution of the universe. The others have a more recent origin and partially dominate, depending on the position on the sky, the CMB light: these are termed foregrounds. In this Chapter I will present the characteristics of these foregrounds. We will see how our Galaxy contributes through large scale foregrounds, such as the thermal radiation of the interstellar medium dust, the non-thermal synchrotron and free-free radiation of cosmic rays. These galactic emissions have an inhomogeneous spatial distribution, being more intense on the galactic plane. At low galactic latitudes, the foreground contamination is so strong that often this part of the sky must be masked and cannot be analysed, since the CMB cannot be reliably recovered. Furthermore we will see that the light of background galaxies and the interaction of CMB photons with the intracluster medium of galaxy clusters contribute to the observed

contamination.
Several methods have been devised to remove these astrophysical emissions. These methods exploit very different strategies, such as a physical modelling of the sources or blind methods based on the various signal properties. Each of these methods has its qualities and its limitations. The last Section of this Chapter is devoted to outline the community's efforts to separate the foregrounds from the CMB.

2.1 Astrophysical emissions in the microwave

The primary mission of the Planck satellite is to measure the cosmic microwave background anisotropies. The CMB black body spectrum peaks in the microwave band, thus observational efforts concentrate in this frequency band. The galactic foregrounds have an anisotropic distribution on the sky, thus some directions are more strongly contaminated by foreground emissions than other. Nevertheless, even when masking these zones, there is no part of the sky which is foreground free, since extragalactic contaminations are also present. To be able to study the CMB, it is crucial to characterize and remove all these astrophysical contaminations.
Since the CMB and the foregrounds have different emission laws, we can develop component separation methods to reduce the foregrounds contamination while preserving the CMB signal. It is thus important to characterize the emission laws of the foregrounds.
All astrophysical emissions have a scientific interest of their own. The microwave data is extremely useful for studying, for example, the dust distribution or the magnetic field of our Galaxy. Also, the extragalactic emission allows us to understand the properties of the high redshift galaxies and to increase the sample of known galaxy clusters. Nevertheless, in this work, all these emissions are considered as foregrounds to remove in order to access the CMB information. For this reason, I focus here only on their properties at scales and frequencies relevant for Planck data, which are the data used in this analysis.
We will define the emission laws through frequency in terms of the specific intensity $I(\nu)$ (W m^{-2} Hz^{-1} sr^{-1}) which is the intensity per unit frequency. Some works prefer to use the brightness temperature T_b, which related to $I(\nu)$ as:

$$T_b = \frac{c^2 I(\nu)}{2k\nu^2}, \tag{2.1}$$

where c is the speed of light and k is the Boltzmann constant. The brightness temperature is the temperature that a black-body of same brightness would have at that frequency and it is measured in K_{RJ}. More details about units of measurement are given in Appendix C.
The emission law of black-body is:

$$B(\nu, T) = 2h\frac{\nu^3}{c^2}\frac{1}{e^{\frac{h\nu}{kT}} - 1}, \tag{2.2}$$

where h is the Planck constant, and T is the temperature of the emitting source.
Emission laws are often given in terms of a power law ν^β, where β is the spectral index: when comparing results in the literature it is important to note that the temperature spectral index is equivalent to the intensity spectral index minus 2. Other authors prefer to refer to the flux density $S(\nu)$:

$$S(\nu) = \int I(\nu) d\Omega, \tag{2.3}$$

where the integral is performed over the solid angle Ω of the source. The flux density is used when the angular size of the source is smaller than the beam, hence the source is not resolved. The spectral index of flux density is equivalent to that of specific intensity.
Since this work does not use polarization data, we will only sketch the polarized foreground content. The main contaminants in polarization data are synchrotron and thermal dust. Synchrotron emission is naturally polarized, while dust polarization arises since dust grains tend to align perpendicularly to the local magnetic field. Extragalactic sources exhibit a polarization level which is typically lower than 1-2 % (Seiffert et al., 2007; Battye et al., 2011; Naess et al., 2014). Only a handful of point sources are reliably identified in polarization, and the point source contamination is not expected to be a strong contaminant in the CMB E-mode angular power spectrum (Tucci & Toffolatti, 2012; Planck Collaboration XI et al., 2016).

2.2 Galactic foregrounds

We observe the sky from within our Galaxy, thus all observations are contaminated by it. A number of different astrophysical components emit radiation in the radio and microwave bands, ranging from dust grains to molecules and free electrons. Figure 2.1 shows the emissions of CMB and the galactic foregrounds at Planck frequencies. Good reviews of the galactic foreground emission can be found in Delabrouille & Cardoso (2009); Ichiki (2014); Dickinson (2016).

2.2.1 Thermal dust

Thermal dust radiation is the infrared black-body emission of dust grains heated by stellar photons. It is the dominant galactic foreground at HFI frequencies $\nu \gtrsim 100$ GHz. Since this analysis uses HFI data only, thermal dust is one of the main foreground contaminations that we have to handle.
Dust grains have very varied sizes, ranging from 1 nm to a fraction of μm (Lagache et al., 2005; Andersson et al., 2015). They are mainly composed of silicates and carbon, and have amorphous shapes. The small grain population comprises also polycyclic aromatic hydrocarbons (PAHs) macromolecules, which behave as dust in the sense that they absorb UV/optical photons and re-emit them at lower frequencies. The thermal emission of dust depends on the temperature, size and composition of grains, and is therefore quite complicated to model, since various grain populations are present. In general, dust properties vary depending on galactic latitude.
Thermal dust emission is usually described as a modified black-body law, or "grey-body":

$$I_d(\nu) \propto \nu^{\beta_d} B(\nu, T_d), \tag{2.4}$$

where β_d is the spectral index of thermal dust, $B(\nu, T_d)$ is the emission law of black-body and T_d is the temperature of the dust grains. Figure 2.2 shows the frequency spectrum of the grey-body model for different parameter choices. This is an empirical model, and more physically motivated solutions (Draine & Li, 2007) have been studied, although external high frequency data are needed in order to constrain all the model parameters (Planck Collaboration et al., 2016a). On the other hand, the grey-body model accurately accounts

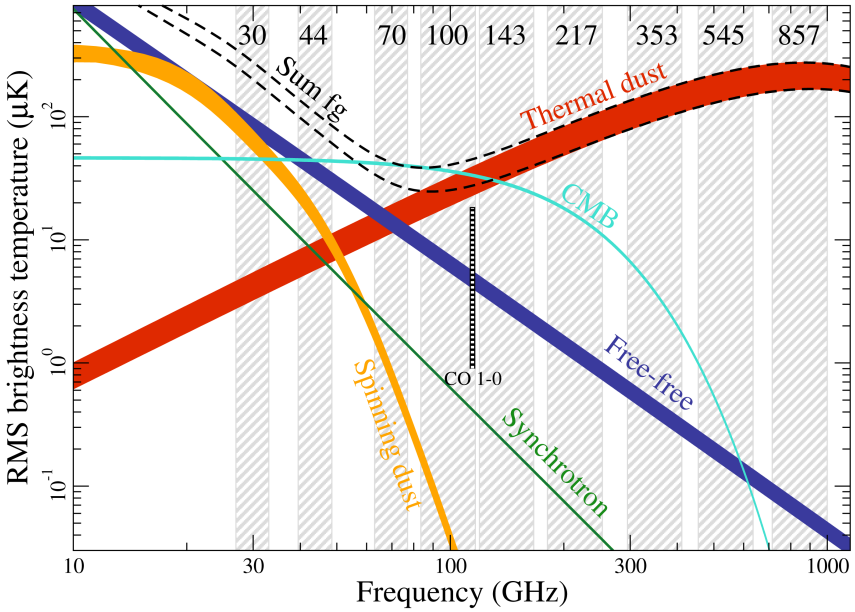

Figure 2.1 – Figure taken from (Planck Collaboration I et al., 2016), showing the frequency spectra of unpolarized galactic foregrounds and the CMB at Planck frequencies. The represented foregrounds are thermal dust, synchrotron, spinning dust, free-free and the lowest CO transition $J1-0$. The total foregroud contribution is represented by the dashed curves. Each component is smoothed to an angular resolution of 1^o FWHM. The foreground emissions are represented by thick bands: the lower and upper edges of each band are defined by a retained sky fraction of 81% and 93%, respectively. The CMB contribution is isotropic and thus is independent of masking.

for the dust emission across Planck frequencies, but fails to describe it at higher frequencies, where the physics of the dust emission becomes more complicated. The spectral index of dust being positive, its contribution increases with frequency, and completely dominates the CMB at 545 GHz and 857 GHz, as seen from Figure 2.1.
The determination of β_d and that of temperature are correlated and also depend on the modelling of other foregrounds: degeneracies between galactic foregrounds are present, in particular with the spinning dust and extragalactic Cosmic Infrared Background (CIB). The *Planck Collaboration* component separation analysis dedicated to foreground maps Planck Collaboration X et al. (2016) finds that the spectral index of dust presents small variations on the sky $\beta_d = 1.54 \pm 0.05$, but performs the analysis at $60'$ and also imposes a tight Gaussian prior on the β_d parameter. In turn they find a wide distribution for the dust temperature $T_d = 20.93 \pm 2.25$. These values roughly correspond to the green curve in Figure 2.2. In the Planck Collaboration XLVIII et al. (2016) analysis, which is dedicated to disentangling the dust and CIB emissions, the resulting dust spectral index has a wider dispersion with a slightly higher value $\beta_d = 1.6 \pm 0.13$, while the dispersion on dust $T_d = 19.40 \pm 1.26$[1] is reduced. This shows how foreground models and prior assumptions can lead to different results on the dust characteristics. Figure 2.3 shows the thermal dust distribution obtained by the Planck Collaboration X et al. (2016) analysis. As shown in Figure 2.4, the dust angular power spectrum can approximately be modelled

[1]Error bars represent the dispersion over the sky of the parameter values.

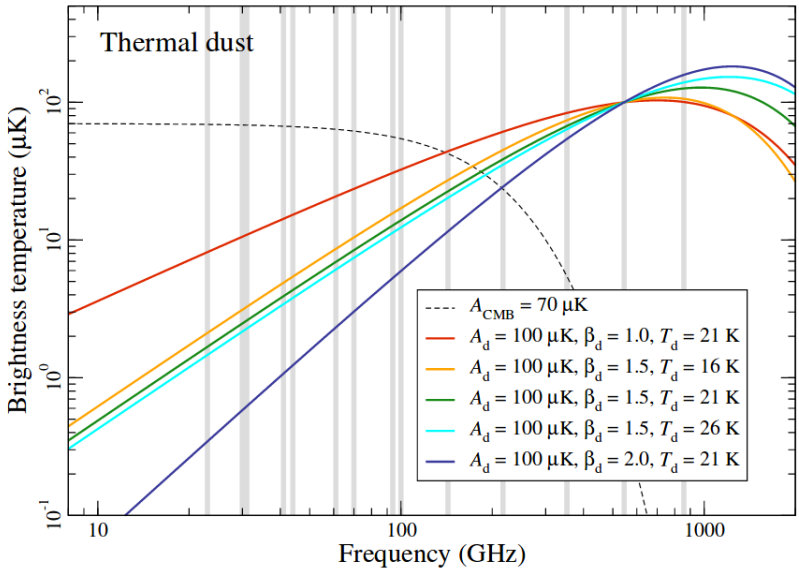

Figure 2.2 – Figure taken from Planck Collaboration X et al. (2016), showing the dust grey-body model for different parameters β_d and T_d. The parameter A_d is the global normalization. The grey bands mark the Planck observed frequencies. Five curves are shown: the reference curve is the green one, and the others change one parameter with respect to it. As we can see from the orange, green and light-blue curves on the plot, the temperature parameter T_d is not well constrained by the emission law of dust in the frequency range observed by Planck. A change in the spectral index β_d instead is more evident, as seen from the red, green and blue curves.

as:

$$C_\ell^{dust} \propto \ell^{-2.6}. \tag{2.5}$$

For the likelihood analysis, Planck Collaboration XI et al. (2016) considers an effective dust model that has bump at $\ell = 200$. This feature appears since the point source mask of the likelihood also removes some of the brightest emission regions of the galaxy that lie outside the galactic mask, thus deforming the dust spectrum. Nevertheless, at high multipoles, the Planck likelihood model coincides with the power-law behaviour of Eq. (2.5).

2.2.2 Synchrotron

The synchrotron emission results from relativistic charged particles spiralling in a magnetic field. Within our Galaxy, it originates from the interaction between cosmic ray electrons and the interstellar magnetic field. The intensity of synchrotron radiation is related to the electrons energy and the strength of the magnetic field perpendicular to the line of sight, thus showing important spatial variations on the sky. The energy distribution of the electrons particle density is $n_e(E) \propto E^p$, where E is the energy of the electrons. For cosmic rays, the slope is about $p \sim -2.5$. The synchrotron specific intensity $I_{sync}(\nu)$ then is (Bradt, 2014):

$$I_{sync}(\nu) \propto B^{\frac{p+1}{2}} \nu^{\beta_{sync}+2}, \tag{2.6}$$

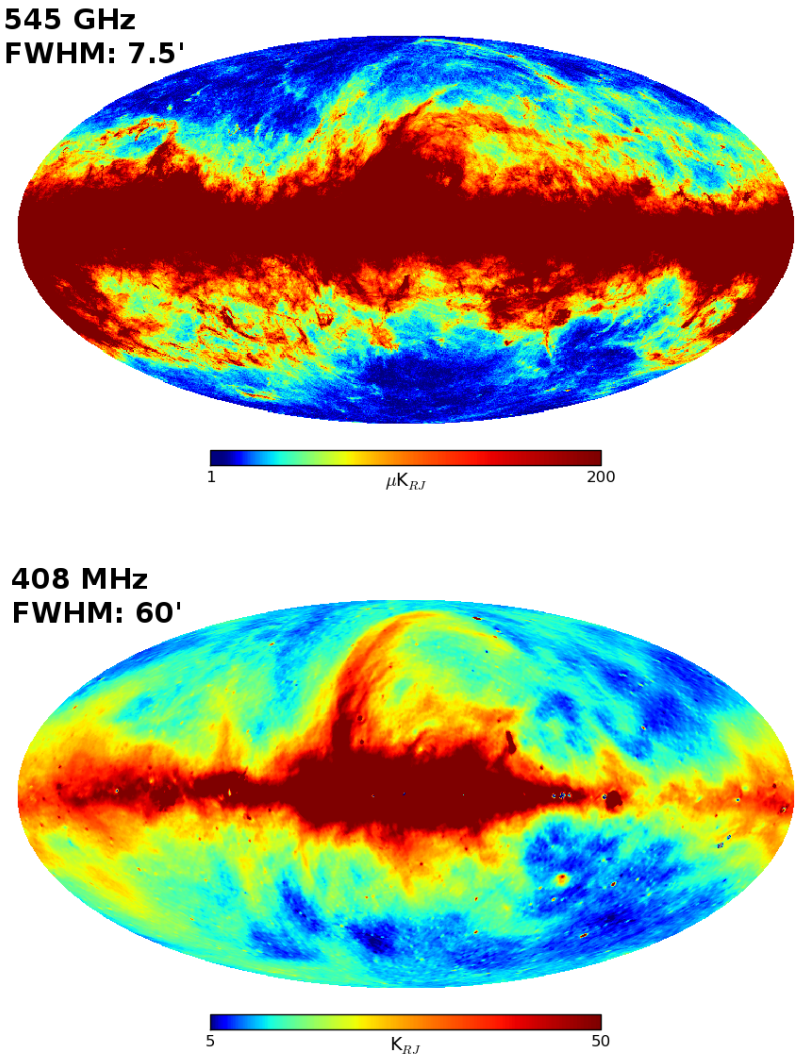

Figure 2.3 – *Top panel:* Thermal dust emission. *Bottom panel:* Synchrotron emission. Both maps are obtained with the Commander component separation method. The synchrotron map is at the reference frequency of 408 MHz, which is outside the Planck observed range: the Commander method applied in Planck Collaboration X et al. (2016) uses also external data such as WMAP data and the Haslam map at 408 MHz. It is the latter that predominantly determines the synchrotron emission, thus the map is given at its reference frequency.

where β_{sync} is the synchrotron spectral index, B is the magnitude of the magnetic field and p is the slope of the electrons particle density. The spectral index depends on p as $\beta_{sync} = (p-3)/2$. Typical value of the spectral index are $\beta_{sync} \simeq -2.7$ at around 1 GHz and $\beta_{sync} \simeq -3$ at higher ν (see (Strong et al., 2011) and references therein). The steepening at high frequencies is likely due to the radiative losses in the high-energy tail of the electrons spectrum.
Given Eq. (2.6) and since $\beta_{sync} + 2 < 0$, it is evident that synchrotron emission increases at low frequencies. Specifically, it is the dominant foreground below $\nu \lesssim 10$ GHz (Planck

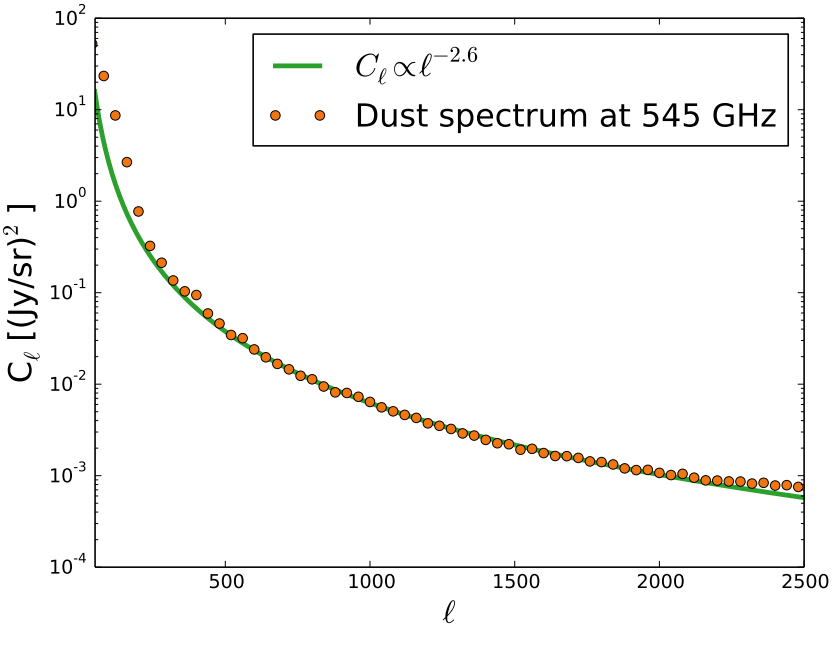

[t!]

Figure 2.4 – The dust C_ℓ spectrum: orange dots are is the agular power spectrum of the 545 GHz map obtained by Planck Collaboration XLVIII et al. (2016), while the green line is the fitted $\ell^{-2.6}$ spectrum. For clarity, only one every 40 data points is shown.

Collaboration et al., 2016e). Even though synchrotron is subdominant at Planck frequencies, it is one of the dominant foregrounds at low ν. Other data can be used to characterize its properties, such as WMAP data and the Haslam 408 MHz map (Haslam et al., 1982), which is often used as a synchrotron template. It is important to note that the Haslam map may not be a perfect template for synchrotron contamination at Planck frequencies, since it is taken at a much lower ν. The bottom panel of Figure 2.3 shows the Planck full sky synchrotron map at the reference frequency of 408 MHz.

2.2.3 Free-free

Free-free radiation is produced by ionized gas interacting with free electrons, which emit Bremsstrahlung radiation. It is the dominant foreground at frequencies between ν ∼10-100 GHz. Its frequency dependence in terms of the specific intensity is:

$$I_{ff}(\nu) \propto \nu^{\beta_{ff}+2}, \tag{2.7}$$

where β_{ff} is the free-free spectral index. Free-free has a flatter spectrum than synchrotron, with its spectral index value ranging between β_{ff} ∼-2.10 at 1 GHz and β_{ff} ∼-2.14 at 100 GHz (Planck Collaboration: et al., 2015).
Synchrotron and free-free emissions are difficult to disentangle, especially at low galactic latitudes where the extinction by dust becomes relevant. In order to obtain a spatial distribution of free-free emission it is necessary to use complementary information. Good tracers of free-free are spectral recombination lines, such as optical Hα and radio recombination lines (Dickinson et al., 2003). Hα emission suffers dust extinction, thus it can

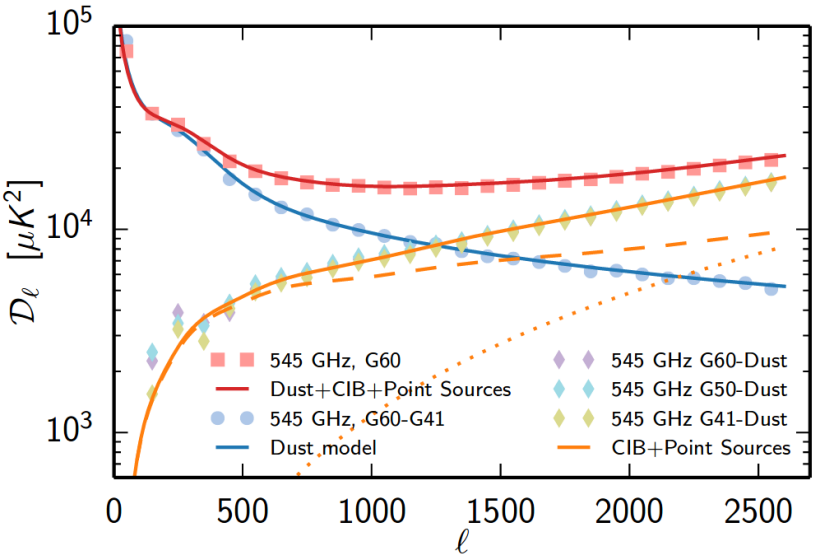

Figure 2.5 – Figure taken from Planck Collaboration XI et al. (2016) that shows the dust effective model (blue line) used by the Planck high-ℓ likelihood. The 545 GHz half-mission cross-spectrum provides a good estimate of the dust behaviour. In order to cancel the extragalactic foreground contribution in this spectrum, the dust template is built considering the G60-G41 mask difference. The blue line shows the dust model while the blue circles represent data points. Coloured diamonds display the extragalactic contribution, obtained as the difference between the dust model and the cross-spectrum of half-mission maps at 545 GHz for three different galactic masks G41, G50 and G61. The convention is that a galactic apodized mask of retained sky fraction X is named GX. The orange solid line shows the fitted extragalactic contribution, composed of clustered CIB (dashed orange line) and shot noise (dotted orange line). The red line is the sum of the dust model, CIB, and point sources for the G60 mask, and the red squares show the 545 GHz half-mission cross-spectrum. The effective dust model and the extragalactic contribution thus well represent the data points.

only be used away from the galactic plane. At low galactic latitude radio lines can be used instead (Planck Collaboration et al., 2016e).
Figure 2.6 shows the free-free emission measure, that is the integrated squared electron density along a line of sight. Comparing Figures 2.3 and 2.6, we expect that galactic emissions correlate among each other due to their similar spatial distribution. This is a strong limitation when trying to separate them.

2.2.4 Spinning dust

An Anomalous Microwave Emission (AME), has been detected by multiple observations in the microwave (Ysard et al., 2010; Gold et al., 2011; Planck Collaboration et al., 2014a). This emission is thought to originate from the electric dipole radiation of spinning dust grains. The very small grains, who spin faster, dominate the spectrum of the emission, determining its peak frequency. This makes spinning dust an interesting observational target to study small grains properties (Tibbs et al., 2016). Theoretical predictions place the peak between 10-60 GHz, depending on the environment and dust grain size (Ysard

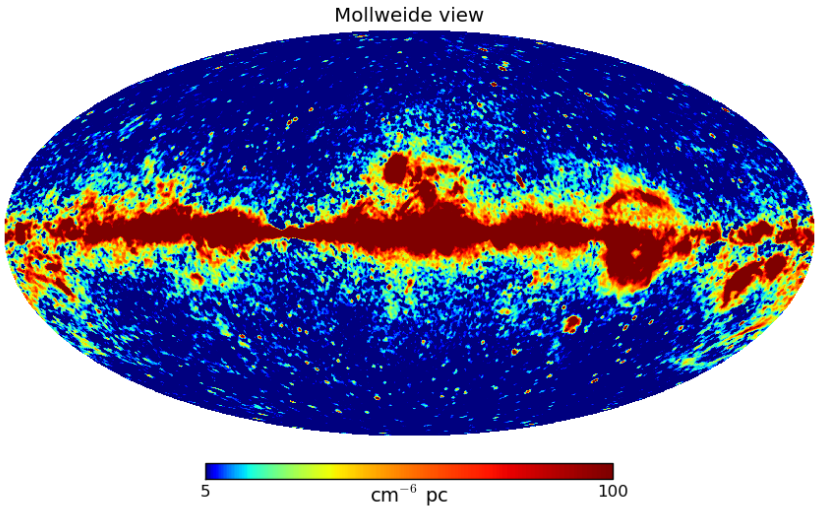

Figure 2.6 – The free-free emission measure as fitted by Commander in Planck Collaboration X et al. (2016). Over the Planck frequency range, the emission measure roughly determines the amplitude of the free-free emission.

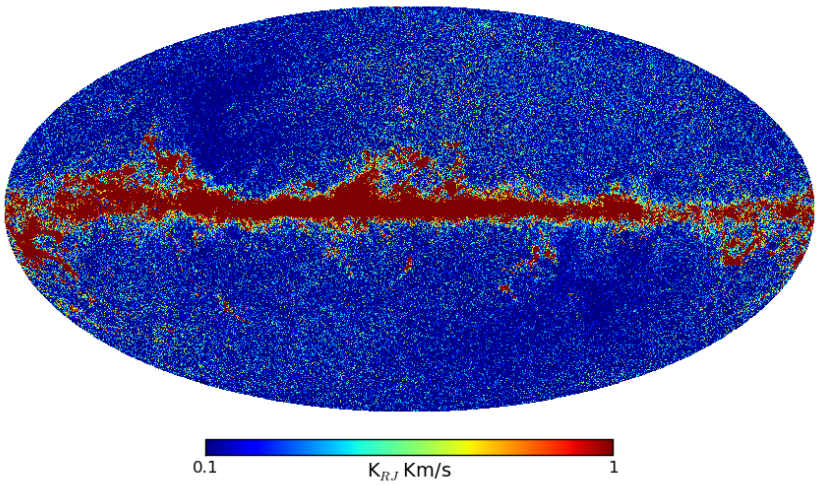

Figure 2.7 – CO J2-1 transition emission with a resolution of 7.5′ at 230 GHz.

et al., 2010; Planck Collaboration: et al., 2015) which is the range at which the AME is detected (Planck Collaboration et al., 2016e). At high and intermediate galactic latitudes however such identification between the AME and spinning dust is still uncertain, and other explanations are possible, such as magnetic dust radiation (Liu et al., 2014; Macellari et al., 2011)

2.2.5 CO

The carbon monoxide (CO) molecules emit in the microwave band via rotational transitions. A detector observes radiation in a frequency band of finite width, thus emission lines that are within the bandpass of a channel are also detected. The rotational transitions most

evident in Planck data are at 115 GHz, 230 GHz and 345 GHz, and are detected in the 100, 217 and 353 GHz channels respectively (Planck Collaboration et al., 2014e). The CO contamination in the Planck data has proven to be more important than expected before launch, especially in the 100 GHz channel (Planck HFI Core Team et al., 2011). The rotational lines observed in Planck data allowed the reconstruction of the galactic distribution of CO. The gas molecules fuel the star formation and thus play an important role in the galactic evolution. Molecular hydrogen is the most abundant molecule in the universe, but it is not observable directly, since its emission lines are weak and hardly excited in cold molecular clouds. The CO molecule also forms in molecular clouds but has a lower excitation energy, thus its rotational transitions are more easily excited. For this reason CO is considered an important tracer of cold molecular hydrogen.
The CO emission becomes important at small scales: Ichiki et al. (2014) find evidence that CO can be a significant contaminant at scales $\ell \gtrsim 900$ at 100 GHz and $\ell \gtrsim 400$ at 217 GHz. The spatial distribution of CO follows that of dust, being even more concentrated on the galactic plane, and thus is easily masked. Figure 2.7 shows the all-sky map obtained by Planck of the J2-1 CO transition at 230 GHz. A recent study by Puglisi et al. (2017) has forecasted the level of unresolved polarized emission from CO molecular clouds by modelling the molecular clouds as tridimensional. authors find that the level of CO contamination is equivalent to a cosmological signal with tensor-to-scalar ratio $r \leq 0.02$ [2].

2.3 Extragalactic foregrounds

Galactic foregrounds are not the only emissions we observe in the microwave domain. The contamination from extragalactic sources is also present, and it becomes important at small angular scales. In particular, the incorrect characterization of extragalactic sources can affect the evaluation of small scale CMB anisotropies, inducing biases in the derived cosmology (Millea et al., 2012). It is therefore very important to accurately evaluate the contribution of these foregrounds to the total observed power. The extragalactic sources observed in the microwave are mainly background galaxies and galaxy clusters.
Before entering into details of the extragalactic contamination, I briefly resume its main components. As light travelling through the universe shifts towards longer wavelengths due to cosmic expansion, the observed emission of background galaxies is redshifted to the infrared and radio bands. The observed individual galaxies are labelled "point sources". Some of these point sources are resolved, and thus can be identified and masked (Planck Collaboration et al., 2016f). Nevertheless a vast majority of sources is unresolved at Planck sensitivity and resolution, and is studied as a diffuse shot noise background. This is particularly important since, contrary to galactic emissions, unresolved extragalactic foregrounds are statistically homogeneous on the sky and their contribution cannot be reduced by the use of masks.
Point sources can be loosely categorized in two main populations, one predominant at radio frequencies, whose emission is dominated by non-thermal synchrotron radiation, and one predominant in the infrared, composed of dusty star-forming galaxies. The emission of star-forming galaxies is termed Cosmic Infrared Background. The background galaxies follow the large scale structure of the universe, thus their position on the sky is correlated. The CIB galaxies, which are more numerous, present a non-negligible degree of correlation,

[2] r is the ratio of the amplitude of the tensor and scalar CMB angular power spectra at low multipoles

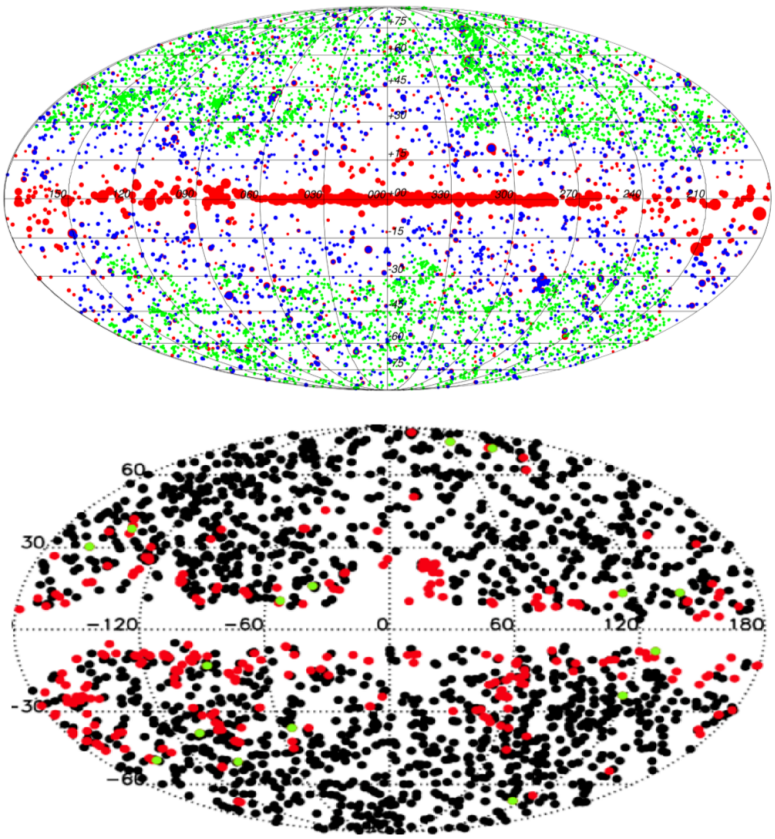

Figure 2.8 – *Top panel:* Figure taken from Planck Collaboration et al. (2016f), showing the distribution of the validated sources from the Second Planck Catalogue of Compact Sources. Red, blue, and green circles show sources detected at 30, 143, and 857 GHz respectively. The size of the filled circles is representative of the relative flux densities of the sources per frequency, where the larger circles correspond to larger flux densities. A different size range for each channel was necessary for visualization purposes, thus circles of different colour are not directly comparable. *Bottom panel:* Figure taken from Planck Collaboration et al. (2016g), where the black dots represent galaxy clusters detected by Planck. Red and green dots represent galaxy clusters candidates which are potentially spurious detections of galactic cold-clumps: the deleted candidates are shown in red and the retained candidates are shown in green. From these two charts it is possible to see that at low galactic latitudes, due to the strong emission of galactic foregrounds, the detection of point sources and galaxy clusters is more challenging.

i.e., they are clustered. Thus background galaxies contribute both shot noise and clustered power to the observed angular power spectra. The radio galaxies are less numerous and their clustered contribution has been shown to be negligible (Hall et al., 2010; Lacasa et al., 2012).

Galaxy clusters are seen due to their gas interaction with the CMB, since photons passing through one galaxy cluster interact with the hot intracluster gas via inverse Compton scattering. This induces local spectral distortions in the CMB black-body spectrum which are detectable in the Planck maps; this is termed Sunyaev-Zel'dovich effect. Figure 2.8

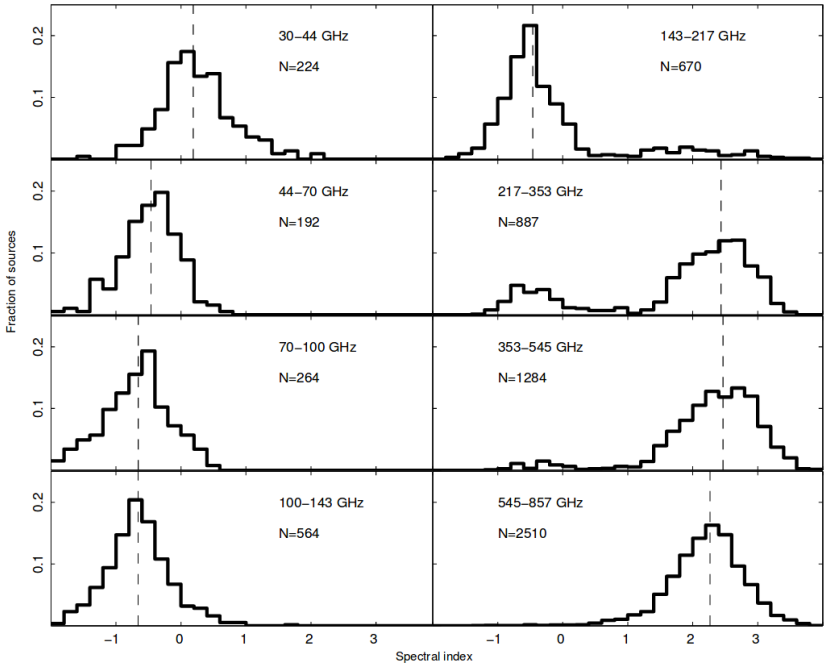

Figure 2.9 – Figure modified from Planck Collaboration et al. (2014f), representing spectral indices of sources which are detected in two neighbouring channels. Data are from the first release of the Planck Catalogue of Compact Sources. For each pair of channels, the number of detected sources is shown.

shows the distribution of point sources and galaxy clusters detected by Planck.

2.3.1 Radio galaxies

Radio point sources are the dominant population at frequencies below $\nu \sim 200$ GHz. They are sources at intermediate to high redshift. The bulk of the source emission at frequencies of interest for the CMB arises from non-thermal synchrotron radiation fuelled by relativistic electrons in Active Galactic Nuclei (AGN) jets (Vieira et al., 2010; Toffolatti et al., 2013). More specifically, the inner part of the AGN jets is believed to be shaped by the superposition of different self-absorbed synchrotron components (Kellermann & Pauliny-Toth, 1969), whose resulting emission has an approximately flat spectrum:

$$S \propto \nu^{\alpha}, \tag{2.8}$$

where $\alpha \simeq 0$. A steepening of the spectral index α of flat spectrum radio sources is observed above 40 GHz, and it is thought to be due to a change in the properties of the AGN jets (Toffolatti et al., 2013). Also other components contribute to the integrated radio emission. For example, sources whose orientation screens the inner jet have a radio emission of steeper spectrum that originates from their extended radio lobes. The power law $S \propto \nu^{\alpha}$ is only a crude approximation, and careful modelling of all the radio contributions compared to counts of resolved sources are needed to correctly describe the radio emission. Different models for radio sources counts exists, such as de Zotti et al. (2005) and Tucci et al. (2011). de Zotti et al. (2005) provides a good fit of source counts at lower frequencies, while Tucci

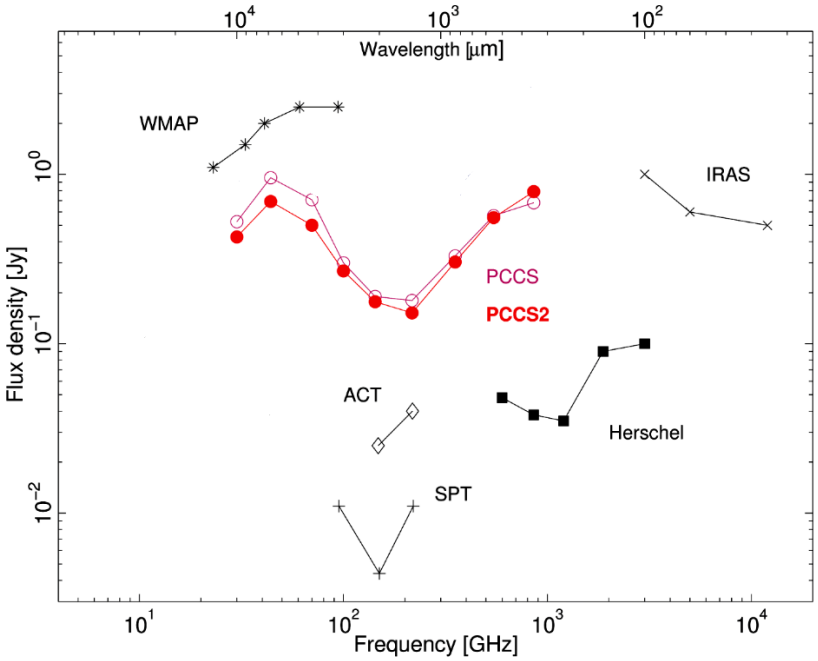

Figure 2.10 – Figure modified from Planck Collaboration et al. (2016f), showing the sensitivities (flux density at 90% completeness) for the first and second release of the Planck Catalogue of Compact Sources (PCCS and PCCS2 respectively). For comparison, the sensitivity of other instruments is shown: WMAP, ACT, SPT, Herschel and IRAS.

et al. (2011) well fits Planck high frequency data (Planck Collaboration et al., 2013) and SPT data (Mocanu et al., 2013). In this respect, ground observations are particularly useful since they probe source counts to lower fluxes than the Planck limit (Vieira et al., 2010), as seen from Figure 2.10.
In general, the spectral index of radio sources is quite different from that of dusty galaxies, and the two populations are clearly distinguishable. While radio sources have a flat spectrum, infrared sources have a steep spectrum increasing towards higher frequencies. Figure 2.9 plots observed spectral indices for detected source matches between contiguous channels in Planck 2013 Compact Sources Catalogue (Planck Collaboration et al., 2014f). One can see how at intermediate frequencies sources present a bimodal distribution, and that the change in the dominant population happens around $\nu \sim 200$ GHz. The steepening of the radio sources spectra towards higher radio frequencies can be seen in the slight shift in the median of the distribution at $\nu \leq 70$ GHz. Given the results of Figure 2.9, as we will see in Chapter 4, in this analysis we model point sources as two population with distinct emission law.
The sources plotted in Figure 2.9 are all resolved and their emission can be removed through masking. There is also a contribution from the unresolved sources, whose emission cannot be masked and has to be carefully evaluated. The unresolved galaxies emission are a discrete number of background sources randomly distributed on the sky: we can approximate their emission as Poisson shot noise. The resulting angular power spectrum is flat, with constant C_ℓ level (Tegmark & Efstathiou, 1996):

$$C_\ell = \int_0^{S_{cut}} d(\ln S)\; S^3\; \frac{dN(S)}{dS}, \tag{2.9}$$

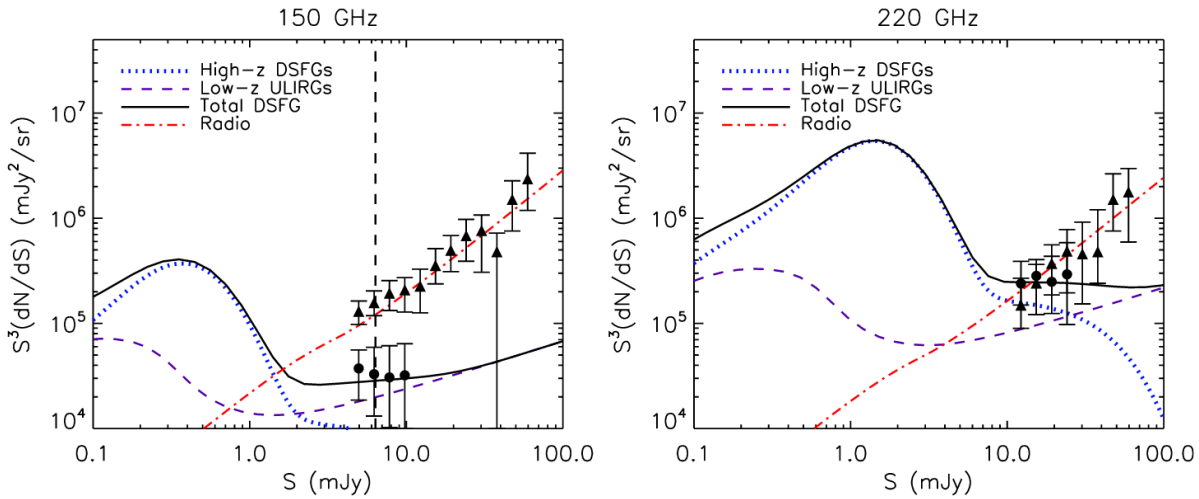

Figure 2.11 – Figure taken from (Hall et al., 2010), showing source counts models and detected sources for radio (filled triangles) and infrared (filled circles) point sources. Infrared source are termed DFSG: Dusty Star-Forming Galaxies. Radio sources are modeled according to de Zotti et al. (2005), while infrared sources according to Negrello et al. (2007).

where S is the flux density, $\frac{dN}{dS}$ is the differential number counts, and S_{cut} is the flux cut above which sources are detected and masked. The resulting angular power spectrum amplitude can be determined by suitable modelling of the differential number counts function using observed sources.
The Planck sky coverage is inhomogeneous on the sky due to the satellite scanning strategy, the high galactic latitudes being observed more often than the galactic plane. This results in a flux cut of detected sources which varies on the sky. Figure 2.11 shows the source counts for both radio and infrared point sources at the 150 GHz and 220 GHz channels of SPT. Radio shot noise emission is particularly sensitive to the flux cut value since $S^3 \frac{dN(S)}{dS}$ increases with the source flux. The bulk of infrared point sources instead lies below the detection threshold, and a change in flux cut does not affect much the angular power spectrum (Millea et al., 2012).

2.3.2 Cosmic Infrared Background

The Cosmic Infrared Background (CIB) arises from the emission of stars and dust in background star-forming galaxies. The CIB galaxies, also termed "dusty" galaxies (see Lagache et al. (2005) for a review), have active star-formation that produces bright massive stars. These are short-lived stars ending their life in supernova explosions, enriching the interstellar medium of metals that form dust grains. The star-forming galaxies emission increases with frequency and peaks around 2 THz. The spectral index of dusty galaxies, in the approximation that their emission between neighbouring channels can be described by a power-law as in Eq. (2.8), is $\alpha \simeq 2.5$, as seen from Figure 2.9. The CIB emission contains (integrated) information from galaxies at different redshifts, which is useful to study the galaxy evolution and the growth of structures. In particular, galaxies are not uniformly distributed in the universe, but tend to cluster due to gravitational attraction.

If galaxies are assumed to reside in dark-matter halos, the CIB can be used to infer dark matter properties on large scales. Due to the spatial correlation of CIB galaxies, their angular power spectrum cannot be simply described by shot noise, but also has a clustered component. The total CIB contribution is thus a sum of these two components, which can be analysed independently in terms of their angular power spectrum.[3].
The clustered CIB angular power spectrum can be described by the so-called "halo-model" (Cooray & Sheth, 2002), which describes the clustering of matter at all scales and is based on the assumption that all galaxies reside in a dark matter halo. The total power comes from two contributions: the large scale power derives from galaxy correlations in different halos (2-halo term), while the small scale power arises from correlations within the same halo (1-halo term). A simpler description is to approximate the clustered power spectrum as a power-law:

$$C_\ell^{clustered} = l^{n_{CIB}}. \tag{2.10}$$

The slope is found to be approximately $n_{CIB} \simeq$ -1.4 when considering Planck in combination with high-ℓ SPT and ACT data (Planck Collaboration XVI et al., 2014). Mak et al. (2017) have shown that a power-law well describes the CIB angular power spectrum at high-Planck frequencies, as seen in Figure 2.12. Indications exist that this value may change with the multipole range considered, being shallower at multipoles $\ell \lesssim 2500$ (Planck Collaboration XXX et al., 2014; Planck Collaboration XI et al., 2016).
The emission law of the CIB depends on various modified black-body spectra of infrared galaxies at different redshifts, whose stellar populations, and thus emission properties, can greatly differ from present day galaxies. For this reason, at Planck frequencies, the CIB emission law is described by a modified black-body (Lagache et al., 1999; Gispert et al., 2000):

$$I_{CIB}(\nu) \propto \nu^{\beta_{CIB}} B(\nu, T_{CIB}) \tag{2.11}$$

where the spectral index β_{CIB} and the temperature T_{CIB} are effective parameters and do not have a direct physical meaning. Planck Collaboration et al. (2011) finds that the CIB anisotropies measured from Planck are well described by the parameters $\beta_{CIB} = 1.4 \pm 0.2$ and $T_{CIB} = 13.6 \pm 1.5$ K. Figure 2.2 shows that small changes in the spectral index and especially in the temperature of a modified black-body law do not produce large shifts in the emission law. It is thus evident, comparing average values of CIB and dust parameters, that these two components have quite similar emission laws, and this is a strong limitation in order to separate their contributions. Separation can be achieved by using spatial information: in Planck Collaboration XLVIII et al. (2016), authors obtain a separation of dust and clustered CIB by exploiting the difference between their angular power spectra.

2.3.3 Sunyaev-Zel'dovich effect

When the CMB photons pass through a medium of hot ionised gas with free electrons, they interact via inverse Compton, scattering off the electrons to higher energies. This results in a distortion of the CMB spectrum in the gas direction, with a depletion of photons at lower frequencies and an increase at higher frequencies. Such effect is called thermal

[3]In this work we differentiate between the clustered and the shot-noise emission of dusty galaxies. In particular, and unless otherwise stated, when using the term CIB we refer to the clustered emission, while the shot noise component is referred to as infrared point sources. Nevertheless, in this Section only, we outline the characteristics of both.

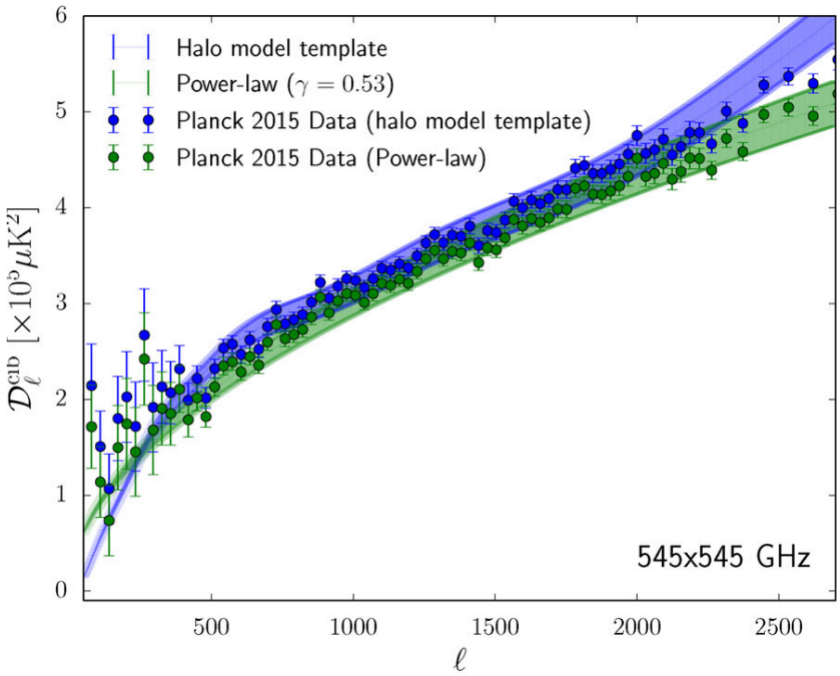

Figure 2.12 – Clustered CIB power spectrum at 545. This Figure is taken from Mak et al. (2017), where two different CIB models, together with a dust model and a shot noise model, are fitted to Planck data. The CIB models are a power-law as in Eq. (2.10), shown in green, and an extended halo model as in Planck Collaboration XXX et al. (2014), shown in blue. The data points are the measured spectra for 40% sky fraction after subtracting the best-fitting Poisson and galactic dust power in the appropriate CIB model. The power-law model has a best-fit slope (which the authors label γ) of $n_{CIB} = 0.53 \pm 0.02$, consistent with results obtained at lower frequencies in Planck Collaboration XV et al. (2014). The thickness of the lines corresponds to the marginalized 1 σ on the CIB amplitude. The steepening of the halo model both at high and low multipoles with respect to the power-law model is disfavoured by the data.

Sunyaev-Zel'dovich effect (tSZ) (Sunyaev & Zeldovich, 1970, 1972) and is most clearly detectable when observations at different frequencies are available, especially around 220 GHz, which is the frequency that divides the photon depletion and increment. The galaxy clusters are gravitationally bound systems of a few hundreds to a few thousands of galaxies. Within these clusters of galaxies, a thin intracluster medium of ionized hot gas is present. The gas temperatures reach 10^7-10^8 K, and the scattering of free electrons off the ions produces strong X-ray emission. Thus the tSZ effect is visible in the CMB in the direction of galaxy clusters.
There is also another effect on the CMB produced by galaxy clusters, also theorized by Sunyaev and Zel'dovich: since clusters have a bulk motion in some direction, their electrons act as a reflecting mirror and impress a Doppler shift on the CMB. This effect is called kinetic Sunyaev-Zel'dovich effect (kSZ) and it is a measure of the cluster velocity along the line of sight. Its frequency dependence is that of a black-body with slightly different temperature from the CMB one and for this reason it is quite difficult observationally to distinguish it from the CMB. Figure 2.13 shows the frequency black-body distortions of both the tSZ and kSZ effect compared to the CMB black-body spectrum.

The SZ effect rises not only in galaxy clusters, but more in general in presence of an ionized gas. During the reionization epoch, early formed quasars ionize the intergalactic medium around them. This can produce a detectable kSZ effect, while the tSZ effect is negligible (Aghanim et al., 1996). The CMB observations and X-ray data are useful complementary pieces of information to study galaxy clusters since they probe in a different way their gas properties. The tSZ effect is a measure of the electron density n_e integrated along the line of sight through the cluster, while the X-ray luminosity depends as the square of the gas particle density. One of the peculiarities of the SZ effect is that the change in the CMB temperature is independent of the distance to the cluster. This makes the SZ an ideal tool to detect high redshift clusters. The Planck satellite is well suited for studying the most massive clusters in the universe and has detected clusters up to $z \lesssim 1$, the limiting factors being the resolution and noise. Planck has detected several hundreds of clusters via SZ effect (Planck Collaboration et al., 2016g). By using optical and X-ray follow-up observations it is possible to confirm the cluster candidates observed by Planck and to estimate the redshift and the mass of these objects. This large sample of very massive clusters can be used to probe cosmology by studying cluster counts (Planck Collaboration et al., 2016d).
While individual clusters can be identified in the Planck maps, the global contribution of the SZ effect in the maps angular power spectra is not well constrained by Planck data alone. In the Planck likelihood analysis, this emission has been constrained by using SPT and ACT small scale data (Planck Collaboration XV et al., 2014) or by imposing a narrow prior (Planck Collaboration XI et al., 2016).

2.4 Component separation

The available data are often a mixture of different astrophysical components, or "sources". In particular, since there is no occlusion of the CMB by the foregrounds, we can model the data as a linear mixture of the different components. The data analysis dedicated to recover an estimate of the original sources from the mixtures is called *foreground removal* or *component separation*. The former expression is used when one chosen source is recovered by removing all the others, which are considered as contaminants. The latter instead implies that the method aims at recovering an estimate for (almost) all the present sources. In practice, these two terms are used indifferently in most cases. Component separation methods are versatile techniques that can be applied to many different problems. I will describe here only the component separation methods applied to the CMB. Other applications exist, such as for example the study of the 21cm cosmological signal. For details on these methods, we refer the reader to the dedicated literature (see for example Alonso et al. (2015); Chapman et al. (2015)).
In general, component separation methods are based on the linear mixture model:

$$\mathbf{y} = \mathbf{A}\mathbf{s} + \mathbf{n}, \tag{2.12}$$

which describes the mixing of sources $\mathbf{s}$ through a set of coefficients contained in the matrix $\mathbf{A}$ with some additive noise $\mathbf{n}$. The observed output are the linear mixtures $\mathbf{y}$. The methods to invert this problem and recover an estimate $\mathbf{x} \equiv \hat{\mathbf{s}}$ of the signal are varied, and no universal solution exists. The separation of sources may rely on the use of additional information or on the statistical properties of the data itself. Also, the technique chosen

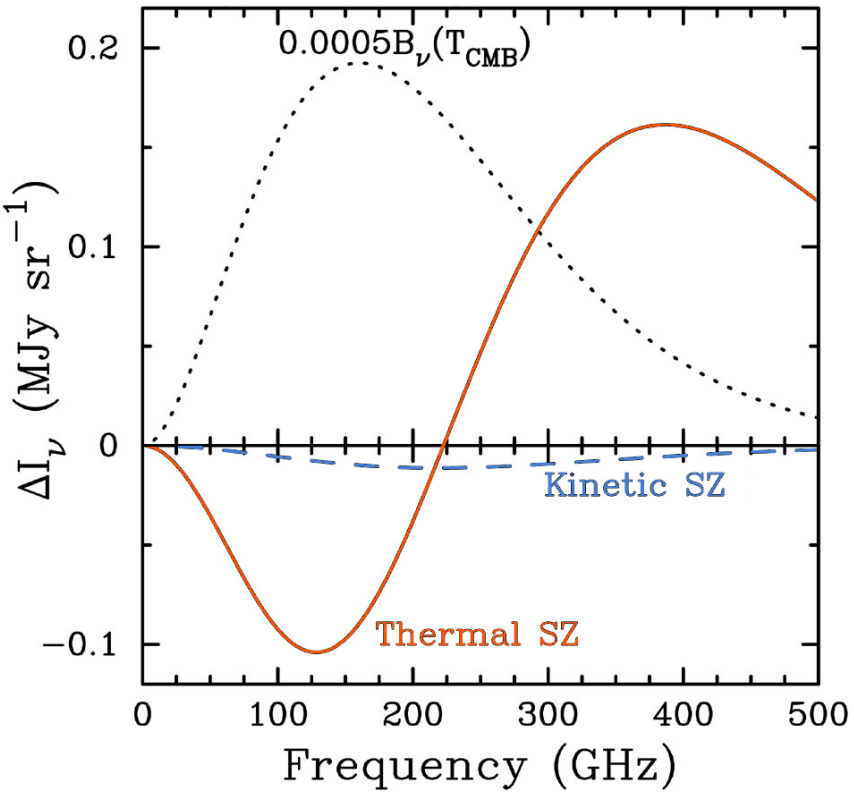

Figure 2.13 – Figure modified from Carlstrom et al. (2002), showing the CMB black-body distortions in the cluster direction for both the thermal and the kinetic SZ effect. For reference, the CMB black-body spectrum scaled by a factor 0.0005 is also shown.

depends on the target of the analysis, such as for example the CMB map, a foreground map, or the CMB angular power spectrum. Most methods presented here estimate the CMB map directly and then obtain the angular power spectrum from it, and only a few (Commander, BICA, SMICA (Planck Collaboration IX et al., 2016; Vansyngel et al., 2016)) obtain direct estimates of the CMB angular power spectrum.
Each component separation technique has its strong and weak points: the *Planck Collaboration* itself has chosen not one, but four different methods to produce foreground-cleaned CMB maps (Planck Collaboration XII, 2014). We can divide the existing methods in three broad categories: template fitting methods, parametric methods and blind methods, that use only minimal assumptions on the sources. In this Section and the following Chapter most of the existing component separation methods for CMB are detailed. A comparison of most of these methods based on Planck simulated data can be found in (Leach et al., 2008). Other publications (Ichiki, 2014; Delabrouille & Cardoso, 2009) provide a review of some of the principal methods.

2.4.1 Template fitting methods

Template fitting relies on the idea of subtracting a set of foreground templates to the data in order to find the desired signal. Considering the model of Eq. (2.12), the foreground-cleaned map $\mathbf{x}$ at the frequency ν is given by:

$$\mathbf{x}(\nu, p) = \mathbf{y}(\nu, p) - \sum_{i}^{N} \alpha_i(\nu)\mathbf{t}_i(p). \tag{2.13}$$

where $\mathbf{t}_i(p)$ are the templates and $\alpha_i(\nu)$ the coefficients to be determined. In its simplest formulation, the templates are considered independent of frequency, while the coefficients are independent of position p. Given a set of N templates, the mixing coefficients are usually obtained minimizing the variance of the reconstructed map:

$$\alpha_i(\nu) = \operatorname{argmin} \sum_{p} \left[\mathbf{y}(\nu, p) - \sum_{i}^{N} \alpha_i(\nu)\mathbf{t}_i(p)\right]^2. \tag{2.14}$$

This procedure produces a set of foreground-cleaned maps at each frequency. In order to combine them to obtain a single CMB map it is necessary to correct for different resolutions, which is easily done in harmonic space Planck Collaboration IX et al. (2016). The resulting map is somehow dependent on the choice of templates.
The *WMAP team* uses a template fitting method for obtaining foreground reduced maps which are used for angular power spectrum analysis (Bennett et al., 2013a). The strong assumption in this technique is that the foregrounds are represented by one single template at all frequencies, not allowing any dependence of the emission law with the position on the sky. If this assumption does not hold, systematics in the data could be introduced. The second assumption is that the chosen templates represent all the significant foreground contributions. The *WMAP team* uses this technique with a combination of physically motivated internal and external templates, and the fitted coefficients provide additional information on the foregrounds.
In the Planck analysis, a template fitting technique called SEVEM (Spectral Estimation Via Expectation Maximization) (Fernández-Cobos et al., 2012) is used. The templates used are internal, since they are built from Planck data itself. To create a template, two

close frequency sky maps are subtracted in order to cancel out the CMB signal. Even though these templates do not properly describe one single foreground component, they are closer to the foregrounds distribution on the sky present in the data. The advantage of using internal templates is that no particular knowledge of the foregrounds is needed, since the information is taken directly from the data.

2.4.2 Parametric methods

These methods fit a parametric model to the data. Two different techniques based on this approach are Commander, which uses a physically motivated model for the foregrounds, and the Maximum Entropy Method (MEM), which defines the model of the sources based on the maximum entropy principle. Since both these methods use Bayes theorem, we recall it here. The Correlated Component Analysis (CCA) uses second-order statistics and, although it is not necessarily a parametric method, often uses a parametrization of the covariance matrix to reduce the dimensionality of the fit.
Bayes theorem states that the *posterior*, which is the probability $p(\theta|\mathbf{d})$ of the model given the data, is:

$$p(\theta|\mathbf{d}) = \frac{\mathcal{L}(\mathbf{d}|\theta)p(\theta)}{p(\mathbf{d})} \tag{2.15}$$

where $\mathcal{L}(\mathbf{d}|\theta)$ is the *likelihood*, $p(\theta)$ is the probability of the model, or *prior*, and $p(\mathbf{d})$ is the probability of the data, or *evidence*.

Commander
This method (Eriksen et al., 2004; Eriksen et al., 2008) does a Bayesian estimate of the CMB angular power spectrum and map, as well as the foreground maps via a set of model parameters. Commander is one of the four methods used by the *Planck Collaboration*, and in particular is the method used for obtaining foreground sky maps (Planck Collaboration X et al., 2016). The foreground sky maps presented in Figures 2.3 and 2.6 are all obtained with this method. Commander uses either the Gibbs sampling algorithm to sample the full parameters posterior, or an iterative method that uses non-linear search algorithms to derive the maximum likelihood estimate of all parameters. The advantage of having the full posterior is that uncertainties on the CMB angular power spectrum are calculated taking into account the errors of the parameters of the model.
The foreground model is constructed on physical assumptions: while information is gained on the foregrounds physical properties, some hypotheses and prior knowledge are needed in order to define the model. Imperfect modelling, as well as bad prior choices, can lead to errors in the estimation. Also, since the model has a large number of parameters, it is difficult to determine if the algorithm is stuck in a local maximum instead of the global one.
Commander works in pixel space and needs all input maps to be at the same resolution: this means that the lowest resolution channel constrains the maximum resolution of the fit. A work around is to first fit for the parameters constrained by the low resolution channels, and then use a smaller high resolution dataset for fitting the remaining parameters. Using this multi-resolution technique, the Commander method obtains estimates of the CMB map at different resolutions and considering a different complexity of the foreground model. Combining them to obtain a single map is not trivial, and the resulting CMB map has an effective sky fraction that varies with the angular scale (Planck Collaboration IX et al.,

2016)
The *WMAP team* also uses a parametric method exploiting a Monte Carlo Markov Chain (MCMC) fitting technique for studying the galactic foregrounds (Bennett et al., 2013a). The model used has less parameters than that of Commander, but *WMAP team* uses less data to constrain the model. In Planck Collaboration X et al. (2016) the foreground model is more refined, but Planck, WMAP and other external data are used in the fit. Differently from Commander, the *WMAP team* jointly fits temperature and polarization data.

MEM
MEM (Hobson et al., 1998; Stolyarov et al., 2002) has a Bayesian approach since it aims at finding the most probable reconstruction (or posterior) given a likelihood and the signal priors. These priors are defined using the maximum entropy principle. This principle states that, when choosing a probability distribution $p(x)$ for a random variable $\mathbf{X}$, the least informative choice should be made, and this is the choice that maximizes the differential Shannon entropy $H(\mathbf{X})$, defined as:

$$H(\mathbf{X}) \equiv \int p(x) \log(p(x)) dx \tag{2.16}$$

The choice of the prior depends also on the available knowledge of the signal: we know for example that foregrounds do not have Gaussian distributions. The chosen form of the prior then is:

$$p(\alpha) \propto e^{\alpha S(\mathbf{s},\mathbf{m})} \tag{2.17}$$

where α is a dimensional regularizing parameter, $\mathbf{s}$ is a signal component, $\mathbf{m}$ is its model, and $S(\mathbf{s},\mathbf{m})$ is the cross entropy between the two. Strictly speaking this prior assumes that $\mathbf{s}$ and $\mathbf{m}$ are only positive, but the method can be easily extended to account for both positive and negative values (Hobson & Lasenby, 1998). We note that the reconstruction of the signal depends on the choice of the parameter α. If the likelihood is expressed as $\mathcal{L}(\mathbf{d}|\theta) \propto e^{-\chi(\mathbf{s})^2}$ and recalling Bayes theorem of Eq. (2.15), then maximizing the posterior distribution is equivalent to minimizing the non-linear function:

$$\Phi_{MEM} = \chi(\mathbf{s})^2 - \alpha S(\mathbf{s},\mathbf{m}). \tag{2.18}$$

Differently from the Gaussian prior, the propagation of errors is not straightforward using the entropic prior: Hobson et al. (1998) approximate the shape of the posterior as a Gaussian in order to estimate the covariance matrix of the errors. Hobson et al. (1999) apply the method to simulated data containing extragalactic point sources, which have not been masked in the analysis. Although some of the brightest sources are still present in the reconstructed map, the CMB signal is recovered quite accurately on most pixels. (Barreiro et al., 2004) extend this method to a more "flexible" configuration that combines both real and harmonic domains, and apply it to COBE data.
A different MEM-based method has been used by the *WMAP team* in order to disentangle the emissions of the different foregrounds. The chosen priors are spatial templates of different emissions and the fit is done by minimizing in pixel space:

$$H(p) = \chi^2(p) + \lambda(p) \sum_s T_s(p) \ln \frac{T_s(p)}{P_s(p)} \tag{2.19}$$

where $P_s(p)$ are the sources s priors, and $T_s(p)$ their model. The parameter $\lambda(p)$ controls the fidelity of the fit to the model. The obtained maps are used to understand the

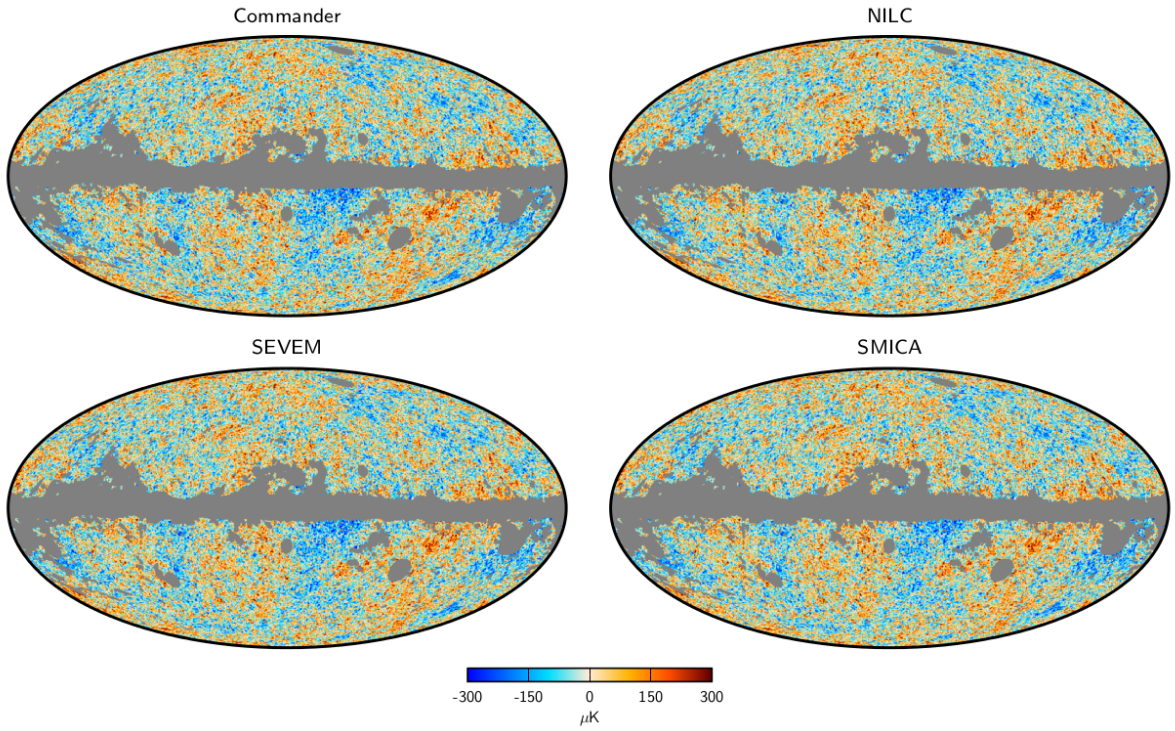

Figure 2.14 – Figure taken from Planck Collaboration IX et al. (2016), showing the four foreground-cleaned temperature CMB maps provided by the *Planck Collaboration* at 5′ resolution.

foregrounds physical properties but cannot be used for foreground removal since their noise properties are quite complicated (Bennett et al., 2013a).

CCA

While the CMB and the foregrounds are independent, the galactic foregrounds have a similar spatial distribution and present some degree of correlation in pixel space. The correlation of the foregrounds can be exploited for source separation by using second-order statistics of the signal (Bedini et al., 2005; Bonaldi et al., 2006). For this reason this method is called Correlated Component Analysis.

The data are modelled as in Eq. (2.12). To be applied, this method requires an estimate of the data and noise covariances: the data covariance matrix $\hat{\mathbf{R}}_y$ can be estimated for different spatial shifts directly from the observations, while the noise covariance matrix $\mathbf{R}_N$ can be evaluated by knowing the noise variance in the data. If the components are correlated, computing covariances for different shifts gives the required constraints to recover the mixing matrix and the covariance of the signal. The sources covariance $\mathbf{R}_S$ and the mixing matrix $\mathbf{A}$ are related to the data and noise covariances as:

$$\mathbf{R}_y = \mathbf{A}\mathbf{R}_S\mathbf{A}^T + \mathbf{R}_N, \tag{2.20}$$

and can be estimated via:

$$\mathbf{A},\ \mathbf{R}_S = \text{argmin} \sum_{\tau,\psi} ||\mathbf{A}\mathbf{R}_S(\tau,\psi)\mathbf{A}^T + \mathbf{R}_N(\tau,\psi) - \hat{\mathbf{R}}_y(\tau,\psi)||, \tag{2.21}$$

where (τ, ψ) are different shifts in the position on the sky and $\mathbf{R}_S$ is the vector of source covariances estimated at all pairs. The minimization is performed over all the available shifts pairs. Once the mixing matrix is estimated, this can be used in other methods, such as MEM, to recover the desired signal.
This method requires the number of observations to be greater than the number of sources to estimate. However, using prior information, the mixing matrix can be parametrized in terms of the spectral indices of the considered emissions, thus reducing the number of parameters to estimate. It must be stressed that this model relies on the assumptions made to evaluate the noise covariance. Also, the different resolutions of the observed channels are not taken into account in the data model, and all maps have to be degraded to the lowest resolution of the observations.
Bedini et al. (2005) use the estimated mixing matrix to invert the problem and obtain $\mathbf{x} = \mathbf{B}\mathbf{y} = \mathbf{s} + \mathbf{B}\mathbf{n}$, where $\mathbf{B} = (\mathbf{A}^T\mathbf{A})^{-1}\mathbf{A}^T$ is the pseudo-inverse of $\mathbf{A}$. The sources are then estimated via Wiener filtering. They apply the method to small flat sky patches only. This model fails at high-galactic latitudes since foregrounds are subdominant with respect to noise, and can be only applied at low galactic latitudes. Bonaldi et al. (2006) extend the method to work on spherical sky patches and on the whole sphere. They also estimate, on simulated data, the errors on the angular power spectrum of the estimated map. In Bonaldi et al. (2007) authors apply the method to WMAP 3-year data and test different foreground models for the reconstruction of the CMB signal and the angular power spectrum. Ricciardi et al. (2010) extend the method to polarized data and test it on simulations.

2.4.3 Blind methods

These methods only use minimal assumptions on the sources to separate, and for this reason they are called "blind". The advantage of blind methods is that no prior knowledge on the foregrounds is needed to extract the CMB information, and the reconstruction is based entirely on the different statistical properties of the signal and the foregrounds. We present here the Internal Linear Combination method (ILC) and the Generalized Morphological Component Analysis method (GMCA). This work is based on one blind component separation method which exploits a technique called Independent Component Analysis (ICA). Since ICA principles are explained in more detail in the following Chapter, all ICA-based methods description is postponed there.

ILC

The ILC is a simple yet powerful foreground removal method based on the idea that CMB is decorrelated from noise and foregrounds and that we want to minimize the contribution of the last two. No assumption is made on the foregrounds or noise, but the CMB emission law must be known precisely. Under these assumptions, the data of one channel y_i can be modelled as:

$$y_i = a_i s_{CMB} + \sum_j f_{ij} + n_i \tag{2.22}$$

where a_i is the i-th entry of the vector $\mathbf{a}$ containing the emission law of CMB, and f_{ij}, n_i are the foregrounds and noise respectively. The method finds a set of weights w_i that minimizes the variance of the reconstructed map $x_{CMB} = \sum_i w_i y_i$, where the sum is performed over all channels. In order to preserve the CMB signal, the weights vector $\mathbf{w}$

must satisfy the condition $\mathbf{w}^T\mathbf{a} = 1$. Then the variance of the recovered signal $\hat{\sigma}_{CMB}$ is:

$$\hat{\sigma}^2_{CMB} = \sigma^2_{CMB} + \sum_{i,j}\langle w_i f_{ij}, w_i f_{ij}\rangle + \sum_i \langle w_i n_i, w_i n_i\rangle \tag{2.23}$$

where σ_{CMB} is the CMB signal variance. To minimize $\hat{\sigma}_{CMB}$, the weights w_i find a trade-off between minimizing the noise and the foregrounds. The weights are:

$$\mathbf{w} = \frac{\mathbf{a}^T\hat{\mathbf{R}}^{-1}}{\mathbf{a}^T\hat{\mathbf{R}}^{-1}\mathbf{a}} \tag{2.24}$$

where $\hat{\mathbf{R}}$ is the empirical covariance matrix of the observations defined as $\hat{\mathbf{R}} = \frac{1}{N_{pix}}\sum_p \mathbf{y}(p)\mathbf{y}(p)^T$, where N_{pix} is the number of pixels and the superscript ^{T} denotes transposition.
In the WMAP formulation the weights do not depend on position. Nevertheless, the foregrounds and noise properties vary with position and scale: in particular foregrounds dominate the large scales, while noise dominates the small scales. The *WMAP team* divides the sky in twelve disjoint regions and applies a different set of weights in each of them (Bennett et al., 2013a). This mitigates the problem since the regions can be chosen to have an almost uniform foreground contamination, but the result depends on how the sky is partitioned (Hinshaw et al., 2007) and also on how the CMB patches are assembled to create the final map.
A different possibility is to work in the harmonic space, with weights that depend on the multipole scale (Tegmark et al., 2003):

$$\mathbf{w}_\ell = \frac{\mathbf{a}^T\hat{\mathbf{R}}_\ell^{-1}}{\mathbf{a}^T\hat{\mathbf{R}}_\ell^{-1}\mathbf{a}} \tag{2.25}$$

where R_ℓ is the data covariance matrix defined as $\hat{\mathbf{R}}_\ell = \frac{1}{2\ell+1}\sum_{m=-\ell}^{m=+\ell}\mathbf{y}_{\ell m}\mathbf{y}^\dagger_{\ell m}$, where the superscript † denotes transpose conjugation. When working in harmonic space it is also easier to take into account the different resolutions of the observed channels.
If there is some correlation between foregrounds and the CMB, the estimated signal x_{CMB} is biased, i.e., a part of the foreground signal is subtracted from the CMB to achieve minimal variance. Even though the CMB signal does not correlate with foregrounds, some small degree of correlation is expected due to chance correlations (Delabrouille et al., 2009). Also, the CMB emission law has to be known precisely, and calibration errors of less than 1% can affect the reconstruction (Dick et al., 2010).
The ILC is one of the methods used by the *Planck Collaboration*: their implementation, the Needlet ILC (NILC) (Delabrouille et al., 2009; Basak & Delabrouille, 2012, 2013), works in needlet space, since this basis allows to localize the weights both in scale and in position. A Generalized NILC (GNILC) (Remazeilles et al., 2011) method has been used to disentangle dust and CIB emissions. Since they both have a similar scaling in frequency, further constraints are needed to achieve separation. These are given by the different spatial distribution of the two emissions, which results in a different angular power spectrum (Planck Collaboration XLVIII et al., 2016). Another ILC implementation, SILC (Scale-discretised, directional wavelet ILC), uses directional wavelets that can possibly better match directional structures in the foregrounds. In the temperature implementation, SILC obtains comparable results to NILC in terms of the CMB map (Rogers et al., 2016).

GMCA

This is a blind method that exploits sparsity. A signal is called *sparse* in a given basis if it can be represented by only a few elements in that basis. The astrophysical sources are not sparse in pixel space, but can be sparsified when transformed in another domain. GMCA (Bobin et al., 2008) uses wavelets since foregrounds are sparse in this basis and since they allow for localisation both in space and spatial frequency. A source can be represented as (Bobin et al., 2013):

$$\mathbf{s}_i = \alpha_i \mathbf{\Phi} \tag{2.26}$$

where $\mathbf{\Phi}$ is a matrix containing the wavelet waveforms, also called dictionary, and α_i is the vector containing the coefficients of the expansion in the wavelet basis, most of which are null or negligible. The data model then becomes:

$$\mathbf{y} = \mathbf{A}\alpha\mathbf{\Phi} + \mathbf{n}. \tag{2.27}$$

The coefficients α_i are found minimizing:

$$\min \frac{1}{2}||\mathbf{y} - \mathbf{A}\alpha\mathbf{\Phi}||_F^2 + \lambda \sum_j ||\alpha_j||_p, \tag{2.28}$$

where $||\mathbf{q}||_F = \sqrt{\mathrm{tr}(\mathbf{q}^T\mathbf{q})}$ and usually $p = 0$. In this way the distance between the data and the reconstructed signal is minimized together with the constraint of having only a few active coefficients. Hence the method recovers the sparsest solution, which is found via an iterative algorithm.
The GMCA method is generalised to Local-GMCA (L-GMCA) to take into account different resolutions of the input channels and the space variability of the foregrounds emissions (Bobin et al., 2013, 2014).

2.4.4 Wiener filtering

Originally developed to reduce noise in time series, in the context of CMB analysis this method is used to minimize the noise and foregrounds contamination in the observed data. Under certain conditions, it can be used for component separation. These conditions include the knowledge of the signal and noise covariances, as well as the mixing matrix. Since these are usually not known, Wiener filtering can be used in combination with other component separation methods as a post-processing step on foreground-cleaned maps in order to minimize the variance of the error in the map (Tegmark et al., 2003; Patanchon et al., 2005; Bonaldi et al., 2007). The SMICA method, presented in the next Chapter, can provide the required information for applying the Wiener filter (Cardoso et al., 2008). The Wiener filter assumes that the noise and the signal are both Gaussian processes. For the foreground-cleaned maps this is a reasonable assumption. Assuming that observations are a sum of signal and noise as in Eq. (2.12), the Wiener filter finds an estimate of the signal whose error has minimum variance. The filter $\mathbf{W}$ in pixel space is (Tegmark & Efstathiou, 1996; Bouchet & Gispert, 1999):

$$\mathbf{x} = \mathbf{W}^T\mathbf{y} \quad \text{where} \quad \mathbf{W} = \mathbf{R}_S\mathbf{A}(\mathbf{A}\mathbf{R}_S\mathbf{A}^T + \mathbf{R}_N)^{-1}, \tag{2.29}$$

but it can also be implemented in the spherical harmonic domain, by replacing $\mathbf{R}_S$ with $\mathbf{R}_S^\ell$ and $\mathbf{R}_N$ with $\mathbf{R}_N^\ell$ (see for example (Tegmark et al., 2003)). This filter is ~ 1 in the

signal dominated regime, while it strongly suppresses the data in the low signal-to-noise regime.
The major drawback of this method is that by suppressing the signal at the noisy scales it biases the power spectrum estimated from the map. This can be corrected by imposing that the filter **W** has unit gain on the diagonal (Tegmark & Efstathiou, 1996), however the resulting map does not have minimum variance of the residuals anymore (Delabrouille & Cardoso, 2009), and the obtained solution is equivalent to the ILC one. In practice, one can switch between the ILC and the Wiener solution by rebeaming the reconstructed map. The ILC beam can be defined to give a precise resolution to the map, while the Wiener map beam falls more sharply at high multipoles, in order to suppress the noise in the reconstructed map. Knowing the shape of the beam of the Wiener filtered map it is possible to rebeam the map to a given resolution. This corresponds to changing the weight at the different scales, and even though it does not change the signal-to-noise ratio (SNR) at each multipole, it increases the importance of multipoles with lower SNR and thus also increases the total SNR of the reconstructed map. In conclusion it is not possible to obtain a map of both minimal integrated error and defined resolution, but it is possible to change from one to another by rebeaming the map.

Chapter 3

SMICA

Contents

Blind methods for source separation present the undeniable advantage of needing only minimal assumptions on the foregrounds emissions. In this Chapter I will present one technique that exploit blindness, which is the Independent Component Analysis. ICA relies on the assumption that the observed data originate from a mixture of independent sources. Different ICA methods have been developed for source separation. Among these, SMICA is a method that estimates directly the CMB angular power spectrum. The more, it does so in the maximum likelihood sense. This Chapter outlines the basic ICA principles and then describes the SMICA method. In the end, the description of two other ICA component separation methods is given.

3.1 Blind Source Separation

The question of recovering the original sources given a (possibly non-linear) mixture is presently a highly investigated problem in signal processing. Doing so by assuming almost nothing on the sources and the way they are combined goes under the name of blind source separation (BSS). BSS is a general name defining a class of techniques and does not refer to one methodology in particular. It comprises very different methods, but all of them are based on the hypothesis that only the signal mixtures are observed.
A typical BSS problem is the so-called "cocktail party problem", where the goal is to distinguish the voices of different speakers at a party, provided the room is equipped with enough sensors. Another example, drawn from the medical field, is the identification of both the heart signal of the mother and the baby in a prenatal electrocardiogram, which displays a combination of them. These practical applications of BSS give an intuitive feeling of the capability of such techniques. In astrophysics, BSS has been applied to different fields, such as analysis of microwave sky maps (Delabrouille et al., 2003; Maino et al., 2002; Bobin et al., 2013), 21cm signal from the epoch of reionization (Alonso et al., 2015), and exoplanet spectroscopy (Waldmann et al., 2013), among others.
As a research field, BSS appears in the 1980s (Herault & Jutten, 1986), and it is now an established research domain that combines expertise from signal processing, statistics and neural networks. It is a wide field that comprises different methods, which adapt to a varied number of problems. In fact, the input sources properties are diverse, and their mixing and transmission characteristics add complexity to the problem. Hence no universal technique exists to solve them all. What all these methods have in common, is that they address the question of recovering an input given the output only. Stating the problem in a general fashion, we can say that BSS aims at solving the following system:

$$\mathbf{y}(t) = \mathscr{A}(\mathbf{s}(t)), \tag{3.1}$$

where $\mathbf{s}$,$\mathbf{y}$ are the vectors containing the input sources and output mixtures respectively, t is the sampling index of the sources and $\mathscr{A}$ is a generic function that encodes the (again not necessarily linear) combination of sources into outputs. We note that $\mathbf{s} \in \mathbb{R}^M$ and $\mathbf{y} \in \mathbb{R}^N$, i.e., the sources and outputs can have different dimensionality.
One method widely employed for BSS problems is Independent Component Analysis, which relies on the statistical independence of sources to separate them. This thesis focuses on ICA techniques, but the interested reader can refer to Jutten & Comon (2010) and Yu et al. (2014) for more details on different approaches to the BSS problem. For a broad review of ICA the reader can look at Hyvärinen et al. (2001) and Roberts & Everson (2001).

3.2 ICA principles

Independent Component Analysis is a class of techniques for statistical data analysis widely used in BSS. In fact, ICA techniques emerged to solve BSS problems. While the solution of BSS is not limited to ICA, it is also true that ICA can be applied to other types of problems, for example in feature extraction (Hyvärinen et al., 2002). Even though some author use these terms indifferently, one should bear in mind the distinction between these two concepts.

As the name implies, ICA assumes statistical independence of sources in order to separate them. This assumption is often physically justified in real life cases, so it poses no huge constraints in terms of applicability. For example, signals originating from different physical processes are often independent. Assuming a linear mixing of the sources, Eq. (3.1) becomes:

$$\mathbf{y}(t) = \mathbf{A}\mathbf{s}(t), \tag{3.2}$$

where $\mathbf{A}$ is a $N \times M$ matrix, often termed "mixing matrix", that contains the coefficients of the linear combinations of the sources $\mathbf{s}(t) = [s_1(t), s_2(t), ..., s_m(t)]$ into the outputs $\mathbf{y}(t) = [y_1(t), y_2(t), ..., y_n(t)]$. For simplicity, we will omit the sampling index t in the following. We also note that Eq. (3.2) refers to the noiseless case, since many methods have been developed for the noiseless case first: the addition of non-negligible noise $\mathbf{n}$ complicates the problem, since Eq. (3.2) becomes not invertible. For noisy mixtures we have:

$$\mathbf{y}(t) = \mathbf{A}\mathbf{s}(t) + \mathbf{n}, \tag{3.3}$$

where $\mathbf{n} \in \mathbb{R}^N$.
The purpose of ICA is then to find the $M \times N$ transformation $\mathbf{W}$ defined as:

$$\mathbf{x} = \mathbf{W}\mathbf{y}, \tag{3.4}$$

such that $\mathbf{x} = \hat{\mathbf{s}}$ is the $M \times 1$ vector containing the noisy estimated sources $\mathbf{s}$, up to rescaling and permutation (see Sect. 3.2.3). This is done without any *a priori* information on either the mixing matrix or the sources, other than their independence. The issue arises then on how to express source independence. Depending on this choice, different implementations of ICA have been designed.

3.2.1 On independence

We say that two variables are independent when no information about one of them can be gained from the other. For example, in the problem under study, the CMB and the foregrounds are statistically independent signals. In a more rigorous way we can say that given a set of n variables $\mathbf{X}_i$, they are statistically independent if their joint probability density function can be written as:

$$p(x_1, x_2, ..., x_n) = \prod_{i=1}^{n} p_i(x_i), \tag{3.5}$$

where $p(x_i)$ are the marginal probability functions of the variables $\mathbf{X}_i$. As a consequence of independence, the covariance of two independent variables $\mathbf{X}, \mathbf{Y}$, which tells us how two variables change together, is zero:

$$Cov(\mathbf{X}, \mathbf{Y}) = E[(\mathbf{X} - E[\mathbf{X}])(\mathbf{Y} - E[\mathbf{Y}])], \tag{3.6a}$$
$$= E[\mathbf{X}\mathbf{Y}] - E[\mathbf{X}]E[\mathbf{Y}] = 0. \tag{3.6b}$$

Likewise, independent variables are uncorrelated. A measure of the degree of correlation between two variables is given by the correlation coefficient $\rho(\mathbf{X}, \mathbf{Y})$:

$$\rho(\mathbf{X}, \mathbf{Y}) = \frac{Cov(\mathbf{X}, \mathbf{Y})}{\sqrt{Var(\mathbf{X})Var(\mathbf{Y})}}, \tag{3.7}$$

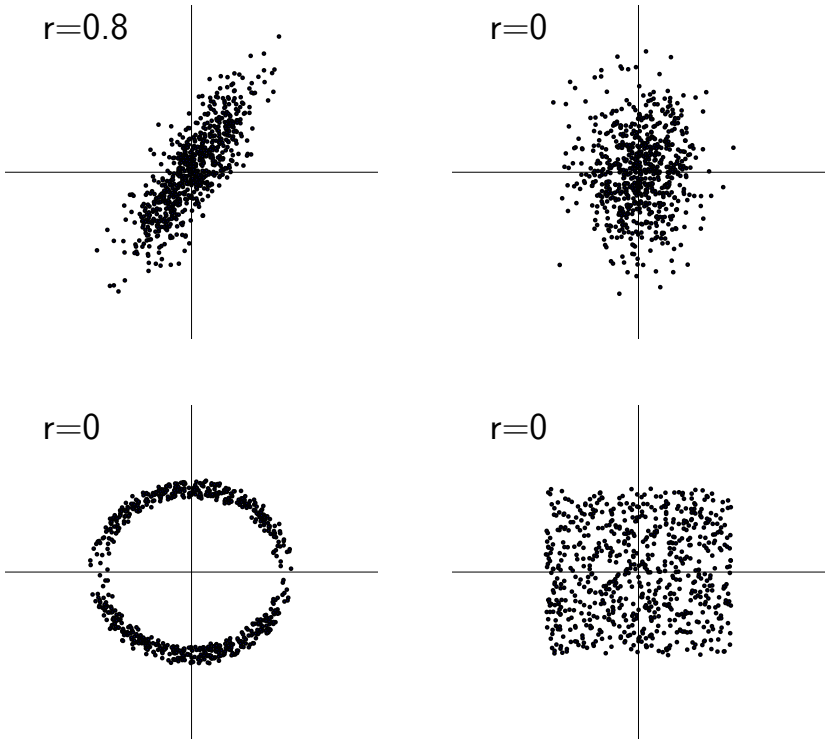

Figure 3.1 – Joint distribution of two variables $\mathbf{X}$ and $\mathbf{Y}$. The upper left panel shows the case of two dependent correlated variables. The lower left panel shows two dependent uncorrelated variables. Both panels on the right show independent variables.

where $r(\mathbf{X}, \mathbf{Y}) \in [-1, 1]$. We can see that since independence implies null covariance, it also implies null correlation.
The opposite is however not true, and null correlation in general does not imply independence, which is a much stronger mathematical property. It is true that, if two variables have a joint probability distribution $p(x, y)$ which is normally distributed and they are uncorrelated then they are also independent, but this is often not the case. Figure 3.1 illustrates this concept: Variables on the left are dependent, while variables on the right panels are independent. However the correlation coefficient r is zero in three cases. The variables in the bottom left panel have no correlation but they present a clear dependence.
One technique exploiting decorrelation is Principal Component Analysis (PCA). PCA performs signal whitening of the data, and returns a set of linearly uncorrelated variables. PCA however is not a source separation method: its goal is to find a small set of variables that can well represent the data. ICA instead goes beyond decorrelation, and restores the source independence. In the following Section we will see how imposing the independence constraint is sufficient for source separation.

3.2.2 How separation works

Several ICA methods can be found in the literature. This variety responds to the need for solutions adapted to specific problems, that is the different possible configurations which can be represented by Eq. (3.3). One has to specify whether or not signal dominates over noise, how many sources and outputs are available, i.e., if the problem is underdetermined,

and what is the (supposed) probability distribution of the sources. All these characteristics allow to completely specify the problem.
The constraints imposed to achieve separation are based on the assumption of independence, and the actual expression of the independence constraint depends on the assumed model for the sources. Once this is specified, the likelihood of the problem can be written straightforwardly. It is interesting to note at this point that ICA methods cannot separate Gaussian stationary signals, or, more precisely, they can separate at most one Gaussian signal. The independence criterion among sources does not give enough constraints to identify the mixing matrix and some extra assumptions on the sources distributions have to be made. We will outline here a few possibilities. In general it is necessary that the sources distributions present some characteristics that make separation possible, such as non-Gaussianity or non-stationarity. While these data distributions are quite different, it can be shown that the independence conditions arising from these various non-properties are connected. (Cardoso, 2001; Pham & Cardoso, 2001).

Non-Gaussianity
This method applies to sources non-normally distributed. It is known that, at first order, the result of the contamination of one non-Gaussian random variable $\mathbf{X}$ with another variable $\mathbf{Y}$ is more Gaussian than the original variable $\mathbf{Y}$ (Pham, 2005). Hence maximizing non-Gaussianity returns independent sources, since any combination of them would be closer to a Gaussian distribution than the original source distribution (Comon, 1994). When restoring independence via non-Gaussianity maximization, it is necessary that such feature is present in the original sources. It is therefore important to note that this ICA formulation cannot separate Gaussian sources, and it imposes to have at most one Gaussian source to ensure separability. The FastICA method, described at the end of this Chapter, is based on this approach.

Non-stationary / Non-white sources
Assuming that sources $\mathbf{s}$ are independent and that different samples are independent, then:

$$p(\mathbf{s}(t)) = \prod_i \prod_t p_{it}(s_i(t)) \tag{3.8}$$

It is not possible to recover blindly all these functions, thus some hypotheses on the source distributions are necessary. One possibility is to assume that the source distributions are Gaussian but with some form of time dependence $p_{it} = \mathcal{N}(0, \sigma_i(t)^2)$. In fact, in order to achieve separability it is important that sources display some kind of diversity, and are either non-stationary or stationary but time-correlated (that is with non-white spectrum)[1]. In case of non-stationary sources, the signal variance of each source $\sigma_i^2(t)$ depends on time. An interesting way to use time correlated sources is to work in Fourier space since, asymptotically for large sampling intervals, the sources are Gaussian random variables with a non-white power spectrum and there is no correlation between wavenumbers. This

[1]Non-stationarity recalls the idea of time series. In this context, this is however just a conventional term to indicate that $\sigma^2(t_1) \neq \sigma^2(t_2)$, i.e., that signal variance changes over the sampled interval. The same can be said about non-white signals: while in the text we explicitly mention time correlation, the same reasoning can be applied to spatial correlation. This is in fact the case for the CMB signal.

is known as the Whittle approximation (Pham & Garat, 1997; Delabrouille et al., 2003). The likelihood of the problem $\mathcal{L}(\mathbf{y}|A)$ is maximized at a point where:

$$\frac{1}{T}\sum_{t=1}^{T}\frac{x_i(t)}{\sigma_i^2(t)}x_j(t) = \delta_{ij}. \tag{3.9}$$

Here x_i,x_j are estimators of the unknown sources, T is the length of the sampled interval and δ_{ij} is the Kronecker delta. This equation gives the required constraints for blind identification (Pham & Cardoso, 2001). The variances $\sigma_i^2(t)$ may not be known in advance, but they can be estimated jointly with the other parameters by implementing an iterative algorithm. It is important to note that the condition of diversity of the variances, or spectral diversity, is essential to ensure separability. If two sources s_i,s_j have variances $\sigma_i^2(t) \propto \sigma_j^2(t)$, Eq. (3.9) is symmetric and thus generates half of the needed constraints. This approach assumes that the variance is slowly varying over the sampled index, in order to estimate the variance over a data bin.

Non-linear correlations

Another possibility to model the source distributions in Eq. (3.8) is to consider that they are stationary but non Gaussian. This corresponds to saying that $p_{it} = p_i$. In this case separation can be obtained through the use of non-linear functions. If two variables are independent, then not only their correlation is zero, but also the correlation of any non-linear function of them. This shows how independence is a stronger feature than uncorrelatedness, since this property does not hold for merely uncorrelated variables. The separation constraints are given by:

$$\frac{1}{T}\sum_{t=1}^{T}\psi_i(x_i(t))x_j(t) = \delta_{ij}. \tag{3.10}$$

where ψ_i is a non-linear function which can be taken to be $\psi_i = p_i'/p_i$ in order to maximize the likelihood. Functions are chosen to be non-linear since this breaks the symmetry of Eq. (3.10), thus imposing a higher number of constraints.

3.2.3 Indeterminacies of ICA

There are two intrinsic indeterminacies in the ICA method, which are scaling and permutation. If we consider Eq. (3.2), we can see that by performing a permutation of the elements of the vector $\mathbf{s}$ and of the corresponding columns of the matrix $\mathbf{A}$, the resulting mixture $\mathbf{y}$ would not be affected. Hence it is not possible to blindly identify the sources order. The same can be said of scaling, since we can write:

$$\mathbf{y} = \mathbf{As} = \mathbf{AD}^{-1}\mathbf{Ds} = \mathbf{A}'\mathbf{s}', \tag{3.11}$$

where $\mathbf{D}$ is a diagonal invertible matrix, $\mathbf{A}' = \mathbf{AD}^{-1}$ and $\mathbf{s}' = \mathbf{Ds}$. From the point of view of the output $\mathbf{y}$, the configurations $\mathbf{As}$ and $\mathbf{A}'\mathbf{s}'$ are equivalent. Hence the scaling of the terms in the vector $\mathbf{s}$ and the columns of the mixing matrix does not affect the result. In this sense, ICA recovers a unique solution *only up to* scaling and permutation. In presence of additional information, this degeneracy can be broken. For this reason this indeterminacy of the ICA method does not affect the analysis presented in this work, since the characteristics and emission law of the CMB signal are well known. Also, prior information is available on the principal foreground emissions at Planck frequencies.

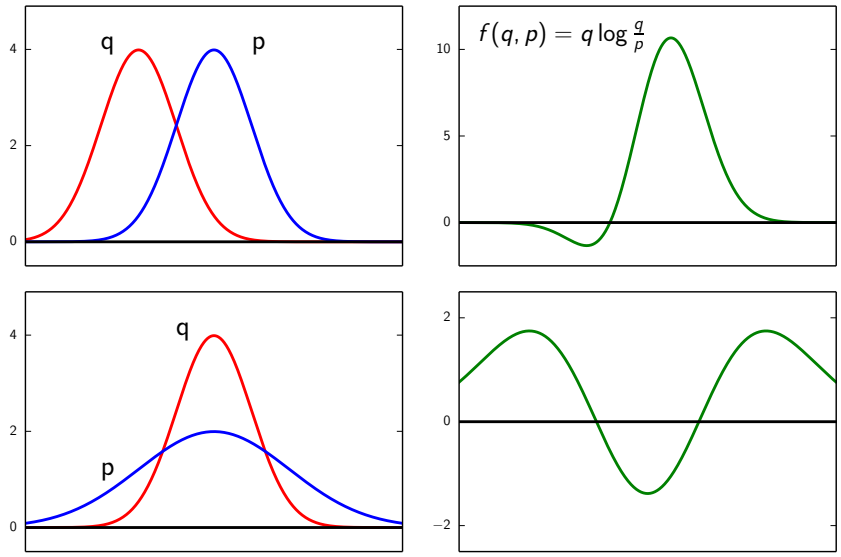

Figure 3.2 – The $f(q,p) = q \log \frac{q}{p}$ function for two Gaussian distribution in case they have different mean (top panel) or different variance (bottom panel).

3.3 Kullback-Leibler divergence

Given two probability distributions, one may ask how similar they are. The Kullback-Leibler (KL) divergence provides a measure of such similarity (Kullback & Leibler, 1951). It is defined as:

$$KL(q,p) = \int q(x) \log \frac{q(x)}{p(x)} dx \tag{3.12}$$

where p and q are two probability distributions. The KL divergence is asymmetric, i.e., $KL(q,p) \neq KL(p,q)$, and thus it is not a proper distance function. It is however a useful indicator of how two distributions differ, since it is always non-negative $KL(q,p) \geq 0$ and it is zero only when the two distributions coincide. This can be easily demonstrated given that $\int p = 1$, $\int q = 1$:

$$\int q \ln \frac{q}{p} = -\int q \ln \frac{p}{q} \geq q(1 - \frac{p}{q}) = \int q - \int p = 0 \tag{3.13}$$

where the inequality $-\ln x \geq 1 - x$ is used.
For two Gaussian multivariate distributions of zero mean and given covariance, $p(x) = \mathcal{N}(0, \mathbf{D})$ and $q(x) = \mathcal{N}(0, \mathbf{R})$, where $\mathbf{D}$ and $\mathbf{R}$ are two $N \times N$ covariance matrices, the Kullback-Leibler divergence is:

$$KL(q,p) = \frac{1}{2}\Big[tr(\mathbf{D}^{-1}\mathbf{R}) + \log \frac{\det \mathbf{D}}{\det \mathbf{R}} - N\Big], \tag{3.14}$$

where det is the matrix determinant. Figure 3.2 shows the $q \log \frac{q}{p}$ function for two Gaussian distributions in case they have either different mean either different variance. The KL divergence is the integral of such function.
The Kullback-Leibler divergence is a widely used function in statistics in various fields, such as machine learning, Bayesian data analysis, and coding theory. The exact interpretation of its meaning depends on the domain of application, but generally speaking we can say

that it measures the departure of the distribution p from q, where q is considered the true or reference distribution. In fact Eq. (3.12) represents the expectation under the q statistics of $\log \frac{q}{p}$, that is $E_q[\log \frac{q}{p}]$. The asymmetry of this measure is then justified because the two distributions are not equivalent, being q the reference and p a deviation from it. In coding theory, the KL divergence is used to measure how many more bits are needed to code data drawn from p when the code is optimized for q (in this case the logarithm in base 2 is used in the KL formula). In the Bayesian framework, the KL divergence of the posterior q from its prior p evaluates the information gained from the data (Hee et al., 2017). Or, conversely, it measures the information lost when p is used to approximate q (Burnham & Anderson, 2001). The SMICA method presented in the next Section uses the Kullback-Leibler divergence to fit the model to the data. This will be shown to be a consequence of modeling the data as Gaussian stationary sources.

3.4 SMICA

SMICA (Delabrouille et al., 2003; Cardoso et al., 2008) is a blind component separation method based on ICA. The acronym "SMICA" stands for *Spectral Matching Independent Component Analysis*, since SMICA works by matching empirical spectral density matrices, or covariance matrices, to a predicted model via ICA. While this method can be applied to other component separation problems, we will explore here its application to CMB science. SMICA has been chosen as one of the four component separation methods used by the *Planck Collaboration* to produce a CMB map. The peculiarity of SMICA is that, since it performs separation at the spectral level, it provides a direct estimate of the CMB angular power spectrum.

The SMICA method substitutes the available data with second-order statistics: the spectral covariance matrices. This choice arises naturally from the shape of the likelihood of the problem. The data can be represented as in Eq. (3.3), only transformed in the harmonic domain:

$$\mathbf{y}_{\ell m} = \mathbf{A}\mathbf{s}_{\ell m} + \mathbf{n}_{\ell m}, \tag{3.15}$$

where $\mathbf{s}_{\ell m}$ is $M \times 1$ a vector containing the spherical harmonics coefficients of the sources, i.e., the CMB and foregrounds, while $\mathbf{n}_{\ell m}$ is a $N \times 1$ vector which describes the noise in each frequency channel. The spherical harmonics coefficients of each data map are in the $N \times 1$ vector $\mathbf{y}_{\ell m}$. From these coefficients one obtains auto- and cross-angular power spectra that are used to build covariance matrices. The method then employs a fitting criterion, which corresponds to a likelihood, to adjust to these empirical statistics their theoretical value predicted by a parametric model. The model can have different specifications, but in its most basic form it simply expresses the independence between the foregrounds and the CMB. Due to intrinsic statistical errors, there is always a difference between the model and the data which cannot be reduced by a change in the model parameters. We term this residual error "mismatch".

SMICA jointly fits for the CMB, foregrounds and noise angular power spectra, as well as their emission law through frequency described by the $N \times M$ matrix $\mathbf{A}$. The necessary condition for separability is that the angular power spectra of the sources present spectral diversity, then Eq. (3.9) can be used to achieve separation. Also, the source emission laws though frequency, represented by the columns of the matrix $\mathbf{A}$, have to differ: two proportional columns cannot be differentiated by the model, that instead fits them as a

single component with angular power spectrum corresponding to their sum (Delabrouille et al., 2003).
In the following we will explore in more detail the main features that characterize the method, which are: the data reduction into spectral covariance matrices, the model specifications, the matching criterion between the data and the model, and the residual mismatch.

3.4.1 Data covariance matrices

The data used are the maps of the microwave sky, which constitute the observed mixtures of signals. Working on the sphere, it is convenient to use spherical harmonics to describe the observations. If we have a set of N sky maps, we can transform them in spherical harmonics coordinates and combine all the coefficients in a single vector $\mathbf{y}_{\ell m}$. At each multipole ℓ, this vector will have an $N \times N$ empirical covariance matrix $\hat{\mathbf{R}}_\ell$ given by:

$$\hat{\mathbf{R}}_\ell = \frac{1}{2\ell+1} \sum_{m=-\ell}^{m=+\ell} \mathbf{y}_{\ell m} \mathbf{y}_{\ell m}^\dagger. \tag{3.16}$$

We term this matrix empirical, since it is an estimate of the true data covariance $\mathbf{R}_\ell$:

$$\mathbf{R}_\ell = \left\langle \hat{\mathbf{R}}_\ell \right\rangle. \tag{3.17}$$

where the average is performed over an ensemble of realisations. As seen in Section 1.4.2, such an average is impossible to obtain in practice since we only observe one realisation of the sky, and it is a purely theoretical limit, while we can only work with empirical estimates.
These empirical matrices $\hat{\mathbf{R}}_\ell$ contain, for a given multipole, all the auto- and cross- spectra between the observations. Each $\hat{\mathbf{R}}_\ell$ matrix is symmetric.
If we assume that angular power spectra are slowly varying across multipoles, we can bin the covariance matrix as:

$$\hat{\mathbf{R}}_q = \frac{\sum_{\ell \in I_q} (2\ell+1) \hat{\mathbf{R}}_\ell}{\sum_{\ell \in I_q} (2\ell+1)} \tag{3.18}$$

where the multipole range is divided in Q intervals $I_q = [\ell_q^{min}, \ell_q^{max}]$. Here we use a flat binning for the data, but other choices are possible. We note that in each interval, the number of modes, or samples, is:

$$w_q = \sum_{\ell=\ell_q^{min}}^{\ell=\ell_q^{max}} (2\ell+1), \tag{3.19}$$

since at each multipole the spectra are the result of an average over $2\ell+1$ modes. Binning has two benefits: it reduces the size of the statistics and mitigates the correlations between multipoles introduced by masking.

3.4.2 Model

The sources are modelled as Gaussian isotropic signals, since the only information retained is their angular power spectrum and their emission law in frequency. While this model

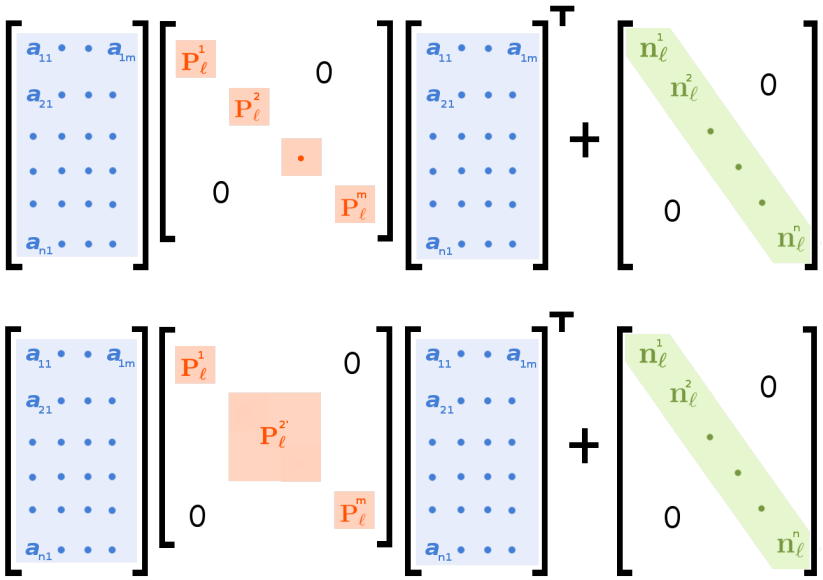

Figure 3.3 – Two different configurations for the SMICA model. The upper panel represents a model in which all components are unidimensional and independent, while the lower panel presents some multidimensional or correlated sources.

holds for the CMB, it does not for the foregrounds. This is however not important for CMB recovery as long as the emission law of CMB is well known. For a discussion on the Gaussian model see Cardoso (2017).
The model of the sources is defined by a set of parameters θ. This model has to express the independence of the sources and their mixing into observed samples. Taking the covariance of the right hand side of Eq. (3.15) we obtain:

$$Cov(\mathbf{y}_{\ell m}, \mathbf{y}_{\ell m}) = \mathbf{A} Cov(\mathbf{s}_{\ell m}, \mathbf{s}_{\ell m}) \mathbf{A}^T + Cov(\mathbf{n}_{\ell m}, \mathbf{n}_{\ell m}) = \mathbf{A} \mathbf{P}_\ell \mathbf{A}^T + \mathbf{N}_\ell, \tag{3.20}$$

where $\mathbf{A}^T$ denotes transposition of the $N \times M$ mixing matrix and $\mathbf{P}_\ell, \mathbf{N}_\ell$ (which in the binned configuration become $\mathbf{P}_q$ and $\mathbf{N}_q$) are the $M \times M$ and $N \times N$ covariances of the sources and of the noise respectively. The noise and the sources being decorrelated, all cross terms between them are null.
If the noise can be modelled as decorrelated between frequencies, the noise covariance $\mathbf{N}_q$ is diagonal. The signal covariance $\mathbf{P}_q$ instead can have different configurations. Assuming that the sources are independent and unidimensional, the matrix $\mathbf{P}_q$ is diagonal and we can write (Cardoso et al., 2008):

$$\mathbf{R}_q(\theta) = \sum_i a_i a_i^T P_{q,ii} + \mathbf{N}_q, \tag{3.21}$$

where $P_{q,ii}$ is the i-th diagonal element of the matrix $\mathbf{P}_q$ and a_i is the corresponding i-th column of the matrix $\mathbf{A}$. If one source is not unidimensional, the matrix $\mathbf{P}_q$ becomes block diagonal. This is the case for complex sources, such as galactic dust, whose emission law changes across the sky and which cannot therefore be described by the scaling in frequency of singular angular power spectrum. The signal covariance is block diagonal also if some sources present some degree of correlation. This poses no problem to the

method itself: these sources will be considered as an unique multidimensional component. However, they will not be separable by SMICA. Figure 3.3 graphically represents these two possible configurations, diagonal and block diagonal. The least stringent model possible only assumes independence between the unidimensional CMB and one multidimensional foregrounds component:

$$\mathbf{R}_q(\theta) = a_{CMB} \quad a_{CMB}^T \quad C_\ell^{CMB} + \mathbf{F} \quad \mathbf{P}_q^{fg} \quad \mathbf{F}^T + \mathbf{N}_q. \tag{3.22}$$

Here a_{CMB}, $\mathbf{F}$ are the $N \times 1$ and $N \times M-1$ columns of the mixing matrix associated to the 1×1 CMB spectrum C_q^{CMB} and $M-1 \times M-1$ foreground spectra $\mathbf{P}_q^{fg}$ respectively. In the case of Planck data analysis, it is safe to assume that the CMB anisotropies have a derivative of a black body emission law, within calibration errors. It is interesting to note that the model fits freely the angular power spectrum of the CMB at each bin.
The model parameters θ are all the sources and noise spectra plus their emission laws through frequency encoded in the mixing matrix $\mathbf{A}$. It is important to observe that the structure of the model has been derived only under two main assumptions, the independence of the sources and their linear mixing in the observed data.

3.4.3 Fitting criterion

The SMICA criterion matches the empirical covariance to the theoretical covariance. The matching criterion is:

$$\phi(\theta) = \sum_{q=1}^{Q} w_q KL(\hat{\mathbf{R}}_q, \mathbf{R}_q(\theta)) \tag{3.23}$$

where w_q is the number of modes per bin. In case of normally distributed full-sky spherical harmonics, the above expression represents the log-likelihood of the model $R_q(\theta)$ given the data. This can be seen as, given a $N \times 1$ vector $\mathbf{y}_{\ell m}$ of spherical harmonics, where N is the number of observations, $\mathbf{y}_{\ell m} \sim \mathcal{N}(0, \mathbf{R}_\ell)$, where $\mathbf{R}_\ell$ is the $N \times N$ covariance matrix, the (negative log-) probability of $\mathbf{y}$ is:

$$-2\log p(\mathbf{y}) = \sum_{\ell} \sum_{m=-\ell}^{m=+\ell} \mathbf{y}_{\ell m}^\dagger \mathbf{R}_\ell^{-1} \mathbf{y}_{\ell m} + \log\det(2\pi\mathbf{R}_\ell). \tag{3.24}$$

If we assume a model $\mathbf{R}(\theta) = \{\mathbf{R}(\theta)\}_{\ell=\ell^{min}}^{\ell=\ell^{max}}$ which contains all the model covariances at each multipole in the range $[\ell^{min},\ell^{max}]$, and we bin the multipoles ℓ in a subset of Q intervals, we obtain (Delabrouille et al., 2003):

$$\begin{aligned}
-2\log p(\mathbf{y}|\mathbf{R}(\theta)) &= \sum_{\ell} \sum_{m=-\ell}^{m=+\ell} \mathbf{y}_{\ell m}^\dagger \mathbf{R}_\ell^{-1}(\theta) \mathbf{y}_{\ell m} + \log\det(2\pi\mathbf{R}_\ell(\theta)) \\
&= \sum_{\ell} \sum_{m=-\ell}^{m=+\ell} \mathrm{tr}(\mathbf{R}_\ell^{-1}(\theta) \mathbf{y}_{\ell m} \mathbf{y}_{\ell m}^\dagger) + \log\det(2\pi\mathbf{R}_\ell(\theta)) \\
&= \sum_{\ell} (2\ell+1) \Big[\mathrm{tr}(\mathbf{R}_\ell^{-1}(\theta) \hat{\mathbf{R}}_\ell) + \log\det(2\pi\mathbf{R}_\ell(\theta)) \Big] \\
&= \sum_{q=1}^{Q} w_q \Big[\mathrm{tr}(\mathbf{R}_q^{-1}(\theta) \hat{\mathbf{R}}_q) + \log\det(2\pi\mathbf{R}_q(\theta)) \Big] \\
&= \sum_{q=1}^{Q} w_q KL(\hat{\mathbf{R}}_q, \mathbf{R}_q(\theta)) + c,
\end{aligned} \tag{3.25}$$

where c is a constant term that does not depend on $\mathbf{R}_q(\theta)$. In the calculations we use the property $\mathbf{y}^\dagger \mathbf{R}^{-1}\mathbf{y} = \mathrm{tr}(\mathbf{R}^{-1}(\theta)\mathbf{y}\mathbf{y}^\dagger)$.
The expression obtained is the matching criterion $\phi(\theta)$ plus a constant term that does not depend on the model, and is thus irrelevant with respect to the fit. By minimizing the criterion $\phi(\theta)$, SMICA achieves an estimate of the model parameters $\hat{\theta}$ which is optimal in the sense of maximum likelihood:

$$\hat{\theta} = \mathrm{argmin} \;\; \phi(\theta). \tag{3.26}$$

3.4.4 Mismatch

It is natural to ask how to evaluate the choice of the model. Whatever[2] the model chosen, the criterion will minimize its distance from the data through the KL divergence. However, achieving minimization does not guarantee a meaningful result, and the model can still be quite non-representative of the data. The distance between the data and the model, or *mismatch*, is the value that the criterion $\phi(\theta)$ takes at its minimum $\hat{\theta}$. SMICA minimizes the global mismatch, but it can be useful to evaluate it at each bin as $\phi_q(\hat{\theta})$, since at different scales the closeness of the model to the data can vary. Given its connection to the likelihood $\mathcal{L}$, the minimum of the criterion can be approximated as $\phi_q = -2\log\mathcal{L} \approx \chi^2_\nu$, where ν is the number of degrees of freedom:

$$\nu = \frac{n(n+1)}{2} - T. \tag{3.27}$$

Here T is the number of parameters to estimate at each bin and n is the number of observations available.
We can view the mismatch as a measure of how the model is representative of the data. If the data is drawn by the model, i.e., the model is correct, due to the inevitable presence of statistical errors we expect the mismatch to be of the order of ν. Larger values of the mismatch, assuming the fit has converged to the true minimum, indicate that the model cannot represent the data complexity. Lower values of the mismatch instead indicate overfitting, that is the model has too many free parameters that cannot be constrained by the observations.
In this work I present a SMICA configuration based on data splits only, in which the statistical properties of the covariance matrices are only approximately represented by the model. In this case the recovered mismatch for a converged fit is not $\sim \nu$, and its value is difficult to predict[3]. Even though we do not have an expected value, the mismatch is still an interesting quantity to look at, since very high values indicate that the model cannot represent the data complexity.

3.4.5 The evaluation of uncertainties

It is important to be able to evaluate the error in the parameters of the fitted model. A useful tool to evaluate errors is given by the Fisher Information Matrix (FIM). The FIM $\mathcal{I}(\theta)$ is a $K \times K$ matrix function of the $K \times 1$ vector θ. It is defined equivalently as:

$$\mathcal{I}(\theta)_{ij} = E\left(\frac{\partial \log\mathcal{L}}{\partial\theta_i}\frac{\partial \log\mathcal{L}}{\partial\theta_j}\right) = -E\left[\frac{\partial^2 \log\mathcal{L}}{\partial\theta_i\partial\theta_j}\right] \tag{3.28}$$

[2] almost
[3] Nevertheless, for our configuration, simulations show that it is of the same order of magnitude.

The FIM is thus a function of the likelihood derivative and it indicates the amount of information the data give with respect to a given parameter.
The Cramer-Rao bound tells us that, if $\hat{\theta}$ is an unbiased estimator of the sample $\mathbf{X}$, then its variance is bounded by the inverse of the FIM:

$$Var(\hat{\theta}(\mathbf{X})) \geq \mathcal{I}^{-1}(\theta). \tag{3.29}$$

This lower bound does not take into account possible systematics in the measurement or uncertainties in the data pre-processing, such as beam and calibration errors. It represents instead the minimum possible variance attainable in the idealised case where no other source of error exists other than that which arises from the randomness of the variables. Deriving from the second derivative of $\mathcal{L}$, it is an indication of the curvature of the likelihood function around its maximum in the direction of a given parameter.
In the absence of another way to compute errors, the inverse of $\mathcal{I}(\theta)$ is a practical estimate of the variance of the model parameters. Since the SMICA criterion $\phi(\theta)$ is a likelihood function, it straightforward to compute the FIM:

$$\mathcal{I}(\theta)_{ij} = \frac{1}{2}\sum_q w_q tr(\frac{\partial \mathbf{R}_q(\theta)}{\partial \theta_i}\mathbf{R}_q(\theta)^{-1}\frac{\partial \mathbf{R}_q(\theta)}{\partial \theta_j}\mathbf{R}_q(\theta)^{-1}). \tag{3.30}$$

All error bars on model parameters presented in this work are obtained by Eq. (3.30). Non-identifiability of the parameters results in a singular and thus not-invertible FIM, while parameters barely identified have very large error bars.

3.5 A geometrical approach

It is useful to visualize the minimization of the criterion, the residual mismatch and the error estimate given by the FIM in a geometrical framework. We can think of the parameter space as a manifold with as many dimensions as the degrees of freedom of the model. Each point on this manifold represents one parameter setting, that is one possible model $\mathbf{R}_q(\theta)$. In this space the metric is given by the FIM. Given two points θ and $\theta + \delta\theta$, the change between them can be evaluated as:

$$||\delta\theta||^2 = \delta\theta^T \;\; \mathcal{I}^{-1}(\theta) \;\; \delta\theta \tag{3.31}$$

Unit norm corresponds to 1-σ difference between the models described by the two parameters sets. Let us assume the available data $\hat{\mathbf{R}}_q$ are drawn from one specific model $\mathbf{R}_q(\theta_*)$. In this case the model lives on the manifold, while the data do not: the observed data are one realisation of the model, which corresponds to their ensemble average. Therefore the model will never be able to completely represent the variability present in the data. Finding the appropriate parameter set can bring us as close as possible to the data.
The SMICA criterion $\phi(\theta)_q$ is the log-likelihood of the problem. The fit performed by the method boils down to adjusting the free parameters, that is moving the model on the manifold, in order to minimize the distance to the data. When $\phi(\theta)$ is minimized, its derivative goes to zero:

$$\frac{\partial \phi}{\partial \theta} = \sum_q w_q tr\left(\mathbf{R}_q(\theta)^{-1}(\mathbf{R}_q(\theta) - \hat{\mathbf{R}}_q)\mathbf{R}_q(\theta)^{-1}\frac{\partial \mathbf{R}_q(\theta)}{\partial \theta}\right). \tag{3.32}$$

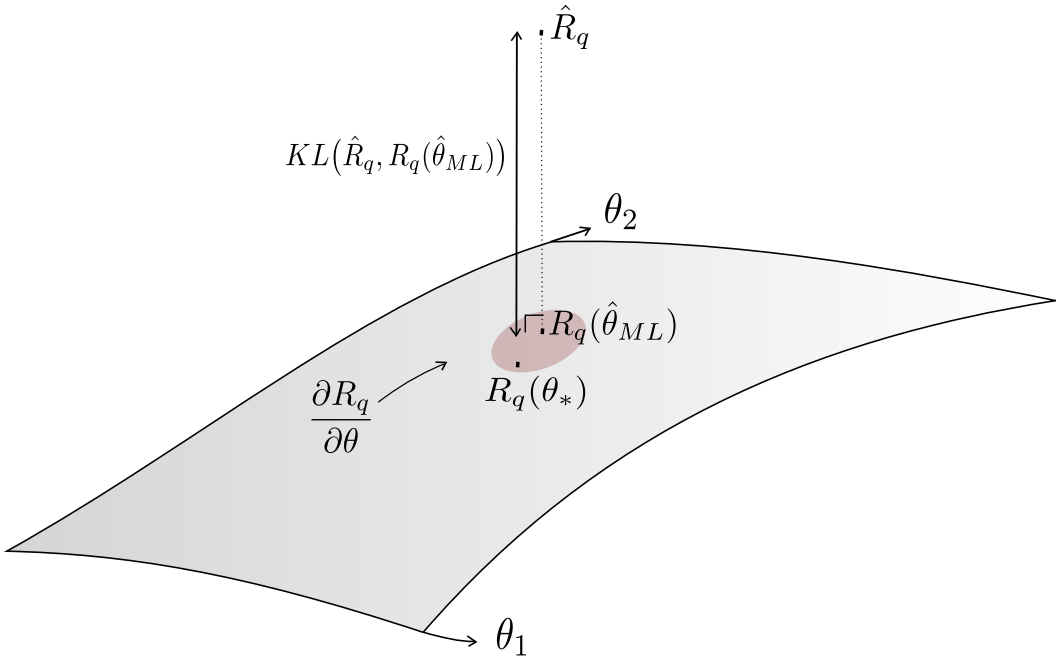

Figure 3.4 – The geometrical representation of the SMICA criterion minimization problem.

Here $(\mathbf{R}_q(\theta) - \hat{\mathbf{R}}_q)$ represents the error we do when we approximate the data with the model, or mismatch, and $\frac{\partial \mathbf{R}_q(\theta)}{\partial \theta}$ is the direction in which the criterion moves on the manifold space. When these two terms are orthogonal, it is not possible to decrease the error by a change in the parameters θ, and the criterion is minimized. We term the parameters set that minimizes the criterion as $\hat{\theta}_{ML}$. The minimum of the criterion does not correspond to the true value θ_*. However the distance on the manifold between the true and maximum likelihood values should not be larger on average than the inverse of the FIM. The inverse FIM thus sets the resolution on the manifold. Figure 3.4 represents the situation described.

3.6 SMICA in practice

SMICA has been developed as a component separation tool for the data analysis of the Planck mission (Cardoso et al., 2008). Component separation in the *Planck Collaboration* analysis aims at recovering reconstructed CMB and foregrounds maps (Planck Collaboration XII, 2014; Planck Collaboration IX et al., 2016; Planck Collaboration X et al., 2016), but not at obtaining an estimate of the CMB angular power spectrum. The SMICA method is used for CMB map reconstruction in both temperature and polarization. SMICA also offers the possibility to estimate directly the CMB angular power spectrum, without the need to derive it from the map. This is particularly interesting for cosmological inference, since the reconstructed map spectrum has some additional foregrounds and noise contribution with respect to the model estimate. Angular power spectrum estimation has also been addressed in the literature (Patanchon et al., 2003, 2005), and it is the focus of this work. SMICA is mainly used in the harmonic domain, but implementation in different spaces

have also been tested (Moudden et al., 2005).

3.6.1 Map reconstruction

Planck Collaboration IX et al. (2016) describes the temperature (and polarization) map produced with the four component separation methods adopted by the *Planck Collaboration*. SMICA is the method that best performed on simulations in the Planck 2013 release. Also, it has the lowest residual high-ℓ foregrounds in the Planck 2015 analysis, and it is therefore chosen as the reference CMB map for other studies, as for example those on primordial non-Gaussianity, and gravitational lensing.
The SMICA temperature map is obtained using data from all the 9 frequency channels. The model used makes minimal assumptions, i.e., assumes only independence between foregrounds and the CMB as in Eq. (3.22). The final CMB map is obtained as a weighted sum of the spherical harmonic coefficients of the input channels through a set of weights w_ℓ. These weights are obtained as in the Eq. (2.25), where at low multipoles the covariance matrix is estimated in a more robust way than simply using the empirical covariance, and is replaced by the fitted model covariance $\mathbf{R}(\hat{\theta})$. The actual implementation implies a two step fit, where the first step is used to evaluate calibration errors in the input data maps and the second step performs the actual fit.
This model specification, which is as blind as possible, has the advantage of needing no physical prior knowledge on the foregrounds. The drawback is that it is not possible to separate the foregrounds and thus to gain information on each of them individually. Also, it is impossible for the model to capture all the foreground complexity, and some emissions are better removed from the CMB than others. Even though the fit is performed multipole per multipole, the mixing matrix $\mathbf{A}$ is common over the whole multipole range, and its values are guided by the emissions with better SNR. The fit favours large scale galactic foregrounds, since their emission at low multipoles is well above the noise level. Small scale emissions such as point sources dominate in a region of the angular power spectrum where noise becomes important, and are thus less favoured by the fit. As a consequence, they are only partially removed, leaving an unknown amount of contamination in the CMB part of the model. The result is a CMB map which is cleaned at large scales, but whose small scales foreground content is poorly understood. Extragalactic foregrounds residuals contaminate in particular the small scales, and cosmological parameters obtained on the maps present biases up to 2-σ when multipoles above ℓ=2000 are used. A comparison of the ΛCDM parameters obtained from the angular power spectra of the four reconstructed maps is presented in Planck Collaboration IX et al. (2016), which advises against using any of the reconstructed maps for cosmological purposes.

3.6.2 Angular power spectrum estimation

The SMICA model directly provides an estimation of the CMB angular power spectrum C_ℓ^{CMB}. In order to use C_ℓ^{CMB} for cosmological parameters estimation, some care is needed in the modeling of high-ℓ foregrounds. For this reason, a highly blind model as for map reconstruction is counterproductive because it fails to properly clean the high multipoles. Even a classical model as in Eq. (3.21), where all components are decorrelated, can be too naïve, neglecting correlations between foregrounds or the fact that some foregrounds are not separable due to similar spectra or emission law.

In Patanchon et al. (2003) a quasi-blind approach is used on simulated data: the input components are correctly recovered, but some constraints are imposed on the mixing matrix in order to separate synchrotron and dust emission. These two galactic emissions have similar angular power spectra, which are hardly separable in a blind fashion by SMICA. Also the authors note that kinetic SZ is not separable from CMB since their emission laws (i.e., the columns of the **A** matrix) are proportional. This is however not a severe limitation since kinetic SZ contamination is very low in Planck data.
In a following analysis, Patanchon et al. (2005) apply SMICA to a set of foreground-cleaned maps provided in the 1-year WMAP data release. The foreground contamination in the data is thus strongly reduced, but galactic and unresolved point sources residuals are still present. These residuals are hardly separable without prior information, again due to their similar spectral behaviour. The authors choice is to strongly constrain the point sources part of the model, by assuming they have a flat angular power spectrum and a specific emission law (up to a normalization factor), while the galactic part is left unconstrained. The recovered CMB spectrum is in excellent agreement with WMAP 1-yr spectrum. It is interesting to note that two different component separation methods have been applied to the data: first templates have been subtracted to lower the foreground content, then a blind method has been applied to characterize the residuals. The authors note that residual galactic contamination they observe could come from imperfect subtraction of the synchrotron template. With the need of ever increasing accuracy in the CMB estimation, this approach is effective thus only if the templates are representative of the contamination in the data and do note introduce biases. This is true also for the model: the assumption of the emission law for point sources is quite strong, and could lead to neglecting part of their contamination.
This work aims at obtaining an estimate for C_ℓ^{CMB} useful for cosmology directly using component separation. The choice is to model point sources as two independent contributions with flat spectrum, without imposing constraints on their emission law. The results of this approach, for both the power spectrum and the derived cosmological parameters, are presented in the next Chapter.

3.7 Other ICA methods

As stated in Sect. 2.4.3, blind algorithms offer many advantages in the component separation domain. It is thus not surprising that different ICA implementations have been developed to address the problem. We describe here two component separation methods that we did not mention in the former Chapter. Since both of them are based on ICA, we preferred to delay their description to this Section. We will introduce here two methods, FastICA, which works by maximizing non-Gaussianity of the different signals in pixel space, and BICA, which uses the SMICA likelihood in a Bayesian framework.

3.7.1 FastICA

Encouraged by previous results using ICA methods in the CMB analysis (Baccigalupi et al., 2000), Maino et al. (2002) have adapted to the CMB case the FastICA method, which was first proposed by Hyvärinen & Oja (1997); Hyvärinen (1999). The method has proven to be effective in recovering both the CMB and the galactic foregrounds (Maino

et al., 2007; Bottino et al., 2008, 2010). Unlike SMICA, FastICA has been employed in real space, and the separation is achieved by maximizing the non-Gaussianity of the recovered components.
In order to apply FastICA, some working assumptions on the data are necessary other than independence of the input signals. First of all the algorithm requires that all but one signal are Gaussian, which is true for the microwave sky. The algorithm assumes that all channels have the same beam, which is not correct since beaming effects of the instrument are frequency dependent: a preprocessing of the data is needed to degrade all channels to the same resolution. Knowledge of the noise properties of the data maps is assumed, and this is used to pre-whiten the data in order to render the problem more tractable. The algorithm fits one by one the columns of the $\mathbf{W}$ matrix in Eq. (3.4). The non-Gaussianity is maximized with the aid of non-linear functions applied to the data. Each column of the matrix $\mathbf{W}$ is searched in a space orthogonal to that spanned by the previously fitted columns, and it is iteratively fitted until reaching convergence.
The algorithm has been applied to COBE (Maino et al., 2003), BEAST (Donzelli et al., 2006) and WMAP (Bottino et al., 2010) data, as well as Planck simulations (Leach et al., 2008). Results obtained are comparable to those of other methods. Working in pixel space, FastICA is able to recover the spatial properties of the independent components, however matching them with physical foregrounds can be tricky. In Bottino et al. (2008) the authors obtain good foreground identification by using external templates in combination with WMAP data. The algorithm cannot however account for spectral variations of the foreground on the sky, resulting in residuals in the CMB map. This issue can be addressed by using FastICA iteratively, i.e., by applying it to data which has been cleaned removing the estimated foreground components, similarly to the approach used by Patanchon et al. (2005). FastICA has also been applied to the polarization case (Baccigalupi et al., 2004) and in particular to B-modes detection (Stivoli et al., 2006), with promising results obtained on simulations.

3.7.2 BICA

The Bayesian ICA (BICA) (Vansyngel et al., 2016) is a method that adds a Bayesian framework on top of the SMICA likelihood (Bayes theorem is presented in Eq. (2.15)). The model assumed for the data is that of Eq. (3.3), and the parameters to fit consist of the mixing matrix $\mathbf{A}$, the angular power spectra C_ℓ and the maps $\mathbf{s}$ of all components. The choice to sample the components maps may seem daring, since this implies a huge number of parameters. The problem is rendered tractable by first sampling on the angular power spectra and mixing matrix via the SMICA likelihood, and then post-processing these samples to sample $\mathbf{s}$.
BICA has been applied on simulations, providing a good reconstruction of the inputs. Some residuals are present in the galactic region due to foregrounds correlations that are not well captured by the model which assumes decorrelation of all spectra. The reconstructed CMB map is taken to be the average of all the sampled maps. A study on Planck 2013 data has been done, still unpublished, which addressed the issue of extragalactic point sources. The choice has been to model point sources as a component fully coherent through frequency plus one non-coherent component at each frequency to account for deviations from the coherent one. This allows to account for the point source emission at each frequency since it is like considering as many point source components as channels.

The advantage of BICA over a different Bayesian method such as Commander is that no assumption is needed on the foregrounds, however the recovered foregrounds maps and spectra have no obvious physical meaning. With respect to SMICA, BICA estimates the CMB angular power spectrum error model by marginalising over the full posterior. Interpreted in the BICA framework, the SMICA fit returns the peak of the posterior distribution assuming flat priors.

Chapter 4

Adapting SMICA for angular power spectrum estimation

Contents

The aim of this work is to obtain an estimate of the CMB angular power spectrum for cosmological parameters estimation. The SMICA method presented in the previous Chapter is ideal for this purpose since it directly estimates the CMB at the spectral level. The more, it is a blind method that does not require previous knowledge on the foregrounds. However some modification with respect to previous configurations is needed to exploit at best the potential of the method. Planck data extend over a large range of multipoles, up to $\ell \sim 3000$. The small scales of CMB are particularly interesting for cosmology because of their high constraining power due to very low cosmic variance. Nevertheless, these scales suffer from the contamination of both noise and extragalactic foregrounds. In this work I focus on the small scales and I configure the SMICA method to address both limitations, by using data splits to build data covariance matrices and by using a semi-blind model for the fit. I present results obtained with this configuration and some additional tests on different configurations, to check stability of the results. The resulting CMB angular power spectrum is used to derive constraints on cosmological parameters. The results of this Chapter are presented in Umiltà et al. (2017).

4.1 Component separation vs Likelihood approach

The CMB angular power spectrum is an important observational constraint for cosmology. However accessing this information is not straightforward due to the contamination of astrophysical foregrounds present in the CMB data. The perfect component separation technique does not exist. The choice of one method above another one depends on the problem at hand and on the desired result. The *Planck Collaboration* used four component separation methods to produce four foreground-cleaned CMB maps. These products are not intended for a cosmological study and are thus not optimized for it. In particular, their residual foreground content at small scales due to extragalactic sources is not well characterized (Planck Collaboration IX et al., 2016). Not knowing the point source power at small scales induces a degeneracy with the CMB small scale power. Nevertheless, component separation techniques applied by Planck have performed extremely well in reconstructing the CMB map and cleaning foregrounds at large angular scales, which was their task. The question arises whether we can adapt component separation for power spectrum estimation and target small scales foregrounds.

Among the existing methods, SMICA has the advantage of being both blind, thus not requiring in principle any assumption on the foregrounds, and of estimating the angular power spectrum directly, i.e., without the need to reconstruct a sky map first. Also, in the Planck nominal 2013 release, SMICA is the method that best performed on temperature simulations (Planck Collaboration XII, 2014), while in the full 2015 release it is the method with the lowest high-ℓ residuals (Planck Collaboration IX et al., 2016). The more, the SMICA method fits the angular power spectrum in the maximum likelihood sense, thus relying on an optimal statistical principle.

The method needs to be adapted to the specific task of power spectrum estimation. In the first place, it is necessary to target the extragalactic foregrounds, whose emission becomes important only at very high-ℓ, where the signal-to-noise ratio is quite low. Without a dedicated model, the method would only partially remove this emissions, since the fit naturally privileges signals that dominate in the low noise regime. A model for extragalactic

foregrounds decreases the blindness of the method but allows in turn to obtain information on the point sources emission law.
Another limitation that is quite important at small scales is noise. In the angular auto-spectra of the data maps, the noise enters as an additional bias at high-ℓ that quickly dominates over the signal, due to the instrument beam. Angular cross-spectra instead are "noise-free": they have a scatter which depends on the noise contamination, but the noise bias disappears. Retaining only a symmetric version of the cross-spectra covariance matrix, SMICA can be adapted to use only cross-angular spectra of data maps. The criterion however is no longer optimal.
In this work I present the results obtained with these two changes in the SMICA method. Since the goal is to exploit the angular power spectrum for a cosmological analysis, the main results are the constraints on cosmological parameters. These have been validated on simulations and data in many slightly different configurations.
The natural comparison of this work is with the cosmological analysis of the *Planck Collaboration* (Planck Collaboration XI et al., 2016; Planck Collaboration XIII et al., 2016). The Planck high-ℓ likelihood (PlikTT) is based on the spectra of a few frequency channels with low foreground content, in the cleaner area of the sky and on a tailored multipole range. In this likelihood, the residual foreground contamination is described by a set of templates controlled by a few parameters for each non-negligible astrophysical contribution. The extragalactic point sources are modelled with a free amplitude parameter at each frequency. The Planck likelihood needs a fiducial model for the CMB, which implies the use of a cosmological model, in order to compute the covariance matrix of the likelihood (Planck Collaboration XV et al., 2014; Planck Collaboration XI et al., 2016). Since the Planck likelihood is then used to test cosmological models, which could be different from ΛCDM (see Chapter 5 for a study of one such model), it is important to cross-check its results with different approaches.
The component separation approach minimizes the foreground contamination and profits from a wide range of observations at different frequencies, especially those where the foreground are strong. The likelihood approach instead is based on the assumption that, using only the data channels where the contamination is low, the foreground content in the data can be fitted with a parametric model jointly with the cosmological parameters. These two approaches thus work on opposite principles. I will show in this work how, similarly to the likelihood approach, the component separation approach needs a precise characterization of the foregrounds residual shapes, even though their contamination is strongly reduced.

4.2 Covariance matrices using data splits

The large scale properties of the CMB can only be explored via a likelihood function (Benabed et al., 2009). The criterion of the SMICA method is a likelihood which takes the form of Kullback-Leibler divergence: the KL divergence requires a model for both the noise and the signal since both of them appear in the data. The angular power spectra of sky maps always contain a noise term which needs to be accurately characterized in order to avoid bias, especially at fine scales, as shown in Figure 4.1. The characterization of noise however is often not trivial. Noise derives from the instrumental measurement, but can also be introduced in the subsequent data processing, making

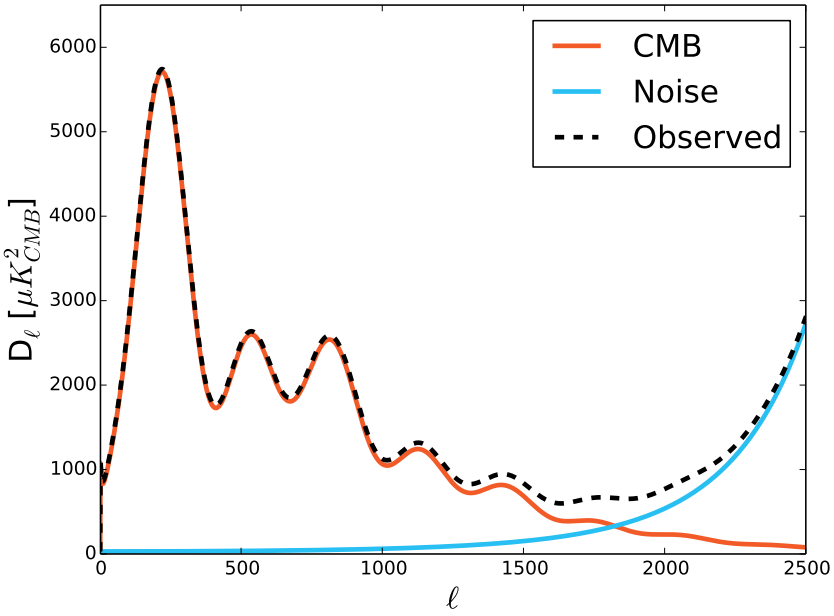

Figure 4.1 – The CMB and noise angular power spectra. Due to the noise bias, it is difficult to estimate the CMB spectrum at small scales: a small error in the noise determination at small scales affects the CMB power spectrum estimation.

its properties difficult to establish. Besides, a wrong modelling or an error in the fitted noise parameters can induce a bias in the recovered signal. For this reason in this work we develop a method that does not need to fit a model for noise by using data splits. These splits are obtained by dividing in two halves the time-ordered data sequences. For sky maps, this consists in generating the map with just half of the time ordered information. Therefore each data split contains the same astrophysical signal, but has a different noise contribution. The *Planck Collaboration* terms these maps "half-mission" maps[1], since each of them contains the data of the first and second half of the total mission.

4.2.1 A simple case: one frequency

We consider here the simple case of two data splits maps at one arbitrary frequency. The spherical harmonics coefficients of the full data, which also contain noise, are:

$$y_{\ell m} = o_{\ell m} + n_{\ell m}, \tag{4.1}$$

where we $o_{\ell m}$ is the signal and $n_{\ell m}$ the noise. By splitting in two parts the data that lead to $y_{\ell m}$ and processing them independently, we obtain two sets $y^a_{\ell m}$ and $y^b_{\ell m}$ of harmonic coefficients such that

$$y^a_{\ell m} = o_{\ell m} + n^a_{\ell m} \quad \text{and} \quad y^b_{\ell m} = o_{\ell m} + n^b_{\ell m} \tag{4.2}$$

where the sky signal in data splits is the same since astrophysical sources do not vary on such a short time scale, and the noise coefficients $n^a_{\ell m}$ and $n^b_{\ell m}$ are assumed to be

[1]The *Planck Collaboration* has released other types of data split, such as for example half-ring maps. These are not used in this work.

uncorrelated.
In the typical and simplest case of a balanced data split, one has:

$$\begin{aligned} y_{\ell m} =& \frac{1}{2}\left(y^a_{\ell m} + y^b_{\ell m}\right) \\ =& o_{\ell m} + \frac{1}{2}\left(n^a_{\ell m} + n^b_{\ell m}\right) \\ =& o_{\ell m} + n_{\ell m}. \end{aligned} \tag{4.3}$$

If we build a vector $y^{\rm full}_{\ell m} = [y^a_{\ell m}, y^b_{\ell m}]$, its covariance matrix will be:

$$\hat{\mathbf{R}}^{\rm full}_\ell = \begin{bmatrix} \hat{O}^{\rm aa}_\ell + \hat{N}^{\rm aa}_\ell & \hat{O}^{\rm ab}_\ell \\ \hat{O}^{\rm ba}_\ell & \hat{O}^{\rm bb}_\ell + \hat{N}^{\rm bb}_\ell \end{bmatrix} \tag{4.4}$$

where we split the signal and the noise component of the angular power spectrum $\hat{C}^{\rm ij}_\ell$ into $\hat{O}^{\rm ij}_\ell$ and $\hat{N}^{\rm ii}_\ell$ respectively. From the data maps we can estimate directly $\hat{O}^{\rm ab}_\ell$, but not $\hat{O}^{\rm aa}_\ell$ or $\hat{O}^{\rm bb}_\ell$ because of the additive noise component.
In the absence of a mask, and to a good approximation for small masks, the angular power spectra are distributed as inverse gamma densities. At small scales, due to the large number of samples, we can approximate the $\hat{C}^{\rm ij}_\ell$ distribution with a Gaussian and we can write:

$$-2\ln\mathcal{L} = [vec(\hat{\mathbf{R}}^{\rm full}_\ell) - vec(\mathbf{R}^{\rm full}_\ell(\theta))]\mathbf{\Sigma}^{-1}_\ell[vec(\hat{\mathbf{R}}^{\rm full}_\ell) - vec(\mathbf{R}^{\rm full}_\ell(\theta))] \tag{4.5}$$

where $\mathbf{R}^{\rm full}_\ell(\theta)$ is the model for $\hat{\mathbf{R}}^{\rm full}_\ell$ and $\mathbf{\Sigma}_\ell$ is the 4×4 matrix containing the variances and covariances of the angular power spectra $\hat{C}^{\rm ij}_\ell$. The same can be obtained from a Taylor expansion of the likelihood (Hamimeche & Lewis, 2008). The diagonal terms of the matrix $\mathbf{\Sigma}_\ell$ are:

$$vec(\mathrm{diag}(\mathbf{\Sigma}_\ell)) = \frac{2}{f_{sky}(2\ell+1)} \begin{pmatrix} (O^{\rm aa}_\ell + N^{\rm aa}_\ell)^2 \\ \frac{1}{2}[(O^{\rm aa}_\ell + N^{\rm aa}_\ell)(O^{\rm bb}_\ell + N^{\rm bb}_\ell) + (O^{\rm ab}_\ell)^2] \\ \frac{1}{2}[(O^{\rm aa}_\ell + N^{\rm aa}_\ell)(O^{\rm bb}_\ell + N^{\rm bb}_\ell) + (O^{\rm ab}_\ell)^2] \\ (O^{\rm bb}_\ell + N^{\rm bb}_\ell)^2 \end{pmatrix}. \tag{4.6}$$

The first and the last term are the variances of the auto-spectra, while the second and third term are the variances of the cross-spectra. Using the full matrix $\hat{\mathbf{R}}^{\rm full}_\ell$ requires to model and fit for the noise component. Instead, we can just use the cross-spectra part of it, where the noise does not appear as an additive bias on the spectra and appears only in their variance, as seen by Eq. (4.6). In order to construct a model that better represents the data, we can add, both in the model and in the data, a known constant to the cross-spectra to account for the noise.
Given that data split maps observe the same sky, if $\hat{N}^{\rm aa}_\ell \approx \hat{N}^{\rm bb}_\ell$, we can approximate $\hat{O}^{\rm aa}_\ell + \hat{N}^{\rm aa}_\ell \approx \hat{O}^{\rm bb}_\ell + \hat{N}^{\rm bb}_\ell \approx \hat{O}^{\rm ab}_\ell + N^{\rm eff}_\ell$. The value of the constant $N^{\rm eff}_\ell$ can be obtained from the angular power spectra of the half-difference maps:

$$\frac{N^{\rm eff}_\ell}{2} \approx \langle \frac{y^a_{\ell m} - y^b_{\ell m}}{2}, \frac{y^a_{\ell m} - y^b_{\ell m}}{2} \rangle = \frac{\hat{N}^{\rm aa}_\ell + \hat{N}^{\rm bb}_\ell}{4} \tag{4.7}$$

where $\frac{y^a_{\ell m} - y^b_{\ell m}}{2}$ is called half-difference.
Since it is known, this constant disappears in the difference $vec(\hat{C}^{ab}_\ell) - vec(C^{ab}_\ell(\theta))$, but

it appears in the weighting matrix $\mathbf{\Sigma}_\ell$, which is obtained from the model. With this additional term, the model cannot represent the exact variance of the cross-spectrum $\hat{O}_\ell^{\rm ab}$, and the weighting is thus only approximately correct. However we expect an error in the weighting to affect the results less than an error on the spectra directly. Even though we used for this derivation a likelihood shape that is different from the SMICA one, the considerations made are the same for the SMICA likelihood. Since we do not use $\hat{O}_\ell^{\rm aa}$ and $\hat{O}_\ell^{\rm bb}$, we neglect a part of the information and this has some consequences on the precision with which we can determine the covariance matrix, as detailed in Appendix A.

4.2.2 A more general case

We consider here the case of multiple frequency channels. Given Eqs. (3.15) and (4.1), we can re-define $\mathbf{o}_{\ell m} \equiv \mathbf{A}\mathbf{s}_{\ell m}$, where $\mathbf{o}_{\ell m}$ is a $N \times 1$ vector containing the spherical harmonics of the $M \times 1$ mixed sources $\mathbf{s}_{\ell m}$ at all observed frequencies. The full sky $N \times 1$ $\mathbf{y}_{\ell m}$ data become:

$$\mathbf{y}_{\ell m} = \mathbf{o}_{\ell m} + \mathbf{n}_{\ell m}, \tag{4.8}$$

and their data splits become:

$$\mathbf{y}^a_{\ell m} = \mathbf{o}_{\ell m} + \mathbf{n}^a_{\ell m} \quad \text{and} \quad \mathbf{y}^b_{\ell m} = \mathbf{o}_{\ell m} + \mathbf{n}^b_{\ell m}. \tag{4.9}$$

The standard $N \times N$ empirical spectral covariance matrices $\hat{\mathbf{R}}_\ell$, used as inputs to the regular SMICA method, are defined as in Eq. (3.4.1), and they contain at each angular frequency ℓ the auto-spectra of each channel in their diagonal entries and the respective cross-spectra in their off-diagonal entries.
In this work instead, we consider using special matrices defined by:

$$\hat{\mathbf{R}}_\ell^{\rm split} = \frac{1}{2\ell+1} \sum_m \frac{1}{2} \left(\mathbf{y}^a_{\ell m} \mathbf{y}^{b\,\dagger}_{\ell m} + \mathbf{y}^b_{\ell m} \mathbf{y}^{a\,\dagger}_{\ell m} \right). \tag{4.10}$$

By construction, these matrices contain only correlations between maps with independent noise realizations and therefore they have a zero-mean noise contribution. More specifically, if we denote $\langle \cdot \rangle_N$ the average over noise realisations, one has:

$$\langle \hat{\mathbf{R}}_\ell \rangle_N = \widehat{\mathbf{O}}_\ell + \mathbf{N}_\ell \qquad \text{but} \qquad \langle \hat{\mathbf{R}}_\ell^{\rm split} \rangle_N = \widehat{\mathbf{O}}_\ell, \tag{4.11}$$

where the $N \times N$ sky part contribution (not averaged over) is:

$$\widehat{\mathbf{O}}_\ell = \frac{1}{2\ell+1} \sum_m \mathbf{o}_{\ell m} \;\; \mathbf{o}^\dagger_{\ell m}, \tag{4.12}$$

and where $\mathbf{N}_\ell$ is $N \times N$ the diagonal matrix with the noise spectra on its diagonal. In the following the expected value of $\hat{\mathbf{R}}_\ell^{\rm split}$ is denoted $\mathbf{O}_\ell(\theta)$ since this is also the expected value of $\widehat{\mathbf{O}}_\ell$.
In practice, one cannot "average over the noise", so we need to take into account the fact that for a single realisation of the data, matrix $\hat{\mathbf{R}}_\ell^{\rm split}$ is <u>not</u> distributed as $\hat{\mathbf{R}}_\ell$ or even as $\hat{\mathbf{R}}_\ell - \mathbf{N}_\ell$. In the previous Section we have seen that, similarly, $\hat{C}_\ell^{ab}$ is not distributed as $\hat{C}_\ell^{aa}$ nor as $\hat{C}_\ell^{aa} - N_\ell^{\rm eff}$.
It would be naive to adjust the spectral model $\mathbf{O}_\ell(\theta)$ by minimizing $\phi(\theta) = \sum_\ell (2\ell + 1)\, KL(\hat{R}_\ell^{\rm split}, \mathbf{O}_\ell(\theta))$. To see that, one can consider the divergence between two matrices

which are close to each other. The second order (quadratic) approximation of the divergence is

$$K(\mathbf{R}, \mathbf{R}+\delta\mathbf{R}) \approx K(\mathbf{R}+\delta\mathbf{R}, \mathbf{R}) \approx \mathrm{tr}\Big(\delta\mathbf{R}\,\mathbf{R}^{-1}\,\delta\mathbf{R}\,\mathbf{R}^{-1}\Big)/4 \tag{4.13}$$

and it shows that the Gaussian likelihood penalizes the (small) deviations $\delta\mathbf{R}$ between covariance matrices through the inverse matrix $\mathbf{R}^{-1}$. This is the proper weight (according to the maximum likelihood principle) to take into account the statistical variability in sample covariance matrices. Hence, if we were to use $KL(\hat{\mathbf{R}}_\ell^{\rm split}, \mathbf{O}_\ell(\theta))$, the statistical weight $\mathbf{O}_\ell^{-1}$ would not take into account the variability due to presence of the noise variance in the spectra of the matrix $\hat{\mathbf{R}}_\ell^{\rm split}$. In order to account for this variability, we use an ansatz and minimize:

$$\phi^{\rm split}(\theta) = \sum_\ell (2\ell+1) KL(\hat{\mathbf{R}}_\ell^{\rm split} + \mathbf{N}_\ell^{\rm eff},\ \mathbf{O}_\ell(\theta) + \mathbf{N}_\ell^{\rm eff}) \tag{4.14}$$

where $\mathbf{N}_\ell^{\rm eff}$ is the $N \times N$ diagonal matrix containing the effective noise auto-spectra. Since $\mathbf{N}_\ell^{\rm eff}$is introduced additively in both arguments of the $KL(\cdot,\cdot)$, it should not introduce noise bias (see Eq. (4.13)).

4.3 A semi-blind model for point sources

A strength of the regular SMICA approach is that very little assumptions are made regarding foreground emissions. In Sect. 3.4.2 different possible configurations for the SMICA model are presented. In the standard configuration of Eq. (3.22), the $N \times M-1$ matrix $\mathbf{F}$ is unconstrained and the symmetric $M-1 \times M-1$ matrix $\mathbf{P}_\ell^{fg}$ is only constrained to be non-negative. This amounts to saying that foreground emission can be represented by a given number of templates with arbitrary spectral energy distributions (SEDs), arbitrary angular spectra and arbitrary correlation. Nothing more can be said about foregrounds. In this work, we consider a more constrained foreground model. The additional constraints include forcing zero-terms in the matrix $\mathbf{P}_\ell^{fg}$, for instance to express independence between different components, as well as imposing a spectral dependence to some entries, when their angular power spectrum is known.

4.3.1 Foregrounds characteristics

Some of the foreground emissions, in particular galactic emissions, present a degree of correlation that prevents their description as separate components. If two emissions are not independent, then ICA methods, on which SMICA is based, cannot separate them. Thus all dependent emissions must be grouped in the analysis and considered as one single multidimensional component. Also, as seen in Section 2.2.1, galactic foregrounds such as thermal dust have varying spectral indices over the sky, which prevents their description as a single angular power spectrum scaled in frequency. These are described as a multidimensional component: in this way they are independent from the CMB and the other foregrounds, and the requirement of ICA is satisfied. The correspondence between the angular power spectra and emission laws of a multidimensional component with a given physical emission is not guaranteed, since the correlated emissions are mixed within it.

Using a large multidimensional component as in Planck Collaboration IX et al. (2016) is

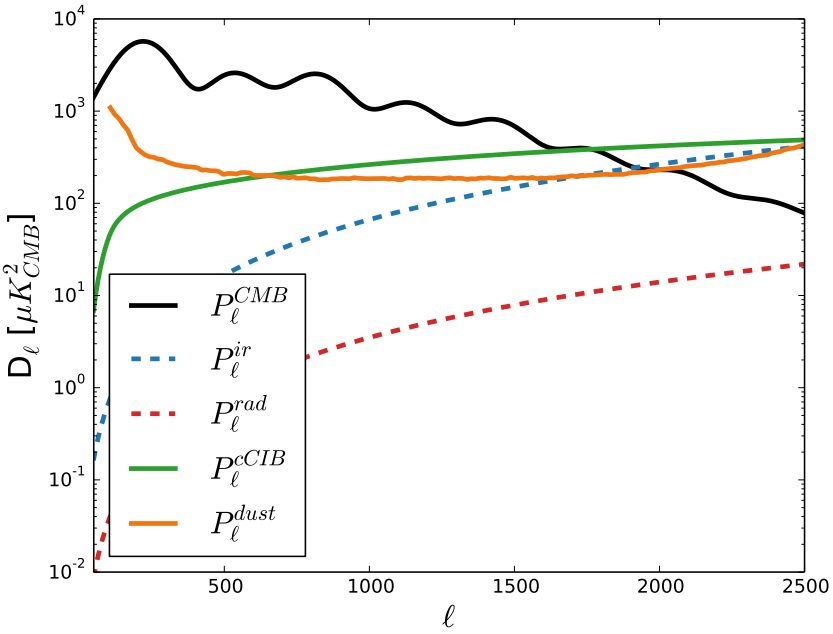

Figure 4.2 – The templates of the angular power spectra of the model $\mathbf{P}_\ell^{fg}$ and the CMB spectrum. The spectra are normalized as in the 217x353 GHz cross-angular power spectrum for a mask of $f_{sky} = 0.5$. Dashed lines correspond to spectra which are fixed in the fit, while solid lines correspond to fitted spectra. Radio and infrared point sources are labelled "rad" and "ir" respectively.

quite effective in capturing all the large scale galactic foreground emissions. Small scale extragalactic foregrounds, instead, may not be accounted for correctly. This translates into a higher final mismatch between the model and the data and possibly a foreground residual in the CMB estimation. This residual is present in the reconstructed SMICA map. However, this map is used for lensing (Planck Collaboration et al., 2016b) and non-Gaussianities (Planck Collaboration et al., 2016c) studies, which are mainly affected by large scales. Still, this residual can be a serious drawback when using the fit results for cosmological estimation, since the unresolved small scale foregrounds are degenerate with the CMB power spectrum. For this reason we use in this work a semi-blind model, by enforcing some minimal constraints on the extragalactic contamination in the foreground part of the model.

4.3.2 Model configuration

The main sources of foreground contamination at the frequencies of interest of this study 100 GHz $\leq \nu \leq$ 545 GHz are thermal dust, the point sources and the clustered CIB. As described in Section 2.3.1, and in particular in Figure 2.9, the point sources emission can be divided into a radio and an infrared component. We build the foreground model as the sum of three uncorrelated components: a bidimensional component that accounts for dust and clustered CIB (cCIB), and two unidimensional components to account for unresolved

radio and infrared point sources:

$$\mathbf{P}_\ell^{fg} = \begin{bmatrix} P_\ell^{dust+cCIB} & 0 & 0 & \\ & 0 & 0 & \\ 0 & 0 & P_\ell^{rad} & 0 \\ 0 & 0 & 0 & P_\ell^{ir} \end{bmatrix}. \tag{4.15}$$

Figure 4.2 shows the shape of the theoretical spectra on the diagonal of this model. In practice, the clustered CIB is fitted together with thermal dust since they have an emission law which is very similar, and thus it is difficult to blindly identify them.
This model does not account for all the foreground contamination. In particular, both cCIB and dust present spatial variations in their spectral properties and would require more spectral dimensions. For point sources, we assume perfect coherence in frequency, which could not be true, but this would also require to describe them as multidimensional components. The dimensionality of the model is fixed by the number of observations, and including more frequency channels increases also the complexity of the foreground emission to describe. We thus find a balance between having enough observations to allow good separation and reducing foregrounds complexity.
In the present configuration it is not possible to disentangle the clustered CIB and dust. A more refined configuration, that includes a zone approach in SMICA and thus exploits the different spatial distributions of dust and clustered CIB, could in principle separate them. The interest of this, apart from studying the properties of dust and cCIB (Mak et al., 2017), is that it could improve the quality of the recovered CMB spectrum. The foreground contamination that is not accounted for by the model results in an increase of the final mismatch. However it is possible that a fraction of it projects on the CMB component. This can be checked with the aid of simulations.
The spectrum and emission law of dust and cCIB are freely fitted. Instead, we impose some constraints on the point sources part of the model, by making use of the physical knowledge we have. Their spectra are constrained to be flat, consistently with the prediction that the point sources can be modelled as shot noise. We expect that at the extrema of our frequency range only one population is clearly detected. This could induce the algorithm to find non-physical values for the emission law of the subdominant population. For this reason, we constrain the columns of the mixing matrix $\mathbf{A}$ relative to point sources to take only positive values, but we make no further assumption on the emission law shape. This configuration allows us to recover the joint emission law of point sources, however it is not possible to disentangle the emission of the two populations, since there is an intrinsic degeneracy between components that have the same shape of the angular power spectrum. For this reason, throughout the text we present results on the joint point sources emission.
The CMB angular power spectrum is freely fitted. Its emission law, which is well known, is instead fixed. Known calibration errors are taken into account. This refined model is more useful for a physical understanding of the foregrounds, especially in the case of point sources, which dominate at scales where the noise becomes important and are thus difficult to characterize. Without a dedicated model for point sources, it is not possible to know what their contribution is to the total foreground level, hence it is not possible to correctly remove them from the CMB. In this sense point sources are degenerate with the CMB emission at small scales. We must note that, since we impose some constraints on the model and we therefore decrease its level of blindness, the extra information gained on point sources comes at the cost of increasing the mismatch between the data and the

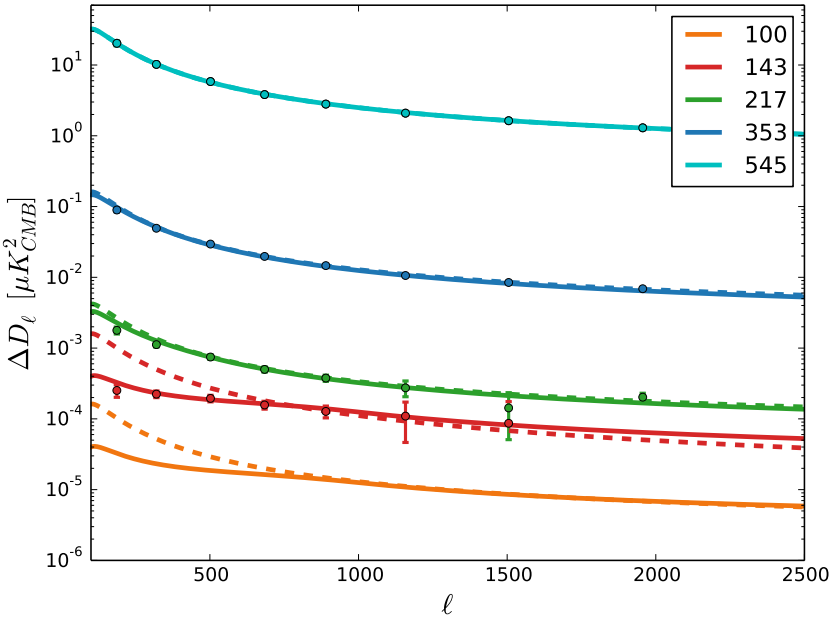

Figure 4.3 – The angular power auto-spectra of the clustered CIB component used in simulations. The dashed line is the 1D clustered CIB, while the solid line is the ND clustered CIB. Overplotted data are taken from Table D2 in Planck Collaboration XXX et al. (2014). No data points are available for the 100 GHz clustered spectrum, which is taken to be one order of magnitude less than the 143 GHz clustered spectrum. Spectra have been corrected for shot noise in order to match observational points.

proposed model.

4.4 Data

In this analysis we use both simulations and Planck 2015 half-mission data. We build three types of simulations of increasing foregrounds complexity. We first give a general description of the simulations content and then more technical details in a following paragraph. The Planck 2015 data are high frequency HFI data.

4.4.1 Simulations

In order to test our model, we construct simulations of sky observations at the frequencies of interest, which are a subset of the Planck HFI frequencies: 100, 143, 217, 353 and 545 GHz. For our main analysis we do not consider the 857 GHz channel, even though we also build simulations for this frequency: more details about this choice are given in Sect. 4.5.3. The astrophysical emissions we simulate are the CMB, the thermal dust and two extragalactic point sources populations, the radio and the infrared ones. For the latter, we simulate the clustered as well as the shot noise emission.
In order to better test our model with respect to extragalactic contamination, we produce three sets of simulations. They all contain CMB, dust, radio and infrared point sources, clustered CIB and noise, but the signals properties differ in each set. The three simulations sets are:

- SET1: these simulations have an idealised foreground content. All the foregrounds are simulated as a single template rigidly scaled through frequency. We refer to foregrounds of these simulations as 1D or unidimensional, since their contribution in all auto-spectra of sky maps can be described by a singular angular power spectrum rescaled in frequency, and they present no decoherence in the cross-spectra;

- SET2: these simulations include one foreground source with some frequency decoherence. Galactic dust and the two point source populations are simulated as a 1D template each, which is rigidly scaled through frequency. The clustered CIB presents some frequency decoherence, i.e.:

$$C_\ell^{CIB\ \nu_1\times\nu_2} = \alpha_{\nu_1\times\nu_2}\sqrt{C_\ell^{CIB\ \nu_1} C_\ell^{CIB\ \nu_2}}, \tag{4.16}$$

  where the coefficients $\alpha_{\nu_1\times\nu_2} \leq 1$. The angular power spectrum shape is modeled on observational estimates: it is not exactly proportional between frequencies, but presents slight deviations. The power spectra are presented in Fig. 4.3. We refer to this CIB component as ND or multidimensional;

- SET3: these simulations have the most realistic foreground content. The two point source populations are simulated as a 1D template each, which is rigidly scaled through frequency. The clustered CIB is simulated as in SET2. The dust component presents spectral index and dust temperature variability on the sky. Again we refer to this dust component as ND or multidimensional.

These three sets are labelled SET1, SET2 and SET3 throughout this work. The SET2 and SET3 cases are studied since observations show that there could be a partial decoherence through frequency of the CIB emission (Planck Collaboration XXX et al., 2014, Sect.6.2), this effect being mostly evident at the two lowest frequencies 100 and 143 GHz. The third case also includes a realistic dust representation, which takes into account the inhomogeneous dust properties on the sky. Both are important tests since the SMICA method assumes no frequency decoherence or variability of the spectral index for the unidimensional sources: this variability is accounted for in the SMICA model as an increase of the dimensionality of the source. However the model has a maximum number of dimensions fixed by the number of observations.
In order to reproduce the Planck half-mission maps used in this analysis, for each simulation we produce 2 maps for each frequency, and each couple of maps at same frequency has identical astrophysical content but a different realization of white Gaussian noise. We produce N=30 simulations for each set.

Building the components The CMB component is simulated from a theoretical CMB temperature angular power spectrum using the HEALPIX tool (Górski et al., 2005). The power spectrum is obtained using the code CosmoMC, with the following set of input cosmological parameters: $H = 67.31$, $\tau = 0.078$, $\omega_b = 0.02222$, $\omega_c = 0.1197$, $n_s = 0.9655$, $\ln(10^{10}A_s) = 3.089$, $y_{He} = 0.24$ and $m_\nu = 0.06$ eV.
There are two different thermal dust components: one is a single template scaled through frequency (SET1 and SET2 simulations), while the other presents more complex features (SET3). The former, labelled "1D", is the thermal dust map at 545 GHz delivered by the *Planck Collaboration* (Planck Collaboration X et al., 2016) and shown in Figure 2.3,

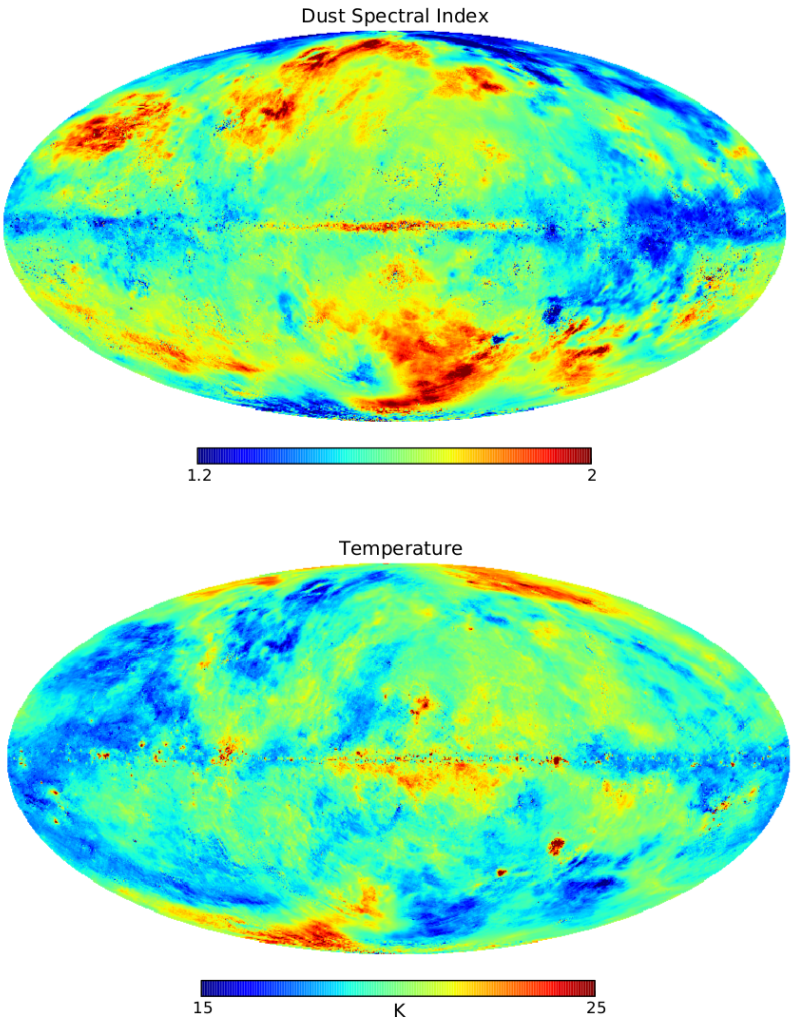

Figure 4.4 – The spectral index (top) and the temperature (bottom) maps recovered by Planck Collaboration XLVIII et al. (2016).

which we choose in order to have a realistic spatial distribution. This template is scaled through frequency according to the grey-body law described by Eq. (2.4) with T=19.4 and β=1.6 (see Section 2.2.1 for more details on the grey-body parameters). Due to the fact that thermal dust and clustered CIB have similar emission laws, as seen in Section 2.3.2, the presence of a residual contamination of CIB in the small scales of the thermal dust template map is not to be excluded (Planck Collaboration X et al., 2016, Sect. 4), i.e., the small scale power of this template could be higher than the real dust distribution due to clustered CIB residuals. The latter, labelled "ND", is simulated using the GNILC model maps for the spectral index β_d, the dust temperature, and the opacity, obtained as described in Planck Collaboration XLVIII et al. (2016). They are combined through Eq. (2.4) to produce a dust map at each ν. The spectral index and the temperature distributions are shown in Figure 4.4.
For the extragalactic content, that is point sources and clustered CIB, we base ourselves on Planck Collaboration XXX et al. (2014), which provides estimates for the radio and infrared point sources shot-noise levels, angular power spectra of CIB emission and its decoherence

Table 4.1 – Simulation parameters for point sources and clustered CIB as $C_{\ell=3000}$ levels in $\mathrm{Jy}^2/\mathrm{sr}$.

	Radio Point Sources	IR Point Sources	1D clustered CIB
100	8.48	0.150	0.136
143	6.05	1.20	3.43
217	3.12	16.0	14.4
353	3.28	225	209
545	2.86	1454	1550
857	4.28	5628	5397

coefficients at Planck frequencies. Shot-noise levels are given at all the frequencies of interest of this work, and we therefore use them for point sources simulations. CIB spectra and decoherence coefficients are given for all frequencies except 100 GHz: we choose for this channel values one order of magnitude lower than the 143 GHz estimates. The CIB angular power spectra reported in Table D2 of Planck Collaboration XXX et al. (2014) contain both the clustered and shot-noise contribution: the latter is subtracted to obtain clustered CIB templates. Also, only the auto-spectra are used, while cross-spectra are derived via Eq. (4.16). The 1D and ND CIB spectra are shown in Figure 4.3.
We model the two point source populations as two realisations of shot noise maps, i.e., with a flat angular spectrum (see Eq. (2.9)). The amplitudes of the shot noise power are taken from Table 6 and 7 in Planck Collaboration XXX et al. (2014) and are summarized in Table 4.1. To produce the clustered CIB component maps at each frequency we compute the covariance matrix $\mathbf{R}_\ell^{CIB}$ of CIB auto- and cross-angular power spectra. More specifically:

- for SET1, i.e., the 1D clustered CIB, we estimate the power spectrum shape at 545 GHz, and all the other auto- and cross-spectra are obtained by scaling this template. Scaling coefficients for auto-spectra are obtained from Planck Collaboration XXX et al. (2014), while for cross-spectra we use Eq. (4.16) with $\alpha_{\nu_1\times\nu_2} = 1$. $C_{\ell=3000}$ values are reported in Table 4.1;

- for SET2 and SET3, i.e., the ND clustered CIB, we use the auto-spectra estimates of Planck Collaboration XXX et al. (2014) at each frequency, and we extrapolate to higher ℓ when necessary. We also introduce a decoherence through frequency in the cross-spectra of the matrix $\mathbf{R}_\ell^{CIB}$. The decoherence coefficients of angular power spectra between different frequencies are detailed in Table 4.2 and are obtained by observational estimates of Planck Collaboration XXX et al. (2014).

Once the covariance matrix $\mathbf{R}_\ell^{CIB}$ is constructed, the procedure for obtaining spherical harmonics is the same for both cases. We build the $N \times 1$ vector $\mathbf{x}_{\ell m}$, whose entries $x^i_{\ell m}$ are sets of spherical harmonics coefficients drawn from the normal distribution,

$$x^i_{\ell m} \sim \mathcal{N}(0,1), \tag{4.17}$$

where $i = 1, 2, ...N$, and N is the number of frequencies we use. We then obtain spherical harmonics for the CIB as:

$$\mathbf{x}^{CIB}_{\ell m} = \mathbf{Z}^{CIB}_\ell \mathbf{x}_{\ell m} \tag{4.18}$$

Table 4.2 – Decoherence coefficients for the ND clustered CIB.

	100	143	217	353	545	857
100	1	-	-	-	-	-
143	0.99	1	-	-	-	-
217	0.78	0.78	1	-	-	-
353	0.54	0.54	0.91	1	-	-
545	0.51	0.51	0.90	0.983	1	-
857	0.45	0.45	0.85	0.911	0.949	1

where $\mathbf{Z}_\ell^{CIB}$ is the square root of the clustered CIB $N \times N$ covariance matrix $\mathbf{R}_\ell^{CIB} = \mathbf{Z}_\ell^{CIB}\mathbf{Z}_\ell^{CIB}$.
In order to build simulations, the CMB and foreground maps are added with their respective amplitude for each frequency and then smoothed with their respective beam window function[2]. By construction, there is no correlation between the foregrounds and the CMB.
The instrumental noise is simulated at the map level as white Gaussian noise. Noise amplitudes are determined using Planck noise simulations as provided at NERSC[3].

4.4.2 Planck data

We use data maps from the 2015 full Planck release and we select the two half-mission maps at each frequency between 100 and 545 GHz. Half-mission maps are data split obtained by dividing the full mission time-ordered data into two halves. The maps are degraded to a lower resolution of Nside = 1024 using *Healpix*.

4.4.3 Masks and binning

In order to reduce the foreground contamination, the central regions of the sky are masked. Masks are produced as a sum of a galactic and a point source part. We use a set of three masks with the same point source masking but different galactic coverage. The masks used have effective $f_{sky} = 0.3, 0.5, 0.6$. More details on the masks preparation are given in Appendix B.
Since SMICA works with spectral covariance matrices, angular power spectra between all couples of maps are calculated with the *PolSpice* (Chon et al., 2004) package. Using the *PolSpice* routine, we correct the resulting power spectra for the point spread function of the instrument using the beam window functions provided by the full Planck release, for the pixel window function and for the mask leakage using the MASTER correction described in Section 1.4.3. All the angular power spectra are binned uniformly with $\Delta\ell = 15$. With these spectra, and following the procedure detailed in Sect. 4.2, we build at each bin a 5×5 covariance matrix $\hat{\mathbf{R}}_\ell^{split}$. We work on the range $\ell = [100, 2500]$: we neglect in this analysis the large angular scales $\ell < 100$, where dust has complex features that cannot be described by a bidimensional component. Also, we limit our analysis around $\ell \sim 2500$,

[2]provided in Planck's RIMO, which can be downloaded from the *Planck Legacy Archive* http://pla.esac.esa.int/pla/
[3]http://crd.lbl.gov/cmb-data

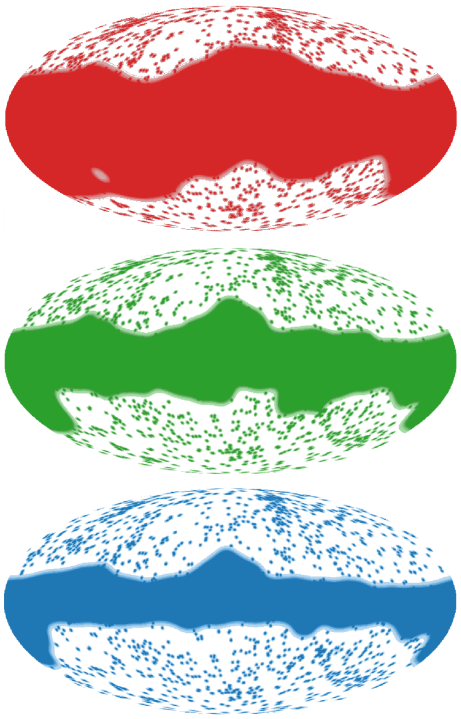

Figure 4.5 – The apodised masks used in this analysis. The retained sky fractions f_{sky}=0.3, 0.5, 0.6 are shown in red, green and blue respectively. The shaded region is the apodised part.

since for higher multipoles noise becomes dominant.

4.5 Testing the method

We detail here the analysis and fitting procedure to obtain the CMB power spectrum. We test this method on simulations first and Planck 2015 temperature data then. The spectra recovered from simulations and data are used to estimate cosmological parameters, which are presented in Sect. 4.6.

4.5.1 Simulation analysis

The simulated foregrounds cannot reproduce the complexity of real data foregrounds, however they are a good test for understanding to which degree we can recover the point source signal. We process the three simulation sets with the foreground model described by Eq. (4.15). For SET1, since foregrounds are all 1D, we constrain the $P_\ell^{dust+cCIB}$ component to be diagonal.

We show in the top panel of Fig. 4.6 the recovered shot noise point source signal for the average of all simulations of each SET at $f_{sky} = 0.5$.

We show results for the intermediate f_{sky}, but we observe no mask dependence in the recovered point source emission. We observe that the model is capable of recovering closely, up to small offsets, the point sources input for all the 3 cases. The SET1 case, which has

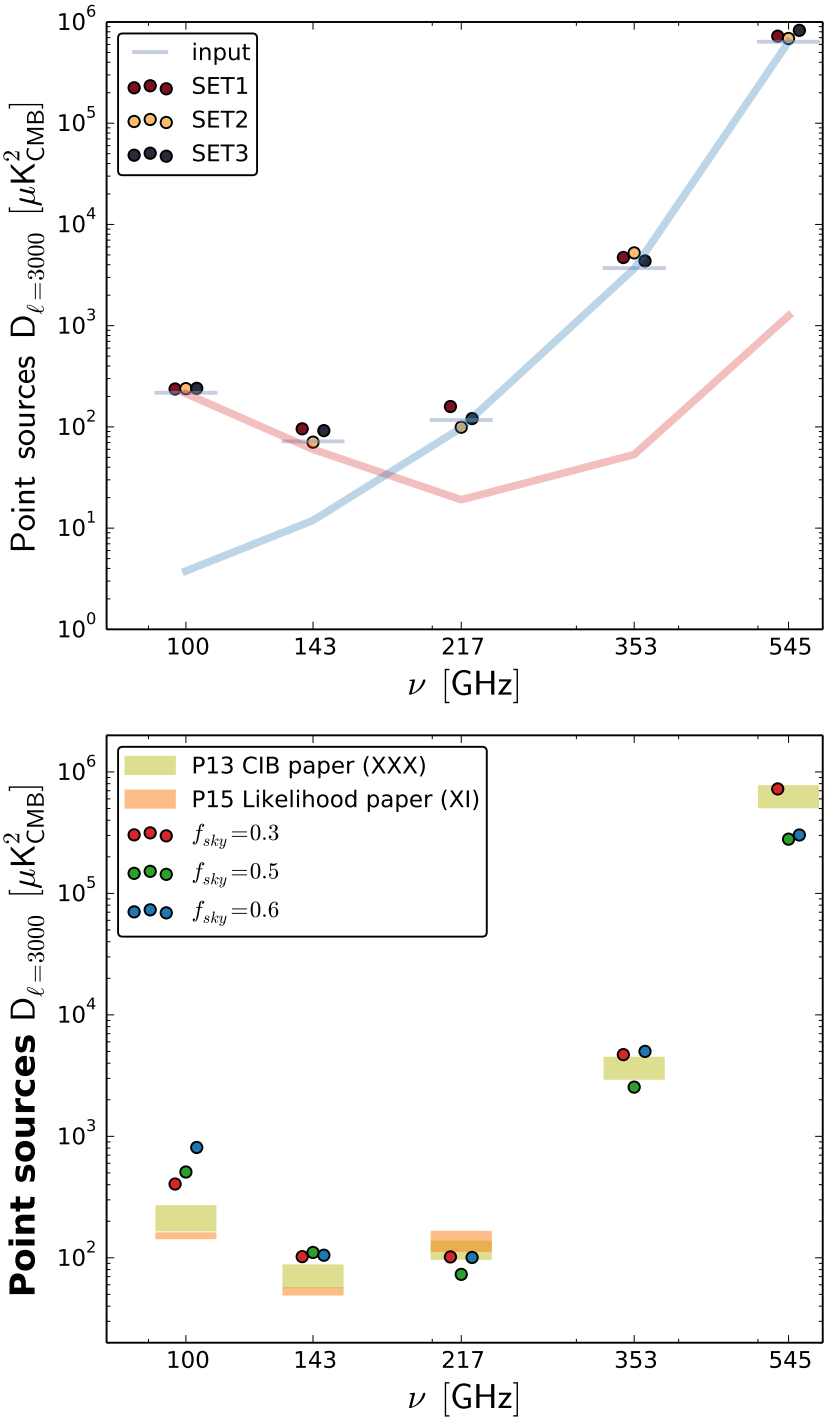

Figure 4.6 – Combined (infrared and radio) shot noise point sources D_ℓ power at $\ell = 3000$ obtained from the fit. *Top panel*: simulations average of point sources at $f_{sky} = 0.5$, shown in dark red for SET1 simulations, yellow for SET2 and black for SET3. The red and blue bands show the simulations input for the radio and infrared point sources respectively, while the light-blue horizontal line at each ν represents the joint point source input. *Bottom panel*: Planck data recovered point sources for the three different masks of $f_{sky} = 0.6, 0.5, 0.3$ in blue, green and red respectively. The yellow and orange bands represent the expected shot noise point source contribution estimated in Planck Collaboration XXX et al. (2014) and Planck Collaboration XI et al. (2016), where the width of the coloured band represents the error on the expected value. Planck Collaboration XI et al. (2016) gives expected values for the three low ν channels only.

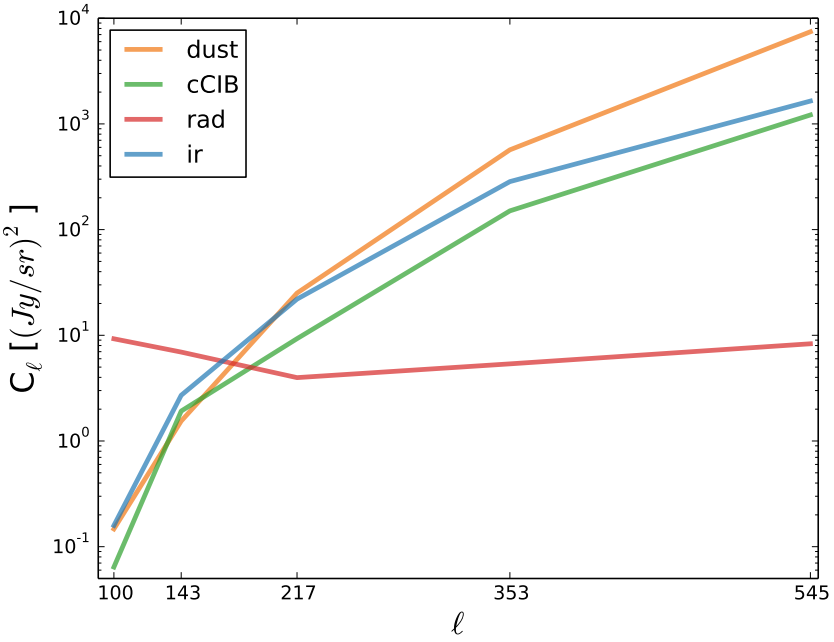

Figure 4.7 – The recovered spectral behaviour of dust, clustered CIB, infrared and radio point sources of one representative simulation of SET1 at $f_{sky} = 0.5$. Because of the intrinsic indeterminacy of ICA methods (see Section 3.2.3), the SMICA fit returns the emission law of a component up to an arbitrary factor. For this reason we plot the frequency behaviour as the scaling of $C_{\ell=2500}$ in frequency. Radio and infrared point sources are labelled "rad" and "ir" respectively.

all 1D foregrounds and is therefore an "ideal" test case for SMICA, presents a small offset in the three central frequencies. This is not surprising: even though the foreground content corresponds exactly to the SMICA model, the clustered CIB, the infrared shot-noise and the galactic dust have similar emission laws, and the corresponding columns of the matrix **A** are almost proportional, as shown in Figure 4.7. This is far from ideal for ICA methods, since it limits the identifiability of the sources. The small offsets in SET2 simulations at 353 GHz and SET3 simulations at 143 GHz are instead likely due to the fact that the model is incapable of representing the foregrounds complexity.
Since in SET1 the $P_\ell^{dust+cCIB}$ is constrained to be diagonal, we can compare the recovered angular power spectra to the dust and clustered CIB components, as shown in Figure 4.8. The figure compares the recovered spectrum with the power law approximation: the recovered thermal dust has a shallower spectrum than expected. This is probably due to CIB residuals in the galactic dust template (Planck Collaboration X et al., 2016, Sect. 4). Also, again due to the similar emission law of CIB and dust, the blind identification of these two emissions is challenging, and a part of the CIB power can leak in the dust component. In SET2 and SET3 simulations, as well as in the data analysis, these two foregrounds are jointly fitted in a multidimensional component.
In the top panel of Figure 4.9 we show average residuals of the high-ℓ tail of the fitted CMB angular power spectrum with respect to the theoretical input. Results show a marked offset for the SET2 and SET3 cases. The misevaluation of the clustered CIB contamination can be one source of bias in the CMB power spectrum estimation. The SMICA method

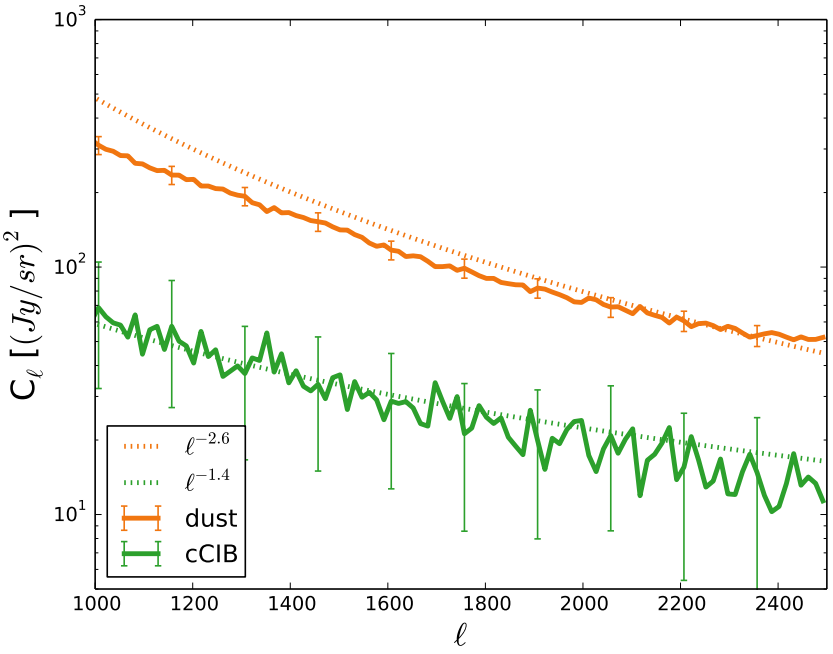

Figure 4.8 – The recovered 217x217 GHz dust and clustered CIB spectra of one representative simulation of SET1 compared to their respective power law approximation at $f_{sky} = 0.5$. The power law is scaled in order to best fit the data. Only one point every 10 is plotted. The dust angular power spectrum is shallower than the expected behaviour $\propto \ell^{-2.6}$ probably due to CIB residuals in the galactic dust template.

assumes full correlation of all components through frequency. A partial decoherence of a component, as for example in SET2 for the clustered CIB, means that its spectral behaviour must be described by a multidimensional component. For galactic dust and clustered CIB, we have a 2D component describing both of them at the same time. While angular power spectra are fitted in each bin, the mixing matrix A is global: galactic dust and clustered CIB, which are important at low and high multipoles respectively, compete for the columns of this matrix. As a consequence, complex features in these two emissions cannot be fully accounted for. We expect that a part of the CIB and dust contamination projects onto the CMB, resulting in an offset with respect to the input spectrum, as shown in the top panel of Fig. 4.9 for SET2 and SET3 simulations.
We can see that such a contamination is not detectable as a considerable increase in the mismatch, while it is clearly visible in the CMB residuals. Results in Fig. 4.9 are presented for $f_{sky} = 0.5$, but no significant trend with sky fraction is visible in most simulations. We see that the observed mismatch is lower than the expected value. This happens because of the peculiar statistical properties of the empirical covariance matrices used in this work. The value of the mismatch is not the one predicted by the standard theory, which we plot anyway as a visual reference of the order of magnitude of the expected mismatch.

4.5.2 Data analysis

We fit a model as described in Section 4.3.2. The obtained CMB angular power spectrum is presented in Fig. 4.11 for the three different masks, while right panel of Fig. 4.9 shows

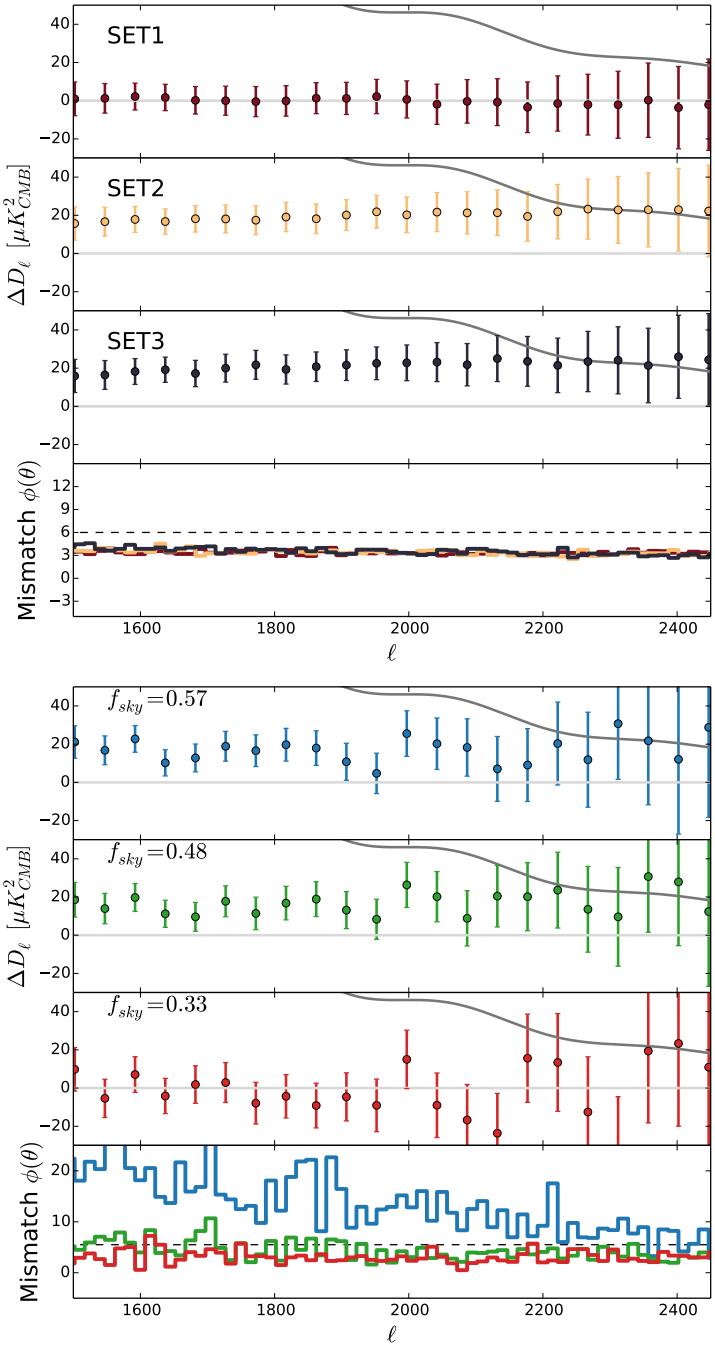

Figure 4.9 – Top three panels of each figure show the residuals in D_ℓ between the fit results and the theoretical CMB power spectrum. Dark grey line shows the theoretical CMB spectrum at 20% power. Bottom panel shows the mismatch between the model and the data after the fit as defined by Eq. (3.23) and the thin dashed line shows the expected mismatch per bin. *Top figure:* Filled dots show differences between CMB spectra obtained from the average of the fits on simulations with respect to input CMB spectrum at each bin, at $f_{sky} = 0.5$, shown in dark red for SET1, yellow for SET2 and black for SET3. As anticipated in Section 3.4.4, in the data split configuration the mismatch compares to its predicted value only as an order of magnitude approximation. *Bottom figure:* Filled dots show differences between CMB spectra obtained from the fit on Planck 2015 half-mission data with respect to the Planck best fit ΛCDM Plik spectrum. Only one point every three bins is displayed.

residuals with respect to the reference CMB Planck spectrum at high-ℓ. The reference Planck spectrum is the theoretical ΛCDM spectrum obtained from best fit parameters of the Planck 2015 Plik likelihood exploration. Error bars are derived with the Fisher matrix and are thus a statistical estimate.
In Figure 4.9 we observe that the results obtained for the CMB are in good agreement between the three different masks. We can see an increasing level of residual contamination, for increasing sky fraction. While this trend is not seen in simulations, we expect such a behaviour in real data since the foreground complexity increases. As observed in simulations, we expect that the model cannot fully capture dust and cCIB emission. Also, our simulations contain two point source populations perfectly correlated through frequency. While this is a good approximation, it might not represent the full extent of contamination produced by background galaxies. Another problem is the similar emission law between dust and CIB, which cannot be fully captured by the model; due to this, a fraction of the foreground contamination projects on the CMB and on the mismatch between the model and the data. We see that the mismatch is much higher than for simulations, in particular for the smallest mask and at low multipoles, where the thermal dust behaviour becomes more complex.
In the bottom panel of Figure 4.6 we show the recovered point sources amplitudes for the three masks at $\ell = 3000$. Results for $f_{sky} = 0.3, 0.5$ are in good agreement with each other and with the expected amplitude as estimated by the Planck Collaboration. The $f_{sky} = 0.6$ results show an offset at the highest and lowest frequencies: again the model fails to fully represent the foregrounds complexity. We expect point sources estimates at smaller f_{sky} to be more accurate, since the galactic contamination is lower. The offset of point source emission law is related to the offset in the CMB power spectrum, but cannot fully explain it. Forcing point sources emission law to the result obtained for the largest mask, i.e., to a value closer to the expected one, reduces only slightly the mismatch and the CMB bias. The recovered spectra of all components for simulations and data are compared in Figure 4.10.

4.5.3 Using 857 GHz

The number of channels used is directly related to the dimensionality of the foreground model. Including more observations allows for a higher dimension, but also adds new features in the data which need to be described. We choose to exclude low frequency observations from our analysis since this would include synchrotron ad free-free emission and thus increase the galactic foreground complexity. We also choose to exclude WMAP 94 GHz observations since they have a lower resolution than Planck data and this would oblige us to use a smaller ℓ range.
Higher ν observations could in principle be useful since they contain mainly dust, IR point sources and clustered CIB. However frequency decoherence of foregrounds makes the effective impact of high frequency channels negligible. We present here results on simulations and Planck data when adding the 857 GHz channel. For the analysis on data, the masks are adapted by adding point sources detected in the 857 GHz maps, but effective sky fractions are substantially unchanged. The fitting procedure is the same as described in Sect. 4.5.1 and Sect. 4.5.2, with the only difference that the $P_\ell^{dust+cCIB}$ part of the model in Eq. (4.15) has now three dimensions instead of two.
For simulations, the recovered CMB spectrum of SET1 now shows an offset, as seen in

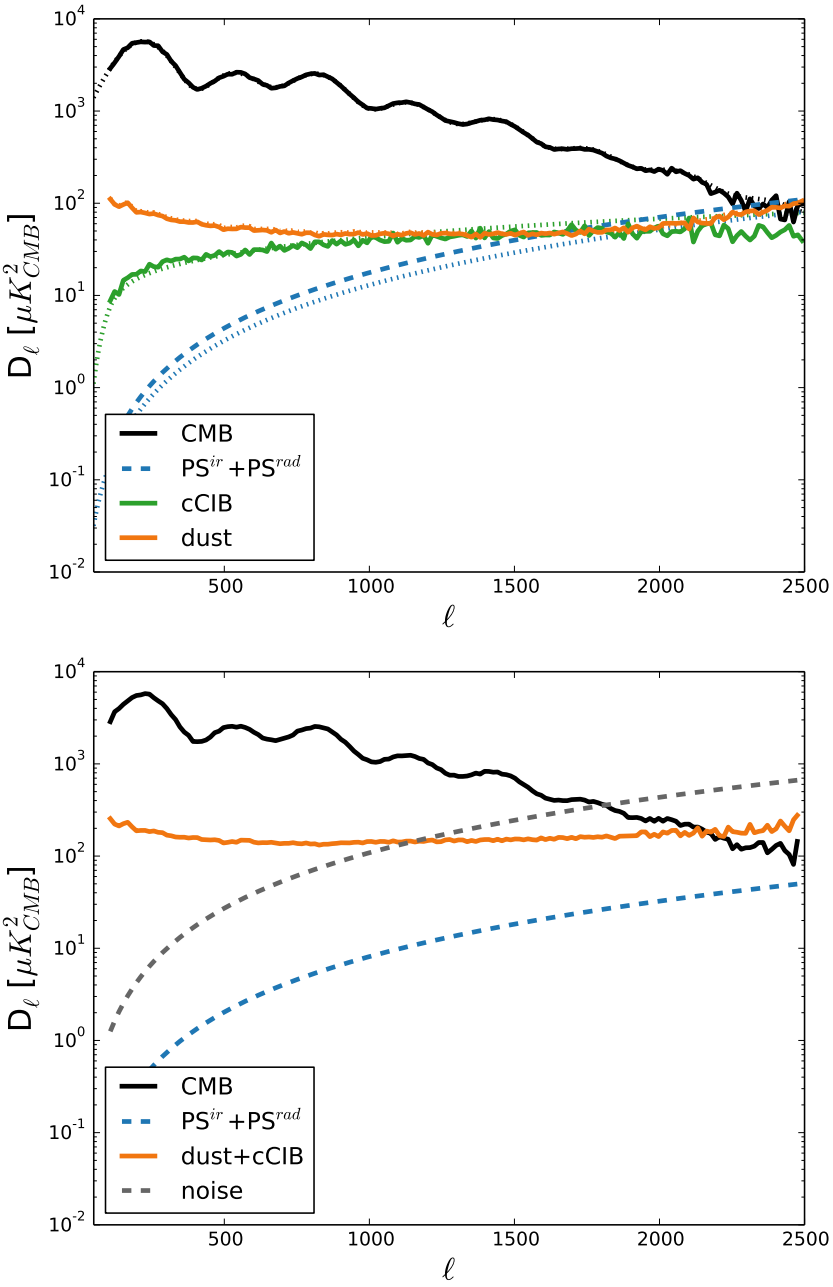

Figure 4.10 – *Top figure:* The recovered and input spectra for one representative simulation of SET1 at 217x217 GHz and $f_{sky} = 0.5$. Dotted lines are the input spectra, dashed lines are the spectra which are fixed in the fit and solid lines are the fitted spectra. Even though point source spectra are fixed, their emission law is freely fitted. Noise spectra instead are kept fixed in the fit. *Bottom figure:* The recovered spectra for Planck data at 217x217 GHz and $f_{sky} = 0.5$. Dashed lines are the fixed spectra and solid lines are the fitted spectra. Since dust and CIB are jointly fitted, their emission cannot be disentangled. Also, the emission of point sources can only be recovered jointly due to the fact that they have the same angular power spectrum. The SMICA method required diversity in both frequency and angular spectrum in order to separate the components without external constraints.

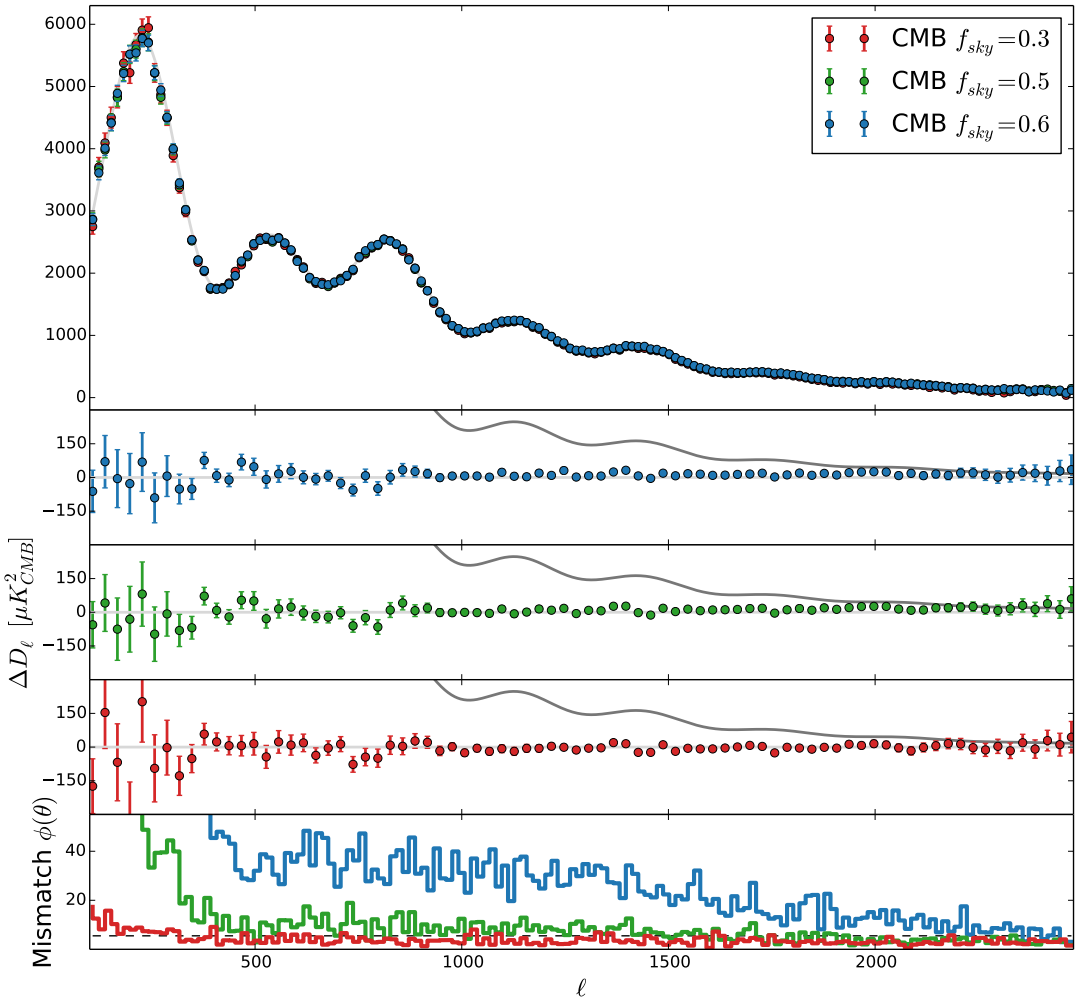

Figure 4.11 – The CMB angular power spectrum obtained from the SMICA fit on Planck 2015 data (top panel). In grey we show the best fit theoretical ΛCDM spectrum obtained with Plik. The second to fourth panel show the residuals of each mask with respect to the theoretical model. In these panels, the grey line shows the CMB power spectrum scaled to 20%. The bottom panel shows the mismatch between the fitted model and the data for the three cases, together with the expected level in black dashed line.

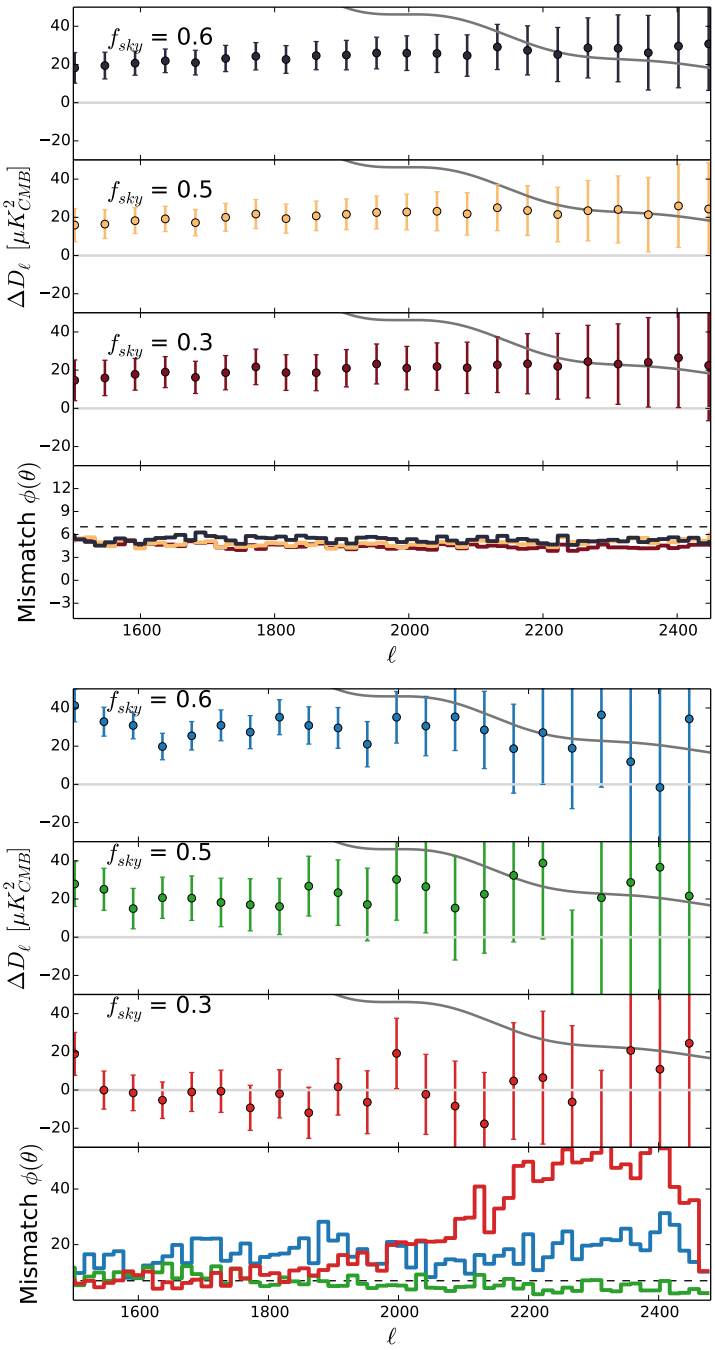

Figure 4.12 – The fit results including the 857 GHz channel. Top three panels of each figure show the residuals in D_ℓ between the fit results and the theoretical CMB power spectrum. Dark grey line shows the theoretical CMB spectrum at 20% power. Bottom panel shows the mismatch between the model and the data after the fit as defined by Eq. (3.23) and the thin dashed line shows the expected mismatch per bin. *Top figure:* Filled dots show differences between CMB spectra obtained from the average of the fits on SET3 simulations with respect to input CMB spectrum at each bin, at $f_{sky} = 0.3, 0.5, 0.6$ in black, yellow and red respectively. *Bottom figure:* Filled dots show differences between CMB spectra obtained from the fit on Planck 2015 half-mission data with respect to the Planck best fit ΛCDM Plik spectrum. Only one point every three bins is displayed. The high mismatch at high ℓ for the smallest mask could be linked to the poor recovery of the point sources emission law, as seen in Figure 4.13.

Figure 4.12, while in SET2 and SET3 we see no evident difference in the SMICA fit between adding or not the 857 GHz channel. For data, while simulations show a good agreement between masks, the point sources emission laws show an evident bias at low frequencies $\nu \leq 217$ GHz. This hints that a degree of decoherence is present between 857 GHz and lower frequencies shot noise emission. The mixing matrix columns reserved to point sources cannot accommodate both high and low frequencies, sacrificing the latter. The recovered point sources for simulations and data are shown in Figure 4.13. The CMB power spectrum for $f_{sky} = 0.5, 0.6$ is shown in Figure 4.14 compared to different SMICA configurations. No improvement is seen with respect to the fit without 857 GHz, and the foreground residuals seem slightly higher.

4.5.4 Without data splits

The configuration described in Sect. 4.2 tests covariance matrices built using data split cross-spectra only.

A simpler configuration would be to use the full $2N \times 2N$ covariance matrix of auto- and cross-spectra, where N is the number of frequency channels and $2N$ is the number of half-mission maps. This matrix is defined as:

$$\hat{\mathbf{R}}_\ell^{\text{full}} = \frac{1}{2\ell+1} \sum_m \mathbf{y}_{\ell,m}^{\text{full}} \mathbf{y}_{\ell,m}^{\text{full}\,\dagger}, \tag{4.19}$$

where the $2N \times 1$ data vector is $\mathbf{y}_{\ell,m}^{\text{full}} = [\mathbf{y}_{\ell,m}^a, \mathbf{y}_{\ell,m}^b]$. The model used in this case is:

$$\mathbf{R}_\ell(\theta) = \begin{bmatrix} \mathbf{a} & \mathbf{F} \end{bmatrix} \begin{bmatrix} C_\ell^{\text{cmb}} & 0 \\ 0 & \mathbf{P}_\ell^{fg} \end{bmatrix} \begin{bmatrix} \mathbf{a} & \mathbf{F} \end{bmatrix}^T + \mathbf{N}_\ell \tag{4.20}$$

where $\mathbf{N}_\ell$ is the $2N \times 2N$ diagonal matrix containing the noise power spectra, $\mathbf{P}_\ell^{fg}$ is the $M-1 \times M-1$ matrix of the source spectra and $\mathbf{F}$ is its associated part in the mixing matrix of dimensions $2N \times M-1$. In this configuration the noise power spectra are part of the fitted parameters. This higher number of parameters to fit is compensated by the increased dimension of the data matrix $\hat{\mathbf{R}}_\ell^{full}$.
On Planck data, we show in Fig. 4.14 that residuals for the cross-spectra only covariances $\hat{\mathbf{R}}_\ell^{\text{split}}$ are lower than those obtained using the auto- and cross-spectra covariances $\hat{\mathbf{R}}_\ell^{full}$. We attribute this difference to the higher number of parameters to fit in the full matrix case. Also, an error in the noise estimation reflects on the astrophysical part of the fit, and potentially on the CMB. Instead, in the configuration chosen for this study, noise spectra are known by construction and are not fit for, and thus they can not bias the fit. The drawback in this case is that the estimated error bars depend on the noise ansatz.

4.6 Cosmological parameters

We test our approach by obtaining cosmological parameters from the SMICA best fit angular power spectra. We do this both on Planck data and on a subset of simulations. We compare the parameters obtained from simulations with the input parameters used to simulate the CMB map. The parameters obtained from Planck data are compared to the baseline Planck 2015 results. Since we have only temperature data, we put a Gaussian

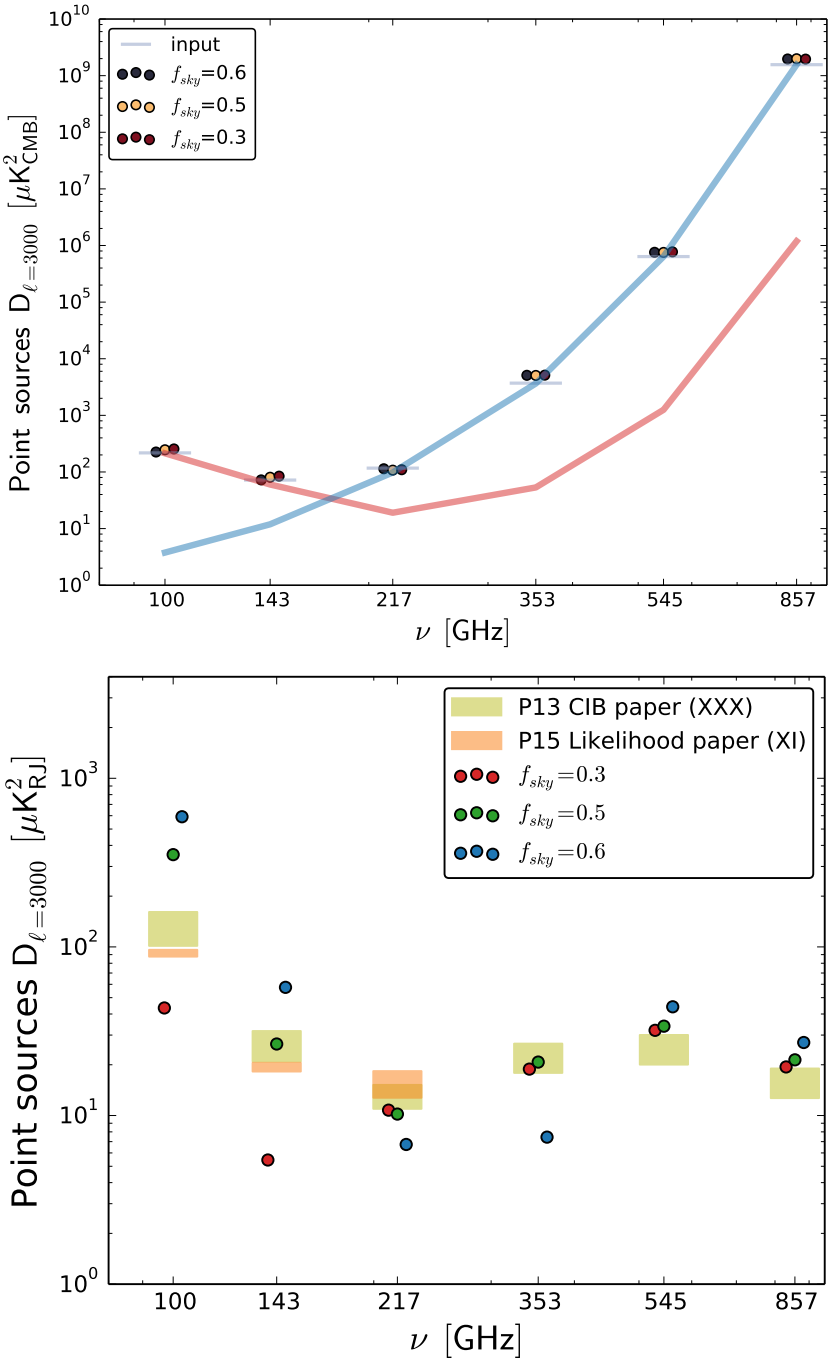

Figure 4.13 – Combined (infrared and radio) shot noise point sources D_ℓ power at $\ell = 3000$ obtained from the fit. *Top panel*: Average recovered point sources levels for SET3 simulations for the three different masks. The red and blue band show the simulations input for the radio and infrared point sources respectively, while the light-blue line represents the joint point source input. *Bottom panel*: Planck data recovered point sources for the three different masks of $f_{sky} = 0.6, 0.5, 0.3$ in blue, green and red respectively. The yellow and orange bands represent the expected shot noise point source contribution estimated in Planck Collaboration XXX et al. (2014) and Planck Collaboration XI et al. (2016), where the width of the coloured band represents the error on the expected value. Planck Collaboration XI et al. (2016) gives expected values for th three low ν channels only.

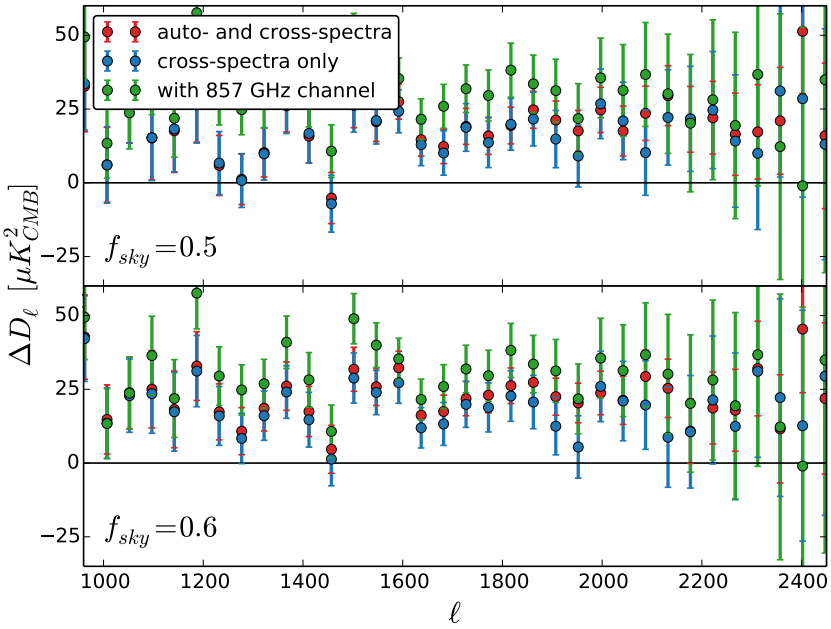

Figure 4.14 – Planck data recovered CMB angular power spectrum D_ℓ residuals with respect to Planck theoretical best fit spectrum for three different SMICA configurations. In blue we show the leading configuration of this thesis using cross-spectra of data splits, in red the one using cross- and auto-spectra are described in Sect. 4.5.4 and in green the results obtained including 857 GHz channel observations, as detailed in Sect. 4.5.3. Only one point every three bins is displayed. We show results for $f_{sky} = 0.5$ in the top panel and $f_{sky} = 0.6$ in the bottom panel.

prior on τ: this configuration in Planck Collaboration XI et al. (2016) is referred to as *PlikTT+tauprior*. For each case studied, we run Monte Carlo Markov Chains (MCMC) with CosmoMC (Lewis & Bridle, 2002a) in combination with PICO[4] (Fendt & Wandelt, 2007). We also cross-check some of our runs using CosmoMC with CAMB (Lewis & Bridle, 2002b), and using CosmoSlik (Millea, 2017) with PICO: we observe that results are consistent with those obtained using CosmoMC with PICO. For this reason, all the results presented in this analysis are obtained using the latter configuration.

4.6.1 The likelihood

We build our likelihoods from the best fit CMB spectra obtained from the SMICA fit for the different cases analysed. We use an idealised form for the likelihood, which considers no intermode correlations. This approximation should not strongly affect our results since we use bins of $\Delta\ell = 15$. The likelihood takes the form:

$$-\ln \mathcal{L}\Big(\hat{\mathbf{C}}|\mathbf{C}(\theta)\Big) = \frac{1}{2}\Big(\hat{\mathbf{C}} - \mathbf{C}(\theta)\Big)^T \, \mathbf{\Sigma}^{-1} \, \Big(\hat{\mathbf{C}} - \mathbf{C}(\theta)\Big) + c \tag{4.21}$$

where $\hat{\mathbf{C}}$ and $\mathbf{C}(\theta)$ are the $Q \times 1$, where Q is the number of bins, best fit and theoretical angular power spectra respectively, $\mathbf{\Sigma}$ is the $Q \times Q$ covariance matrix given by the SMICA

[4]available for download at https://github.com/marius311/pypico

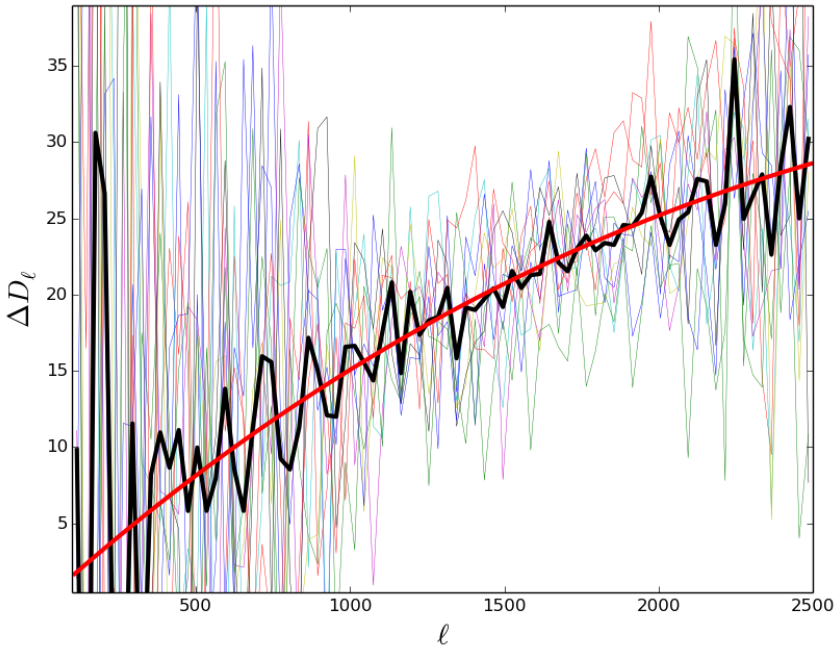

Figure 4.15 – Difference between the SMICA best fit and the input maps CMB angular power spectra for 10 SET3 simulations. The average of the differences is plotted in black, while the chosen template for the likelihood is plotted in red.

error bars on the best fit and c is a constant. The error bars are a statistical estimate derived from the Fisher matrix. They represent the cosmic variance, foregrounds, noise and mask contribution to the error budget, but do not include uncertainties on calibration and beams.

We explore a minimal ΛCDM model with two approximately massless neutrinos and one massive neutrino with $\sum_{m_\nu} = 0.06$ eV. We also use a Gaussian prior on the optical depth to reionization: for the MCMC on data we use $\tau = 0.07 \pm 0.02$, the same as in Planck analysis (Planck Collaboration XI et al., 2016), while for simulations we choose $\tau = 0.078 \pm 0.02$, since $\tau = 0.078$ corresponds to the input value of the simulated CMB maps.

There is a small amount of foreground residuals in the CMB spectra, as evident from Fig. 4.9. This residual has to be accounted for in the likelihood formulation with a nuisance model. Finding a shape for the foregrounds residuals is not trivial, since nuisance parameters can bias the cosmological parameters when incorrectly chosen. We opt for a physical modeling of the nuisance parameters based on our foreground knowledge. Paoletti et al. (2012) find that two terms for the shot noise and clustered contribution suffice to account for the background galaxies contribution. Also, we need to account for residuals of the galactic dust. We do not consider any term for the SZ residual contamination.

The *Planck Collaboration* derives cosmological parameters from the CMB maps, including the SMICA one (Planck Collaboration IX et al., 2016). The SMICA map cosmological parameters cannot be directly compared to this analysis parameters since the map-making procedure, which is based on the ILC weights of Eq. (2.25), can add some foreground contribution. Nevertheless, similarly to what it is done in this analysis on CMB maps, we use a nuisance model that comprises:

- a point source term with flat spectrum. Its amplitude is regulated by the parameter

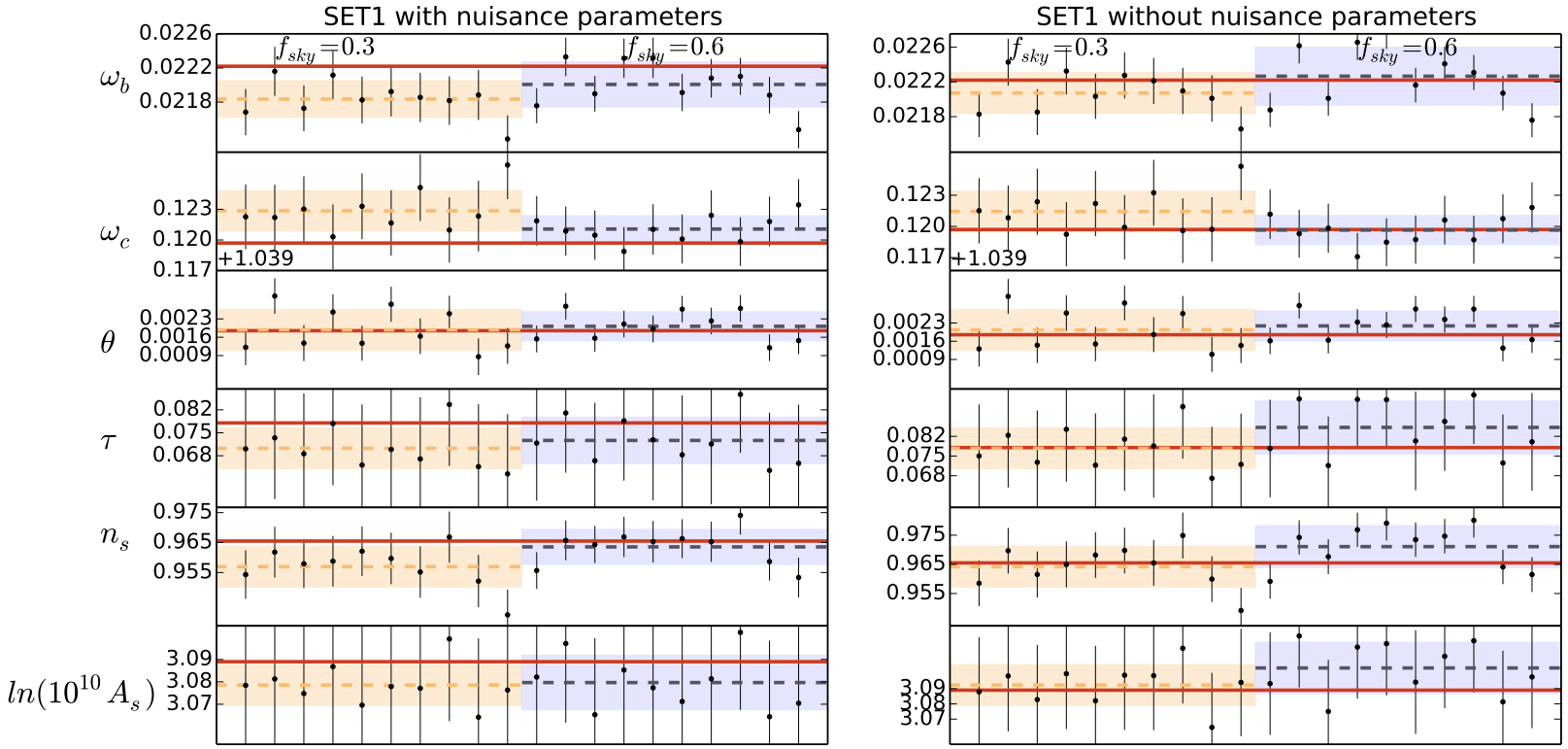

Figure 4.16 – Cosmological parameters for a subset of 10 simulation of SET1 with (left) and without (right) a model for nuisance parameters in the likelihood. Results are presented for f_{sky}=0.3 in yellow and f_{sky}=0.6 in blue. For each f_{sky}, the dashed line represents the average of the simulations marginal means and the shaded band represents the 1-σ scatter around this average. Each dot represents the marginal mean and 68% CL error bar of the parameters in a given simulation. The red line shows the input parameters of the theoretical C_ℓ used for simulations.

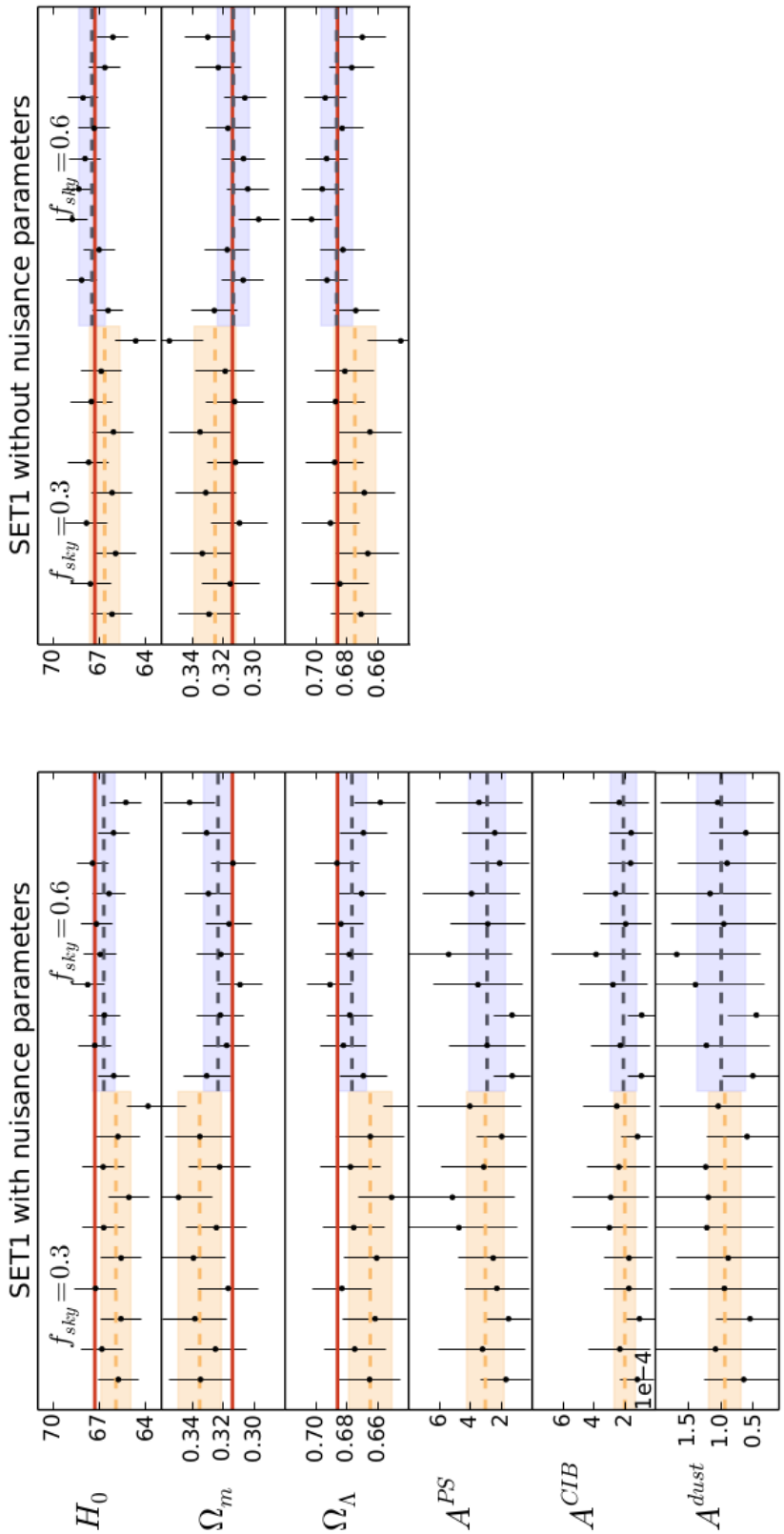

Figure 4.17 – Derived and nuisance parameters for a subset of 10 simulation of SET1 with (left) and without (right) a model for nuisance parameters in the likelihood. Results are presented for f_{sky}=0.3 in yellow and f_{sky}=0.6 in blue. For each f_{sky}, the dashed line represents the average of the simulations marginal means and the shaded band represents the 1-σ scatter around this average. Each dot represents the marginal mean and 68% CL error bar of the parameters in a given simulation. The red line shows the input parameters of the theoretical C_ℓ used for simulations.

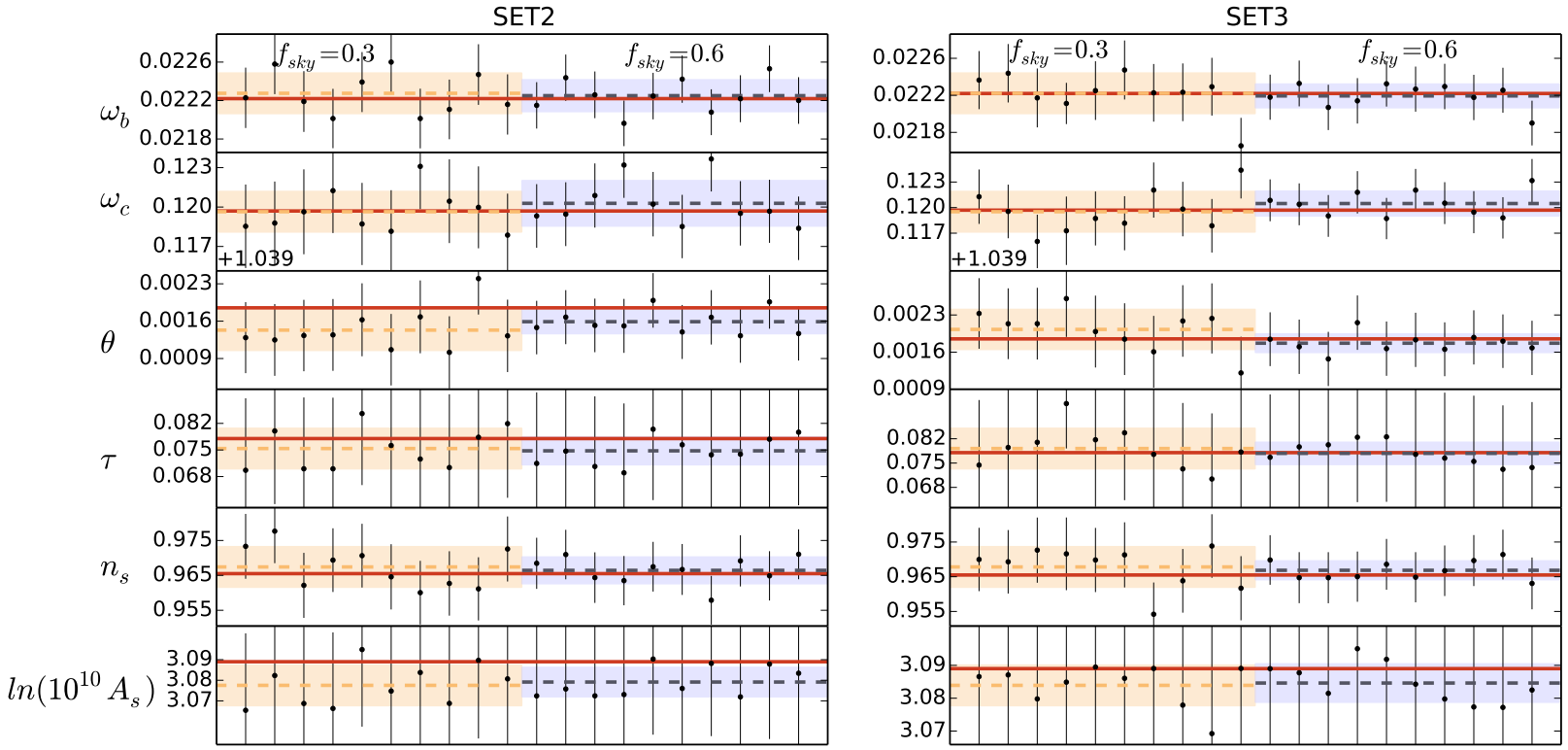

Figure 4.18 – Cosmological parameters for a subset of 10 simulation of SET2 (left) and SET3 (right). Results are presented for f_{sky}=0.3 in yellow and f_{sky}=0.6 in blue. For each f_{sky}, the dashed line represents the average of the simulations marginal means and the shaded band represents the 1-σ scatter around this average. Each dot represents the marginal mean and 68% CL error bar of the parameters in a given simulation. The red line shows the input parameters of the theoretical C_ℓ used for simulations.

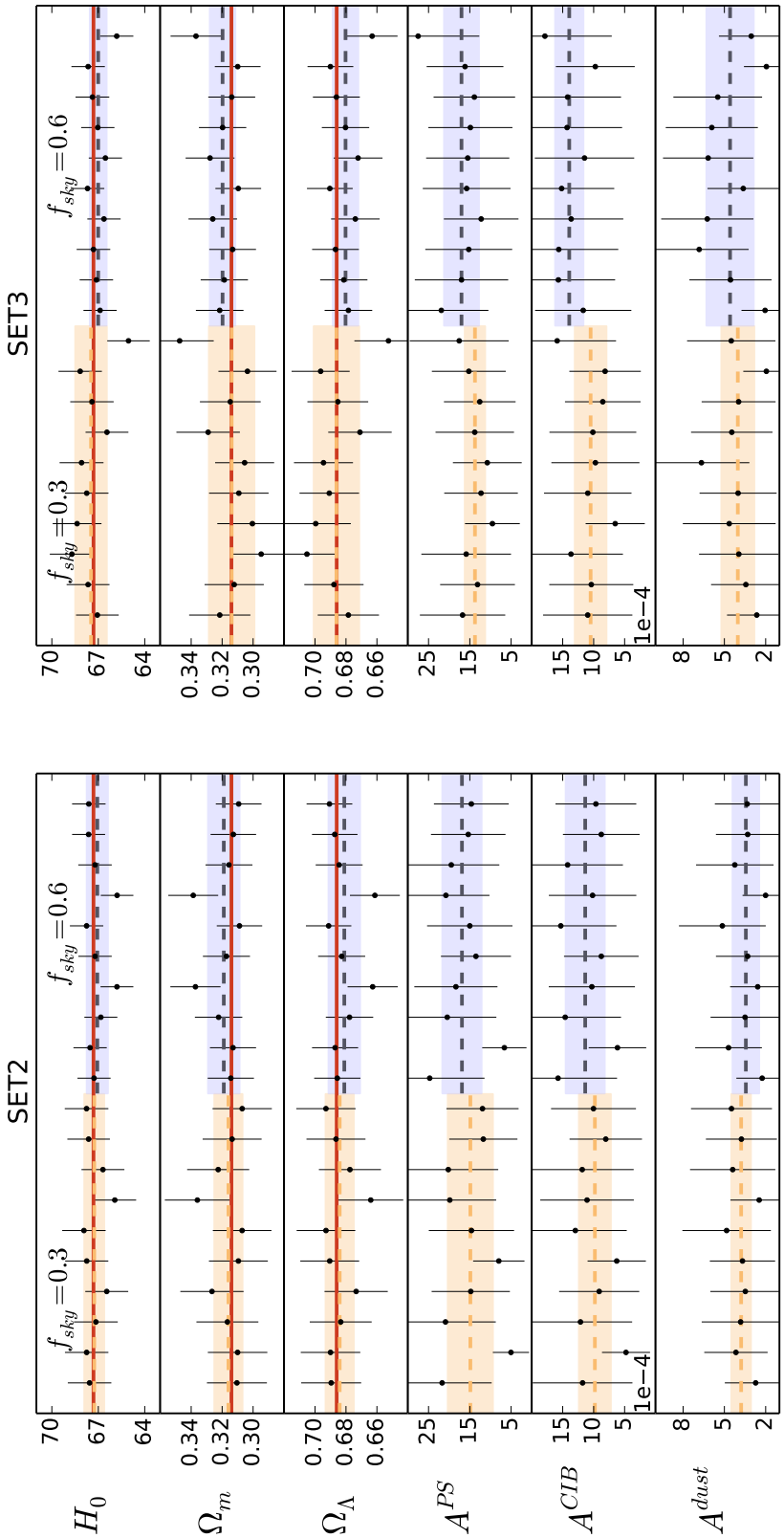

Figure 4.19 – Derived and nuisance parameters for a subset of 10 simulation of SET2 (left) and SET3 (right). Results are presented for f_{sky}=0.3 in yellow and f_{sky}=0.6 in blue. For each f_{sky}, the dashed line represents the average of the simulations marginal means and the shaded band represents the 1-σ scatter around this average. Each dot represents the marginal mean and 68% CL error bar of the parameters in a given simulation. The red line shows the input parameters of the theoretical C_ℓ used for simulations.

Parameter	Prior range	Planck 2015
$\omega_{\rm b}h^2$	$[0.005, 0.1]$	0.02221 ± 0.00023
$\omega_{\rm c}h^2$	$[0.001, 0.99]$	0.1208 ± 0.0022
$100\theta_{MC}$	$[0.5, 10.0]$	1.04182 ± 0.00048
$\ln(10^{10}A_{\rm s})$	$[2, 4]$	3.107 ± 0.035
$n_{\rm s}$	$[0.8, 1.2]$	0.9612 ± 0.0062
τ	$[0.01, 0.8]$ (0.07 ± 0.02)	0.085 ± 0.018
A^{PS}	$[0, 100]$	–
A^{CIB}	$[0, 100]$	–
A^{dust}	$[0, 1]$	–
H_0	–	66.85 ± 0.98
$\Omega_{\rm m}$	–	0.322 ± 0.014
Ω_Λ	–	0.678 ± 0.014

Table 4.3 – Prior ranges for cosmological parameters and results of the reference MCMC exploration with Planck high-ℓ likelihood. Uniform priors are in square brackets, while Gaussian priors are in parenthesis. Constraints on parameters are given as marginal mean with 68% CL error on: main parameters (top), nuisance parameters (middle) and derived parameters (bottom).

A^{PS}, which corresponds to the point sources contribution for $D_{\ell=3000}$;

- a clustered CIB term with a spectrum $\ell^{n_{CIB}}$. We fix n_{CIB} = -1.3 for most explorations, unless otherwise stated. The amplitude A^{CIB} represents the CIB contribution for $D_{\ell=3000}$;

- a dust term with an angular power spectrum $\ell^{-2.6}$. The nuisance parameter A^{dust} is defined as the emission for $C_{\ell=500}$.

We also add a total calibration parameter y_{cal}. Similarly to what it is done in the Planck analysis (Planck Collaboration XI et al., 2016), in the Planck baseline configuration the calibration parameter is explored with a Gaussian prior $y_{cal} = 1 \pm 0.0025$. We observe that our results on data are insensitive to calibration, thus we choose to keep it fixed to 1. The physical nuisance model is our reference configuration. In a subset of cases we also test using a smaller number of nuisance parameters, as well as the use of a single template derived from simulations. The template is based on the shape of the average foreground residuals in SET3 simulations at the largest f_{sky}, i.e., the case with the strongest residual contamination in the CMB spectrum. Its shape does not represent any particular foreground contamination, however is very close to the clustered CIB theoretical shape, meaning that this is the major contribution that we expect in the residuals according to simulations. Fig. 4.15 shows the difference between the best fit CMB spectrum and the spectrum of the input CMB map for 10 SET3 simulations. The input maps are unmasked, thus the low-ℓ scatter is largely driven by cosmic variance. From these we compute the average residuals and fit a shape for the template. We use this template as a unique nuisance component in the likelihood exploration, only changing its amplitude.

Parameter	Like-F03	Like-F05	Like-F06
$\omega_{\rm b}h^2$	0.02174 ± 0.00030	0.02225 ± 0.00027	0.02230 ± 0.00025
$\omega_{\rm c}h^2$	0.1210 ± 0.0033	0.1204 ± 0.0027	0.1189 ± 0.0025
$100\theta_{MC}$	1.04088 ± 0.00071	1.04082 ± 0.00057	1.04074 ± 0.00053
$\ln(10^{10}A_{\rm s})$	3.066 ± 0.037	3.072 ± 0.039	3.082 ± 0.037
$n_{\rm s}$	0.9548 ± 0.0089	0.9639 ± 0.0081	0.9704 ± 0.0073
τ	0.068 ± 0.019	0.075 ± 0.019	0.079 ± 0.019
A^{PS}	3.9 ± 3.4	15 ± 11	7.0 ± 5.6
A^{CIB}	2.8 ± 2.4	1341 ± 8.6	5.7 ± 4.3
A^{dust}	0.00013 ± 0.00011	0.0052 ± 0.00032	0.00031 ± 0.00020
H_0	66.5 ± 1.4	67.1 ± 1.2	67.6 ± 1.1
$\Omega_{\rm m}$	0.325 ± 0.021	0.318 ± 0.017	0.311 ± 0.015
Ω_Λ	0.675 ± 0.021	0.681 ± 0.017	0.690 ± 0.015

Table 4.4 – Results of the MCMC exploration on Planck 2015 data with the three considered likelihoods: Like-F03, Like-F05 and Like-F06. Constraints on parameters are given as marginal mean with 68% CL error on: main parameters (top), nuisance parameters (middle) and derived parameters (bottom).

4.6.2 Cosmological parameters from simulations

We explore cosmological parameters for the first 10 simulations of each set. For these simulations, we obtain parameters for both the largest and the smallest masks, to check for effects that depend on retained sky fraction. For each simulation and sky fraction, we use the best fit CMB angular power spectrum of SMICA to build a likelihood as described in the previous Section. The main analysis is done using the physical parametrization of the nuisance model. The list of all parameters and their prior ranges is detailed in the first column of Table 4.3. Cosmological parameters are presented in Figures 4.16 and 4.17 for SET1 and Figures 4.18 and 4.19 for SET2 and SET3, where the red line shows simulation inputs and the wide colored band shows 1σ scatter of the marginal mean values.
The shape of the SET1 simulations are those that best recover the input CMB power spectrum in the SMICA fit, thus we expect their residual foreground content to be very low. We test SET1 simulations in two different configurations, letting the nuisance parameters free and setting all of them to zero, i.e., not accounting for any residuals in the likelihood exploration. As shown in the right panel of Figure 4.16, the MCMC exploration with nuisance parameters shows evident biases with both masks. As a cross-test, we obtain cosmological parameters from theoretical spectra to which we add some scatter according to the expected cosmic variance. In this case the average parameters obtained coincide with the input, meaning that the shift we observe in Figure 4.16 are due to foreground residuals and not to mistakes in the pipeline.
There is a degeneracy between the shape of the foreground residuals and the cosmological parameters, and a wrong estimation of the nuisance parameters can induce biases. In particular, when we have a low f_{sky}, the error bars are larger and we can more easily mix up the CMB and the foregrounds. This is evident in Figure 4.16, which shows how most biases are strongly reduced when nuisance parameters are removed, especially for $f_{sky} = 0.3$, where we expect to have the lowest, and thus most degenerate, residuals. Due to the

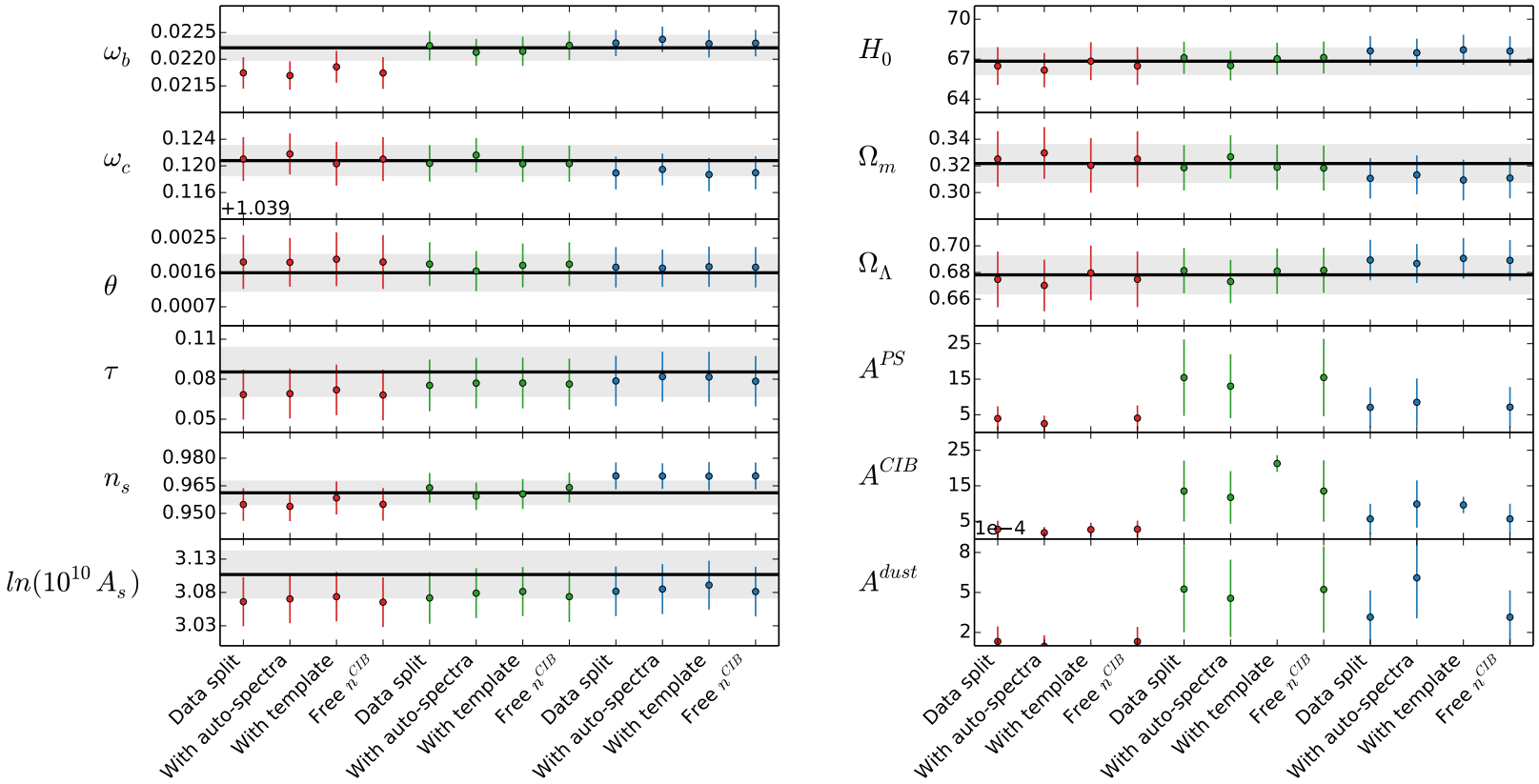

Figure 4.20 – Marginal mean and 68% CL error bars for cosmological parameters obtained on Planck 2015 data with Like-F03 in red, Like-F05 in green and Like-F06 in blue. For comparison, Planck 2015 high-ℓ temperature likelihood results are shown in background, with the marginal mean drawn in black and 68% CL as a grey band. On the left we show the six standard ΛCDM cosmological parameters and on the right some derived and nuisance parameters. Nuisance parameters show no Planck comparison since they are specific to the likelihood. The values of nuisance parameters are in units of μK^2.

low level of residuals in the CMB spectra, the nuisance parameters are not well estimated and are in most cases compatible with zero. A level of residuals is present in the data, but since this is not well determined, it is not correctly accounted for. For SET2 and SET3 simulations we obtain less biased results: in Fig. 4.18 we can see that biases of parameters are less evident, especially for the SET3 case. In this case we did not run the nuisance-free likelihood since the level of foreground residuals is too high to justify such a test. Since the level of residuals in these simulations is higher than in SET1, it is better constrained in the parameters exploration. We observe very small changes with sky fraction, the most relevant one being the decrease in size of the 1σ scatter band with increasing f_{sky}, as expected. We note that marginal errors on τ and A_s for individual simulations are quite large, while the scatter of the mean is not: this is not surprising since the marginal error on τ, and consequently on A_s, is regulated by the Gaussian prior $\tau = (0.07 \pm 0.02)$ we impose.
Since the nuisance parameters are not well constrained, a model for the residuals with less parameters could in principle reduce the uncertainty in the exploration. For the SET3 case only we test the template configuration of the likelihood described in the previous Section. In this configuration only one nuisance parameter is fitted, which is the amplitude of the template. In terms of biases, the results are equivalent to those obtained with the physical nuisance model. The only relevant change is that the discrepancy on A_s is reduced, while that on ω_b is increased. This suggests that the average foreground contamination represented by the template does not fully describe the details of the residuals in each CMB spectrum of simulations, and that the details of foreground modelling in the likelihood are important for accurate estimation of cosmological parameters.

4.6.3 Cosmological parameters from Planck data

We build a likelihood for each mask from best fit spectra obtained from the analysis detailed in Sect. 4.5.2. We call these three likelihoods Like-F03, Like-F05 and Like-F06, where FX refers to the f_{sky} of the mask used. We run a MCMC exploration with Planck high-ℓ temperature likelihood and compare the results with the Planck published ones. We find good agreement between these two runs of the Planck likelihood, meaning that our configuration is the same as that used for the Planck analysis.
We give results for our three likelihoods and compare them to the Planck likelihood run. In Table 4.3 we list the parameters used in the cosmological exploration and their priors. The respective values for the Planck likelihood can be found in Planck Collaboration XI et al. (2016), where Table 17 lists the cosmological parameters and Table 10 the nuisance parameters. We note that a Gaussian prior is imposed on the absolute map calibration for Planck likelihood $y_{cal} = 1 \pm 0.0025$, while we keep this value fixed to $y_{cal} = 1$ for explorations of Like-FX. We adopt this choice after testing that including this parameter in the explorations does not affect the results.
We plot a comparison of the cosmological parameters estimated in Fig 4.20, while the full list including derived parameters can be found in Table 4.3. Shifts of cosmological parameters in units of 1-σ Planck error bars are presented in Table 4.5: for most parameters we observe a progressive shift increasing with the retained sky fraction, the most evident case being for n_s. On the whole, parameters show at most 1-σ deviation with respect to the Planck analysis, with the only exception of ω_b for $f_{sky} = 0.3$, which shows a deviation of -2.04-σ, and n_s for $f_{sky} = 0.6$, which shows a deviation of 1.48-σ. We caution the

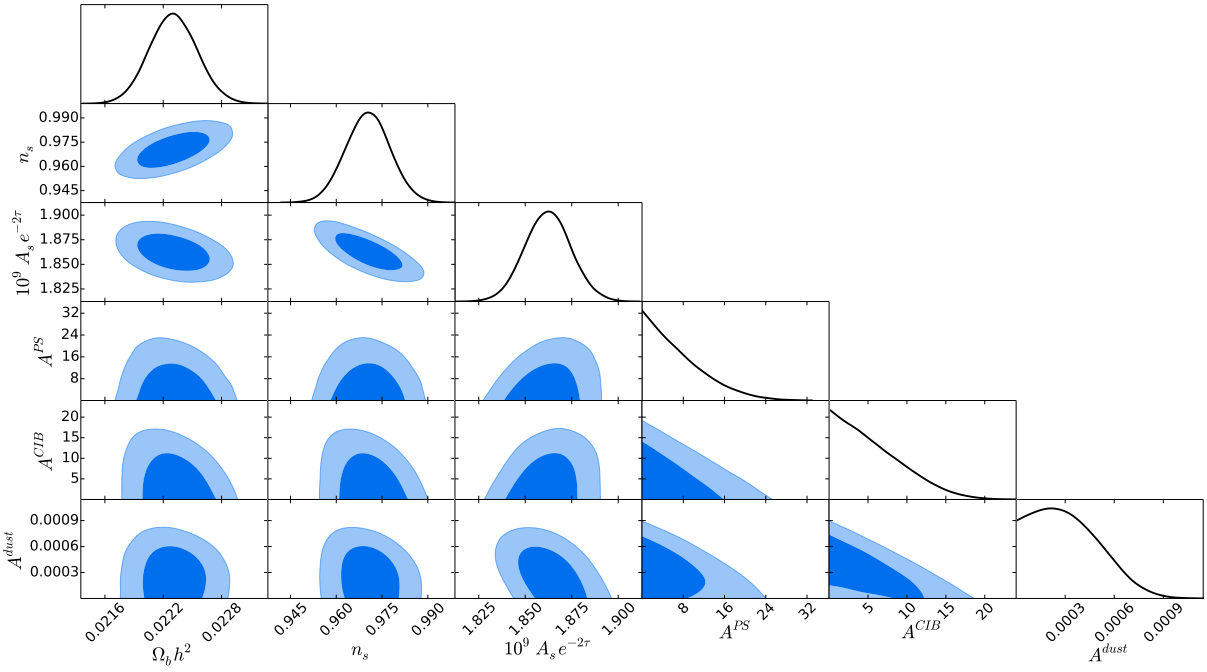

Figure 4.21 – Triangle plot showing the relation between the main cosmological parameters and the nuisance parameters, for the analysis on Planck data with $f_{sky} = 0.6$. Similar plots are obtained for SET3 simulations and for different f_{sky}. The blue and light-blue contours represent the 68% and 95% CL respectively.

reader on the fact that Planck results are obtained for one fixed sky fraction while we use three different sky fractions, thus the available data on which cosmological parameters are computed is different.

At low f_{sky} the residuals are weak and not clearly constrained by the nuisance model. As seen in simulations, there is an uncertainty in the value of the nuisance parameters that induces a shift in the cosmological parameters. In Figure 4.21 we can see that nuisance parameters are consistent with zero and are also strongly degenerate among them. Some degeneracies are also visible with the cosmological parameters, as for example between $A_s e^{-2\tau}$ and A^{dust}. Due to the strong correlation between all cosmological parameters, these degeneracies can induce biases. Also, as noted by Huffenberger et al. (2006), the parameter n_s is particularly sensitive to incorrect subtraction of the point source component. The biases we obtain are representative of the uncertainty on the determination of the foreground model.

The results of the analysis using a template are also shown in Fig. 4.20. The template amplitude is show in the A^{CIB} column since the template shape is very close to that of the CIB term in the nuisance physical model. This configuration performs slightly better, especially at low f_{sky}, reducing the biases on n_s and ω_b. No significant improvement is seen however at high f_{sky}. The more, the total foreground power detected by the template is lower at $f_{sky} = 0.6$ than at $f_{sky} = 0.5$. This is an indication that for high sky fraction the template is not representative anymore of the residual contamination in the CMB spectrum. This is partially true also for the physical nuisance model, meaning that the residuals at large sky fraction are not well represented by neither model.

It is important to note that the biases observed on the data analysis are different from

Table 4.5 – Shift of parameters between the three Planck data likelihoods Like-F03, Like-F05 and Like-F06 and the Planck high-ℓ likelihood results in units of 1-σ Planck errors.

Parameter	Like-F03	Like-F05	Like-F06
$\omega_{\rm b}h^2$	-2.04	0.17	0.39
$\omega_{\rm c}h^2$	0.11	-0.19	-0.84
$100\theta_{MC}$	0.59	0.48	0.30
τ	-0.93	-0.55	-0.37
$n_{\rm s}$	-1.02	0.43	1.48
$\log(10^{10}A_{\rm s})$	-1.17	-1.00	-0.72
H_0	-0.37	0.26	0.79
$\Omega_{\rm m}$	0.24	-0.23	-0.79
Ω_Λ	-0.24	0.23	0.79

those observed on simulations. This suggests that the foreground complexity is not well represented by our simulations and that the nuisance model strongly depends on the details of the foreground contamination.

4.6.4 Cross-tests on data

Results presented in Tables 4.3, 4.4, 4.5 refer to the main exploration detailed above. As a cross-check we present in Fig. 4.20 results of two different configurations. The first uses best fit CMB spectra as obtained from Sect. 4.5.4, that is using both auto- and cross-spectra to build covariance matrices. The second adds as nuisance parameter the CIB index which defines the angular power spectrum shape of the CIB residuals as $\ell^{n^{CIB}}$. This parameter is varied with a Gaussian prior $n^{CIB} = -1.3 \pm 0.2$. We observe no relevant shift in the obtained cosmological parameters from this two additional configurations.
We also obtain parameters from the best fit obtained using the 857 GHz channel as described in Sect. 4.5.3. We run MCMC for $f_{sky} = 0.6$ on SET3 simulations and obtain cosmological parameters which are consistent with those shown in Fig. 4.18 within maximum 0.022σ (σ here is the scatter of the marginal mean among various simulations). Instead, on the Planck data analysis, cosmological parameters are more strongly biased than those obtained without the 857 GHz channel, in particular n_s and ω_b. While the increase in foreground residuals in the spectrum is modest, we expect their characteristics to be quite complex and not adjustable by the minimal nuisance model we use.

4.6.5 Conclusions

We developed a method that, by using data splits, diminishes the SMICA sensitivity to noise. By using a dedicated model, we recover the joint emission law of point sources, which are a relevant contamination for the small scales of the CMB angular power spectrum. With this method we recover a CMB foreground-cleaned angular power spectrum that we can use for cosmological parameter estimation. Due to the limitations of the SMICA model to represent the foregrounds complexity, in particular the thermal dust and the CIB contaminations, a level of foreground residuals is still present in the data. These residuals, if not accounted for in the cosmological exploration, can bias the cosmological parameters.

We address them with two different parametrizations, a physical one and an empirical one. In both cases the foreground model is not able to represent the residuals, also because they are very low and it is difficult to constrain them. The level of biases that we observe on the simulations shows us the level of bias to expect on the real data.
In order to tackle the residual level, the dust and clustered CIB contributions need to be better characterized. A model that fits the foregrounds at different scales depending on the frequency could be a potential solution. Also, exploiting the anisotropy of the galaxy with respect to the isotropy of the CIB by performing the fit in different zones of the sky for different components could help to better determine these two foreground emissions.

Chapter 5

Testing Induced Gravity

Contents

Modified theories of Gravity, also called Modified Gravity, have recently emerged as one major field of research, based on the idea that General Relativity is not the correct theory to describe the gravitational interaction. These theories represent an observational challenge, since it is hard to find observables that can differentiate between a modification of gravity and General Relativity, but may also represent a key to see the problems of cosmology in a different framework with respect to the standard ΛCDM model.
In this framework, the CMB is a very important cosmological observable to test Modified Gravity theories, and the determination of cosmological parameters via different methodologies is essential in order to asses robustness of our estimations. In this respect, the work presented in the previous Chapter, in which cosmological parameters are obtained via a component separation technique rather than using the standard Planck likelihood approach, is a first step towards in this direction. This Chapter instead is devoted to showing a possible exploitation of such work, by analysing a specific cosmological model.

Due to the fact that the CMB reconstruction presented in the previous Chapter still presents some issues related to foreground residuals, the cosmological analysis of this Chapter is based on the Planck Collaboration likelihoods.
In this Chapter I present a model called Induced Gravity, in which the observed accelerated expansion of the universe is driven by a scalar potential coupled to the metric. The evolution of the scalar field is regulated by a single parameter γ, which can be constrained observationally. The results presented in this Chapter are resumed in (Umiltà et al., 2015) and (Ballardini et al., 2016). For a more detailed description of Induced Gravity and the code that is used in the analysis, which was partially developed during my PhD, see (Umiltà, 2014). This Chapter is self-consistent and can be read separately from the rest of the manuscript, however the reader is invited to check the introduction to the Standard Cosmological model given in Section 1.1.

5.1 Modified theories of Gravity

General Relativity (GR) is recognized as the standard theory of gravitation. Proposed in 1915, it has proven very successful in explaining different astrophysical phenomena, from the shift in Mercury's perihelion to the deflection of light rays passing near a massive object. The field equations of General Relativity are:

$$R_{\alpha\beta} - \frac{1}{2} g_{\alpha\beta} R = 8\pi G \, T_{\alpha\beta}, \tag{5.1}$$

where G is Newton's constant, $T_{\alpha\beta}$ is the energy-momentum tensor of the source producing the gravitational field, $g_{\alpha\beta}$ is the metric tensor, $R_{\alpha\beta}$ the Ricci tensor and R, the Ricci scalar or scalar curvature, is the contraction of the former two. In this equation the left hand side defines the geometry of space-time, the right hand side instead defines the matter content of the space-time.
The discovery of the accelerated expansion of the universe has imposed a change in the reference cosmological model, since Eq. (5.1) as it is cannot describe an accelerated expansion of the universe. This problem has been solved by adding an extra term $\Lambda g_{\alpha\beta}$ that produces such expansion, where Λ is called cosmological constant. The cosmological constant is equivalent to a dark energy fluid of constant equation of state $\omega_{DE} = -1$. The nature of dark energy is yet unknown, and the simplest model describes it as a component of constant energy density. The resulting cosmological model is called the ΛCDM model. However, this is not the only possible explanation, and approaches that consider alternative theories to describe the gravitation have been developed. Since GR has proven successful to explain observations in the solar system, any novel theory needs to behave as GR on these scales, while on large scales it should reproduce the observed acceleration.
The class of theories alternative to GR is named Modified Gravity (MG). The name "Modified Gravity" is a slight abuse of terminology, since there is no such thing as a modification of gravity, what exists is gravitation and our theory to describe it. Thus Modified Gravity is a modification with respect to the reference theory which is General Relativity. This class of alternative theories has become now popular under the name of Modified Gravity, so we adapt to this terminology. Within MG theories, scalar-tensor theories extend GR by adding a scalar field σ non minimally coupled to the Ricci scalar R. In this formulation, the scalar field does not couple to matter, and it interacts only

with the metric tensor field. Through this interaction, the scalar field mediates the way all sources of matter generate the gravitational potentials. The generic action S for this formulation of theories of scalar-tensor is (Gannouji et al., 2006):

$$S = \int d^4x\sqrt{-g}\left[F(\sigma)R - Z(\sigma)g^{\mu\nu}\partial_\mu\sigma\partial_\nu\sigma - V(\sigma) + \mathcal{L}_m\right], \tag{5.2}$$

where $g^{\mu\nu}$ is the metric, $\mathcal{L}_m$ the Lagrangian of matter, $F(\sigma)$ and $Z(\sigma)$ two functions of the scalar field σ which influence the dynamics of the field, and $V(\sigma)$ its potential. The Lagrangian $\mathcal{L}_m$ is decoupled from the field σ, so its action depends only on the metric $g_{\mu\nu}$.

5.2 Induced Gravity theory

Induced Gravity (IG) is a scalar tensor theory obtained from the above expression by setting $F(\sigma) \equiv \frac{\gamma\sigma^2}{2}$ and $Z(\sigma) \equiv \frac{1}{2}$. The parameter γ is an adimensional parameter of the theory. The resulting action becomes:

$$S = \int d^4x\sqrt{-g}\left[\frac{\gamma\sigma^2 R}{2} - \frac{1}{2}g^{\mu\nu}\partial_\mu\sigma\partial_\nu\sigma - V(\sigma) + \mathcal{L}_m\right], \tag{5.3}$$

The Friedmann equations for the Induced Gravity model in conformal time and for a flat geometry of the universe become:

$$H^2 = \frac{\sum_i \rho_i + V(\sigma)}{3\gamma\sigma^2} + \frac{\sigma'^2}{6a^2\gamma\sigma^2} - \frac{2H\sigma'}{a\sigma}, \tag{5.4a}$$

$$H' = -\frac{\sum_i(\rho_i + P_i)a}{2\gamma\sigma^2} - \frac{\sigma'^2}{2a\gamma\sigma^2} + \frac{H\sigma'}{\sigma} - \frac{\sigma''}{a\sigma} - \frac{\sigma'^2}{2a\gamma\sigma^2}, \tag{5.4b}$$

and the field equation for σ:

$$\sigma'' = -2aH\sigma' - \frac{\sigma'^2}{\sigma} + \frac{\sum_i(\rho_i - 3P_i)a^2}{(1+6\gamma)\cdot\sigma} - \frac{4V}{\sigma} + V_{,\sigma}, \tag{5.5}$$

where a prime denotes a derivation with respect to conformal time τ[1], $V_{,\sigma}$ denotes the derivative of the potential $V(\sigma)$ with respect to σ, and the index i runs over all fluid components. The ΛCDM model is recovered from the Induced Gravity model in the limit $\gamma \to 0$. The parameter γ is the only free parameter of this theory. The left panel of Figure 5.1 shows the evolution of the scalar field in time: the scalar field does not change in the radiation epoch, and starts to move at matter radiation equality. The right panel of Figure 5.1 shows the density contrasts for the ΛCDM model and the IG model for different values of the parameter γ. One can see that for smaller values of γ IG approaches ΛCDM: the cosmological background dynamics is shown to be consistent with observations for $\gamma \lesssim 10^{-2}$ (Finelli et al., 2008).

The present value of the field σ_0 can be connected to the gravitational constant G_N measured in laboratory Cavendish-type and solar system experiments by the relation:

$$\gamma\sigma_0^2 = \frac{1}{8\pi G_N}\frac{1+8\gamma}{1+6\gamma}. \tag{5.6}$$

The scalar field regulates the value of Newton's constant in time: the quantity $\dot{G}_N/G_N$, which is strictly zero in GR, is non-zero in IG and its evolution depends on γ and on the shape of the potential $V(\sigma)$.

[1]Conformal time relates to cosmic time through the relation $d\tau = dt/a$

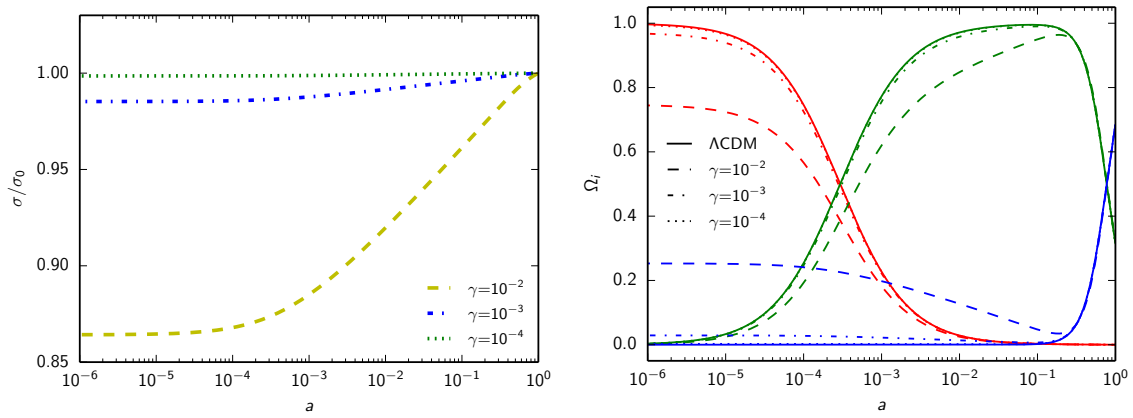

Figure 5.1 – *Left panel*: evolution of σ/σ_0. *Right panel* : evolution of the density contrasts of radiation in red - $\Omega_{\rm R} \equiv (\rho_\nu + \rho_\gamma)/(3\gamma\sigma_0^2 H^2)$ -, matter in green - $\Omega_{\rm M} \equiv (\rho_b + \rho_{\rm CDM})/(3\gamma\sigma_0^2 H^2)$ - and effective dark energy in blue - $\Omega_{\rm DE} \equiv \rho_{\rm DE}/(3\gamma\sigma_0^2 H^2)$ - together with their ΛCDM counterparts for different choices of γ.

5.2.1 The potential V(σ)

The choice of the potential is crucial, since the evolution of the scalar field depends on the form of the potential. In particular, the potential term can drive the universe into acceleration at recent times. We consider a power law form of potential as (Finelli et al., 2008):

$$V(\sigma) = \frac{\lambda\sigma^4}{4} \tag{5.7}$$

where λ is a dimensionless parameter whose value is determined by imposing a flat geometry of the universe $\Omega_k = 0$. A different possibility is to parametrize the form of the potential with an index n_{IG}, which becomes an additional parameter of the theory:

$$V(\sigma) = \lambda_n \sigma^{n_{IG}}. \tag{5.8}$$

This possibility is explored in Ballardini et al. (2016). The CMB is quite insensitive to changes in n_{IG}, while some difference is observed in the matter power spectrum, as seen from Figure 5.3. Thus a possible way of constraining n_{IG} is through large scale structure data.

5.2.2 The evolution of cosmological fluctuations

For describing scalar perturbations, different gauge choices are possible. In the Newtonian or "longitudinal" gauge the line element of the metric can be parametrized as $ds^2 = a^2(\tau)[-(1+2\Psi)d\tau^2 + (1-2\Phi)\delta_{ij}dx_i dx_j]$, where Ψ and Φ are the Newtonian scalar potentials (Ma & Bertschinger, 1994). The perturbed Einstein equations for IG with a quartic potential

in the longitudinal gauge are:

$$3H(\dot{\Phi}+H\Psi)+\frac{k^2}{a^2}\Phi+3\frac{\dot{\sigma}}{\sigma}(\dot{\Phi}+2H\Psi)-\frac{\dot{\sigma}^2}{2\gamma\sigma^2}\Psi= \\ -\frac{1}{2\gamma\sigma^2}\Big[3\dot{\sigma}\,\delta\dot{\sigma}-6H^2\gamma\sigma\,\delta\sigma-6H\gamma(\dot{\sigma}\,\delta\sigma+\sigma\,\dot{\delta\sigma})-\frac{2\gamma k^2}{a^2}\delta\sigma+\sum_i\delta\rho_i+\lambda\sigma^3\delta\sigma\Big], \tag{5.9a}$$

$$\dot{\Phi}+\Psi\Big(H+\frac{\dot{\sigma}}{\sigma}\Big)=\frac{a}{2k^2}\frac{\sum_i(\rho_i+p_i)\theta_i}{\gamma\sigma^2}+\frac{\delta\sigma}{\sigma}\Big[\Big(1+\frac{1}{2\gamma}\Big)\frac{\dot{\sigma}}{\sigma}-H\Big]+\frac{\delta\dot{\sigma}}{\sigma}, \tag{5.9b}$$

$$\Phi-\Psi=\frac{2\delta\sigma}{\sigma}+\frac{3a^2}{2k^2}\frac{\sum_i(\rho_i+p_i)\bar{\sigma}_i}{\gamma\sigma^2}\,. \tag{5.9c}$$

In the above $\rho_i\,, p_i$ $(\delta\rho_i\,, \delta p_i)$ denote the energy and (longitudinal) pressure density perturbations for each matter component, respectively. The velocity potential and the anisotropic stress are denoted by θ_i and $\bar{\sigma}_i$. We refer to Ma & Bertschinger (1994) for the equations of the CDM, baryons, photons and neutrino energy-momentum tensors, since these equations are unchanged from those in Einstein gravity.
The field equation for σ at linear order in the longitudinal gauge is:

$$\ddot{\delta\sigma}+\dot{\delta\sigma}\Big(3H+2\frac{\dot{\sigma}}{\sigma}\Big)+\Big[\frac{k^2}{a^2}-\frac{\dot{\sigma}^2}{\sigma^2}+\frac{\sum_i(\rho_i-3p_i)}{(1+6\gamma)\sigma^2}\Big]\delta\sigma \\ =\frac{2\Psi\sum_i(\rho_i-3p_i)}{(1+6\gamma)\sigma}+\frac{\sum_i(\delta\rho_i-3\delta p_i)}{(1+6\gamma)\sigma}+\dot{\sigma}\Big(3\dot{\Phi}+\dot{\Psi}\Big) \tag{5.10}$$

It is interesting to note that the equation for the field fluctuation does not depend explicitly on the potential in the case of a quartic potential, as for the background in Eq. (5.5).

5.2.3 Brans-Dicke theory

In the framework of scalar tensor theories, the Brans-Dicke model (Brans & Dicke, 1961) was the first to be introduced. It is sometimes referred to as Jordan-Brans-Dicke (JBD) for the work that P. Jordan brought on independently (Jordan, 1955). The JBD model can be recovered as a special case of Induced Gravity by setting the potential to zero and substituting:

$$\gamma=\frac{1}{4\omega_{JBD}}, \qquad \gamma\sigma^2=\frac{\phi}{8\pi}, \tag{5.11}$$

where ϕ is a redefinition of the scalar field in the JBD theory and ω_{JBD} is an adimensional parameter of the theory. In the JBD model, General Relativity is recovered in the limit $\omega_{JBD}\to\infty$. Translating constraints from JBD to IG cannot be done by simply inverting Eq. (5.11), since, contrary to IG, JBD assumes a vanishing potential for the scalar field.

5.3 Quantifying the departure from GR

Distinguishing between dark energy and modified gravity at the observational level is not easy, since none of them can be observed directly. It is important to define a set of observables which can discriminate between the different models. Modified theories

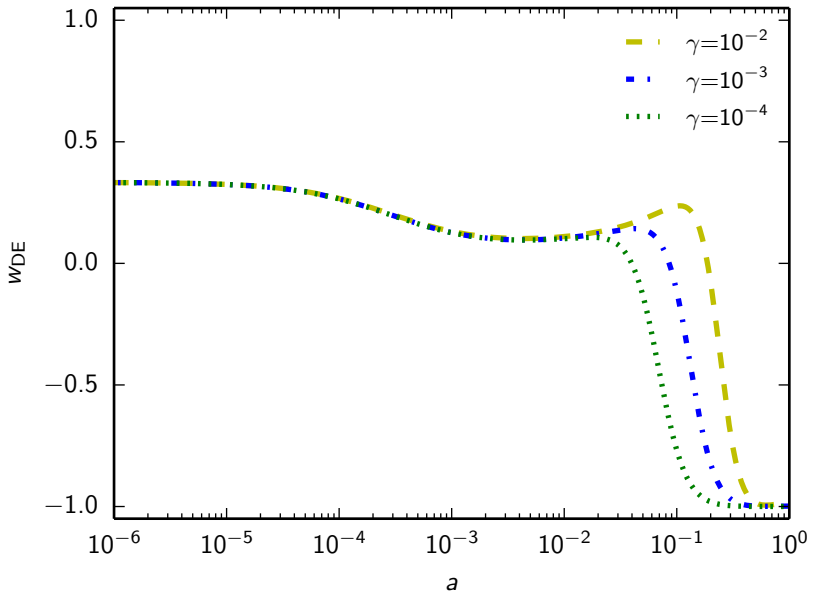

Figure 5.2 – Evolution of $\omega_{\rm DE}$ as function of $\ln(a)$ for different choices of γ.

of Gravitation have an expected effect on large scales, thus data on the growth rate of structures (Huterer & Linder, 2007) or weak lensing measurements (Kunz & Sapone, 2007), the CMB angular power spectra and the matter power spectrum are good observational tests.

5.3.1 The equation of state ω_{DE}

If dark energy is considered as a fluid, the behaviour in time of its equation of state ω_{DE} in time is a powerful observable to distinguish between different types of dark energy. To test IG, one can consider an effective model of dark energy in order to define an effective equation of state. This effective model consist in defining a density ρ_σ and a pressure P_σ that encode all the changes due to the presence of a scalar field σ. These quantities are "effective" in the sense that they are defined as the density and pressure of a dark energy fluid whose effect would correspond to that of the scalar field. Using these effective quantities, Friedmann equations can be rewritten as (Finelli et al., 2008):

$$3F_0H^2 = \sum_i \rho_i + \rho_\sigma, \tag{5.12a}$$

$$-2F_0\dot{H} = \sum_i (\rho_i + P_i) + \rho_\sigma + P_\sigma, \tag{5.12b}$$

and the effective equation of state of the scalar field becomes:

$$\omega_\sigma = \frac{P_\sigma}{\rho_\sigma}. \tag{5.13}$$

As it is shown in Figure 5.2, for the Induced Gravity model the parameter ω_σ follows the dominant component: in the radiation epoch it has a value of $\sim \frac{1}{3}$, which corresponds to the value of the equation of state of photons. In the matter dominated epoch its value decreases towards zero, since the equation of state of matter is zero. Finally, at present epoch, it becomes negative $\omega_\sigma \sim -1$, behaving like a cosmological constant.

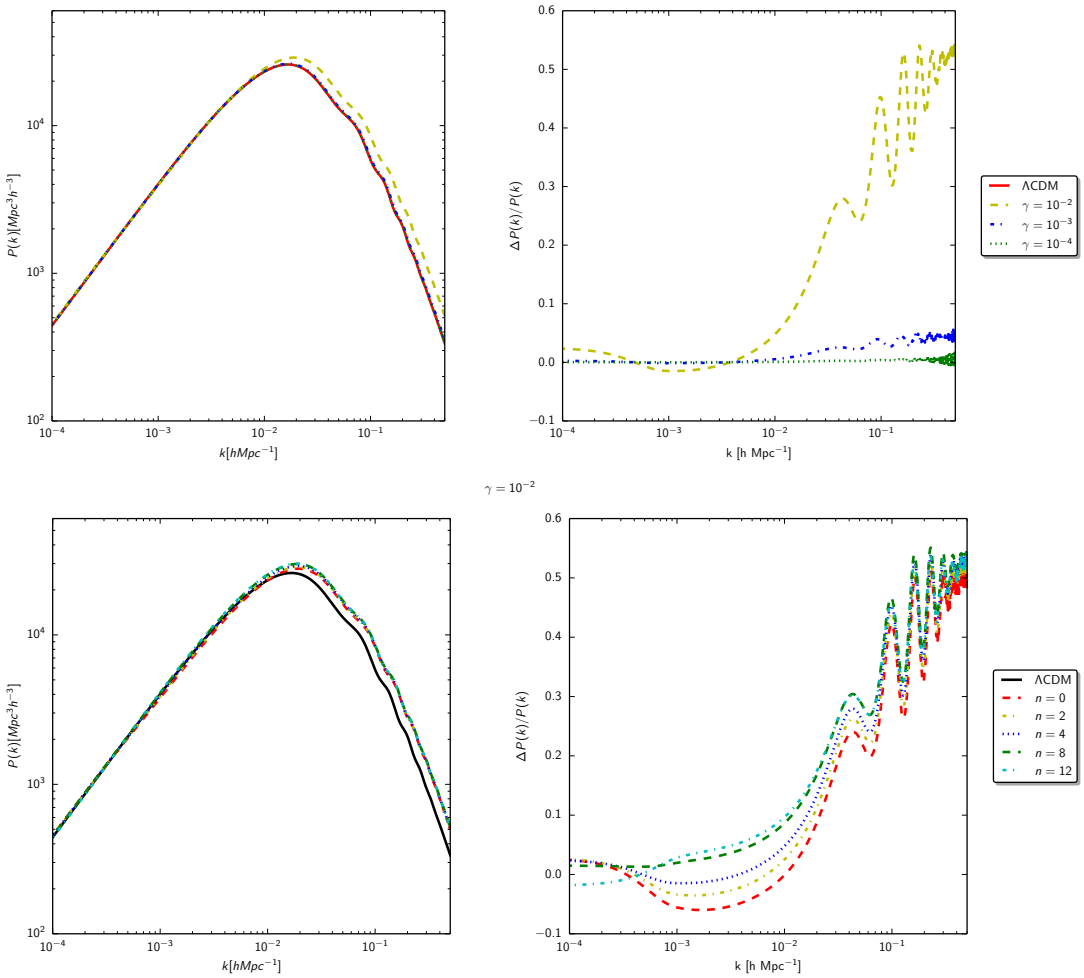

Figure 5.3 – *Top panel*: the matter power spectrum for $n_{IG} = 4$ at $\gamma = 10^{-2}$ in yellow dashed line, 10^{-3} in blue dot-dashed line and 10^{-4} in green dotted line. *Bottom panel*: figure taken from Ballardini et al. (2016), which shows the matter power spectrum at $\gamma = 10^{-2}$ for different values of n_{IG}.

5.3.2 CMB anisotropies and matter power spectrum

The spatial density perturbations of matter can be defined as:

$$\delta_m(\mathbf{x}, t) = \frac{\rho_m(\mathbf{x}, t) - \langle \rho_m \rangle}{\langle \rho_m \rangle}, \tag{5.14}$$

where $\rho_m(\vec{x}, t)$ is the matter density. Transforming the density perturbations in Fourier space, i.e., working with spatial frequencies k instead of position x, one can define the power spectrum of perturbations $P(k)$ as:

$$\langle \hat{\delta}(\mathbf{k})\, \hat{\delta}(\mathbf{k}') \rangle \equiv (2\pi)^3 P(k)\, \delta_D(\mathbf{k} + \mathbf{k}'), \tag{5.15}$$

where δ_D is the three-dimensional Dirac delta function, and the average is ideally performed over an ensemble of different realizations. The shape of the primordial power spectrum can be described as a power law:

$$P(k) = A_s\, k^{n_s}, \tag{5.16}$$

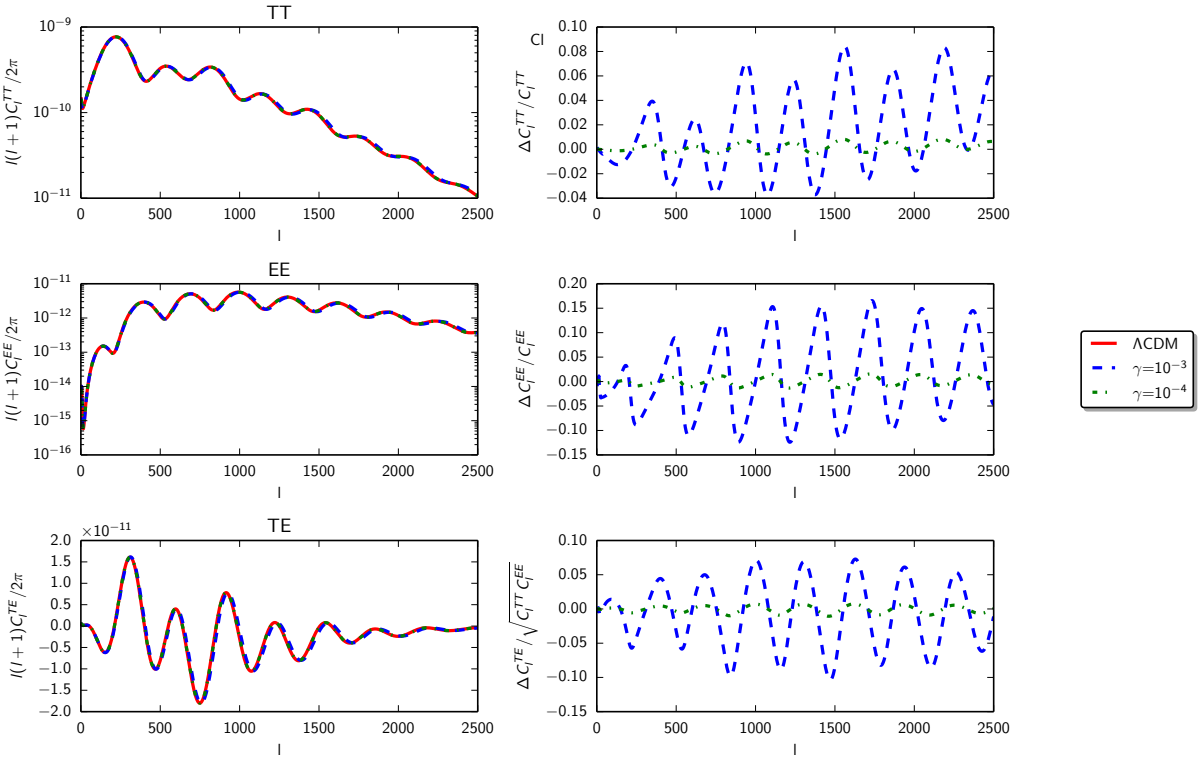

Figure 5.4 – On the left, from the upper to the lower panel respectively, CMB TT, EE and TE power spectra for $\gamma = 10^{-3}$, 10^{-4} for $n = 4$. TT, EE and TE spectra refer to the temperature and polarization auto-spectra and the temperature-polarization cross-spectrum respectively. The upper and middle right panels show the relative differences for TT and EE spectra with respect to a reference ΛCDM model. The lower right panel shows the differences for C_ℓ^{TE} normalized to $\sqrt{C_\ell^{TT} C_\ell^{EE}}$. Figure taken from Ballardini et al. (2016).

where A_s is the scalar amplitude and n_s the spectral index. The shape of the matter power spectrum depends on the evolution of perturbations, which in turn depend on gravity. Shifts from the ΛCDM paradigm are expected in modified theories of gravity. Figure (5.3) shows the linear matter power spectrum at $z = 0$ and the relative differences with respect to the ΛCDM reference model, when varying γ and in case of varying n_{IG}.
The power spectra of the CMB temperature and polarization anisotropies for different values of γ are shown in the left panels of Figure (5.4), while the relative differences with respect to the ΛCDM reference model are shown in its right panels. The change at the matter-radiation equality present in this scalar-tensor model (Liddle et al., 1998) induces relative differences in the temperature power spectrum at a few percent level for $\gamma = 10^{-3}$, and slightly larger shifts in polarization. Overall, differences at the percent level are obtained for $\gamma \sim 10^{-3}$ in different cosmological observables. This sets the order of magnitude on the expected constraints on γ.

5.3.3 The parametrized Post-Newtonian formalism

The parametrized Post-Newtonian (PN) formalism has been developed to compare different theories of gravity. In this formalism, the metric of a theory is written as an expansion about Minkowski's metric in terms of dimensionless gravitational potentials. Metrics derived by different theories have different coefficients for the terms of the expansion. These coefficients can be parametrized and constrained by observations. For IG and JBD theory, only one parameter differs from GR. This is $\gamma_{\rm PN}$ which is given by:

$$\gamma_{\rm PN} = 1 - \frac{4\gamma}{1+8\gamma}, \tag{5.17}$$

where $\gamma_{\rm PN} = 1$ in the GR limit. This parameters is used as a measure of the departure from GR and can be translated on a constraint on γ via Eq. (5.17).
The parameter $\gamma_{\rm PN}$ can be constrained by astronomical observations within the Solar System. Observational constraints come for example from the deflection of light rays passing near the Sun (Shapiro et al., 2004), the shift in Mercury's perihelion (Ashby et al., 2005) and the Doppler tracking of the Cassini spacecraft. The latter experiment measures the Shapiro delay, that is the delay of a light ray which passes in the vicinity of a massive object and thus crosses a region where the space is locally curved. The Shapiro delay from the Cassini spacecraft gives the tightest constraint available today: $\gamma_{\rm PN} = 1 - (2.1 \pm 2.3) \cdot 10^{-5}$ (Bertotti et al., 2003).

5.3.4 Analytical approximations

In order to study this model, I evolve numerically the background and linear perturbations using IG equations with a dedicated Einstein-Boltzmann code. I test the numerical results against analytic approximations which are valid in the matter era. The two quantities tested are useful to describe deviations from GR: the quantity $\mu(k,a)$ parametrizes the deviations of Ψ from GR (Zhao et al., 2009, 2012), while $\delta(k,a)$ parametrizes the difference between the Newtonian potentials Ψ and Φ. The chosen definition for these quantities holds both in the radiation and matter dominated regime (Hojjati et al., 2011):

$$k^2\Psi = -4\pi G a^2 \mu(k,a)\left[\Delta + 3(\rho+p)\bar{\sigma}\right], \tag{5.18a}$$

$$k^2[\Phi - \delta(k,a)\Psi] = 12\pi G a^2 \mu(k,a)(\rho+p)\bar{\sigma} \tag{5.18b}$$

where $\bar{\sigma}$ is the shear, $\Delta = \sum_i \delta\rho_i + 3aH(\rho_i+p_i)\theta_i/k^2$, $\delta_i = \delta\rho_i/\rho_i$ and where θ_i is the velocity potential. The quasi-static analytic approximations for $k \gg aH$ are (Zhao et al., 2012; Boisseau et al., 2000; Amendola et al., 2008; Tsujikawa, 2007):

$$\mu(k,a) = \frac{\sigma_0^2}{\sigma^2}, \tag{5.19a}$$

$$\delta(k,a) = \frac{1+4\gamma}{1+8\gamma}. \tag{5.19b}$$

Results are shown in Figure 5.5, for wavenumbers $k = 0.05$ and 0.005 Mpc^{-1} and values of the coupling to the Ricci curvature $\gamma = 10^{-2}$ and 10^{-3}. These approximations are obtained for the matter dominated epoch and are both well recovered by numerical results. This agreement means that the self-consistent treatment of background and linear perturbations of the code used is sufficiently ready for precision cosmology.

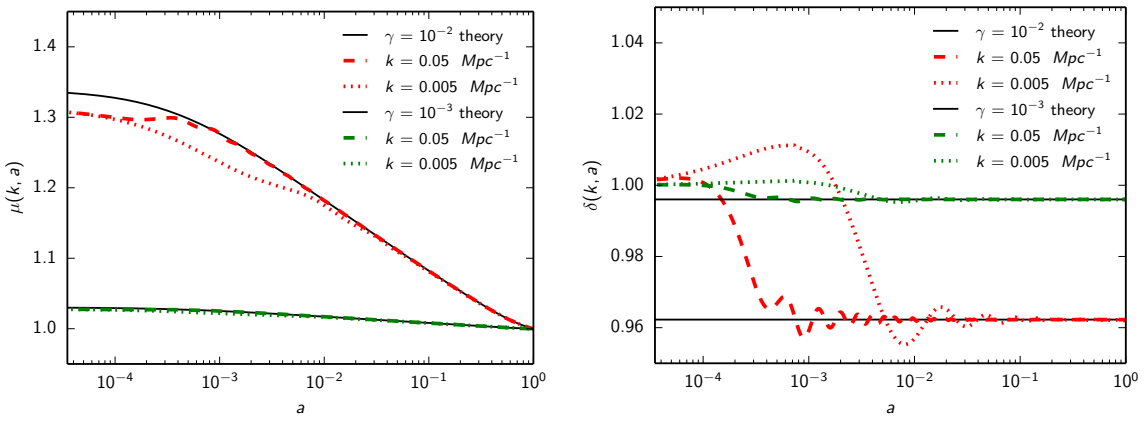

Figure 5.5 – Comparison of theoretical approximations for μ and δ which parametrize deviations from Einstein gravity (black lines) with our numerical results for two wavenumbers ($k\text{Mpc} = 0.05\,, 0.005$) and two values of the coupling to the Ricci curvature ($\gamma = 10^{-2}\,, 10^{-3}$).

5.4 Observational constraints

I have modified the publicly available Einstein-Boltzmann code CLASS[2] (Lesgourgues, 2011; Blas et al., 2011) to evolve background and linear fluctuations within IG. Linear perturbations equations are not shown in this Chapter but are detailed in Umiltà et al. (2015). The final product is a modified version of CLASS for Induced Gravity: CLASSig. CLASSig computes the time evolution of background quantities as well as the angular power spectra of CMB temperature and polarization and the matter power spectrum. Bellini et al. (2017) have compared various Einstein-Boltzmann solvers including CLASSig, showing that their predictions on the angular power spectrum of the cosmic microwave background and the power spectrum of dark matter agree to subpercent level. Thus CLASSig is sufficiently accurate for constraining cosmological parameters. Other implementations of IG or of similar models in Einstein-Boltzmann codes include Chen & Kamionkowski (1999); Perrotta et al. (2000); Riazuelo & Uzan (2002); Nagata et al. (2002); Wu et al. (2010); Zumalacarregui et al. (2016).

5.4.1 Constraints from cosmological observations

Cosmological parameter extraction is done by exploring the parameter space by the Monte Carlo code MONTE PYTHON[3] (Audren et al., 2013) connected to CLASSig. In (Umiltà et al., 2015) we use the 2013 nominal mission data release from Planck, available from the Planck Legacy Archive[4] (Planck Collaboration et al., 2014b). The Planck likelihood which covers temperature anisotropies from $\ell = 2$ to 2500 is combined with the low-ℓ WMAP polarisation data (Page et al., 2007; Bennett et al., 2013b; Hinshaw et al., 2013b): this combination is denoted as PLANCK 2013 in the following. The PLANCK 2013 likelihood is used in combination with constraints on $D_V(\bar{z})/r_\mathrm{s}$ (the ratio between the spherically

[2] `www.class-code.net`
[3] `www.montepython.net`
[4] `http://pla.esac.esa.int/pla/`

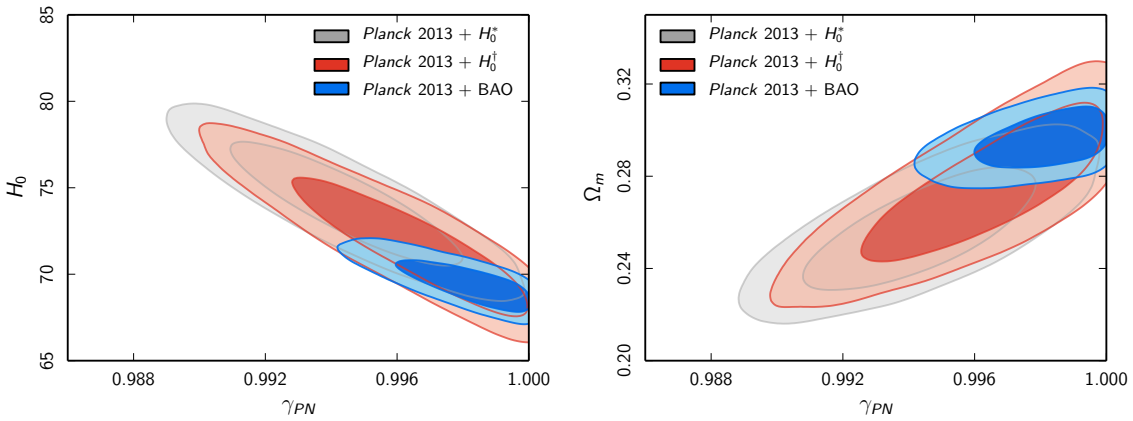

Figure 5.6 – Comparison of marginalized joint 68 % and 95 % CL for $(\gamma_{\rm PN}, H_0)$ (left panel) and $(\gamma_{\rm PPN}, \Omega_{\rm m})$ (right panel) for Planck 2013 + H_0^* (grey contours), Planck 2013 + $H_0^\dagger$ (red contours) and Planck 2013 + BAO + $H_0^\dagger$ (blue contours).

averaged distance scale D_V to the effective survey redshift, $\bar{z}$, and the sound horizon, $r_{\rm s}$) inferred from a compilation of BAO data. These are 6dFGRS data (Beutler et al., 2011) at $\bar{z} = 0.106$, the SDSS-MGS data (Ross et al., 2015) at $\bar{z} = 0.15$, and the SDSS-DR11 CMASS and LOWZ data (Anderson et al., 2014) at redshifts $\bar{z} = 0.57$ and 0.32. The parameters varied in the exploration are the standard parameters of the flat ΛCDM model, i.e., the baryon density ($\Omega_b h^2$), the CDM density ($\Omega_{\rm CDM}$), the reduced Hubble parameter ($h = H_0/(100 {\rm kms}^{-1}{\rm Mpc}^{-1})$), the reionization optical depth τ, the amplitude and tilt of the primordial spectrum of curvature perturbations ($A_{\rm s}$ and $n_{\rm s}$) at the pivot scale $k_* = 0.05$ Mpc^{-1}. The IG dark energy model with quartic potential is described by these six plus one extra parameter which quantifies the coupling to the Ricci curvature[5]. Following Li et al. (2013), the sampling is done on the quantity ζ, defined as:

$$\zeta \equiv \ln\left(1 + 4\gamma\right) = \ln\left(1 + \frac{1}{\omega_{\rm BD}}\right) \tag{5.20}$$

with the prior $[0, 0.039]$ used in Li et al. (2013). Three massless neutrinos are considered[6]. Nuisance parameters for foregrounds, calibration and beam uncertainties are also varied (Planck Collaboration et al., 2014b; Planck Collaboration XVI et al., 2014).
Results with Planck 2013 + BAO data for the main and derived parameters are summarized and compared with the ΛCDM values in Table 5.1. The induced gravity model with a quartic potential is not preferred over Einstein gravity with Λ ($\Delta\chi^2 \simeq -2\ln\mathcal{L} = 0.7$). The Planck 2013 + BAO 95% constraint on the coupling to the Ricci curvature is:

$$\gamma < 0.0012 \,(95\,\%\ {\rm CL},\ {\rm Planck}\ 2013 + {\rm BAO})\,. \tag{5.21}$$

[5]The initial value of the scalar field σ_i deep in the radiation is chosen to reproduce the present value of the field in Eq. (5.6).

[6]Note that the *Planck Collaboration* assumes one massive neutrinos with a mass of 0.06 eV (Planck Collaboration XVI et al., 2014). The assumption of a mass of 0.06 eV has a small effect on the cosmological parameters at the Planck precision (as a $0.5\,\sigma$ shift to smaller value for H_0 (Planck Collaboration XVI et al., 2014)), thus the quoted results are for a ΛCDM cosmology with three massless neutrinos for a consistent comparison with the class of dark energy models studied.

	Planck 2013 + BAO ΛCDM	Planck 2013 + BAO
$10^5\Omega_{\rm b}h^2$	2215^{+24}_{-25}	2203 ± 25
$10^4\Omega_{\rm c}h^2$	1187^{+13}_{-14}	1207^{+18}_{-22}
H_0 [km s^{-1} Mpc^{-1}]	$68.4^{+0.6}_{-0.7}$	$69.5^{+0.9}_{-1.2}$
τ	$0.091^{+0.012}_{-0.014}$	$0.088^{+0.012}_{-0.013}$
$\ln(10^{10}A_{\rm s})$	$3.089^{+0.024}_{-0.027}$	$3.090^{+0.024}_{-0.026}$
$n_{\rm s}$	0.9626 ± 0.0053	0.9611 ± 0.0053
ζ	–	< 0.0047 (95% CL)
$10^3\gamma$	–	< 1.2 (95% CL)
γ_{PN}	1	> 0.9953 (95% CL)
$\Omega_{\rm m}$	0.301 ± 0.008	0.295 ± 0.009
$\delta G_{\rm N}/G_{\rm N}$	–	$-0.015^{+0.013}_{-0.006}$
$10^{13}\dot{G}_{\rm N}(z=0)/G_{\rm N}$ [yr^{-1}]	–	$-0.61^{+0.55}_{-0.25}$
$10^{23}\ddot{G}_{\rm N}(z=0)/G_{\rm N}$ [yr^{-2}]	–	$0.86^{+0.33}_{-0.78}$

Table 5.1 – Constraints on main and derived parameters (at 68% CL if otherwise stated).

The corresponding constraint on the post-Newtonian parameter $\gamma_{\rm PN}$ is:

$$0.9953 < \gamma_{\rm PN} < 1 \ (95\,\%\ \text{CL, Planck 2013 + BAO})\,. \tag{5.22}$$

It is also useful to quote the derived constraints on the change of the Newton constant between the radiation era and the present time $\delta G_N/G_N \equiv (\sigma_i^2 - \sigma_0^2)/\sigma_0^2$:

$$\frac{\delta G_N}{G_N} = -0.015^{+0.013}_{-0.006}\,(95\,\%\ \text{CL, Planck 2013 + BAO})\,. \tag{5.23}$$

and the constraint on its derivative ($\dot{G}_N/G_N \equiv -2\dot{\sigma}_0/\sigma_0$) at present time:

$$\frac{\dot{G_N}}{G_N}(z=0) = -0.61^{+0.55}_{-0.25}\,[10^{-13}yr^{-1}]\,,(95\,\%\ \text{CL, Planck 2013 + BAO})\,. \tag{5.24}$$

The derived constraints are tighter than those obtained in the literature with Planck 2013 data for similar scalar-tensor models with a power-law potential (Avilez & Skordis, 2014; Li et al., 2013) (see Nagata et al. (2004); Acquaviva et al. (2005); Wu & Chen (2010) for analysis with pre-Planck data).

Avilez & Skordis (2014) consider the case of a constant potential in Brans-Dicke-like theory and quote $(1+6\gamma)/(1+8\gamma) = 1.07^{+0.11}_{-0.10}$ at 95% CL as the tightest constraint with a prior $\omega_{\rm BD} > -3/2$. Instead this analysis obtains [0.998,1] as the 95% CL range for the same quantity with Planck 2013 + BAO by varying ζ in the interval $[0, 0.039]$.

Li et al. (2013) consider the case of a linear potential in Brans-Dicke, i.e., a quadratic potential in induced gravity, and quote $0 < \zeta < 0.549\times10^{-2}$ at 95% CL and $\dot{G}_N/G_N = -1.42^{+2.48}_{2.27}$ at 68 % CL from Planck 2013 with the same prior on ζ, although in combination with a different compilation of BAO data (Li et al., 2013). In case of a quartic potential, the scalar field evolves during the matter epoch and does not evolve in future epochs. For power-law potentials different from the quartic case, the value of the scalar field evolves also in future epochs (Cerioni et al., 2009). For this reason, the models studied in Avilez & Skordis (2014) and Li et al. (2013) could differ from the case of a quartic potential, in particular at recent redshifts.

	Planck 2013 + H_0^*	Planck 2013 + $H_0^\dagger$	Planck 2013 + BAO + $H_0^\dagger$
$10^5\Omega_b h^2$	2219 ± 28	2213^{+28}_{-29}	2203 ± 26
$10^4\Omega_c h^2$	1188^{+25}_{-26}	1194 ± 25	1207^{+18}_{-22}
H_0 (km s^{-1} Mpc^{-1})	$74.1^{+2.3}_{-2.4}$	$72.1^{+2.2}_{-3.1}$	$69.6^{+0.9}_{-1.1}$
τ	$0.092^{+0.013}_{-0.014}$	$0.091^{+0.013}_{-0.015}$	$0.088^{+0.012}_{-0.014}$
$\ln(10^{10}A_s)$	$3.098^{+0.025}_{-0.027}$	$3.095^{+0.025}_{-0.028}$	$3.091^{+0.024}_{-0.027}$
n_s	$0.9704^{+0.0070}_{-0.0072}$	$0.9667^{+0.0075}_{-0.0078}$	$0.9613^{+0.0055}_{-0.0054}$
ζ	0.0056 ± 0.0023	< 0.0083 (95% CL)	< 0.0047 (95% CL)
$10^3\gamma$	1.4 ± 0.60	< 2.1 (95% CL)	< 1.2 (95% CL)
γ_{PN}	$0.9944^{+0.0023}_{-0.0022}$	> 0.9918 (95% CL)	> 0.9954 (95% CL)
Ω_m	$0.257^{+0.016}_{-0.019}$	$0.274^{+0.022}_{-0.021}$	$0.294^{+0.009}_{-0.008}$
$\delta G_N/G_N$	$-0.041^{+0.017}_{-0.016}$	-0.028 ± 0.012	$-0.016^{+0.010}_{-0.006}$
$10^{13}\dot{G}_N(z=0)/G_N$ [yr^{-1}]	$-1.56^{+0.61}_{-0.58}$	$-1.10^{+0.83}_{-0.49}$	$-0.64^{+0.52}_{-0.25}$
$10^{23}\ddot{G}_N(z=0)/G_N$ [yr^{-2}]	$2.4^{+0.9}_{-1.0}$	$1.7^{+0.7}_{-1.5}$	$0.89^{+0.24}_{-0.75}$

Table 5.2 – Constraints on main and derived parameters at 68% CL (unless otherwise stated).

5.4.2 Combination with local measurements

As evident from Table 5.1, IG with quartic potential prefers a higher value of the Hubble parameter H_0 with respect to the one of ΛCDM. It is thus interesting to study the combination of the local measurements of the Hubble constant in combination with Planck 2013 and BAO data. The local estimates of H_0 are consistently higher than those from CMB (and BAO) and this discrepancy becomes a 2.5 σ tension after the Planck 2013 release (Planck Collaboration XVI et al., 2014). This tension might be sign of new physics, although reanalysis subsequent to the Planck 2013 release have highlighted how hidden systematics and underestimated uncertainties could hide in the local measurements of H_0 (Humphreys et al., 2013; Efstathiou, 2014). More recent estimates of H_0 (Riess et al., 2016) are still in tension with Planck data. For these reasons the impact of two different local estimates of H_0 is considered separately: $H_0 = 73.8 \pm 2.4$ km s^{-1} Mpc^{-1} (Riess et al., 2011), denoted as H_0^*, and $H_0 = 70.6 \pm 3.0$ km s^{-1} Mpc^{-1} (Efstathiou, 2014), denoted as $H_0^\dagger$. Results are summarized in Table 5.2.
With the higher local estimate of H_0^* (Riess et al., 2011) the posterior on ζ is different at 2 σ level from GR. With the lower estimate for H_0 obtained by Efstahiou (Efstathiou, 2014) with the new revised geometric maser distance to NGC 4258 (Humphreys et al., 2013), the posterior probability for ζ is compatible with GR. As can be seen by comparing the last columns of Table 5.1 and 5.2, the lower local estimate of $H_0^\dagger$ has almost a negligible impact when Planck 2013 and BAO data are combined. Two-dimensional constraints are shown in Figure 5.6.

5.4.3 Updated constraints with Planck 2015

In Ballardini et al. (2016), we extend the analysis of Umiltà et al. (2015) by computing constraints on γ with Planck 2015 likelihood and by studying a potential with index $n_{IG} \neq 4$. The model is studied using Planck 2015 TT, TE, EE data in combination with the Planck low-ℓ polarization data (labelled lowP likelihood), the Planck lensing likelihood and a new compilation of BAO. The updated contraint on γ, that uses only the temperature

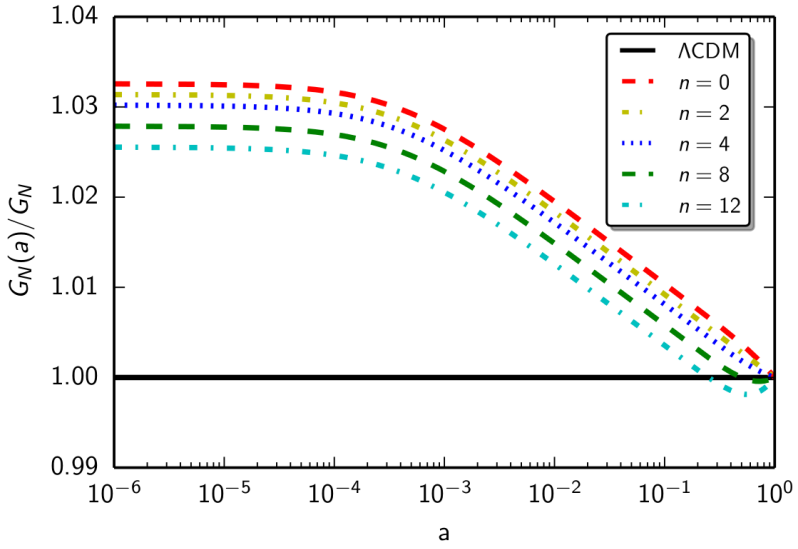

Figure 5.7 – Evolution of $G_N(a)/G_N \equiv \frac{\sigma_0^2}{\sigma^2}$ as a function of the scale factor a for $\gamma = 10^{-3}$ at differen values of n_{IG}. Figure taken from Ballardini et al. (2016).

data and low-ℓ polarization as in Umiltà et al. (2015), improves by 25%:

$$\gamma < 0.00089\,(95\,\%\ \text{CL, Planck TT + lowP + BAO})\,. \tag{5.25}$$

Lensing measurements tend to favour lower values of τ and A_s, and constraints on these two parameters as well as on γ are tighter when adding Planck lensing likelihood. Adding high-ℓ polarization and lensing gives the tightest constraint:

$$\gamma < 0.00075\,(95\,\%\ \text{CL, Planck TT,TE,EE + lowP + lensing + BAO})\,. \tag{5.26}$$

Constraints on $\frac{\dot{G_N}}{G_N}$ also improve with the updated datasets:

$$\frac{\dot{G_N}}{G_N}(z=0) = -0.08^{+0.55}_{-0.08}\,[10^{-13} yr^{-1}]\,,(95\,\%\ \text{CL, Planck TT,TE,EE + lowP + BAO})\,. \tag{5.27}$$

For a comparison, the 95% CL constraint from pulsar timing is $\frac{\dot{G_N}}{G_N} = (\text{-}0.6 \pm 1.1) \cdot 10^{-12}$ yr^{-1} (Zhu et al., 2015).

For the analysis on the potential index, we find that current data cannot discriminate at a statistically significant level different values of n_{IG}, thus a set of fixed values is studied. The impact of different potentials is observable on CMB temperature and polarization angular power spectra only at $\ell \lesssim 30$, thus CMB alone cannot constrain the potential shape.

On the other hand, the CMB lensing power spectrum and the matter power spectrum, shown in Figure 5.3, show some degree of dependence on n_{IG}. However, with the dataset used in Ballardini et al. (2016), we cannot constrain the index n_{IG}. We observe also that the constraints on $\frac{\dot{G_N}}{G_N}$ and $\frac{\ddot{G_N}}{G_N}$ depend on the index n_{IG}: Figure 5.7 shows the time evolution $G_N(a)/G_N$ for different potential shapes. This dependence must be kept in mind when comparing constraints on these quantities to solar system constraints.

5.5 Conclusions

We studied a MG model in which a scalar field regulated by one single parameter γ drives the accelerated expansion of the universe. The field depends on a potential which we parametrize as a power law. We have obtained constraints on the parameter γ with Planck 2013 and Planck 2015 data in combination with different data sets. Current constraints from cosmological large scale probes are nevertheless weaker than constraints from solar system experiments. With current data it is not yet possible to constrain the power law index.
New data on weak lensing and galaxy clustering from the Euclid mission (Laureijs et al., 2011), as well as CMB ground observations (Abazajian et al., 2016) could help to improve the constraints on this model (Ballardini et al., 2017).

Conclusions

The CMB is an important observable for cosmology, but its information content is not directly accessible due to the contamination by the foregrounds. In this work, I use the SMICA component separation method to estimate the CMB angular power spectrum directly from the data, without the need to reconstruct a map first. I adapt SMICA in order to better characterize the small scale properties of the CMB angular power spectrum. The determination of the small scales of the CMB angular power spectrum is limited by the small scale foreground contamination from point sources and the noise bias in autospectrum. Both limitations are addressed in this work. For point sources I use a dedicated model that is based on the physical knowledge available. I consider two independent point source populations with free emission law but with flat angular power spectrum. This model allows to recover the joint emission law of point sources, at the price of a partial loss of blindness of the method. For the noise bias, I exploit the properties of Planck data split maps. These are data maps produced with observations taken at different times: while their astrophysical content is the same, their noise is decorrelated. To build the data statistics used in SMICA, I only use cross-angular power spectra between data splits. While auto-spectra present a small scale bias due to instrumental noise, cross-spectra present no average noise contribution. However, the presence of noise in the data has an effect on the scatter of the cross-spectra. The SMICA method requires both auto- and cross-spectra in input: I replace auto-spectra with cross-spectra plus a known contribution that mimics the noise bias in the auto-spectra. As a result, the noise contribution does not enter in the fit since the noise bias in the spectra is known by construction. The input data statistics do not exactly have the properties required by the SMICA method, which is no longer optimal. This however constitutes a minor problem, since it only affects the weighting of the different modes in the fit, while an error in the estimation of the noise contribution affects the angular power spectrum reconstruction directly.
This method is tested on three different sets of simulations, in which the foreground content is increasingly complex, and on Planck 2015 full mission release data. The analysis is performed with three sky cuts, in order to test different regimes of galactic contamination and investigate the impact of its spatial inhomogeneity. I also performed some cross-check tests, by adding more frequency channels in the fit and by running SMICA without the data split approach, i.e., with both auto- and cross-spectra in the data input. I observed that adding a high frequency channel such as 857 GHz does not improve the results of the fit. Instead, the results of the fit with the auto-spectra are very close to those obtained with the data split. The emission law of point sources is well recovered in simulations, while a mild departure with respect to theoretical values obtained from the *Planck Collaboration* is observed in the Planck data analysis. However, theoretical values depend on the model chosen, and the contribution of point sources depends on masking, especially at

low frequency. This can explain, at least partially, the observed departure between the emission law obtained by this analysis and estimations from the *Planck Collaboration*.
The average CMB angular power spectrum from recovered simulations shows no residuals for the simplest case of foreground contamination and shows residuals of the order of 20 μK^2 for the two more complex configurations. Some degree of residuals in the CMB spectrum is expected in these two cases since, contrary to the simplest case, the SMICA model does not perfectly represent the foreground content of these simulations. In the fit on Planck data, the residuals are of the same order of magnitude.
The obtained CMB spectra of simulations and Planck data have been used for cosmological parameters estimation. This has allowed to better understand the origin of the parameters shifts. These CMB spectra contain a residual of foregrounds that needs to be parametrized. I used two different parametrizations for these residuals, a physical one and a phenomenological one. The recovered parameters in simulations present biases of the order of one standard deviation of the posterior. Depending on which parametrization is used for the residuals, the biases on each of the cosmological parameters improve or worsen, and the overall result is that neither model can correctly account for the residuals. A similar result is observed in the exploration on Planck data.
In conclusion, with this method I recovered an estimation of the CMB angular power spectrum with a low foreground contribution, in particular with respect to the extragalactic contamination at small scales. The residual foreground content in this spectrum is lower than what is present in the spectra used by the Planck likelihood, thus in principle it can be modelled by a smaller number of parameters. Also, it is not necessary to assume a fiducial model for the CMB in the computation of the likelihood covariance matrix, as it is the case for the the Planck likelihood. However, an accurate determination of cosmological parameters still depends on a correct parametrization of the foreground contribution. The correct shape of this contribution is not known and presumably varies with sky fraction. At small sky fractions, this contribution is weak, so it is difficult to constrain it and this induces biases in the cosmological parameters. At large sky fractions, this contribution is more evident but its shape is also more complex.
For this reason, it is not evident whether this blind approach grants any advantage with respect to the Planck likelihood approach, at least for the CMB temperature analysis, where foregrounds are particularly complex. When considering polarization, a blind approach could still be useful since the foreground contamination is more simple.

CMB reconstruction is fundamental to test cosmological models. The work presented in this thesis is a first step towards a determination of cosmological parameters via component separation. An interesting exploitation of this approach is the study of alternative cosmological models. I presented in this work a study on Modified Gravity model called Induced Gravity. In this model a scalar field σ drives the accelerated expansion. I first analysed the case where the field has a quartic potential $V(\sigma) \propto \sigma^4$. This model is regulated by a single parameter γ that can be constrained by observations. In particular, I used Planck 2013 nominal mission data, BAO and two different local estimations of H_0 to jointly derive constraints on γ and cosmological parameters. Due to a positive correlation of γ and H_0, using local measurements of H_0 does not better constrain the model, and tightest limit is obtained with Planck 2013 and BAO data only. The obtained constraint is $\gamma \leq 0.0012$ (95% CL).
In a following analysis that used also Planck 2015 data, which include polarization

and lensing information, this constraint has been updated to $\gamma \leq 0.00075$ (95% CL). These values are compatible but still weaker than current constraints set by solar system experiments, which are of the order of $\sim 10^{-5}$. In this analysis other forms of the potential have been studied, and it has been observed that CMB data cannot differentiate much between changes in the shape of the scalar field potential of this model.

Perspectives

This analysis has shown that the main limitation of the component separation approach to cosmological parameter estimation is the incorrect characterization of foregrounds residuals. This work has implemented a first approach to the problem by parametrizing point sources as two independent components. This is however not sufficient to characterize the foregrounds residuals, since a non-negligible level is still present in the recovered CMB spectrum. A more refined approach could consist in using tailored scale ranges for each frequency maps, similarly to what it has been done in the Planck likelihood. For example, the estimation of large scale foreground emission such as the thermal dust could be done only at large scales, using the small scales to characterize other emissions such as the clustered CIB. This is in some sense equivalent to performing a zone fit in SMICA, where some parameters as the dust emission law and angular power spectrum are estimated on a given area of the sky, while other parameters such as the CMB spectrum are estimated globally. These modifications would further reduce the blindness of the model, and their impact on the CMB estimation must be carefully checked.
This work presents a method that is based only on cross-spectra between maps. Even though this method has an approximate weighting of the different modes in the fit, its results are consistent with those obtained using also auto-spectra and fitting for the noise contribution. This means we can expect that this method performs consistently with the SMICA optimal configuration. However I only tested one ansatz for the noise contribution in the data split matrix: checking whether or not results change with a different added noise contribution is left to future work. Also, while I applied it only on Planck data, it would be interesting to combine data coming from ground missions, that observe the angular power spectrum of the CMB at smaller scales than Planck.
For the Induced Gravity model, future data could further improve the constraints on the model. Euclid galaxy clustering and weak lensing data in combination with CMB data may have the potential to reach an uncertainty comparable with the current constraints from solar system. Since the shape of the potential of scalar field σ has some effect on the matter power spectrum, it is possible that Euclid data will also allow us to characterize it.

Appendices

Appendix A

Further considerations on the use of data splits

Given a set of data splits that observe the same sky defined as in Eq. (4.9), it is convenient to construct half-sum (HS) and half-difference (HD) spherical harmonics as:

$$\mathbf{y}^{\rm HS}_{\ell m} \equiv \frac{\mathbf{y}^a_{\ell m} + \mathbf{y}^b_{\ell m}}{2} = \mathbf{o}_{\ell m} + \frac{\mathbf{n}^a_{\ell m} + \mathbf{n}^b_{\ell m}}{2}, \tag{A.1}$$

and

$$\mathbf{y}^{\rm HD}_{\ell m} \equiv \frac{\mathbf{y}^a_{\ell m} - \mathbf{y}^b_{\ell m}}{2} = \frac{\mathbf{n}^a_{\ell m} - \mathbf{n}^b_{\ell m}}{2}. \tag{A.2}$$

The covariances of the of these two vectors are:

$$\begin{aligned} \hat{\mathbf{R}}^{\rm HS}_\ell &\approx \mathbf{O}_\ell + \frac{\mathbf{N}_\ell}{2}, \\ \hat{\mathbf{R}}^{\rm HD}_\ell &\approx \frac{\mathbf{N}_\ell}{2}, \end{aligned} \tag{A.3}$$

where we considered $\mathbf{n}^a_{\ell m} \approx \mathbf{n}^b_{\ell m}$ with covariance $\mathbf{N}_\ell$. The HD part can be used to estimate the noise properties. The HS maps instead contains the signal and can be used for component separation. Differently from the data split matrix in Eq. (4.10), the HS matrix contains also the auto-spectra information. These two matrices have thus different properties.
At high multipoles, the dominant term in both matrices is the noise. If we write their variances we see that[1]:

$$Cov(\hat{R}^{\rm HS}_{ik}, \hat{R}^{\rm HS}_{jl}) \approx \frac{1}{4T}(N_{ik}N_{jl} + N_{il}N_{jk}), \tag{A.4}$$

while

$$Cov(\hat{R}^{\rm split}_{ik}, \hat{R}^{\rm split}_{jl}) \approx \frac{1}{2T}(N_{ik}N_{jl} + N_{il}N_{jk}), \tag{A.5}$$

where T is the number of samples. Since we neglect a part of the signal, by using data splits covariances we double the variance of the data matrices in the low signal-to-noise regime. This influences the results since the weighting of the SMICA fit depends on the variance of the matrix $\hat{\mathbf{R}}^{\rm split}_\ell$.

[1]For clarity, we omit here the subscript ℓ that indicates the multipole.

Appendix B

Masks

The masks we use are the sum of a galactic and a point source part: while the point source part is the same, the galactic sky coverage changes. For the galactic part we create a set of masks starting from those delivered by the *Planck Collaboration*[1]. From these, we choose the three galactic masks of retained sky fraction $f_{sky} = 0.4, 0.6, 0.7$. These mask are not apodized, thus need to be smoothed at the edges. First we smooth them with a Gaussian beam of $FWHM = 3^o$ and then we threshold them to obtain a new set of slightly smaller masks of $f_{sky} = 0.45, 0.65, 0.75$. This step is needed in order to avoid that the subsequent apodization results in a large decrease of the retained sky fraction. Using the *process_mask* function of the Healpix package, for each of these masks we obtain a distance map, i.e., a map in which each pixel contains the distance to the nearest masked pixel. Such a map is used to apodize the galactic masks by convolution with a Gaussian of $FWHM = 4^o$. The use of distance maps instead of a simple Gaussian smoothing avoids leakage into the original mask.
We create the point source mask based on the Planck 2015 Catalog of Compact Sources[2] as the union of the point sources masks at the five frequency channels of interest. This point source mask is apodized with $FWHM = 1^o$, using a distance map. We combine our point source apodized mask with our apodized galactic masks to obtain the final set of masks we use in this analysis. Their respective retained sky fraction is f_{sky}=0.31, 0.48, 0.57, but to enhance readability we refer to them as f_{sky}=0.3, 0.5, 0.6 throughout the text. We also create a second set of masks for cross-check analysis that include point sources at 857 GHz. These masks have a similar sky fraction to the leading set, and they are used only for the tests performed in Sect. 4.5.3

[1] available for download at http://pla.esac.esa.int (*HFI_Mask_GalPlane-apo0_2048_R2.00.fits*)
[2] v2.0, also available for download at http://pla.esac.esa.int

Appendix C

Notation and units

Throughout this thesis we will use the following notation. Random variables are majuscule and bold as $\mathbf{X}$, while their possible values are denoted as x_i, and their probability as $p(\mathbf{X}) = Pr\mathbf{X} = x_i$.
The expectation of a variable is:

$$\langle \mathbf{X} \rangle = E[\mathbf{X}] = \int x \;\; p(x) \;\; dx. \tag{C.1}$$

We remind here the definitions of variance $Var(\cdot)$ and covariance $Cov(\cdot, \cdot)$

$$Var(\mathbf{X}) = \left\langle (\mathbf{X} - \langle \mathbf{X} \rangle)^2 \right\rangle = E[(\mathbf{X} - E[\mathbf{X}])^2], \tag{C.2}$$

$$Cov(\mathbf{X}, \mathbf{Y}) = \langle (\mathbf{X} - \langle \mathbf{X} \rangle)(\mathbf{Y} - \langle \mathbf{Y} \rangle) \rangle = E[(\mathbf{X} - E[\mathbf{X}])(\mathbf{Y} - E[\mathbf{Y}])]. \tag{C.3}$$

The symbol log denotes the natural logarithm unless stated otherwise. Vectors and matrices are in bold.

Planck data are given in different temperature units, depending on convenience. The detectors do not measure temperature directly, and different ways to convert to temperature units are possible.
The CMB has a black-body emission:

$$I(\nu) = B(\nu, T_0) = B(\nu, T_0 + T_1 + \delta T) \simeq B(\nu, T_0) + \frac{\partial B}{\partial T}(\nu, T_0)(T_1 + \delta T), \tag{C.4}$$

where the black-body equation is defined in Eq. (2.4), T_0 is the average CMB temperature or monopole, T_1 is the dipole, that is differential temperature that we observe due to the detector motion with respect to the reference frame of the CMB, and δT are the temperature anisotropies. In practice, a detector measures the power W integrated over a frequency band, that is:

$$W \int_{\nu - \frac{d\nu}{2}}^{\nu + \frac{d\nu}{2}} I(\nu) \; s \; \Omega \; \tau(\nu) \; d\nu \tag{C.5}$$

where $\frac{d\nu}{2}$ is the bandwidth, $\tau(\nu)$ is the spectral transmission curve of the band, s is the detector area and Ω is the beam width. Thus we do not measure the intensity at a precise frequency, but only as an integrated quantity over a bandpass.
When studying the CMB, we are interested in temperature anisotropies: it is thus necessary

to convert from the intensity measurement, whose natural units are [W m^{-2} Hz^{-1} sr^{-1}] or [Jy /sr] to temperature units. The Planck detectors measure differential source intensity (that means they can not measure the term $B(\nu, T_0)$ in Eq. (C.4)) which can be converted in temperature anisotropies. Intrinsically, δT do not depend on ν, but the fluctuations on the detector do through the term $\frac{\partial B}{\partial T}(\nu, T_0)$. By knowing the shape of $B(\nu, T)$ we can use Eq. (C.4) to convert the detector measurements to temperature (Tegmark & Efstathiou, 1996). We can thus construct data maps in units of temperature in which the CMB temperature anisotropies are independent of frequency. We call these temperature units K_{CMB}. These units are practical to study the CMB anisotropies, but they change the spectral behaviour of foregrounds in the maps. The foregrounds do not have a black-body emission law, but often have a power-law emission law. When the intensity is integrated over the bandpass, since the integration assumes a black-body shape, this alters the foreground contribution in the reconstructed maps in K_{CMB}. When considering emission others than the CMB it is necessary to use colour corrections, that take into account this effect (Planck Collaboration et al., 2014c,d). Also, the K_{CMB} units are not useful at high frequencies where the CMB contribution is negligible.
Another type of temperature units used for Planck maps are K_{RJ} (Rayleigh-Jeans). These are the units of the brightness temperature T_b, defined by Eq. (2.1), which is the temperature that a black-body of same brightness would have at that frequency. This means that, for any value $I(\nu)$, we can define $T_b(\nu)$ by the relation:

$$I(\nu) = B(\nu, T_b). \tag{C.6}$$

Thus we can view brightness temperature as a convention for expressing an arbitrary flux density $I(\nu)$ in temperature units. For a black-body emission law, and in the limit $h\nu \ll kT$, then the brightness temperature corresponds to the thermodynamic temperature of the source, measured in K.

Annexes

Journal of Cosmology and Astroparticle Physics
An IOP and SISSA journal

CMB and BAO constraints for an induced gravity dark energy model with a quartic potential

C. Umiltà,[a,b,c] **M. Ballardini,**[d,e,f] **F. Finelli**[e,f] **and D. Paoletti**[e,f]

[a]Institut d'Astrophysique de Paris, CNRS (UMR7095),
98 bis Boulevard Arago, F-75014, Paris, France
[b]UPMC Univ Paris 06, UMR7095,
98 bis Boulevard Arago, F-75014, Paris, France
[c]Sorbonne Universités, Institut Lagrange de Paris (ILP),
98 bis Boulevard Arago, 75014 Paris, France
[d]DIFA, Dipartimento di Fisica e Astronomia, Alma Mater Studiorum Università di Bologna,
Viale Berti Pichat, 6/2, I-40127 Bologna, Italy
[e]INAF-IASF Bologna,
via Gobetti 101, I-40129 Bologna, Italy
[f]INFN, Sezione di Bologna,
Via Irnerio 46, I-40126 Bologna, Italy
E-mail: umilta@iap.fr, ballardini@iasfbo.inaf.it, finelli@iasfbo.inaf.it,
paoletti@iasfbo.inaf.it

Received July 7, 2015
Accepted July 12, 2015
Published August 10, 2015

Abstract. We study the predictions for structure formation in an induced gravity dark energy model with a quartic potential. By developing a dedicated Einstein-Boltzmann code, we study self-consistently the dynamics of homogeneous cosmology and of linear perturbations without using any parametrization. By evolving linear perturbations with initial conditions in the radiation era, we accurately recover the quasi-static analytic approximation in the matter dominated era. We use Planck 2013 data and a compilation of baryonic acoustic oscillation (BAO) data to constrain the coupling γ to the Ricci curvature and the other cosmological parameters. By connecting the gravitational constant in the Einstein equation to the one measured in a Cavendish-like experiment, we find $\gamma < 0.0012$ at 95% CL with Planck 2013 and BAO data. This is the tightest cosmological constraint on γ and on the corresponding derived post-Newtonian parameters. Because of a degeneracy between γ and the Hubble constant H_0, we show how larger values for γ are allowed, but not preferred at a significant statistical level, when local measurements of H_0 are combined in the analysis with Planck 2013 data.

Keywords: modified gravity, cosmological parameters from CMBR, dark energy theory

ArXiv ePrint: 1507.00718

doi:10.1088/1475-7516/2015/08/017

JCAP08(2015)017

JCAP08(2015)017

Contents

1 Introduction

Inflation or quintessence are naturally embedded in scalar-tensor theories of gravity. In these models the scalar field which regulates the gravitational coupling also drives the acceleration of the Universe. The non-minimal coupling to gravity can change significantly the perspective on inflation or quintessence in Einstein general relativity. In the inflationary context, for instance, a large coupling of the inflaton to gravity allows potentials with a self-coupling which would be excluded in the minimally coupled case [1–4]. In the dark energy context, for example the coupling to gravity could allow super-acceleration (i.e. $\dot{H} > 0$) with standard kinetic terms for the scalar field [5].

In this paper we consider *induced gravity* (IG) with a quartic potential $V(\sigma) = \lambda\sigma^4/4$ as a simple scalar-tensor dark energy model:

$$S = \int d^4x\sqrt{-g}\left[\frac{\gamma\sigma^2 R}{2} - \frac{g^{\mu\nu}}{2}\partial_\mu\sigma\partial_\nu\sigma - \frac{\lambda}{4}\sigma^4 + \mathcal{L}_m\right] \tag{1.1}$$

where $\mathcal{L}_m$ denotes the contribution by matter and radiation. Under a simple field redefinition $\gamma\sigma^2 = \phi/(8\pi)$, the above action can be cast in a Brans-Dicke-like model [6] with a quadratic potential:

$$S = \int d^4x\sqrt{-g}\left[\frac{1}{16\pi}\left(\phi R - \frac{\omega_{\rm BD}}{\phi}g^{\mu\nu}\partial_\mu\phi\partial_\nu\phi\right) - \frac{m^2}{2}\phi^2 + \mathcal{L}_m\right], \tag{1.2}$$

with the following relation between the dimensionless parameters of the two theories:

$$\omega_{\rm BD} = \frac{1}{4\gamma} \qquad m = \frac{\sqrt{2\lambda}}{16\pi\gamma}. \tag{1.3}$$

The action in eq. (1.1), which contains only dimensionless parameters, was introduced to generate the gravitational constant and inflation by spontaneous breaking of scale invariance in absence of matter [7, 8]. In the context of late cosmology, this action was studied in refs. [8, 9] to reduce the time dependence of the effective gravitational constant in the original Brans-Dicke model (i.e. with a vanishing potential [6]) and to generate an effective cosmological

constant. The cosmological background dynamics from eq. (1.1) was shown to be consistent with observations for small γ, i.e. $\gamma \lesssim 10^{-2}$ [10].

The potential term in eq. (1.1) is important for the global dynamics of the model and modifies the original Brans-Dicke attractor with power-law time dependence of the scalar field in presence of non-relativistic matter, i.e. $a(t) = (t/t_0)^{(2\omega_{\rm BD}+2)/(3\omega_{\rm BD}+4)}$ and $\Phi = \Phi_0 (t/t_0)^{2/(3\omega_{\rm BD}+4)}$. At recent times, the potential term drives the Universe into acceleration and Einstein gravity plus a cosmological constant with a time-independent value of the scalar field emerge as an attractor among homogeneous cosmologies for the model in eq. (1.1).

In this paper we study structure formation in the IG dark energy with a quartic potential in eq. (1.1). We study how gravitational instability at linear level depends on γ through a dedicated Einstein-Boltzmann code. We then use these theoretical predictions for cosmological observables to constrain the model with the Planck 2013 data [11–13], a compilation of baryonic acoustic oscillations (BAO) data [14–16] and local measurements of the Hubble constant [17–19].

2 Dark energy within induced gravity

The Friedmann and the Klein-Gordon equations for IG in a flat Robertson-Walker metric are respectively:

$$H^2 + 2H\frac{\dot\sigma}{\sigma} = \frac{\sum_i \rho_i + V(\sigma)}{3\gamma\sigma^2} + \frac{\dot\sigma^2}{6\gamma\sigma^2} \tag{2.1}$$

$$\ddot\sigma + 3H\dot\sigma + \frac{\dot\sigma^2}{\sigma} + \frac{1}{(1+6\gamma)}\left(V_{,\sigma} - \frac{4V}{\sigma}\right) = \frac{1}{(1+6\gamma)}\frac{\sum_i(\rho_i - 3p_i)}{\sigma} \tag{2.2}$$

once the Einstein trace equation:

$$-\gamma\sigma^2 R = T - (1+6\gamma)\partial_\mu\sigma\partial^\mu\sigma - 4V - 6\gamma\sigma\Box\sigma \tag{2.3}$$

is used. In the above $V_{,\sigma}$ denotes the derivative of the potential $V(\sigma)$ with respect to σ, the index i runs over all fluid components, i.e. baryons, cold dark matter (CDM), photons and neutrinos, and we use a dot for the derivative with respect to the cosmic time. When considering $V \propto \sigma^4$ the potential cancels out from the Klein-Gordon equation and the scalar field is driven by non-relativistic matter. In the rest of the paper we will restrict ourselves to $V(\sigma) = \lambda\sigma^4/4$.

We consider the scalar field σ at rest deep in the radiation era, since an initial non-vanishing time derivative would be rapidly dissipated [10]. The scalar field is then driven by non-relativistic matter to an asymptotically value higher than the one it had in the radiation era as can be seen in the left panel of figure 1; when the scalar field freezes the Universe is driven in a de Sitter era by the scalar field potential which behaves as an effective cosmological constant [8, 10], as can be seen in the central panel of figure 1. Since σ regulates the gravitational strength in the Friedmann equations, the present value of the field σ_0 can be connected the gravitational constant G measured in laboratory Cavendish-type and solar system experiments by the relation:

$$\gamma\sigma_0^2 = \frac{1}{8\pi G}\frac{1+8\gamma}{1+6\gamma} \tag{2.4}$$

where $G = 6.67 \times 10^{-8}$ N cm^3 g^{-1} s^{-2}. The above equation assumes that σ is effectively massless on Solar System scales. Note that the scalar field σ is effectively massless in the radiation dominated era, as can be seen in eq. (2.2).

JCAP08(2015)017

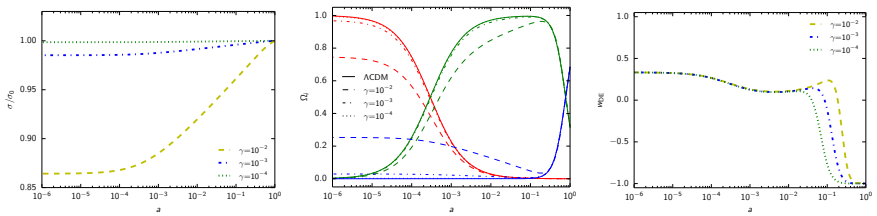

Figure 1. Evolution of σ/σ_0 (left panel), Ω_i (middle panel) and $w_{\rm DE}$ (right panel) as function of $\ln(a)$ for different choices of γ.

The evolution of the background cosmology can be easily compared with dark energy in Einstein gravity with a Newton's constant $\tilde{G}_N$ given by the scalar field value at present $\tilde{G} = (8\pi\gamma\sigma_0)^{-1}$. The Friedmann equation can be therefore rewritten by introducing an effective dark energy component [20], whose energy and pressure densities for this model are [10]:

$$\rho_{\rm DE} = \frac{\sigma_0^2}{\sigma^2}\left(\frac{\dot\sigma}{2} - 6\gamma H\dot\sigma\sigma + \lambda\frac{\sigma^4}{4}\right) + \sum_i \rho_i\left(\frac{\sigma_0^2}{\sigma^2} - 1\right)$$
$$p_{\rm DE} = \frac{\sigma_0^2}{\sigma^2}\left[\frac{\dot\sigma}{2} - 2\gamma H\dot\sigma\sigma - \lambda\frac{\sigma^4}{4} + \sum_i \frac{2\gamma\rho_i + p_i}{1+6\gamma}\right] - \sum_i p_i\,. \tag{2.5a}$$

In the central panel of figure 1 we display the time evolution of the density contrasts of radiation — $\Omega_{\rm R} \equiv (\rho_\nu + \rho_\gamma)/(3\gamma\sigma_0^2H^2)$ — in red, matter — $\Omega_{\rm M} \equiv (\rho_b + \rho_{\rm CDM})/(3\gamma\sigma_0^2H^2)$ — in green and effective dark energy — $\Omega_{\rm DE} \equiv \rho_{\rm DE}/(3\gamma\sigma_0^2H^2)$ — in blue. As a third panel in figure 1, we display the time evolution of the parameter of state of the effective dark energy component, $w_{\rm DE} \equiv p_{DE}/\rho_{DE}$.

3 The evolution of cosmological fluctuations

As for the background, we study linear fluctuations in the Jordan frame. We consider metric fluctuation in the longitudinal gauge:

$$ds^2 = -dt^2\,(1 + 2\Psi(t,\mathbf{x})) + a^2(t)\,(1 - 2\Phi(t,\mathbf{x}))\,dx^i dx_i \tag{3.1}$$

and for the scalar field:

$$\sigma(t,\mathbf{x}) = \sigma(t) + \delta\sigma(t,\mathbf{x})\,. \tag{3.2}$$

The perturbed Einstein equations for our IG model with a quartic potential in the longitudinal gauge are:

$$3H\left(\dot\Phi + H\Psi\right) + \frac{k^2}{a^2}\Phi + 3\frac{\dot\sigma}{\sigma}\left(\dot\Phi + 2H\Psi\right) - \frac{\dot\sigma^2}{2\gamma\sigma^2}\Psi =$$
$$-\frac{1}{2\gamma\sigma^2}\left[3\dot\sigma\,\delta\dot\sigma - 6H^2\gamma\sigma\,\delta\sigma - 6H\gamma\left(\dot\sigma\,\delta\sigma + \sigma\,\delta\dot\sigma\right) - \frac{2\gamma k^2}{a^2}\delta\sigma + \sum_i \delta\rho_i + \lambda\sigma^3\delta\sigma\right], \tag{3.3a}$$
$$\dot\Phi + \Psi\left(H + \frac{\dot\sigma}{\sigma}\right) = \frac{a}{2k^2}\frac{\sum_i(\rho_i + p_i)\theta_i}{\gamma\sigma^2} + \frac{\delta\sigma}{\sigma}\left[\left(1 + \frac{1}{2\gamma}\right)\frac{\dot\sigma}{\sigma} - H\right] + \frac{\delta\dot\sigma}{\sigma}, \tag{3.3b}$$
$$\Phi - \Psi = \frac{2\delta\sigma}{\sigma} + \frac{3a^2}{2k^2}\frac{\sum_i(\rho_i + p_i)\bar\sigma_i}{\gamma\sigma^2}\,. \tag{3.3c}$$

JCAP08(2015)017

In the above $\rho_i\,, p_i$ $(\delta\rho_i\,, \delta p_i)$ denote the energy and (longitudinal) pressure density perturbations for each matter component, respectively. The velocity potential and the anisotropic stress are denoted by θ_i and $\bar{\sigma}_i$. We refer to ref. [21] for the conservation of the CDM, baryons, photons and neutrino energy-momentum tensors, since these equations are unchanged from those in Einstein gravity.

The Klein-Gordon equation at linear order in the longitudinal gauge is:

$$\begin{aligned}\delta\ddot{\sigma} + \delta\dot{\sigma}\left(3H + 2\frac{\dot{\sigma}}{\sigma}\right) + \left[\frac{k^2}{a^2} - \frac{\dot{\sigma}^2}{\sigma^2} + \frac{\sum_i(\rho_i - 3p_i)}{(1+6\gamma)\sigma^2}\right]\delta\sigma \\ = \frac{2\Psi\sum_i(\rho_i - 3p_i)}{(1+6\gamma)\sigma} + \frac{\sum_i(\delta\rho_i - 3\delta p_i)}{(1+6\gamma)\sigma} + \dot{\sigma}\left(3\dot{\Phi} + \dot{\Psi}\right)\,.\end{aligned} \tag{3.4}$$

It is interesting to note that the equation for the field fluctuation does not depend on the potential explicitly for the self-interacting case, as for the background in eq. (2.2).

We have modified the publicly available Einstein-Boltzmann code CLASS[1] [22, 23] to evolve background and linear fluctuations within induced gravity. Previous implementations of induced gravity in Einstein-Boltzmann codes include refs. [24–28].

We initialize the fluctuation of the metric and of the matter components with adiabatic initial condition deep in the radiation era. We have tested our numerical results from our modified code against analytic approximations derived within the matter era. To this purpose we consider the quantity $\mu(k,a)$ which parametrize the deviations of Ψ from Einstein gravity [29, 30]. We consider the definition for $\mu(k,a)$ which holds also during the radiation dominated regime as in ref. [31]:

$$k^2\Psi = -4\pi G a^2\mu(k,a)\left[\Delta + 3(\rho+p)\bar{\sigma}\right] \tag{3.5}$$

where $\Delta = \sum_i \delta\rho_i + 3aH(\rho_i + p_i)\theta_i/k^2$, with $\delta_i = \delta\rho_i/\rho_i$ and θ_i is the velocity potential. Analogously we consider the deviations from Einstein gravity of the difference between the Newtonian potentials, parametrized by δ, whose definition valid also in the radiation dominated regime is [31]:

$$k^2[\Phi - \delta(k,a)\Psi] = 12\pi G a^2\mu(k,a)(\rho+p)\bar{\sigma} \tag{3.6}$$

Our results are shown in figure 2. In the left panel we show the evolution of $\mu(k,a)$ for two wavenumbers ($k = 0.05\,, 0.005$ Mpc^{-1}) and two values of the coupling to the Ricci curvature ($\gamma = 10^{-2}\,, 10^{-3}$). We compare our numerical results for $\mu(k,a)$ to the analytic approximation in the matter era:

$$\mu(k,a) = \frac{\sigma_0^2}{\sigma^2} \tag{3.7}$$

which is derived from ref. [30] for our choice of the potential and for our identification of the gravitational constant in eq. (2.4). Well after matter-radiation equivalence, the quasi-static analytic approximation for $k \gg aH$ in the matter era for $\mu(k,a)$ independent on k is well recovered. In the right panel of figure 2, we compare the evolution of $\delta(k,a)$ for the same two wavenumbers and two values of the coupling γ with the quasi-static approximation [5, 32, 33]:

$$\delta(k,a) = \frac{1+4\gamma}{1+8\gamma}\,. \tag{3.8}$$

Again, the analytic quasi-static approximation holds well after matter-radiation equality for sub-Hubble scales.

[1] www.class-code.net.

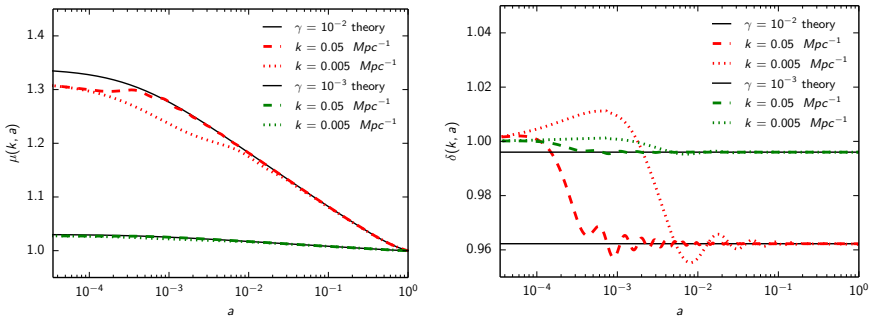

Figure 2. Comparison of theoretical approximations for μ and δ which parametrize deviations from Einstein gravity (black lines) with our numerical results for two wavenumbers (k Mpc $= 0.05\,, 0.005$) and two values of the coupling to the Ricci curvature ($\gamma = 10^{-2}\,, 10^{-3}$).

The agreement between our numerical treatment and the quasi-static approximation means that our self-consistent treatment of background and linear perturbations is sufficiently ready for precision cosmology. The two panels in figure 2 also show how the time evolution for μ and δ, independent on k, recovered within the quasi-static approximation is not valid when the wavelength is larger than the Hubble radius: predictions for CMB anisotropies in this model would be therefore affected by considering δ constant and equal to the value obtained within the quasi-static approximation at *all* times.

4 CMB anisotropies and matter power spectrum

In the left panel of figure 3 are shown the power spectra of the CMB temperature anisotropies for different values of γ (10^{-2}, 10^{-3}, 10^{-4}). The relative differences with respect to the ΛCDM reference model are shown in the right panel of figure 3. The change in the matter-radiation equality present in this scalar-tensor model [34] induces relative differences in the temperature power spectrum at few percent level for $\gamma = 10^{-3}$.

In figures 4, 5 we display the predictions for the spectrum of lensing potential and its correlation with the temperature field. In figure 6 we display the (linear) matter power spectrum at $z = 0$ and the relative differences with respect to the ΛCDM reference model. Overall, differences at the percent level are obtained for $\gamma = 10^{-3}$ in different cosmological observables.

5 Constraints from cosmological observations

We explore the parameter space by the Monte Carlo code for Cosmological Parameter extraction MONTE PYTHON[2] [35] connected to the modified version of the Einstein-Boltzmann code CLASS used in the previous sections. We use the nominal mission data release from PLANCK, available from the Planck Legacy Archive[3] [11]. The PLANCK likelihood covering

[2] www.montepython.net.
[3] http://pla.esac.esa.int/pla/#cosmology.

JCAP08(2015)017

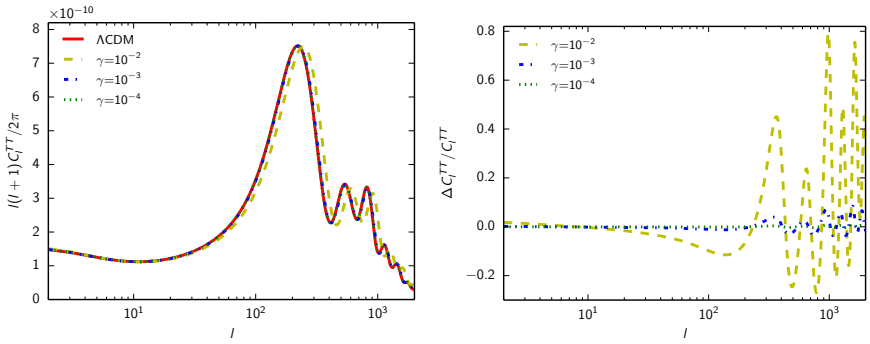

Figure 3. CMB temperature anisotropies power spectrum for different values of γ (left panel) and relative differences with respect to a reference ΛCDM (right panel).

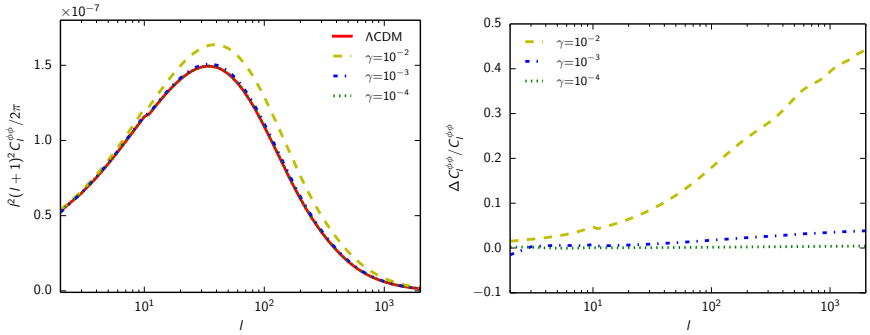

Figure 4. Lensing power spectrum for different values of γ (left panel) and relative differences with respect to a reference ΛCDM (right panel).

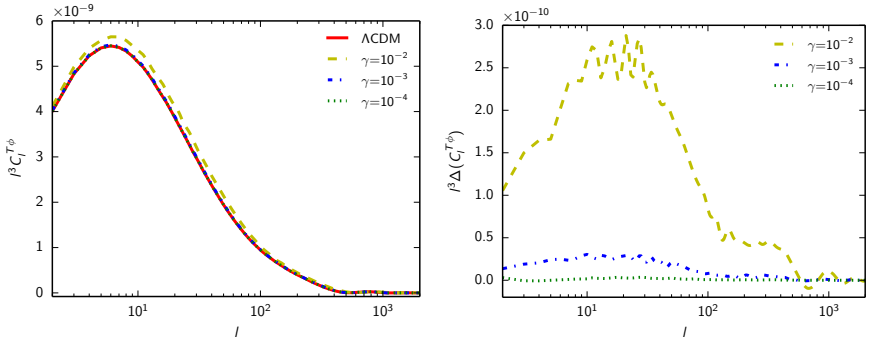

Figure 5. Temperature-lensing cross-correlation power spectrum for different values of γ (left panel) and differences with respect to a reference ΛCDM (right panel).

JCAP08(2015)017

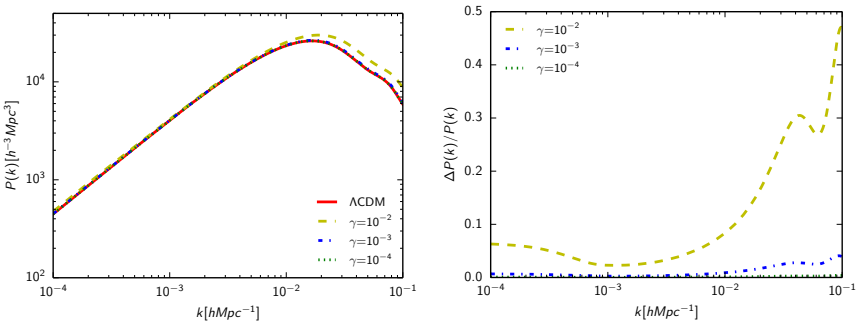

Figure 6. Linear matter power spectrum (at $z = 0$) for different values of γ (left panel) and relative differences with respect to a reference ΛCDM (right panel).

temperature anisotropies from $\ell = 2$ to 2500 is combined with the low-ℓ WMAP polarization data [36–38] (this combination is denoted as Planck 2013 in the following).

We use the Planck 2013 likelihood in combination with constraints on $D_V(\bar{z})/r_s$ (the ratio between the spherically averaged distance scale D_V to the effective survey redshift, $\bar{z}$, and the sound horizon, r_s) inferred from a compilation of BAO data. These are 6dFGRS data [14] at $\bar{z} = 0.106$, the SDSS-MGS data [15] at $\bar{z} = 0.15$, and the SDSS-DR11 CMASS and LOWZ data [16] at redshifts $\bar{z} = 0.57$ and 0.32.

We vary the parameters of the flat ΛCDM model, i.e. the baryon density ($\Omega_b h^2$), the CDM density ($\Omega_{\rm CDM}$), the reduced Hubble parameter ($h = H_0/(100\ {\rm km\ s^{-1}Mpc^{-1}})$), the reionization optical depth τ, the amplitude and tilt of the primordial spectrum of curvature perturbations (A_s and n_s) at the pivot scale $k_* = 0.05\ {\rm Mpc}^{-1}$. The IG dark energy model with quartic potential is described by these six plus *one extra* parameter which quantifies the coupling to the Ricci curvature.[4] Following ref. [39] we sample on the quantity ζ, defined as:

$$\zeta \equiv \ln(1 + 4\gamma) = \ln\left(1 + \frac{1}{\omega_{\rm BD}}\right) \tag{5.1}$$

with the prior $[0, 0.039]$ used in ref. [39]. In this paper we consider three massless neutrinos.[5] Nuisance parameters for foreground, calibration and beam uncertainties [11, 13].

Our results with Planck 2013 + BAO data for the main and derived parameters are summarized and compared with the ΛCDM values in table 1. The induced gravity model with a quartic potential is not preferred over Einstein gravity with Λ ($\Delta\chi^2 \simeq -2\ln\mathcal{L} = 0.7$).

[4]The parameter of the Lagrangian λ and the initial value of the scalar field σ_i deep inside the radiation era are chosen to reproduce the present value of h and of the field in eq. (2.4) by evolving the Friedmann and Klein-Gordon background equations.

[5]Note that the Planck collaboration assumes one massive neutrinos with a mass of 0.06 eV [13]. Given the interest in neutrino masses within modified gravity (see for example [40]), we will study this issue in the context of induced gravity in a separate publication. Even if the assumption of a mass of 0.06 eV has a small effect on the cosmological parameters at the Planck precision (as a $0.5\,\sigma$ shift to smaller value for H_0 [13]), we quote the results for a ΛCDM cosmology with three massless neutrinos in the following for a consistent comparison with the class of dark energy models studied here.

JCAP08(2015)017

	Planck 2013 + BAO ΛCDM	Planck 2013 + BAO
$10^5\Omega_{\rm b}h^2$	2215^{+24}_{-25}	2203 ± 25
$10^4\Omega_{\rm c}h^2$	1187^{+13}_{-14}	1207^{+18}_{-22}
H_0 [km s^{-1} Mpc^{-1}]	$68.4^{+0.6}_{-0.7}$	$69.5^{+0.9}_{-1.2}$
τ	$0.091^{+0.012}_{-0.014}$	$0.088^{+0.012}_{-0.013}$
$\ln\left(10^{10}A_{\rm s}\right)$	$3.089^{+0.024}_{-0.027}$	$3.090^{+0.024}_{-0.026}$
$n_{\rm s}$	0.9626 ± 0.0053	0.9611 ± 0.0053
ζ	...	< 0.0047 (95% CL)
$10^3\gamma$	...	< 1.2 (95% CL)
γ_{PN}	...	> 0.9953 (95% CL)
$\Omega_{\rm m}$	0.301 ± 0.008	0.295 ± 0.009
$\delta G_{\rm N}/G_{\rm N}$	...	$-0.015^{+0.013}_{-0.006}$
$10^{13}\dot{G}_{\rm N}(z=0)/G_{\rm N}$ [yr^{-1}]	...	$-0.61^{+0.55}_{-0.25}$
$10^{23}\ddot{G}_{\rm N}(z=0)/G_{\rm N}$ [yr^{-2}]	...	$0.86^{+0.33}_{-0.78}$

Table 1. Constraints on main and derived parameters (at 68% CL if not otherwise stated).

We quote the following Planck 2013 + BAO 95% CL constraint on the coupling to the Ricci curvature:

$$\gamma < 0.0012\,(95\,\%\ \text{CL, Planck 2013 + BAO})\,. \tag{5.2}$$

We quote as a derived parameter the corresponding constraint on the post-Newtonian parameter $\gamma_{\rm PN} = (1+4\gamma)/(1+8\gamma)$:[6]

$$0.9953 < \gamma_{\rm PN} < 1\ (95\,\%\ \text{CL, Planck 2013 + BAO})\,. \tag{5.3}$$

It is also useful to quote the derived constraints on the change of the Newton constant between the radiation era and the present time $\delta G_N/G_N \equiv (\sigma_i^2 - \sigma_0^2)/\sigma_0^2$:

$$\frac{\delta G_N}{G_N} = -0.015^{+0.013}_{-0.006}\,(95\,\%\ \text{CL, Planck 2013 + BAO}) \tag{5.4}$$

and the constraint on its derivative ($\dot{G}_N/G_N \equiv -2\dot{\sigma}_0/\sigma_0$) at present time:

$$\frac{\dot{G}_N}{G_N}(z=0) = -0.61^{+0.55}_{-0.25}\left[\times 10^{-13}\ yr^{-1}\right]\ (95\,\%\ \text{CL, Planck 2013 + BAO})\,. \tag{5.5}$$

The constraints derived here are tighter than those obtained in the literature with Planck 2013 data for similar scalar-tensor models with a power-law potential [39, 41] (see refs. [42–44] for analysis with pre-Planck data). Avilez and Skordis [41] considered the case of a constant potential in Brans-Dicke-like theory and quote $(1+6\gamma)/(1+8\gamma) = 1.07^{+0.11}_{-0.10}$

[6] In this class of models $\beta_{\rm PN} = 1$.

JCAP08(2015)017

	Planck 2013 + H_0^*	Planck 2013 + $H_0^\dagger$	Planck 2013 + BAO + $H_0^\dagger$
$10^5\Omega_b h^2$	2219 ± 28	2213^{+28}_{-29}	2203 ± 26
$10^4\Omega_c h^2$	1188^{+25}_{-26}	1194^{+25}_{-25}	1207^{+18}_{-22}
H_0 (km s^{-1} Mpc^{-1})	$74.1^{+2.3}_{-2.4}$	$72.1^{+2.2}_{-3.1}$	$69.64^{+0.88}_{-1.11}$
τ	$0.092^{+0.013}_{-0.014}$	$0.091^{+0.013}_{-0.015}$	$0.088^{+0.012}_{-0.014}$
$\ln(10^{10}A_s)$	$3.098^{+0.025}_{-0.027}$	$3.095^{+0.025}_{-0.028}$	$3.091^{+0.024}_{-0.027}$
n_s	$0.9704^{+0.0070}_{-0.0072}$	$0.9667^{+0.0075}_{-0.0078}$	$0.9613^{+0.0055}_{-0.0054}$
ζ	0.0056 ± 0.0023	< 0.0083 (95% CL)	0.0047 (95% CL)
$10^3\gamma$	1.4 ± 0.6	< 2.1 (95% CL)	< 1.2 (95% CL)
γ_{PN}	$0.9944^{+0.0023}_{-0.0022}$	> 0.9918 (95% CL)	> 0.9954 (95% CL)
Ω_m	$0.257^{+0.016}_{-0.019}$	$0.274^{+0.022}_{-0.021}$	$0.294^{+0.009}_{-0.008}$
$\delta G_N/G_N$	$-0.041^{+0.017}_{-0.016}$	-0.028 ± 0.012	$-0.016^{+0.010}_{-0.006}$
$10^{13}\dot{G}_N(z=0)/G_N$ [yr^{-1}]	$-1.56^{+0.61}_{-0.58}$	$-1.10^{+0.83}_{-0.49}$	$-0.64^{+0.52}_{-0.25}$
$10^{23}\ddot{G}_N(z=0)/G_N$ [yr^{-2}]	$2.4^{+0.9}_{-1.0}$	$1.7^{+0.7}_{-1.5}$	$0.89^{+0.24}_{-0.75}$

Table 2. Constraints on main and derived parameters at 68% CL (if not otherwise stated).

at 95% CL as the tightest constraint with a prior $\omega_{BD} > -3/2$; we obtain [0.998,1] as the 95% CL range for the same quantity with Planck 2013 + BAO by varying ζ in the interval $[0, 0.039]$. Li et al. [39] considered the case of a linear potential in Brans-Dicke (i.e. a quadratic potential in induced gravity) and quote $0 < \zeta < 0.549 \times 10^{-2}$ at 95% CL and $\dot{G}_N/G_N = -1.42^{+2.48}_{-2.27} \times 10^{-13}$ yr^{-1} at 68% CL from Planck 2013 with the same prior on ζ, although in combination with a different compilation of BAO data [39]. Note that for power-law potentials different from the quartic case studied here, Einstein gravity plus a cosmological constant with σ independent on time is not the attractor at future times [45]. We therefore expect that the models studied in refs. [39, 41] differ from the case of a quartic potential, in particular at recent redshifts.

5.1 Combination with local measurements

As from table 1, the model considered here prefers a higher value of the Hubble parameter H_0 with respect to ΛCDM. We therefore analyze the combination of the local measurements of the Hubble constant with Planck 2013 and BAO data. The local estimates of H_0 are consistently higher than those from CMB (and BAO) and this discrepancy became a 2.5 σ tension after the Planck 2013 release [13]. This tension might be sign of new physics, although reanalysis subsequent to the Planck 2013 release have highlighted how hidden systematics and underestimated uncertainties could hide in the local measurements of H_0 [18, 19]. For these reasons we consider separately the impact of two different local estimates of H_0, such as $H_0 = 73.8 \pm 2.4$ km s^{-1} Mpc^{-1} [17], denoted as H_0^*, and $H_0 = 70.6 \pm 3.0$ km s^{-1} Mpc^{-1} [19], denoted as $H_0^\dagger$. Our results are summarized in table 2 and figure 7.

With the higher local estimate of H_0^* [17] we obtain a posterior on ζ which is different at 2 σ level from Einstein gravity. With the lower estimate for H_0 obtained by Efstahiou [19] with the new revised geometric maser distance to NGC 4258 [18], we obtain a posterior probability for ζ compatible with Einstein gravity. As can be seen by comparing the last columns of table 1 and 2, the lower local estimate of $H_0^\dagger$ has almost a negligible impact when Planck 2013 and BAO data are combined.

JCAP08(2015)017

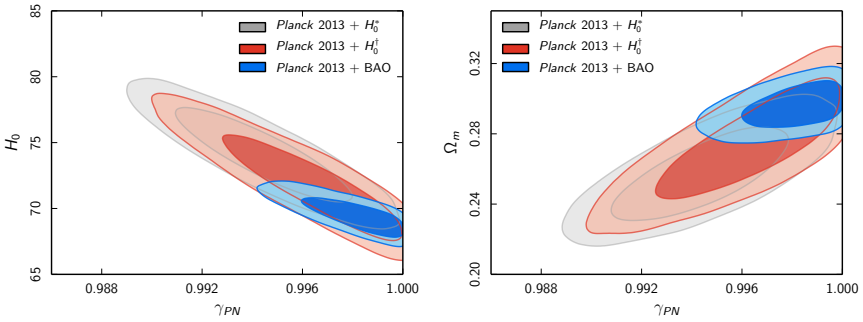

Figure 7. Comparison of marginalized joint 68% and 95% CL for (γ_{PN}, H_0) (left panel) and (γ_{PN}, Ω_m) (right panel) for Planck 2013 + H_0^* (grey contours), Planck 2013 + $H_0^\dagger$ (red contours) and Planck 2013 + BAO (blue contours).

6 Conclusions

We have studied structure formation in a induced gravity dark energy model with a quartic potential. In this model the current acceleration stage of the Universe and an accompanying change in the gravitational constant on large scales are due to a change in the background scalar field triggered by the onset of the matter dominated stage [8, 10].

We have shown that the model approaches Einstein gravity plus a cosmological constant in the limit $\gamma \to 0$ *also* at linear level. We have shown how the quasi-static parametrization with μ and γ independent on k holds only well after matter-radiation equality for sub-Hubble scales.

We have derived CMB and BAO combined constraints on γ for the case of induced gravity with a quartic potential. By using Planck 2013 [12] and BAO [14–16] data we derive the 95% CL constraint $\gamma < 0.0012$, which is tighter than previous cosmological constraints on similar models [39, 41]. This cosmological constraint is compatible, but weaker than those within the Solar System [10] which can be derived by Cassini data [46]. Since there is a positive correlation between γ and H_0, the combination of local measurements of H_0 [17, 19] allows larger values of γ, but not at statistical significant level. This analysis shows how a self-consistent variation of G from the radiation era to the present time can be tightly constrained from Planck 2013 and BAO data at the percent level. It will be interesting to see how Planck 2015 data [47] change these constraints [48].

Acknowledgments

We wish to thank Julien Lesgourgues, Thomas Tram and Benjamin Audren for many useful suggestions on the use of the CLASS code and MONTEPYTHON code. We wish to thank Massimo Rossi for careful checking of the equations for cosmological perturbations, Kazuya Koyama for discussions on the quasi-static approximation and Levon Pogosian for useful comments on the draft. This work has been done within the Labex ILP (reference ANR-10-LABX-63) part of the Idex SUPER, and received financial state aid managed by the Agence Nationale de la Recherche, as part of the programme Investissements d'avenir under the reference ANR-11-IDEX-0004-02. The support by the "ASI/INAF Agreement 2014-024-R.0 for the Planck LFI Activity of Phase E2" is acknowledged.

JCAP08(2015)017

References

[1] B.L. Spokoiny, *Inflation and generation of perturbations in broken symmetric theory of gravity*, *Phys. Lett.* **B 147** (1984) 39 [INSPIRE].

[2] F. Lucchin, S. Matarrese and M.D. Pollock, *Inflation With a Nonminimally Coupled Scalar Field*, *Phys. Lett.* **B 167** (1986) 163 [INSPIRE].

[3] D.S. Salopek, J.R. Bond and J.M. Bardeen, *Designing Density Fluctuation Spectra in Inflation*, *Phys. Rev.* **D 40** (1989) 1753 [INSPIRE].

[4] R. Fakir and W.G. Unruh, *Improvement on cosmological chaotic inflation through nonminimal coupling*, *Phys. Rev.* **D 41** (1990) 1783 [INSPIRE].

[5] B. Boisseau, G. Esposito-Farese, D. Polarski and A.A. Starobinsky, *Reconstruction of a scalar tensor theory of gravity in an accelerating universe*, *Phys. Rev. Lett.* **85** (2000) 2236 [gr-qc/0001066] [INSPIRE].

[6] C. Brans and R.H. Dicke, *Mach's principle and a relativistic theory of gravitation*, *Phys. Rev.* **124** (1961) 925 [INSPIRE].

[7] A. Zee, *The Horizon Problem and the Broken Symmetric Theory of Gravity*, *Phys. Rev. Lett.* **44** (1980) 703 [INSPIRE].

[8] F. Cooper and G. Venturi, *Cosmology and Broken Scale Invariance*, *Phys. Rev.* **D 24** (1981) 3338 [INSPIRE].

[9] C. Wetterich, *Cosmology and the Fate of Dilatation Symmetry*, *Nucl. Phys.* **B 302** (1988) 668 [INSPIRE].

[10] F. Finelli, A. Tronconi and G. Venturi, *Dark Energy, Induced Gravity and Broken Scale Invariance*, *Phys. Lett.* **B 659** (2008) 466 [arXiv:0710.2741] [INSPIRE].

[11] Planck collaboration, P.A.R. Ade et al., *Planck 2013 results. I. Overview of products and scientific results*, *Astron. Astrophys.* **571** (2014) A1 [arXiv:1303.5062] [INSPIRE].

[12] Planck collaboration, P.A.R. Ade et al., *Planck 2013 results. XV. CMB power spectra and likelihood*, *Astron. Astrophys.* **571** (2014) A15 [arXiv:1303.5075] [INSPIRE].

[13] Planck collaboration, P.A.R. Ade et al., *Planck 2013 results. XVI. Cosmological parameters*, *Astron. Astrophys.* **571** (2014) A16 [arXiv:1303.5076] [INSPIRE].

[14] F. Beutler, C. Blake, M. Colless, D.H. Jones, L. Staveley-Smith, L. Campbell et al., *The 6dF Galaxy Survey: Baryon Acoustic Oscillations and the Local Hubble Constant*, *Mon. Not. Roy. Astron. Soc.* **416** (2011) 3017 [arXiv:1106.3366] [INSPIRE].

[15] A.J. Ross, L. Samushia, C. Howlett, W.J. Percival, A. Burden and M. Manera, *The clustering of the SDSS DR7 main galaxy sample — I. A 4 per cent distance measure at $z = 0.15$*, *Mon. Not. Roy. Astron. Soc.* **449** (2015) 835 [arXiv:1409.3242] [INSPIRE].

[16] BOSS collaboration, L. Anderson et al., *The clustering of galaxies in the SDSS-III Baryon Oscillation Spectroscopic Survey: baryon acoustic oscillations in the Data Releases 10 and 11 Galaxy*, *Mon. Not. Roy. Astron. Soc.* **441** (2014) 24 [arXiv:1312.4877] [INSPIRE].

[17] A.G. Riess, L. Macri, S. Casertano, H. Lampeitl, H.C. Ferguson, A.V. Filippenko et al., *A 3% Solution: Determination of the Hubble Constant with the Hubble Space Telescope and Wide Field Camera 3*, *Astrophys. J.* **730** (2011) 119 [*Erratum ibid.* **732** (2011) 129] [arXiv:1103.2976] [INSPIRE].

[18] E.M.L. Humphreys, M.J. Reid, J.M. Moran, L.J. Greenhill and A.L. Argon, *Toward a New Geometric Distance to the Active Galaxy NGC 4258. III. Final Results and the Hubble Constant*, *Astrophys. J.* **775** (2013) 13 [arXiv:1307.6031] [INSPIRE].

JCAP08(2015)017

[19] G. Efstathiou, *H_0 revisited*, *Mon. Not. Roy. Astron. Soc.* **440** (2014) 1138 [arXiv:1311-3461] [INSPIRE].

[20] R. Gannouji, D. Polarski, A. Ranquet and A.A. Starobinsky, *Scalar-Tensor Models of Normal and Phantom Dark Energy*, *JCAP* **09** (2006) 016 [astro-ph/0606287] [INSPIRE].

[21] C.-P. Ma and E. Bertschinger, *Cosmological perturbation theory in the synchronous and conformal Newtonian gauges*, *Astrophys. J.* **455** (1995) 7 [astro-ph/9506072] [INSPIRE].

[22] J. Lesgourgues, *The Cosmic Linear Anisotropy Solving System (CLASS) I: Overview*, arXiv:1104.2932 [INSPIRE].

[23] D. Blas, J. Lesgourgues and T. Tram, *The Cosmic Linear Anisotropy Solving System (CLASS) II: Approximation schemes*, *JCAP* **07** (2011) 034 [arXiv:1104.2933] [INSPIRE].

[24] X.-l. Chen and M. Kamionkowski, *Cosmic microwave background temperature and polarization anisotropy in Brans-Dicke cosmology*, *Phys. Rev.* **D 60** (1999) 104036 [astro-ph/9905368] [INSPIRE].

[25] F. Perrotta, C. Baccigalupi and S. Matarrese, *Extended quintessence*, *Phys. Rev.* **D 61** (1999) 023507 [astro-ph/9906066] [INSPIRE].

[26] A. Riazuelo and J.-P. Uzan, *Cosmological observations in scalar-tensor quintessence*, *Phys. Rev.* **D 66** (2002) 023525 [astro-ph/0107386] [INSPIRE].

[27] R. Nagata, T. Chiba and N. Sugiyama, *Observational consequences of evolution of primordial fluctuations in scalar - tensor cosmology*, *Phys. Rev.* **D 66** (2002) 103510 [astro-ph/0209140] [INSPIRE].

[28] F. Wu, L.-e. Qiang, X. Wang and X. Chen, *Cosmic microwave background with Brans-Dicke Gravity: I. Covariant Formulation*, *Phys. Rev.* **D 82** (2010) 083002 [arXiv:0903.0384] [INSPIRE].

[29] G.-B. Zhao, L. Pogosian, A. Silvestri and J. Zylberberg, *Searching for modified growth patterns with tomographic surveys*, *Phys. Rev.* **D 79** (2009) 083513 [arXiv:0809.3791] [INSPIRE].

[30] G.-B. Zhao, H. Li, E.V. Linder, K. Koyama, D.J. Bacon and X. Zhang, *Testing Einstein Gravity with Cosmic Growth and Expansion*, *Phys. Rev.* **D 85** (2012) 123546 [arXiv:1109.1846] [INSPIRE].

[31] A. Hojjati, L. Pogosian and G.-B. Zhao, *Testing gravity with CAMB and CosmoMC*, *JCAP* **08** (2011) 005 [arXiv:1106.4543] [INSPIRE].

[32] L. Amendola, M. Kunz and D. Sapone, *Measuring the dark side (with weak lensing)*, *JCAP* **04** (2008) 013 [arXiv:0704.2421] [INSPIRE].

[33] S. Tsujikawa, *Matter density perturbations and effective gravitational constant in modified gravity models of dark energy*, *Phys. Rev.* **D 76** (2007) 023514 [arXiv:0705.1032] [INSPIRE].

[34] A.R. Liddle, A. Mazumdar and J.D. Barrow, *Radiation matter transition in Jordan-Brans-Dicke theory*, *Phys. Rev.* **D 58** (1998) 027302 [astro-ph/9802133] [INSPIRE].

[35] B. Audren, J. Lesgourgues, K. Benabed and S. Prunet, *Conservative Constraints on Early Cosmology: an illustration of the Monte Python cosmological parameter inference code*, *JCAP* **02** (2013) 001 [arXiv:1210.7183] [INSPIRE].

[36] WMAP collaboration, L. Page et al., *Three year Wilkinson Microwave Anisotropy Probe (WMAP) observations: polarization analysis*, *Astrophys. J. Suppl.* **170** (2007) 335 [astro-ph/0603450] [INSPIRE].

[37] WMAP collaboration, C.L. Bennett et al., *Nine-Year Wilkinson Microwave Anisotropy Probe (WMAP) Observations: Final Maps and Results*, *Astrophys. J. Suppl.* **208** (2013) 20 [arXiv:1212.5225] [INSPIRE].

JCAP08(2015)017

[38] WMAP collaboration, G. Hinshaw et al., *Nine-Year Wilkinson Microwave Anisotropy Probe (WMAP) Observations: Cosmological Parameter Results*, *Astrophys. J. Suppl.* **208** (2013) 19 [arXiv:1212.5226] [INSPIRE].

[39] Y.-C. Li, F.-Q. Wu and X. Chen, *Constraints on the Brans-Dicke gravity theory with the Planck data*, *Phys. Rev.* **D 88** (2013) 084053 [arXiv:1305.0055] [INSPIRE].

[40] H. Motohashi, A.A. Starobinsky and J. Yokoyama, *Cosmology based on f(R) gravity admits 1 eV sterile neutrinos*, *Phys. Rev. Lett.* **110** (2013) 121302 [arXiv:1203.6828].

[41] A. Avilez and C. Skordis, *Cosmological constraints on Brans-Dicke theory*, *Phys. Rev. Lett.* **113** (2014) 011101 [arXiv:1303.4330] [INSPIRE].

[42] R. Nagata, T. Chiba and N. Sugiyama, *WMAP constraints on scalar- tensor cosmology and the variation of the gravitational constant*, *Phys. Rev.* **D 69** (2004) 083512 [astro-ph/0311274] [INSPIRE].

[43] V. Acquaviva, C. Baccigalupi, S.M. Leach, A.R. Liddle and F. Perrotta, *Structure formation constraints on the Jordan-Brans-Dicke theory*, *Phys. Rev.* **D 71** (2005) 104025 [astro-ph/0412052] [INSPIRE].

[44] F. Wu and X. Chen, *Cosmic microwave background with Brans-Dicke gravity II: constraints with the WMAP and SDSS data*, *Phys. Rev.* **D 82** (2010) 083003 [arXiv:0903.0385] [INSPIRE].

[45] A. Cerioni, F. Finelli, A. Tronconi and G. Venturi, *Inflation and Reheating in Induced Gravity*, *Phys. Lett.* **B 681** (2009) 383 [arXiv:0906.1902] [INSPIRE].

[46] B. Bertotti, L. Iess and P. Tortora, *A test of general relativity using radio links with the Cassini spacecraft*, *Nature* **425** (2003) 374 [INSPIRE].

[47] PLANCK collaboration, R. Adam et al., *Planck 2015 results. I. Overview of products and scientific results*, arXiv:1502.01582 [INSPIRE].

[48] M. Ballardini et al., *Planck 2015 constraints on induced gravity dark energy models*, in preparation.

JCAP08(2015)017

Bibliography

Abazajian K. N., et al., 2016, preprint, (arXiv:1610.02743) 17, 117

Acquaviva V., Baccigalupi C., Leach S. M., Liddle A. R., Perrotta F., 2005, Phys. Rev., D71, 104025 114

Aghanim N., Desert F. X., Puget J. L., Gispert R., 1996, Astronomy & Astrophysics, 311, 1 37

Aghanim N., Majumdar S., Silk J., 2008, Reports on Progress in Physics, 71, 066902 10

Alonso D., Bull P., Ferreira P. G., Santos M. G., 2015, Monthly Notices of the Royal Astronomical Society, 447, 400 37, 48

Amendola L., Kunz M., Sapone D., 2008, Journal of Cosmology and Astroparticle Physics, 4, 013 111

Anderson L., et al., 2014, Monthly Notices of the Royal Astronomical Society, 441, 24 113

Andersson B.-G., Lazarian A., Vaillancourt J. E., 2015, Annual Review of Astronomy and Astrophysics, 53, 501 23

Arcadi G., Dutra M., Ghosh P., Lindner M., Mambrini Y., Pierre M., Profumo S., Queiroz F. S., 2017, preprint, (arXiv:1703.07364) 5

Ashby N., Bartlett D., Wyss W., 2005, General Relativity and Gravitation, 1989: Proceedings of the 12th International Conference on General Relativity and Gravitation. Cambridge University Press 111

Audren B., Lesgourgues J., Benabed K., Prunet S., 2013, Journal of Cosmology and Astroparticle Physics, 2, 001 112

Avilez A., Skordis C., 2014, Physical Review Letters, 113, 011101 114

BICEP2 and Keck Array Collaborations et al., 2015, The Astrophysical Journal, 806, 206 17

Baccigalupi C., et al., 2000, Monthly Notices of the Royal Astronomical Society, 318, 769 62

Baccigalupi C., Perrotta F., de Zotti G., Smoot G. F., Burigana C., Maino D., Bedini L., Salerno E., 2004, Monthly Notices of the Royal Astronomical Society, 354, 55 63

Ballardini M., Finelli F., Umiltà C., Paoletti D., 2016, Journal of Cosmology and Astroparticle Physics, 5, 067 104, 106, 109, 110, 115, 116

Ballardini M., Sapone D., Umiltà C., Finelli F., Paoletti D., 2017, in preparation for submission to MNRAS 117

Barreiro R. B., Hobson M. P., Banday A. J., Lasenby A. N., Stolyarov V., Vielva P., Górski K. M., 2004, Monthly Notices of the Royal Astronomical Society, 351, 515 41

Basak S., Delabrouille J., 2012, Monthly Notices of the Royal Astronomical Society, 419, 1163 44

Basak S., Delabrouille J., 2013, Monthly Notices of the Royal Astronomical Society, 435, 18 44

Battye R. A., Browne I. W. A., Peel M. W., Jackson N. J., Dickinson C., 2011, Monthly Notices of the Royal Astronomical Society, 413, 132 23

Bedini L., Herranz D., Salerno E., Baccigalupi C., Kuruouglu E. E., Tonazzini A., 2005, EURASIP Journal on Applied Signal Processing, 2005, 2400 42, 43

Bellini E., et al., 2017, in preparation 112

Benabed K., Cardoso J.-F., Prunet S., Hivon E., 2009, Monthly Notices of the Royal Astronomical Society, 400, 219 67

Bennett C. L., et al., 2003, The Astrophysical Journal, 583, 1 14

Bennett C. L., et al., 2013a, Astrophysical Journal, Supplement, 208, 20 14, 39, 41, 42, 44

Bennett C. L., et al., 2013b, Astrophysical Journal, Supplement, 208, 20 112

Bersanelli, M. et al., 2010, Astronomy & Astrophysics, 520, A4 15

Bertotti B., Iess L., Tortora P., 2003, Nature, 425, 374 111

Beutler F., et al., 2011, Monthly Notices of the Royal Astronomical Society, 416, 3017 113

Blas D., Lesgourgues J., Tram T., 2011, Journal of Cosmology and Astroparticle Physics, 7, 034 112

Bobin J., Moudden Y., Starck J.-L., Fadili J., Aghanim N., 2008, Statistical Methodology, 5, 307 45

Bobin J., Starck J.-L., Sureau F., Basak S., 2013, Astronomy & Astrophysics, 550, A73 45, 48

Bobin J., Sureau F., Starck J.-L., Rassat A., Paykari P., 2014, Astronomy & Astrophysics, 563, A105 45

Boisseau B., Esposito-Farèse G., Polarski D., Starobinsky A. A., 2000, Physical Review Letters, 85, 2236 111

Bonaldi A., Bedini L., Salerno E., Baccigalupi C., De Zotti G., 2006, Monthly Notices of the Royal Astronomical Society, 373, 271 42, 43

Bonaldi A., Ricciardi S., Leach S., Stivoli F., Baccigalupi C., de Zotti G., 2007, Monthly Notices of the Royal Astronomical Society, 382, 1791 43, 45

Bottino M., Banday A. J., Maino D., 2008, Monthly Notices of the Royal Astronomical Society, 389, 1190 63

Bottino M., Banday A. J., Maino D., 2010, Monthly Notices of the Royal Astronomical Society, 402, 207 63

Bouchet F. R., Gispert R., 1999, New Astronomy, 4, 443 45

Bradt H., 2014, Astrophysics Processes. Cambridge University Press 25

Brans C., Dicke R. H., 1961, Phys. Rev., 124, 925 107

Burnham K. P., Anderson D. R., 2001, Wildlife Research, 28, 111 54

Cardoso J.-F., 2001, in In Proc. ICA 2001. pp 1–6 51

Cardoso J.-F., 2017, On Extracting the Cosmic Microwave Background from Multi-channel Measurements. Springer International Publishing, Cham, pp 403–413, doi:10.1007/978-3-319-53547-0$_3$8, https://doi.org/10.1007/978-3-319-53547-0_38 56

Cardoso J.-F., Le Jeune M., Delabrouille J., Betoule M., Patanchon G., 2008, IEEE Journal of Selected Topics in Signal Processing, 2, 735 45, 54, 56, 60

Carlstrom J. E., Holder G. P., Reese E. D., 2002, Annual Review of Astronomy and Astrophysics, 40, 643 38

Cerioni A., Finelli F., Tronconi A., Venturi G., 2009, Phys.Lett., B681, 383 114

Chapman E., et al., 2015, Advancing Astrophysics with the Square Kilometre Array (AASKA14), p. 5 37

Chen X., Kamionkowski M., 1999, Phys. Rev. D, 60, 104036 112

Chon G., Challinor A., Prunet S., Hivon E., Szapudi I., 2004, Monthly Notices of the Royal Astronomical Society, 350, 914 78

Cirelli M., 2015, preprint, (arXiv:1511.02031) 5

Comon P., 1994, Signal Process., 36, 287 51

Conley A., et al., 2011, Astrophysical Journal, Supplement, 192, 1 4

Cooray A., Sheth R., 2002, Physics Reports, 372, 1 35

Crill B. P., et al., 2008, in Space Telescopes and Instrumentation 2008: Optical, Infrared, and Millimeter. p. 70102P (arXiv:0807.1548), doi:10.1117/12.787446 16

Delabrouille J., Cardoso J.-F., 2009, Diffuse Source Separation in CMB Observations. Springer Berlin Heidelberg, Berlin, Heidelberg, pp 159–205 23, 39, 46

Delabrouille J., Cardoso J.-F., Patanchon G., 2003, Monthly Notices of the Royal Astronomical Society, 346, 1089 48, 52, 54, 55, 57

Delabrouille J., Cardoso J.-F., Le Jeune M., Betoule M., Fay G., Guilloux F., 2009, Astronomy & Astrophysics, 493, 835 44

Dick J., Remazeilles M., Delabrouille J., 2010, Monthly Notices of the Royal Astronomical Society, 401, 1602 44

Dickinson C., 2016, preprint, (arXiv:1606.03606) 23

Dickinson C., Davies R. D., Davis R. J., 2003, Monthly Notices of the Royal Astronomical Society, 341, 369 27

Dodelson S., 2003, Modern cosmology 8

Donzelli S., et al., 2006, Monthly Notices of the Royal Astronomical Society, 369, 441 63

Draine B. T., Li A., 2007, The Astrophysical Journal, 657, 810 23

Duff S. M., et al., 2016, Journal of Low Temperature Physics, 184, 634 17

Dunkley J., et al., 2013, Journal of Cosmology and Astroparticle Physics, 7, 025 16

Efstathiou G., 2014, Monthly Notices of the Royal Astronomical Society, 440, 1138 115

Efstathiou G., Bond J. R., 1999, Monthly Notices of the Royal Astronomical Society, 304, 75 12

Eriksen H. K., et al., 2004, Astrophysical Journal, Supplement, 155, 227 40

Eriksen H. K., Jewell J. B., Dickinson C., Banday A. J., Górski K. M., Lawrence C. R., 2008, The Astrophysical Journal, 676, 10 40

Errard J., et al., 2015, The Astrophysical Journal, 809, 63 15

Fendt W. A., Wandelt B. D., 2007, Submitted to: Astrophys. J. 90

Fernández-Cobos R., Vielva P., Barreiro R. B., Martínez-González E., 2012, Monthly Notices of the Royal Astronomical Society, 420, 2162 39

Fields B. D., Molaro P., Sarkar S., 2014, preprint, (arXiv:1412.1408) 4

Finelli F., Tronconi A., Venturi G., 2008, Physics Letters B, 659, 466 105, 106, 108

Fixsen D. J., 2009, ApJ, 707, 916 13

Fort B., Mellier Y., 1994, The Astronomy and strophysics Review, 5, 239 4

Gamow G., 1946, Phys.Rev., 70, 572 4

Gannouji R., Polarski D., Ranquet A., Starobinsky A. A., 2006, JCAP, 9, 16 105

Gispert R., Lagache G., Puget J. L., 2000, Astronomy & Astrophysics, 360, 1 35

Gold B., et al., 2011, The Astrophysical Journal Supplement Series, 192, 15 28

Górski K. M., Hivon E., Banday A. J., Wandelt B. D., Hansen F. K., Reinecke M., Bartelmann M., 2005, The Astrophysical Journal, 622, 759 75

Grayson J. A., et al., 2016, in Millimeter, Submillimeter, and Far-Infrared Detectors and Instrumentation for Astronomy VIII. p. 99140S (arXiv:1607.04668), doi:10.1117/12.2233894 17

Guilloux F., Fay G., Cardoso J.-F., 2007, preprint, (arXiv:0706.2598) 18

Guth A. H., 1981, Phys.Rev.D, 23, 347 7

Hall N. R., et al., 2010, The Astrophysical Journal, 718, 632 31, 34

Hamimeche S., Lewis A., 2008, Phys. Rev. D, 77, 103013 69

Haslam C. G. T., Salter C. J., Stoffel H., Wilson W. E., 1982, Astronomy & Astrophysics, 47, 1 27

Hee S., Vázquez J. A., Handley W. J., Hobson M. P., Lasenby A. N., 2017, Monthly Notices of the Royal Astronomical Society, 466, 369 54

Herault J., Jutten C., 1986, in American Institute of Physics Conference Series. pp 206–211, doi:10.1063/1.36258 48

Hinshaw G., et al., 2007, Astrophysical Journal, Supplement, 170, 288 44

Hinshaw G., et al., 2013a, Astrophysical Journal, Supplement, 208, 19 14

Hinshaw G., et al., 2013b, Astrophysical Journal, Supplement, 208, 19 112

Hivon E., Górski K. M., Netterfield C. B., Crill B. P., Prunet S., Hansen F., 2002, The Astrophysical Journal, 567, 2 20

Hobson M. P., Lasenby A. N., 1998, Monthly Notices of the Royal Astronomical Society, 298, 905 41

Hobson M. P., Jones A. W., Lasenby A. N., Bouchet F. R., 1998, Monthly Notices of the Royal Astronomical Society, 300, 1 41

Hobson M. P., Barreiro R. B., Toffolatti L., Lasenby A. N., Sanz J., Jones A. W., Bouchet F. R., 1999, Monthly Notices of the Royal Astronomical Society, 306, 232 41

Hojjati A., Pogosian L., Zhao G.-B., 2011, Journal of Cosmology and Astroparticle Physics, 8, 005 111

Hu W., Dodelson S., 2002, Annual Review of Astronomy and Astrophysics, 40, 171 7

Hu W., Sugiyama N., Silk J., 1996, ArXiv Astrophysics e-prints, 8

Huffenberger K. M., Eriksen H. K., Hansen F. K., 2006, The Astrophysical Journal Letters, 651, L81 12, 100

Humphreys E. M. L., Reid M. J., Moran J. M., Greenhill L. J., Argon A. L., 2013, The Astrophysical Journal, 775, 13 115

Huterer D., Linder E. V., 2007, Phys. Rev. D, 75, 023519 108

Hyvärinen A., 1999, IEEE Signal Processing Letters, 6, 145 62

Hyvärinen A., Oja E., 1997, Neural Computation, 9, 1483 62

Hyvärinen A., Karhuen J., Oja E., 2001, Independent Component Analysis. John Wiley & Sons 48

Hyvärinen A., Karhunen J., Oja E., 2002, Feature Extraction by ICA. John Wiley & Sons, Inc., pp 389–406, doi:10.1002/0471221317.ch21, http://dx.doi.org/10.1002/0471221317.ch21 48

Ichiki K., 2014, Progress of Theoretical and Experimental Physics, 2014, 06B109 23, 39

Ichiki K., Kaji R., Yamamoto H., Takeuchi T. T., Fukui Y., 2014, The Astrophysical Journal, 780, 13 30

Inoue Y., et al., 2016, in Millimeter, Submillimeter, and Far-Infrared Detectors and Instrumentation for Astronomy VIII. p. 99141I (arXiv:1608.03025), doi:10.1117/12.2231961 17

Jordan P., 1955, Schwerkraft und Weltall: Grundlagen d. theoret. Kosmologie. Mit 13 Abb. Die Wissenschaft, Vieweg, http://books.google.it/books?id=snJTcgAACAAJ 107

Jutten C., Comon P., 2010, in Comon P., Jutten C., eds, , Handbook of Blind Source Separation. Academic Press, Oxford, pp 1 – 22, doi:10.1016/B978-0-12-374726-6.00006-0 48

Kamionkowski M., Kosowsky A., 1999, Annual Review of Nuclear and Particle Science, 49, 77 7

Keisler R., et al., 2015, The Astrophysical Journal, 807, 151 17

Kellermann K. I., Pauliny-Toth I. I. K., 1969, The Astrophysical Journal, 155, L71 32

Kullback S., Leibler R. A., 1951, Ann. Math. Statist., 22, 79 53

Kunz M., Sapone D., 2007, Physical Review Letters, 98, 121301 108

Lacasa F., Aghanim N., Kunz M., Frommert M., 2012, Monthly Notices of the Royal Astronomical Society, 421, 1982 31

Lagache G., Abergel A., Boulanger F., Désert F. X., Puget J.-L., 1999, Astronomy & Astrophysics, 344, 322 35

Lagache G., Puget J.-L., Dole H., 2005, Annual Review of Astronomy and Astrophysics, 43, 727 23, 34

Lamarre J.-M., et al., 2010, Astronomy & Astrophysics, 520, A9 15

Laureijs R., et al., 2011, preprint, (arXiv:1110.3193) 117

Lazear J., et al., 2014, in Millimeter, Submillimeter, and Far-Infrared Detectors and Instrumentation for Astronomy VII. p. 91531L (arXiv:1407.2584), doi:10.1117/12.2056806 16

Leach S. M., et al., 2008, Astronomy & Astrophysics, 491, 597 39, 63

Lesgourgues J., 2011, preprint, (arXiv:1104.2932) 112

Lewis A., Bridle S., 2002a, Phys. Rev. D, 66, 103511 90

Lewis A., Bridle S., 2002b, Phys. Rev., D66, 103511 90

Li Y.-C., Wu F.-Q., Chen X., 2013, Phys. Rev. D, 88, 084053 113, 114

Liddle A. R., Mazumdar A., Barrow J. D., 1998, Phys. Rev. D, 58, 027302 110

Liu H., Mertsch P., Sarkar S., 2014, The Astrophysical Journal Letters, 789, L29 29

Louis T., et al., 2017, Journal of Cosmology and Astroparticle Physics, 6, 031 16, 17

Ma C.-P., Bertschinger E., 1994, ArXiv Astrophysics e-prints, 106, 107

Macellari N., Pierpaoli E., Dickinson C., Vaillancourt J. E., 2011, Monthly Notices of the Royal Astronomical Society, 418, 888 29

Maino D., et al., 2002, Monthly Notices of the Royal Astronomical Society, 334, 53 48, 62

Maino D., Banday A. J., Baccigalupi C., Perrotta F., Górski K. M., 2003, Monthly Notices of the Royal Astronomical Society, 344, 544 63

Maino D., Donzelli S., Banday A. J., Stivoli F., Baccigalupi C., 2007, Monthly Notices of the Royal Astronomical Society, 374, 1207 62

Mak D. S. Y., Challinor A., Efstathiou G., Lagache G., 2017, Monthly Notices of the Royal Astronomical Society, 466, 286 35, 36, 73

Marsh D. J. E., 2016, Physics Reports, 643, 1 5

Millea M., 2017, CosmoSlik: Cosmology sampler of likelihoods, Astrophysics Source Code Library (ascl:1701.004) 90

Millea M., Doré O., Dudley J., Holder G., Knox L., Shaw L., Song Y.-S., Zahn O., 2012, The Astrophysical Journal, 746, 4 30, 34

Mocanu L. M., et al., 2013, The Astrophysical Journal, 779, 61 33

Moudden Y., Cardoso J.-F., Starck J.-L., Delabrouille J., 2005, EURASIP Journal on Applied Signal Processing, 2005, 484606 61

Naess S., et al., 2014, Journal of Cosmology and Astroparticle Physics, 10, 007 23

Nagata R., Chiba T., Sugiyama N., 2002, Phys. Rev. D, 66, 103510 112

Nagata R., Chiba T., Sugiyama N., 2004, Phys. Rev., D69, 083512 114

Narcowich F. J., Petrushev P., Ward J. D., 2006, SIAM Journal on Mathematical Analysis, 38, 574 18

Negrello M., Perrotta F., González J. G.-N., Silva L., De Zotti G., Granato G. L., Baccigalupi C., Danese L., 2007, Monthly Notices of the Royal Astronomical Society, 377, 1557 34

Page L., et al., 2003, Astrophysical Journal, Supplement, 148, 233 12

Page L., et al., 2007, Astrophysical Journal, Supplement, 170, 335 112

Paoletti D., Aghanim N., Douspis M., Finelli F., De Zotti G., Lagache G., Pénin A., 2012, Monthly Notices of the Royal Astronomical Society, 426, 496 91

Patanchon G., Snoussi H., Cardoso J. F., Delabrouille J., 2003, ArXiv Astrophysics e-prints, 60, 62

Patanchon G., Cardoso J.-F., Delabrouille J., Vielva P., 2005, Monthly Notices of the Royal Astronomical Society, 364, 1185 45, 60, 62, 63

Perrotta F., Baccigalupi C., Matarrese S., 2000, Phys. Rev. D, 61, 023507 10, 112

Pham D.-T., 2005, IEEE Signal Processing Letters, 12, 536 51

Pham D.-T., Cardoso J.-F., 2001, IEEE Trans. Signal Processing, 49, 1837 51, 52

Pham D. T., Garat P., 1997, IEEE Transactions on Signal Processing, 45, 1712 52

Planck Collaboration I et al., 2016, Astronomy & Astrophysics, 594, A1 4, 9, 24

Planck Collaboration IX et al., 2016, Astronomy & Astrophysics, 594, A9 7, 11, 39, 40, 42, 60, 61, 66, 71, 91

Planck Collaboration X et al., 2016, Astronomy & Astrophysics, 594, A10 24, 25, 26, 29, 40, 41, 60, 75, 76, 81

Planck Collaboration XI et al., 2016, Astronomy & Astrophysics, 594, A11 14, 23, 25, 28, 35, 37, 67, 80, 89, 90, 91, 96, 99

Planck Collaboration XII 2014, Astronomy & Astrophysics, 571, A12 39, 60, 66

Planck Collaboration XIII et al., 2016, Astronomy & Astrophysics, 594, A13 4, 12, 67

Planck Collaboration XLVIII Aghanim, N. Ashdown, M. Aumont, J. Baccigalupi, C. Ballardini, M. Banday, A. J. et al. 2016, Astronomy & Astrophysics, 596, A109 24, 27, 35, 44, 76

Planck Collaboration XV et al., 2014, Astronomy & Astrophysics, 571, A15 36, 37, 67

Planck Collaboration XVI et al., 2014, Astronomy & Astrophysics, 571, A16 35, 113, 115

Planck Collaboration XXX et al., 2014, Astronomy & Astrophysics, 571, A30 35, 36, 74, 75, 76, 77, 80, 89

Planck Collaboration et al., 2011, Astronomy & Astrophysics, 536, A18 35

Planck Collaboration et al., 2013, Astronomy & Astrophysics, 550, A133 33

Planck Collaboration et al., 2014a, Astronomy & Astrophysics, 565, A103 28

Planck Collaboration et al., 2014b, Astronomy & Astrophysics, 571, A1 112, 113

Planck Collaboration et al., 2014c, Astronomy & Astrophysics, 571, A6 130

Planck Collaboration et al., 2014d, Astronomy & Astrophysics, 571, A8 130

Planck Collaboration et al., 2014e, Astronomy & Astrophysics, 571, A13 30

Planck Collaboration et al., 2014f, Astronomy & Astrophysics, 571, A28 32, 33

Planck Collaboration: et al., 2015, Astronomy & Astrophysics, 580, A13 27, 29

Planck Collaboration et al., 2016a, Astronomy & Astrophysics, 586, A132 23

Planck Collaboration et al., 2016b, Astronomy & Astrophysics, 594, A15 72

Planck Collaboration et al., 2016c, Astronomy & Astrophysics, 594, A17 8, 72

Planck Collaboration et al., 2016d, Astronomy & Astrophysics, 594, A24 37

Planck Collaboration et al., 2016e, Astronomy & Astrophysics, 594, A25 26, 28, 29

Planck Collaboration et al., 2016f, Astronomy & Astrophysics, 594, A26 30, 31, 33

Planck Collaboration et al., 2016g, Astronomy & Astrophysics, 594, A27 31, 37

Planck HFI Core Team et al., 2011, Astronomy & Astrophysics, 536, A6 30

Puglisi G., Fabbian G., Baccigalupi C., 2017, Monthly Notices of the Royal Astronomical Society, 469, 2982 30

Reichardt C. L., et al., 2012, The Astrophysical Journal, 755, 70 17

Remazeilles M., Delabrouille J., Cardoso J.-F., 2011, Monthly Notices of the Royal Astronomical Society, 418, 467 44

Riazuelo A., Uzan J.-P., 2002, Phys. Rev. D, 66, 023525 112

Ricciardi S., et al., 2010, Monthly Notices of the Royal Astronomical Society, 406, 1644 43

Riess A. G., et al., 2011, The Astrophysical Journal, 730, 119 115

Riess A. G., et al., 2016, The Astrophysical Journal, 826, 56 4, 115

Roberts S., Everson R., 2001, Independent Component Analysis: Principles and Practice. Cambridge University Press 48

Rogers K. K., Peiris H. V., Leistedt B., McEwen J. D., Pontzen A., 2016, Monthly Notices of the Royal Astronomical Society, 460, 3014 44

Ross A. J., Samushia L., Howlett C., Percival W. J., Burden A., Manera M., 2015, Monthly Notices of the Royal Astronomical Society, 449, 835 113

Samtleben D., Staggs S., Winstein B., 2007, Annual Review of Nuclear and Particle Science, 57, 245 8, 13

Scott D., Srednicki M., White M., 1994, The Astrophysical Journal Letters, 421, L5 19

Seiffert M., Borys C., Scott D., Halpern M., 2007, Monthly Notices of the Royal Astronomical Society, 374, 409 23

Seljak U., Zaldarriaga M., 1997, Physical Review Letters, 78, 2054 10

Shapiro S. S., Davis J. L., Lebach D. E., Gregory J. S., 2004, Phys. Rev. Lett., 92, 121101 111

Stivoli F., Baccigalupi C., Maino D., Stompor R., 2006, Monthly Notices of the Royal Astronomical Society, 372, 615 63

Stolyarov V., Hobson M. P., Ashdown M. A. J., Lasenby A. N., 2002, Monthly Notices of the Royal Astronomical Society, 336, 97 41

Strong A. W., Orlando E., Jaffe T. R., 2011, Astronomy & Astrophysics, 534, A54 26

Sunyaev R. A., Zeldovich Y. B., 1970, Comments on Astrophysics and Space Physics, 2, 66 36

Sunyaev R. A., Zeldovich Y. B., 1972, Comments on Astrophysics and Space Physics, 4, 173 36

Suzuki A., et al., 2016, Journal of Low Temperature Physics, 184, 805 17

Tegmark M., Efstathiou G., 1996, Monthly Notices of the Royal Astronomical Society, 281, 1297 33, 45, 46, 130

Tegmark M., de Oliveira-Costa A., Hamilton A. J., 2003, Phys. Rev. D, 68, 123523 44, 45

The EBEX Collaboration et al., 2017, preprint, (arXiv:1703.03847) 16

The POLARBEAR Collaboration et al., 2017, preprint, (arXiv:1705.02907) 17

Thornton R. J., et al., 2016, Astrophysical Journal, Supplement, 227, 21 17

Tibbs C. T., et al., 2016, Monthly Notices of the Royal Astronomical Society, 456, 2290 28

Toffolatti L., Burigana C., Argueso F., Diego J. M., 2013, preprint, (arXiv:1302.3355) 32

Tsujikawa S., 2007, Phys. Rev. D, 76, 023514 111

Tsujikawa S., 2013, Classical and Quantum Gravity, 30, 214003 5

Tucci M., Toffolatti L., 2012, Advances in Astronomy, 2012, 624987 23

Tucci M., Toffolatti L., de Zotti G., Martínez-González E., 2011, Astronomy & Astrophysics, 533, A57 32

Umiltà C., 2014, Master's thesis, Alma Mater Studiorum - Università di Bologna, Bologna (Italy) 104

Umiltà C., Ballardini M., Finelli F., Paoletti D., 2015, Journal of Cosmology and Astroparticle Physics, 8, 017 104, 112, 115, 116

Umiltà C., Cardoso J., Benabed K., Le Jeune M., 2017, in preparation for submission to A&A 66

Vansyngel F., Wandelt B. D., Cardoso J.-F., Benabed K., 2016, Astronomy & Astrophysics, 588, A113 39, 63

Vieira J. D., et al., 2010, The Astrophysical Journal, 719, 763 32, 33

Waldmann I. P., Tinetti G., Deroo P., Hollis M. D. J., Yurchenko S. N., Tennyson J., 2013, The Astrophysical Journal, 766, 7 48

Weinberg S., 1989, Rev. Mod. Phys., 61, 1 5

Weinberg S., 2008, Cosmology. Oxford University Press 8

Wu F.-Q., Chen X., 2010, Phys. Rev. D, 82, 083003 114

Wu F.-Q., Qiang L.-E., Wang X., Chen X., 2010, Phys. Rev. D, 82, 083002 112

Ysard N., Miville-Deschênes M. A., Verstraete L., 2010, Astronomy & Astrophysics, 509, L1 28

Yu X., Hu D., Xu J., 2014, Blind Source Separation: Theory and Applications. John Wiley & Sons, Singapore Pte. Ltd 48

Zaldarriaga M., Spergel D. N., Seljak U., 1997, The Astrophysical Journal, 488, 1 10, 12

Zhao G.-B., Pogosian L., Silvestri A., Zylberberg J., 2009, Phys. Rev. D, 79, 083513 111

Zhao G.-B., Li H., Linder E. V., Koyama K., Bacon D. J., Zhang X., 2012, Phys. Rev. D, 85, 123546 111

Zhu W. W., et al., 2015, The Astrophysical Journal, 809, 41 116

Zumalacarregui M., Bellini E., Sawicki I., Lesgourgues J., Ferreira P. G., 2016, preprint, (arXiv:1605.06102) 112

de Zotti G., Ricci R., Mesa D., Silva L., Mazzotta P., Toffolatti L., González-Nuevo J., 2005, Astronomy & Astrophysics, 431, 893 32, 34